Technische Universität München

ANNUAL REPORT 2007
Forschungs-Neutronenquelle Heinz Maier-Leibnitz (FRM II)

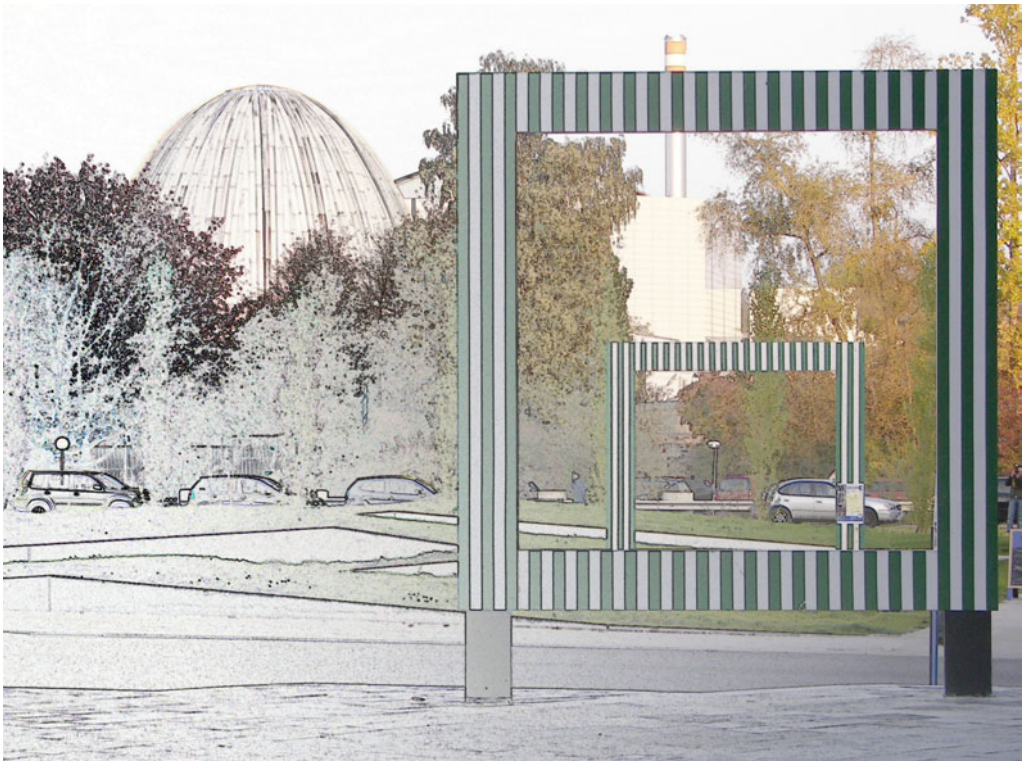

Title image: View on the FRM and FRM II on the “Lange nacht der Wissenschaften”

Contents

Directors' report

In 2007 - the 3rd year of its routine operation - the Forschungs-Neutronenquelle Heinz Maier-Leibnitz (FRM II) operated for 233 days with full power (20 MWatt). The originally envisaged 5 reactor cycles could not yet be reached, due to a failure of a pump in the D_2O moderator system which occurred in the course of the 10th reactor cycle right at the beginning of the year. The repair of that pump required the painstaking opening of the D_2O circuit. But with the enthusiastic commitment of our staff and help from the hot workshop of Kernkraftwerk Isar FRM II was able to restart with the 11th reactor cycle on time.

In early spring 2007 the east building with its large second neutron guide hall was finished and the Jülich Centre for Neutron Sciences (JCNS) moved into its offices and labs on top of the guide hall. This all together was celebrated in an inauguration event on 9th of May 2007. Step by step the first instruments of the JCNS went into operation and typical gains in performance by factors 10 to 100 are achieved, compared with their performance at DIDO, FZ-Jülich. In this case gain in performance is defined by increase in flux at the detector times increase in resolution. This gain is the result of both, higher flux of the neutron guides at FRM II and a sophisticated upgrade of each of the instruments. Two proposal rounds for the JCNS instruments took already place in 2007.

With its instrumentation for nuclear and particle physics FRM II participates actively in the excellence cluster "Structure and Origin of the Universe". On the other hand the excellence cluster is heavily engaged in the realisation of the Ultra Cold Neutron Source at the FRM II.

In July 2007 the Federal Ministry for Education and Science (BMBF) renewed its engagement in funding instruments at FRM II. PUMA, SPODI, polarized HEIDI and biological sample environment at RefSANS which continue to be under the patronage of BMBF. Also further funds for three more instruments or upgrades were allocated, such as POWTEX, KOMPASS and automatic sample set-up at StressSpec. The universities in charge of the BMBF instruments are Universität Göttingen, TU Darmstadt, RWTH Aachen, LMU Munich, Universität zu Köln and TU Clausthal. Some of them are even engaged in several instruments.

So in 2007, for the first time, laboratory courses for the advanced semesters of the study of physics at the Physics Department took place at selected instruments of FRM II. During each course a 24-hour hands-on-training on a particular instrument was practiced with subsequent evaluation of the results.

Similar training was conducted within the annually organized neutron school of the FZ-Jüich, where during a one week crash course about 40 PhD students from all over Europe learnt the essentials of neutron scattering and which was completed by a one week training at the instruments installed at FRM II.

In early 2007 FRM II got the approval for treating tumors by fast neutron irradiation from the Bavarian State Authority for Environment Protection (Landesamt für Umweltschutz). This was subsequently executed by the irradiation of the first patient, sent from TUM's own clinic. The typical treatment of a tumor is up to 5 irradiations, each treatment taking 60 - 90 seconds of irradiation time.

On October 31, 1957 the Forschungsreaktor München, better known as Atomic Egg, produced its first neutrons. The Atomic Egg became Germany's first nuclear facility. It became the seed of what is now-a-days Germany's largest campus for science and engineering. On 31st of October 2007 we celebrated the 50th anniversary of that event by a colloquium "50 years of neutron research at Garching - and its future". Being just three weeks in office the Bavarian Minister President Dr. Günther Beckstein emphasized the importance of the Neutron Research Source Heinz Maier-Leibnitz for the scientific and economic development of Bavaria and highlighted its role as a contribution of Germany to the European Research Area. He renewed the commitment of the Bavarian Free State for its largest research facility with great enthusiasm. "Neutrons are light", with these words Prof. Dr. Dr. h.c. mult. Wolfgang Herrmann, President of the TUM, explained the unique potential of science with neutrons. He welcomed FZ-Jülich, which had taken in use its new outstation "Jülich Center for Neutron Sciences" at the FRM II short time before. Dr. Walther Hohlefelder, member of the board of the electricity producer E.ON spoke about "The Future of Nuclear Power in Europe and Germany", a future clearly decided for Europe, but less evidently for Germany. In his speech "The neutron, in nuclear and particle physics" Prof. Dr. Schreckenbach, former Technical Director of FRM II, delivered insight into the beauty of fundamental physics with neutrons. These neutrons are a powerful tool for engineering science and were impressively demonstrated by the talk "Industrial research with neutrons" of Prof. Dr. Richard Wagner, Director of the Institute Laue Langevin. The colloquium was finished by an outlook of Prof. Bernhard Keimer, MPI for

Solid State Research on "Correlated electron systems, on the way to new materials".

Obviously FRM II did very well in 2007. So the Bavarian nuclear regulatory authority made a Christmas gift to FRM II. On 19th of December 2007 FRM II was authorized to use its single compact core for 60 days, instead of 52 days. In fact this is a further proof of the extremely conservative and reliable design of the FRM II fuel element. The decision itself has considerable impact onto the future operation of FRM II. About one fuel element less is needed per year and consequently the work load of changing the fuel element is reduced in addition to the reduced nuclear transports and amount of spent fuel. Also annual operating costs will be reduced by maintaining the availability of the neutron source.

Further progress has been achieved in developing high density fuels for future use in FRM II. Large fuel plates made of UMo particles embedded in an Al matrix and with an Uranium density of 8g Ucm^3 were irradiated to neutron fluences exceeding the burn-up at FRM II by 50%. A conservative swelling of these fuel plates at low and medium burn-up is followed by a critical increase of the fuel plates thickness for high burn-up. Clearly further R & D has to be done before such a fuel can be used in high performance research reactors. However, these and other tests have shown the way to pursuit.

Altogether 20 beam hole instruments have been operating by the end of 2007. Another 10 instruments are under construction. Finances for the new instruments are mainly coming from FRM II, JCNS and BMBF, but also from the universities engaged. A prominent example is the contribution of the excellence cluster "Structure and Origin of the Universe" for the implementation of the Ultra Cold Neutron Source (UCN). As the last of these new instruments the UCN will be taken in operation in 2012.

Excellent science is done at the instruments of FRM II. An example for many of them is the experiment conducted by Christian Pfleiderer, (Science 316, 1871 (2007)). By means of resonant spin echo techniques he was able to measure changes in lattice parameters with a 10^{-6} precision. Part of the beauty of this experiment is that this can be done under extreme sample conditions like Millikelvin temperatures or high pressure and there is hope to ameliorate the precision to a 10^{-7} level.

With deepest sympathy we have to report about the sudden death of Guido Engelke, former Administrative Director. He passed away on 4 March 2008 on a trip through Namibia. In December 1994 Mr. Guido Engelke started working for FRM II as project supervisor. From 1st of January 2002 until December 2006 he filled the position of Administrative Director of FRM II. From the very beginning Mr. Engelke was in charge of the licensing process and the construction of the neutron source. His experience acquired during many years world-wide as well as his hard work and dedication were essential for the successful commissioning of FRM II. We will continue to honour the memory of Mr. Guido Engelke.

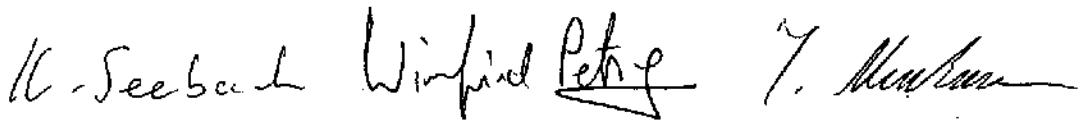

Klaus Seebach Winfried Petry Ingo Neuhaus

The year in pictures

22 January 07: Students from the German-French Lycée Jean Renoir in Munich enjoy their visit at the neutron research source (photo: Ulla Baumgart).

5 – 7 February 2007: Fortgeschrittenen-Praktikum (Hands-on training for advanced students): Students from the TU Physics Department during the theoretical part of the course together with Prof. Schreckenbach, one of the speakers.

9 May 07: Inauguration ceremony of the new East Building providing labs and offices for staff of JCNS and GKSS: The rainy weather could not spoil the cheerful atmosphere of that day.

9 May 07: From right to left: Prof. Dr.-Ing. Th. Hugues, the responsible architect; Mr. Solbrig, Mayor of the town of Garching; Dr. Ingo Neuhaus and G. Engelke, Technical respectively former Administrative Director FRM II; Mr. H. Mayer, responsible Building Director, BATUM; Prof. Dr. h.c. mult. Wolfgang A. Herrmann, President of Technische Universität München; Dr. R. Koepke, BMBF; Prof. Dr. Winfried Petry and Dr. Klaus Seebach, Scientific respectively Administrative Director of FRM II.

9 May 07: Happy about the new premises for the Jülich Centre for Neutron Science (JCNS) – Prof. Dr. Th. Brückel, head of JCNS, (together with Prof. Petry) and Dr. Alexander Ioffe, head of the outstation JCNS at FRM II.

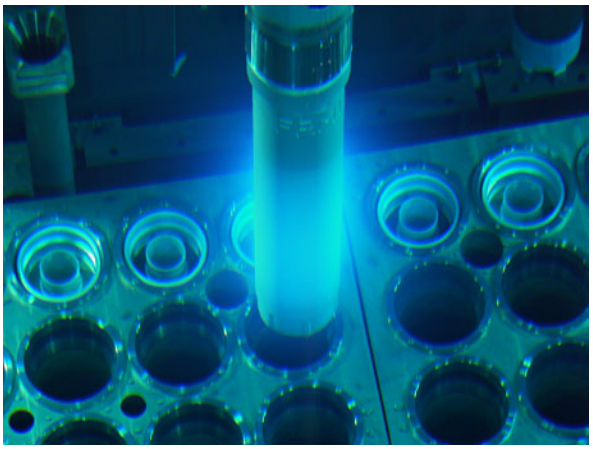

23 May 07: The spent fuel unit is moved into the neutralization pool.

3 – 14 September 07: Attendees of the 11th JCNS Laboratory Course organized jointly by JCNS and FRM II in front of the Jülich neutron spin echo spectrometer (J-NSE).

27 September 07: “Reading in unusual places” – In the neutron guide hall of FRM II the well-known German novelist Asta Scheib read chapters from her book “Sei froh, dass Du lebst” describing feelings and life in Germany in the fifties and sixties.

27 September 07: Tunes of the postwar period played by the group “Garchinger Pfeiffer” made memories come back.

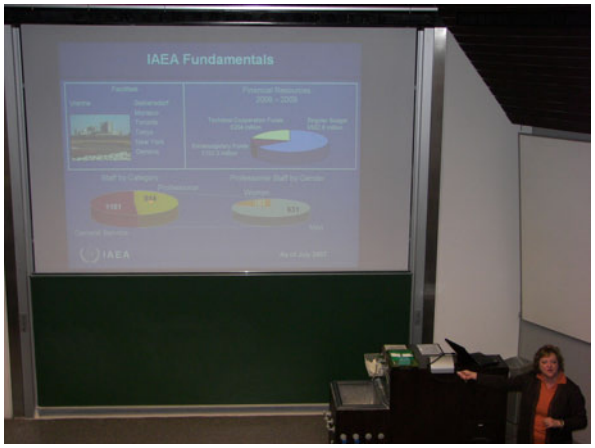

08 October 2007: The IAEA offers a variety of career chances to scientists, explained Catherine Monzel, responsible for recruitment and staff development at IAEA, during her speech on aims and tasks of International Atomic Energy Agency.

13 October 2007: Open Doors in 2007 - The Long Night of Science attracts a large number of persons interested in guided tours and topics related to FRM II.

13 October 2007: Radioprotection staff is explaining the tools they need to fulfil their tasks.

13 October 2007: Dr. Tobias Unruh is showing round children and youth – a unique opportunity at the Open Doors.

30 October 07: 1st user meeting at FRM II - Scientific discussions in a relaxed atmosphere: Dr. Peter Geltenbort, ILL Grenoble, together with Prof. Böni, Dr. Georgii and Dr. Zeitelhack, FRM II respectively Physics (clockwise).

31 October 07: On a beautiful autumn day the campus of Garching celebrated the 50th anniversary of it's first neutrons with a colloquium "50 years of research with neutrons at Garching and its future". Dr. Günther Beckstein, Minister President of Bavaria and the President of Technische Universität München, Prof. Dr. h. c. mult. W.A. Herrmann, in front of the Atomic Egg, the symbol for the commencement of neutron research in Germany.

Part I

Instrumentation

1 Central services and reactor

1.1 Detector and electronics lab

I. Defendi [1], **C. Hesse** [1], **M. Panradl** [1], **T. Schöffel** [1], **K. Zeitelhack** [1]
[1] ZWE FRM II, TU München

Beside the standard activities concerning service and maintenance of the detectors installed at the scientific instruments, two outstanding new detector projects distinguished our activities in 2007. In the following sections we will report on the development of the new SANS1 detector presently under construction and the first beam test results of a readout system for 320×320 individual channels of a fast, medium resolution MWPC developed in the framework of the NMI3-JRA2 (MILAND) project.

The SANS1 Detector

The new small-angle scattering instrument SANS1 presently being installed in the neutron guide hall will be equipped with a 2D-position sensitive detector with $1\times1\,\mathrm{m}^2$ active area, 8 mm×8 mm position resolution and 1 MHz global count rate capability. Similar to the D22 detector at ILL, the detector consists of a linear array of 1 m long position sensitive ^{3}He-detectors of type Reuter Stokes P4-0341-201 (length $L = 1$ m, diameter $d = 8$ mm, $p_{He} = 15$ bar) mounted inside the evacuated flight tube.

The individual detectors will be readout by the *PSD8+* readout system for position sensitive proportional counters developed by *mesytec*[1]. It consists of 16 *MSPD-8+* front end modules mounted inside the flight tube which are connected via bus signals to 2 *MCPD-8+* modules mounted in the counting house. In November 2007, we performed first system tests with a set of prototype readout modules at our test beam facility TREFF using a prototype detector consisting of 8 PSDs shown in Figure 1.1.

The *PSD8+* system used has been specifically adapted to the P4-0341-201 PSDs and features a shaping time constant $\tau = 1.0\mu$s. In Figure 1.2 the pulse height spectra of $\lambda = 4.7$Å neutrons recorded at TREFF are depicted as a function of the PSD anode voltage. Even at highest operation voltage the detectors allow an efficient separation of neutrons from gammas.

It was the main intention of the test to study the performance of the prototype detector system in terms of position resolution, linearity and homogeneity. The PSDs were scanned along the tube axis with a $\lambda = 4.7$Å neutron beam which was collimated by a slit system resulting in an intrinsic beam width of $d \approx 0.7$ mm. For each beam position the position spectrum was fitted using a Gaussian distribution and a linear fit was used for position calibration. Figure 1.3 shows a plot of the measured beam position versus the real beam position for 7 illuminated PSDs.

For a representative PSD, Figure 1.4 shows the resulting position resolution (FWHM) at five beam positions along the detector axis for various operating voltage settings. It reveals the symmetrical shape expected from theory and clearly surpasses the performance required for SANS1 ($\Delta x < 8$ mm).

Figure 1.1: Prototype detector consisting of 8 PSDs mounted at TREFF during the *PSD8+* readout system test

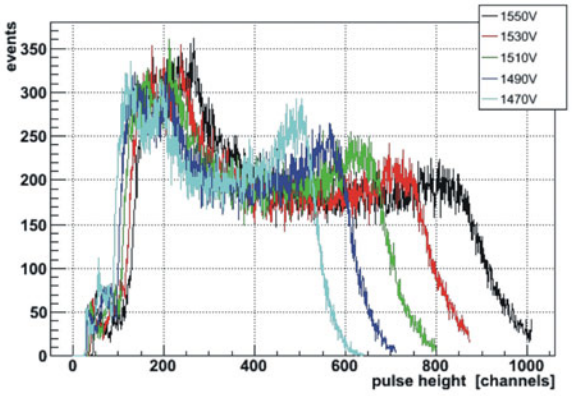

Figure 1.2: Neutron pulse height spectra for various anode voltage settings recorded with a P4-0341-201 PSD read out by the *PSD8+* system

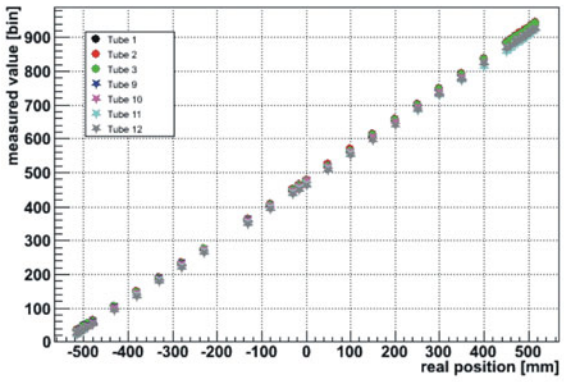

Figure 1.3: Measured beam position versus real beam position for 7 illuminated PSDs

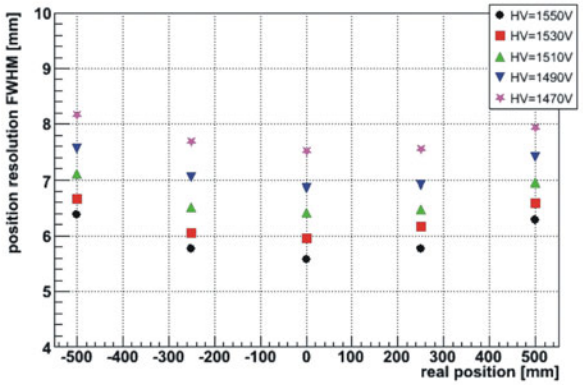

Figure 1.4: Position resolution (FWHM) along the detector axis for various anode voltage settings

Meanwhile all 128 PSDs of the SANS1 detector have been delivered and were successfully tested in a measurement campaign at TREFF in terms of homogeneity, active length and position resolution.

MILAND signal processing electronics

The NMI3-JRA2 (MILAND) project is dedicated to the development of a fast, high resolution ($\Delta x \approx 1$ mm) 2D-neutron detector based on a MWPC with 320×320 individual channel readout. Based on the layout already presented in[2] we built a 128×128 channel prototype of the corresponding signal processing electronics. In September 2007, a first system test was performed with the MILAND prototype detector[3] mounted at the ILL beam station CT2. A collimated beam of $\lambda = 2.5$Å neutrons was used to study the achievable resolution in the direction orthogonal to the anode wires using different algorithms for the position determination based on a Time-over-Threshold (ToT) measurement. Figure 1.5 shows the result for a fine scan along 2 mm covering 2 anode wires with the position resolution coming close to the envisaged performance. At present the series production of all modules required to fully equip the MILAND detector is in progress.

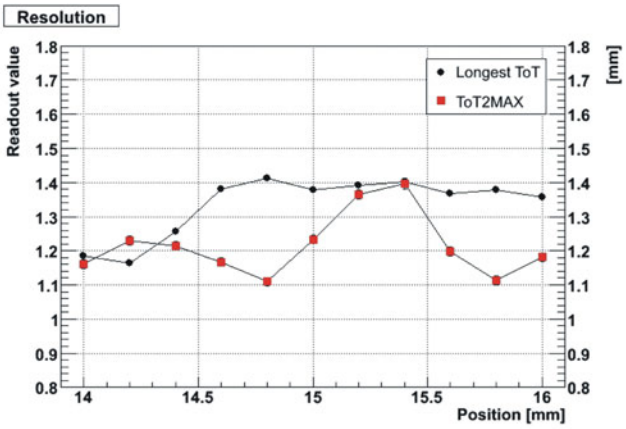

Figure 1.5: Position resolution (FWHM) of the MILAND detector (orthogonal to the anodes) for two different algorithms of position determination

[1] Fa. mesytec; Germany. `http://www.mesytec.com`.

[2] Defendi, I., *et al. FRM-II annual report 2006*, 8–9.

[3] Guerard, B., *et al. NMI3-JRA2 annual report 2006*, (2006).

1.2 HELIOS – polarized ^{3}He gas for neutron instrumentation

S. Masalovich[1], **O. Lykhvar**[1], **G. Borchert**[1], **W. Petry**[1,2]
[1]ZWE FRM II, TU München
[2]Physik-Department E13, TU München

HELIOS, the optical pumping facility, provides the ability of a large-scale production of a dense spin-polarized ^{3}He gas at FRM II. The use of polarized ^{3}He gas is of significant importance in many research areas where polarized gas is considered as a subject or a tool in investigations. In particular, it makes a great impact on the instrumentation for neutron polarization and polarization analysis since polarized nuclei of helium-3 possess very high spin-dependent neutron absorption efficiency over a wide range of neutron energies. Neutron spin filters (NSF) based on a dense hyperpolarized ^{3}He gas may compete in polarization efficiency with common devices such as magnetized single crystals or supermirrors [1]. Although these other methods are rather simple in operation, their applications are strongly limited by the acceptable neutron energy and the allowed range of scattering angles. In contrast, broadband neutron spin filters can be built to a predetermined size and shape in such a way that they will meet just about all practical needs (see Fig.1.6).

About sixty NSF cells have been filled with polarized ^{3}He gas in the year 2007. More than half of them were used in neutron experiments, while the other part served for testing of NSF cells and magnetostatic cavities.

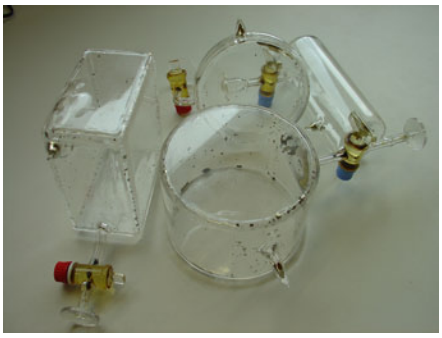

Figure 1.6: NSF cells at FRM II: for common use and instrument-oriented

Magnetostatic cavity

Magnetostatic cavity is an important unit used to hold the polarized ^{3}He NSF in a homogeneous guiding magnetic field and to screen the polarized gas against environmental magnetic field at a neutron instrument. Generally, the relaxation rate of a gas polarization in a NSF cell may be represented as a sum:

$$\frac{1}{T_1} = \frac{1}{T_{cell}} + \frac{1}{T_{mag}}$$

Here T_1 is the total relaxation time, T_{cell} – the relaxation time related to the cell (relaxation due to interactions with the cell walls and due to dipole-dipole interactions) and T_{mag} – the relaxation time related to the gradient of the magnetic field over the cell volume. The last term can be written as

$$\frac{1}{T_{mag}\,[h]} = \frac{1.7\cdot 10^4}{p\,[bar]} \left(\frac{\nabla |\vec{B}_\perp|}{B_0} \frac{1}{[cm]} \right)^2$$

where p is the gas pressure, B_0 refers to the mean value of a holding magnetic field and $B_\perp$ – to the component of the magnetic field normal to B_0. It follows then that the field gradient less than $3\cdot 10^{-4} cm^{-1}$ is required to assure $T_{mag} \geq 500h$ in a 1 bar pressure cell. Magnetostatic cavities aimed to provide such a homogeneous magnetic field have been developed in many groups working with polarized gas (see, for example, [2]). Typically they are based on an accurate design with a fixed geometry of a cavity and on an assumption about the value and space distribution of the environmental magnetic field at a neutron instrument. Actually, the last assumption brings about a free parameter in the design, which often cannot be evaluated in advance. As a result, the field gradients over the cell volume may differ significantly at different instruments. The other solution would be to build a cavity with excessive screening factor and hence heavy and/or large.

We have proposed and developed a new approach in designing a magnetostatic cavity. This approach is also based on an accurate design of a cavity capable to provide a highly uniform magnetic field. However, some magnetic components of the cavity are not fixed and can be moved and/or tilted. This additional movement can be used to perform a correction (tuning) of a magnetic field, if necessary. Of particular interest is the ability to tune an internal magnetic field in the presence of an inhomogeneous external field, which is usually the case at a neutron instrument with polarization analysis. Such TUneable Magnetostatic cavity (TUM-box) has been designed and built by the Neutron Optics group at FRM II (Fig.1.7).

Fig.1.8 shows the effect of tuning on the homogeneity of the holding field in the presence of a local external magnetic source.

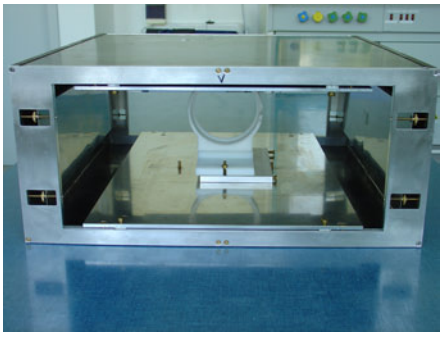

Figure 1.7: TUneable Magnetostatic cavity (TUM-box)

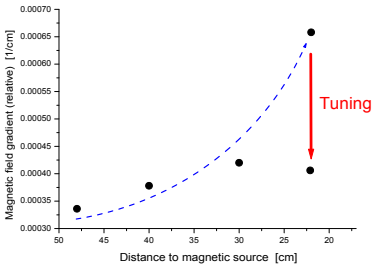

Figure 1.8: Effect of tuning in the presence of an external magnetic source. Bold circles – measured gradient of the holding field averaged over the cell volume ($10 \times 10 \times 10cm$). The dashed curve is only an eye-guiding line

It is clearly seen in Fig.1.8 that the field gradient over the cell volume increases as the distance between the TUM-box and external source decreases. After the gradient has been doubled the additional tuning was applied to bring the gradient down to the required value. This proves the ability to tune a holding field at a neutron instrument. The first TUM-box was used successfully in experiments at FRM II.

Experiments with neutrons

Because of a failure of one of our lasers, the mean value of a ^{3}He gas polarization in NSF cells reached only 71% instead of 76%. Nevertheless such a polarization was still good enough to perform neutron experiments. As an example, Fig.1.9 shows the result of the first SANS measurements on a protein sample with polarization analysis based on the use of a ^{3}He NSF, performed at the MIRA instrument [3].

Polarization analysis provides the ability to resolve spin-flip and non spin-flip components of the scattered beam, which can be used to distinguish coherent nuclear scattering from spin-incoherent nuclear scattering [4].

Neutron imaging with polarization analysis is another example of successful implementation of a ^{3}He NSF. This is based on the fact that a ^{3}He NSF does not disturb straight-line neutron trajectories and hence any imaging system with polarization analysis can profit from the use of a ^{3}He NSF. Such type of measurements have been performed at the instrument RESEDA with the aim of mapping the beam polarization over the entire beam cross section (see section 2.7).

An opaque spin filter [5] has been used successfully in many experiments at FRM II. Such a filter almost completely suppresses the transmission of one spin component of a neutron beam while another spin component has noticeable, even if very low, transmission. This filter possesses practically 100% analyzing efficiency and can be implemented in accurate measurements of beam polarization. The opaque spin filter was used, for example, at the instrument MIRA for testing the new V-shaped polarizer (2.5 m long) designed and constructed for the new SANS instrument at FRM II [6].

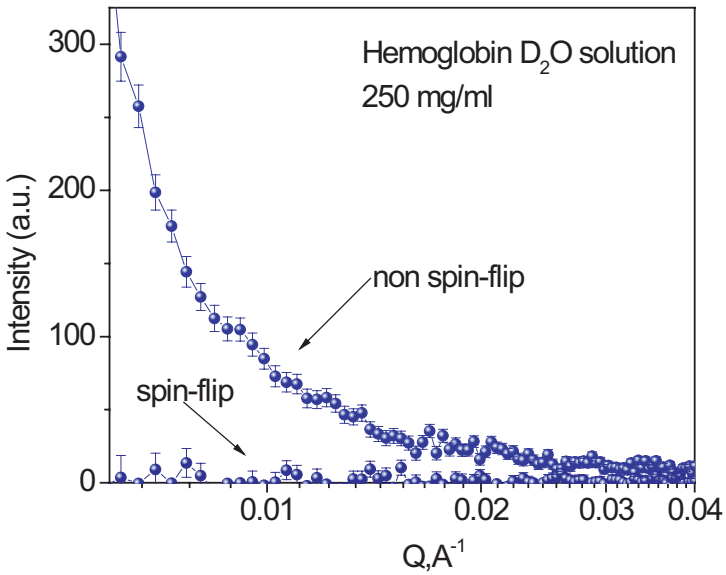

Figure 1.9: Corrected spin-flip and non spin-flip components of the small angle scattered beam resolved with a ^{3}He NSF analyzer. Results are reproduced from [3].

2×1 NSF

An alternative to an opaque spin filter is a new proposed 2×1 NSF [7] capable to provide a very accurate number of a beam polarization for a wide range of NSF parameters. The geometry of such NSF might be, for example, a rectangular cell with two sides sized 2:1 (2×1 NSF) (see Fig.1.10).

In this method the transmission of the neutron beam with initial polarization and with reversed one (the spin-flipper is either OFF or ON) is measured alternately along two sides of the same cell. Calculations show that the uncertainties in either ^{3}He gas polarization or cell opacity do not affect the accuracy of the measured neutron polarization and this accuracy is mostly limited by statistical errors. Experimental test of this method is planned for 2008.

[1] Cussen, L., Goossens, D., Hicks, T. *Nucl.Instr.Meth.*, A440, (2000), 409.

[2] Petoukhov, A., Guillard, V., Andersen, K., Bourgeat-Lami, E., Chung, R., Humblot, H., Jullien, D., Lelièvre-Berna, E., Soldner, T., Tasset, F., Thomas, M. *Nucl.Instr.Meth.*, A560, (2006), 480.

[3] Gaspar, A., Doster, W., Appavou, M.-S., Busch, S., Diehl, M., Häußler, W., Georgii, G., Masalovich, S. Report on FRM II experiment 665.

[4] Gentile, T., Jones, G., Thompson, A., Barker, J., Glinka, C., Hammouda, B., Lynn, J. *J.Appl.Cryst.*, 33, (2000), 771.

[5] Zimmer, O., Müller, T., Hautle, P., Heil, W., Humblot, H. *Phys.Lett.*, B455, (1999), 62.

[6] Gilles, R., Ostermann, A., *et al.* To be published.

[7] Masalovich, S. *Nucl.Instr.Meth.*, A581, (2007), 791.

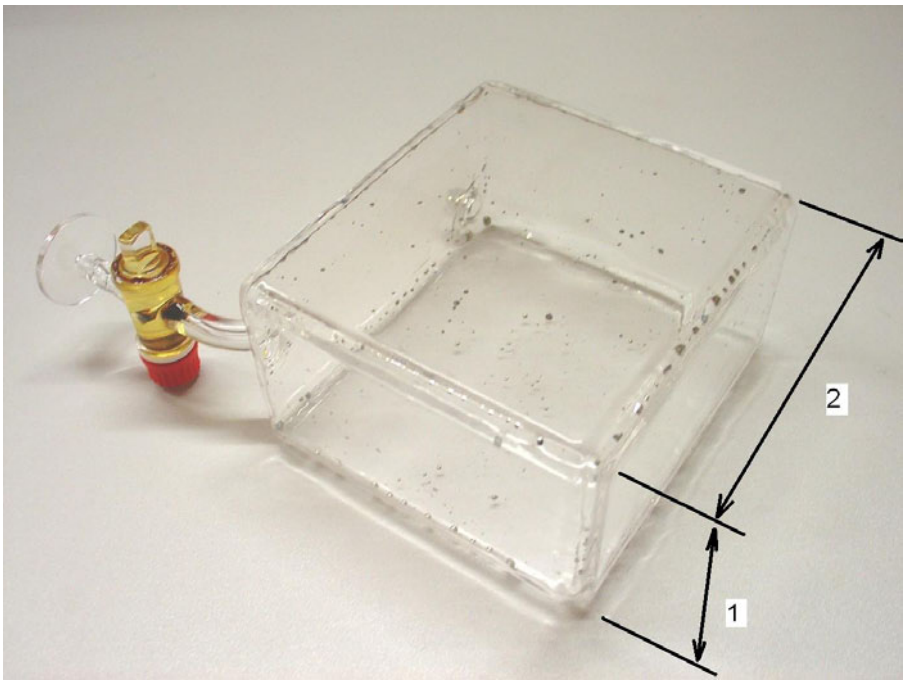

Figure 1.10: 2×1 NSF at FRM II

1.3 Sample environment

J. Peters[1], **H. Kolb**[1], **A. Schmidt**[1], **A. Pscheidt**[1], **J. Wenzlaff**[1], **P. Biber**[1]
[1]ZWE FRM II, TU München

In addition to instrument support in routine operation considerable work was done to improve the handling and availability of sample environment equipment. Now all closed cycle cryostats (CC) and the cryogen free 7,5 T magnet (CCM) are equipped with rotary feedthrough to allow maximum movability. In 2007 the CCM was operated for the first time on the instruments REFSANS, N-REX+, MIRA and SPODI resulting in considerable effort to integrate the magnet into the instrument set up.

A rotatable test bar fitting into our closed cycle cryostat (CCR) was developed and tested, being one alterative for sample rotation. The design of our 3He- and dilution inserts was re-engineered to decrease possibility of failure and facilitate adaptation to diverse experimental needs (e.g. feedthrough of capillaries, additional wiring etc.). The first cryogen free dilution insert was tested successfully reaching a base temperature of 42 mK. Unfortunately a cross over leak occurred in the unit. The problem will be fixed in early 2008.

The FRM II gas pressure generator was operated successfully in a high pressure, high temperature experiment on TOFTOF. The PLC controlled pressure generator provides a maximum pressure of 10 kbar and allows automation of pressure profile operation and remote control.

By reason of a strong request for larger sample tube diameters a new CCR was developed in cooperation with VeriCold Technologies GmbH. The cryostat provides a sample tube of 80mm diameter; all other dimensions are almost unchanged.

In the field of high temperatures, the second generation of our high temperature furnace (HTF) rack is now available. The rack is more powerful (400 A heater current) with a modular electronics design for operation of a DC power supply alternatively. A new HTF sample holder allows in situ vertical and rotational adjustment.

Figure 1.11: 10kbar gas generator

1.4 Reduced enrichment for the FRM II core

W. Petry[1], **H. Breitkreutz**[1], **K. Böning**[1], **R. Hengstler**[1], **R. Jungwirth**[1], **A. Röhrmoser**[1], **W. Schmid**[1], **P. Boulcourt**[2], **A. Chabre**[2], **S. Dubois**[2], **P. Lemoine**[2], **Ch. Jarousse**[3], **J.L. Falgoux**[3], **S. van den Berghe**[4], **A. Leenaers**[4]
[1]ZWE FRM II, TU München
[2]CEA Saclay, Gif-sur-Yvette, France
[3]AREVA-CERCA, Romans & Lyon, France
[4]SCK-CEN, Institute for Nuclear Materials Science, Mol, Belgium

The collaboration CEA-CERCA-TUM

In 2003 the Technische Universität München (TUM) launched a program for the development of high density fuel for research reactors with highest neutron flux. Principally this gain in density can then be used to reduce the enrichment of the fuel. Still a single compact core like that of FRM II can for physical reasons not be replaced by a compact core of Uranium enriched to less than 20 %(LEU). However, reduction to medium enrichment (MEU) is conceivable [1]. In a collaboration with the French Commissariat à l'Energie Atomique (CEA) and the company AREVA with its divisions NP and CERCA different metallurgical and methodological options are persecuted: i) irradiation of full size fuel plates made of UMo alloy particles dissolved in an Al matrix with an AlFeNi cladding, ii) tests of modified UMo alloys in various dispersions by heavy ion irradiation, iii) development of manufacturing processes for full size UMo monolithic foils including cladding, iv) calculation of the neutronics and thermohydraulics of possible high density fuel elements for the high flux reactor FRM II. For the purpose of post irradiation examinations (PIE) of the irradiated UMo fuel plates the Belgium Institute for Nuclear Materials Sciences SCKCEN joined this collaboration. v) Further, the irradiation tests for the qualification of the currently used U_3Si_2 dispers fuel have been re-evaluated. Detailed progress reports concerning i) - iv) can be found in the proceedings of the International Conference on Research Reactors Fuel Management RRFM [2, 3, 4, 5, 6], whereas the re-evaluation of the tests of the present fuel used for FRM II has been published in [7]. In the following summaries of the present progress states are given.

Irradiation of full size fuel plates made of UMo alloy particles dispersed in an Al matrix

Six large fuel plates with UMo alloy particles dissolved in an Al matrix had

been produced. The UMo powder was produced by means of grinding. An Uranium enrichment of 50% has been chosen and the Mo content in the UMo alloy has been set to 8 wt%. The Uranium density was set to nominal 7 gU/cm^3 for two of the test plates (No. 700x), the others were produced with a density of 8 gU/cm^3 (No. 800x). Further two of the test plates with a density of 8 gU/cm^3 (No. 850x) were dispersed in Al containing 2 wt% of Si. Irradiation at the MTR reactor OSIRIS at CEA-Saclay started in Sept. 2005 and most of the plates were irradiated for a total of 5 reactor cycles, whereas one plate was irradiated for a total of seven cycles. The four plates with nominal 8 gU/cm^3 density were distributed into two irradiation devices (core position 11 & 17). The plates with 7 gU/cm^3 were not inserted in the core and served as a reserve. The neutron spectra were rather identical for both positions, since they are at two similar edges of the OSIRIS core. Measurements of the swelling were done in situ mechanically after each cycle. In the course of the irradiation one of the plates with density of 8 gU/cm^3 had to be replaced by a plate of 7 gU/cm^3 due to technical reasons. The last irradiation cycle ended March 2007.

Fig. 1.12 summarizes the swelling at the hot spot of all irradiated IRIS-TUM plates. The following is easily perceived: i) All plates retain the fission products even at highest burn-up. ii) Swelling is minimal during the first 2 irradiation cycles, most probably due to the consumption of the build-in porosity of about 8 vol.%. iii) A more or less linear increase up to a fission density of about $2.0 \times 10^{21}\mathrm{cm}^{-3}$ is followed by a steeper and steeper increase in the course of adding up fission densities. iv) Plates with Si addition (850x) show a reduced swelling when compared to those without Si addition.

In comparison to other full size tests with UMo dispersive fuel it is observed: i) The swelling is higher than in IRIS-1 (also ground powder)[8] or IRIS-3 (atomized powder) [9], presumably because of the higher heat load and subsequent higher temperatures during the IRIS-TUM irradiation. ii) The "best" UMo plate with Si addition swells at a the target FD of $2.3 \times 10^{21}\mathrm{cm}^{-3}$ by 22 %, which is clearly more than the silicide fuel with a density ρ = 3 gU/cm^3.

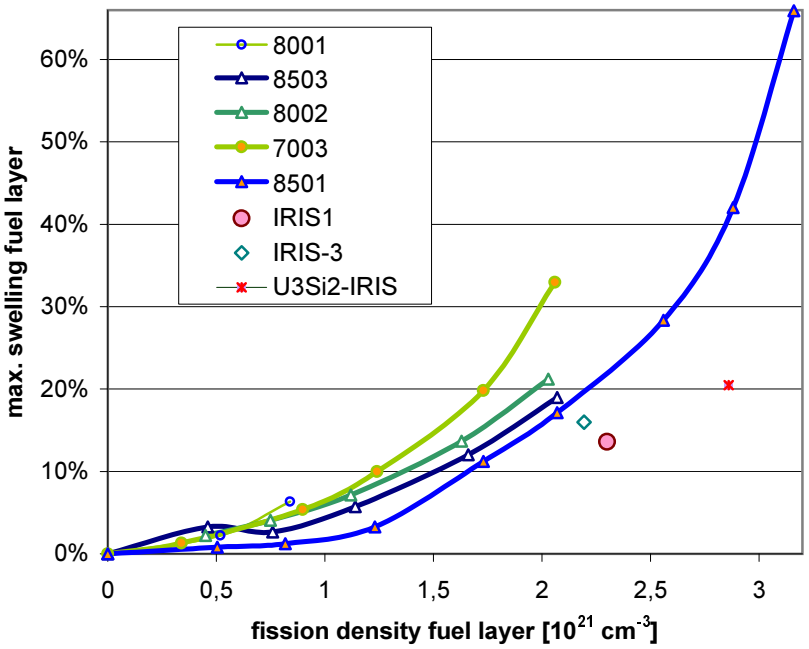

Figure 1.12: Comparison of the swelling at the hot spot of all IRIS-TUM plates. For comparison the maximum swelling observed for other full plate irradiation programs are also shown as there were IRIS-1 (ground powder), IRIS-3 (atomized powder) and IRIS-U_2Si_2 (ρ = 3 gU/cm^3) [7].

After about 1 year of cooling time the plates 8002 and 8503, both irradiated during the first 5 cycles, could be transported to CEA-Cadarache, where small samples have been cut out from the top corner and along the maximum flux plane (mfp) of the meat zone. These have been transported to SCKCEN, Mol, Belgium, where the samples have been prepared metallographically, and optical and scanning electron microscope examinations have been performed in hot cells. Fig. 1.13 (top) shows optical microscopy images of samples taken from the top end of the meat zone, i.e. a region of lower fission density. The shredded shape of the ground powder particles is clearly discernable. Dark lines within the UMo particles are presumably oxidized layers formed during the fabrication process. In the top-right image the Si precipitates in the Al meat are visible. In both samples an interdiffusion layer, known to be rich in Al, has been formed around the UMo particles. Scanning electron microscopy pictures with larger magnification - not shown here - show the distribution of the fission gas bubbles within the UMo particles mainly along grain boundaries. No fission gas bubbles are observed in the interdiffusion layer. The bottom part of Fig. 1.13 displays the average thickness of the interdiffusion layer measured along the mfp. Data have been grouped into 3 zones: thickness of the interdiffusion layer at the interface between cladding and meat, separately for the top and bottom interface (top and bottom with respect to the sample orientation) and in the centre of the meat. This interdiffusion layer forms during irradiation and is suspected to be related to the break-away swelling observed in previous irradiation tests of UMo fuel plates like IRIS-2 and FUTURE [8].

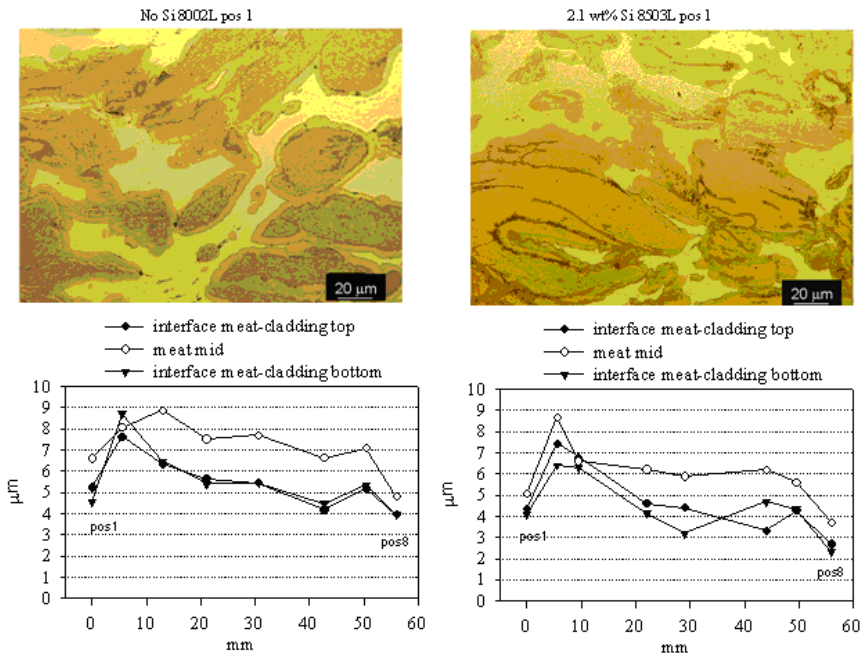

Figure 1.13: Top: Optical microscopy images of samples taken from the top end of plate 8002 (left) and 8503 (right) where the flux and fission densities are at about $\frac{2}{3}$ of the corresponding maximum flux plane (mfp) values. Bottom: Measured mean thickness of the Al rich interdiffusion layer along the mfp for three different positions: at the top interface between meat and cladding, in the middle of the meat layer and at the bottom interface between meat and cladding.

The post irradiation examinations (PIEs) of plates 8002 and 8503 will be continued, in particular electron probe micro-analysis is planned. Further, plates 8501 and 7003 with higher fission densities are awaiting their transport to hot cells, once their radiation level has lowered to tolerable values. A few preliminary conclusions can already be drawn at the actual state: i) In the mfp the matrix material is consumed to a very high extent. ii) From the metallurgical preparation of samples along the mfp it can be derived that the irradiated meat becomes extremely brittle, that means has a high tendency for developing cracks. iii) The interdiffusion layer is - if at all - only slightly reduced in the samples containing additional Si. iv) For the irradiation doses achieved in plate 8503 and 8002 the fission bubbles are accommodated in the UMo particles mainly along grain boundaries.

Summary/Outlook

For the first time large UMo dispersion fuel plates have been irradiated up to meat fission densities as high as $3.2 \times 10^{21}\mathrm{cm}^{-3}$ or to a LEU equivalent burn-up of 88 % - and at high heat load of $260 W/cm^2$. No failure of the first barrier - the cladding - has been observed, even at a thickness increase of 323 (which corresponds to 66% of "swelling"). Large build-in porosity delays the onset of linear swelling. During the irradiation, a period of almost linear increase of thickness is followed by a steeper, non linear increase of thickness. In the most favourable case this nonlinear increase begins at about $2.0 \times 10^{21}\mathrm{cm}^{-3}$, in the case of no additional Si at lower fission densities. The beginning of this nonlinear increase can be seen most clearly in the time and spatial dependence of the swelling. Fuel with Si added to the Al matrix swells a little less than that without Si additive. The microscope images from samples of plate 8503 and 8002 yet do not give a clear indication why this is the case. Growth of the interdiffusion layer is - if at all - only slightly hindered by addition of Si.

The progress achieved in this irradiation campaign is dominantly ascribed to the usage of ground powder. Why does ground powder show a more controlled swelling than atomized powder? A final answer has to wait for more detailed PIEs, as they are in progress. Certainly the ground particles have a defect density orders of magnitude higher than that of atomized particles. This higher defect density - and we explicitly include oxidation and additional impurities - form seeds for the nucleation of medium large fission bubbles, which again prevents diffusion of fission gases into the interdiffusion layer.

In spite of the progress reported here, we are still far away from high density fuel ($\rho \geq 8$ gU/cm^3) which withstands the high irradiation doses and rates as they occur in research reactors with highest neutron fluxes like FRM II. Also the best behaving fuel plate 8501 is far away from satisfying safety criteria as they are achieved in the present U_3Si_2 fuel. For instance, it has to be examined, how UMo fuel behaves under higher heat load because it is to suspect, that irradiation at higher temperature in the UMo grains will enhance diffusivity of the fission products. Fig. 1.12 gives a first hint on that. Both, IRIS-1 and IRIS-3 show less swelling than IRIS-TUM, and in both cases the temperature in the UMo grain has been much lower.

Therefore, TUM and its partners aim at future irradiation of large scale UMo dispersed test plates at heat loads in the order of 400 W/cm^2. Further it seems to be unrealistic to produce ground powder with 50% enrichment on an industrial scale as necessary to produce the annual needs of FRM II fuel element production [10]. Therefore we have to come back to atomized powder, but now with different metallurgical treatment like oxidization, addition of diffusion block-

ers like Si in Al and/or modified defect structure.

Tests of modified UMo alloys in various dispersions by heavy ion irradiation

During in-pile irradiation of fuel plates made of UMo particles dissolved in Al matrix, growth of an undesired interdiffusion layer (IDL) has been observed - see chapter 1.4. It has been shown that bombardment of nuclear fuel specimens with heavy ions produces effects comparable to those after in-pile irradiation [11]. Especially the growth of an IDL around UMo particles inside an aluminium matrix has been observed after bombardment with I-127. It has been shown that this IDL is comparable to the one observed after in-pile irradiation [12]. We continued bombardment of UMo/Al dispersion fuel at Maier-Leibnitz Laboratory in Garching.

The samples contain atomized U10Mo inside a pure aluminium matrix. All samples were cut out of miniplates provided by Argonne National Lab and polished before irradiation. Sample size was $3\ times 7.6mm^2 \times 300\mu m$. We used I-127 at 80MeV for the irradiation simulating a typical fission product. The incident angle between the ion beam and the sample surface was 60°. The size of the beam spot was $\sim 3 \times 3mm^2$. The sample temperature was monitored during irradiation by a thermocouple and did not exceed 100°C. The irradiations have been carried out under a vacuum of $\sim 1 \times 10^{-7} mbar$. The total integral fluency was $\sim 1 \times 10^{17} \mathrm{ions}/cm^2$. The penetration depth of 80MeV I-127 ions in UMo is $\sim 6.5\mu m$ respectively $\sim 16.5\mu m$ in Al. This results in an ion density of at least $1.6 \times 10^{21} \mathrm{ions}/cm^3$ in UMo and $6 \times 10^{20} \mathrm{ions}/cm^3$ in Al. Due to the energy deposition profile of heavy ions entering matter, the ion impact is even larger in certain depths. This means, that at least the final fission density of FRM II ($2.1 \times 10^{21} \mathrm{fissions}/cm^3$) has been reached [13].

After the irradiation light microscope and scanning electron microscope pictures were taken. Also a qualitative and quantitative analysis of the isotope distribution at certain points of the sample was performed using EDX technique.

Optical inspection revealed that a large IDL has grown around the UMo particles inside the area hit by the ion beam. Electron microscopy shows a large, asymmetric IDL around every UMo particle hit by the ion beam (Fig. 1.14). No IDL was found around UMo particles which had not been hit by the ion beam.

By local EDX it has been found that the composition of the IDL is aluminium rich and approximately the same in all examined positions ($\sim$ 20at%U, $\sim$ 3at%Mo, $\sim$77at%Al). The composition of the unaffected UMo core (Fig.1.14) and of the unirradiated UMo grain did not change.

Conclusion and outlook

For the first time UMo/Al samples have been irradiated by heavy ions up to a fluency which corresponds to fission densities typically reached during the burn up of such fuel in research reactors. SEM pictures and EDX data have been taken on several points on the sample. It has been found, that the composition of the IDL ($\sim$ 20at%U, $\sim$ 3at%Mo, $\sim$77at%Al) does not change significantly on different positions on the irradiated area. The composition of the IDL is in good agreement with values found after in-pile irradiation tests [14].

It is planned to examine the crystal phases contained in the IDL using XRD. Further heavy-ion bombardment experiments are scheduled in collaboration with CEA-Cadarache (H. Palancher, E. Welcomme).

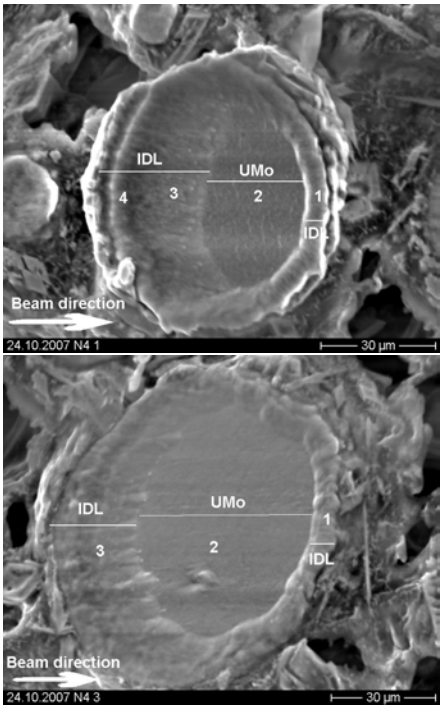

Figure 1.14: SEM image of UMo grains which were directly hit by the ion beam. The incident beam direction is marked in the pictures. A large, asymmetric IDL around a remaining UMo core is visible. The asymmetry of the IDL is associated to the direction of the incident beam. EDX measurements have been taken at the marked positions.

Manufacturing processes for full size UMo monolithic foils

Monolithic UMo foils allow densities around 15 gU/cm^3. It is therefore a promising alternative to disperse UMo-Al fuel for converting high flux research reactors to lower enrichment. Unfortunately it is not possible so far to produce full size fuel plates on an industrial scale from monolithic UMo, because the demanding mechanical and metallurgical properties of the materials to be used make common processing techniques hardly applicable [15, 16].

A new approach to solve this problem is the use of DC-magnetron sputtering [17]. Sputtering is a commonly used process for growing metal layers on a micrometer or sub-micrometer

scale on different substrates. The sputter deposited layers provide excellent substrate adhesion and high density. In contrast to thermal vacuum deposition methods the sputtering process will not change the composition of the deposited materials, because it is independent of the vapour pressure of the materials being used.

We intend using this technique in a first step to grow a massive full size meat layer of UMo. In a second step, sputtering will be used to cover the meat layer with several ten micrometers of Al or other materials as precladding. The resulting UMo / Al sandwich structure will then be further processed by common and more economic welding, rolling or hot pressing techniques to finalize the Al cladding and thus to produce a full size fuel plate.

For this purpose a DC magnetron sputtering facility was built. The dimensions of the apparatus were chosen to enable the production of samples with a size of $700 \times 65\,mm^2$ which corresponds to the size requirements of the currently used FRM II fuel plates.

In preliminary tests the deposition of different surrogate metals (Cu, Al, Zn) and alloys (brass, stainless steel) on Al and stainless steel substrates for process pressures between 1×10^{-3} and 1 mbar were studied. As most important limiting factors for the deposition rate and therefore for the process speed we identified the heat removal from the target and the maximum voltage provided by the DC-power supply. In about 40 hours we succeeded to deposit Cu layers with a thickness of up to $1300\mu m$ (Fig. 1.15a). The deposits had an elasticity and strength that was similar to bulk material. However, the layers showed a gradient in thickness from centre to the edges of up to 50% of the maximum in length and of up to 20% in width.

Finally we produced multilayer structures to show the feasibility of our two step production procedure mentioned in the first paragraph. We were able to produce a multilayer

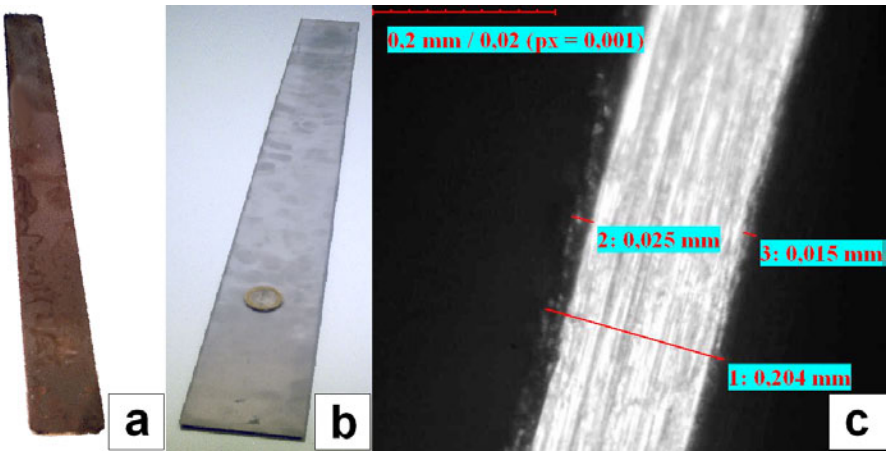

Figure 1.15: a) Sputtered sheet of Cu with a thickness of $1300\mu m$ and a size of $700x65mm^2$. (b) Sputtered multilayer foil from Cu with Al cladding, size $700 \times 65mm^2$. (c) Microscopy image of a cross section of the multilayer structure shown in (b). Here the inner Cu layer has a thickness of $200\mu m$, the Al cladding has on one side a thickness of $15\mu m$ and on the other side a thickness of $25\mu m$.

structure of 300 μm thick Cu covered by 40 μm of Al (Fig. 1.15b&c). Again the deposits were as stable as foils made from bulk material. The Al cladding showed a good adhesion to the Cu layer. Thickness gradients occurred as expected.

Conclusion and outlook

Our tests demonstrate that it is possible to deposit different metals and alloys as blank sheets and foils of $700 \times 65\,mm^2$ size and several hundred micrometers thickness by DC-magnetron sputtering. We also showed, that it is possible to clad this structures in a second step with several tens of micrometers of Al using sputtering. We plan to repeat the sputter process to fabricate blank sheets of depleted UMo and clad them with AlFeNi.

Re-evaluation of the tests of the present U_3Si_2 fuel used for FRM II

In the course of the licensing procedure of the FRM II, extensive test irradiations have been performed to qualify the $U_3Si_2 - Al$ dispersion fuel with a high density of highly enriched uranium (93 wt% of ^{235}U) up to very high fission densities [7].

Two of the three FRM II type fuel plates used in the irradiation tests contained $U_3Si_2 - Al$ dispersion fuel with HEU densities of 3.0 gU/cm^3 or 1.5 gU/cm^3, and one plate two adjacent zones of either density ("mixed plate"). They were irradiated in the French MTR reactors SILOE and OSIRIS in the years before 2002. The local plate thickness was measured along the plates during interruptions of the irradiation. The maximum fission density obtained in the U_3Si_2 fuel particles FDP was $14 \times 10^{21} f/cm^3$ and $11 \times 10^{21} f/cm^3$ in the $1.5gU/cm^3$ and $3.0gU/cm^3$ fuel zones, respectively. In the course of the irradiations the plate thickness increased monotonously and approximately linearly, leading to a maximum plate thickness swelling of 14 % and 21 % and a corresponding volume increase of the fuel particles of 81 % and 106 %, respectively.

As an example, Fig. 1.16 shows a micrograph of the specimen with FDP = $12 \times 10^{21} f/cm^3$. Since in every fission an uranium atom is converted into two fission fragments the volume of the fuel particles increases, in this case by about 70 %. The as-fabricated porosity (VP = 0.95 %) has disappeared, but many small pores (bubbles) have been produced during irradiation to accommodate the gaseous fission fragments. In Fig.

1.16 most of these "fission gas bubbles" have a diameter of below $2\mu m$ with only a few larger ones. The very uniform distribution of small gas bubbles that show no tendency to interlink is the reason for the stable swelling behaviour of U_3Si_2 [18, 19, 20]. The interdiffusion layer which builds up at the surface of the particles is about $6-10\mu m$ wide.

Fig. 1.17 demonstrates that the swelling of the fuel particles PS, which is independent of the uranium density in the U_3Si_2-Al fuel meat, is a monotonous and well predictable function of FDP over this very large range. It is clear that the swelling is a uniform function of the fission density - without any indication of a rapid increase which would have been related to a build up and interlinkage of very large gas bubbles in the fuel particles ultimately leading to excessive swelling (pillowing) and failure of the fuel plate. This uniform behaviour of PS also excludes any build up of larger pores in the Al matrix of the fuel since such an effect would be misinterpreted as a particle swelling.

In conclusion it is evident that U_3Si_2-Al dispersion fuel - under realistic operating conditions and for not too high uranium densities so that there is always sufficient matrix aluminium available in the fuel meat - represents an excellent fuel for being used in high performance research reactors up to very high fission densities, fission rates and fuel temperatures.

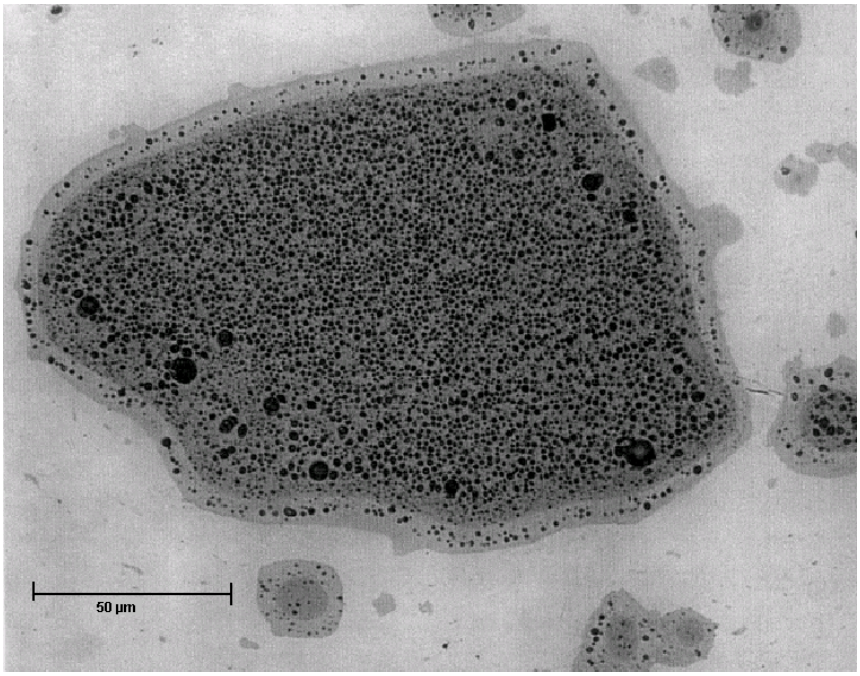

Figure 1.16: Micrograph of the specimen with an uranium density of $1.5gU/cm^3$ and a fission density of $12\times10^{21}f/cm^3$ in the U_3Si_2 particles to $1.6\times10^{21}f/cm^3$in the meat. This examination has been performed in the hot cell laboratories of the CEA Grenoble [7, 11]

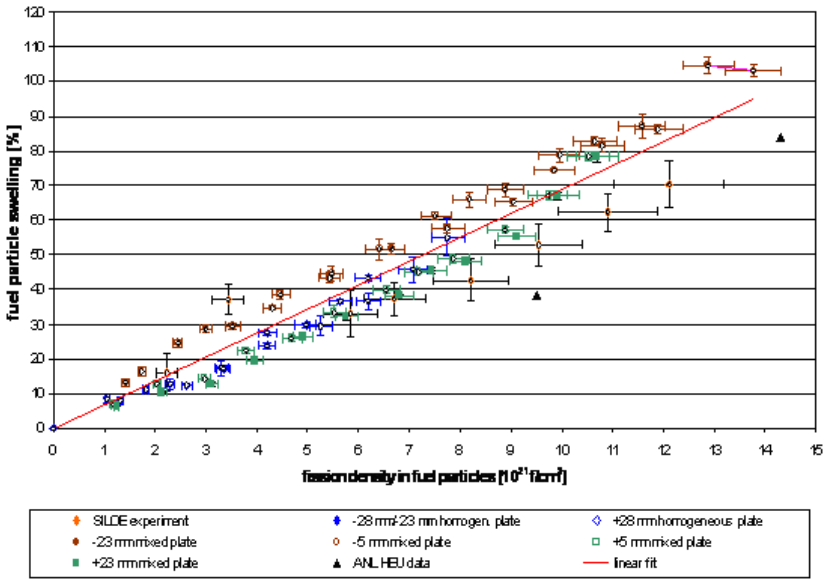

Figure 1.17: Increase of the volume of the U_3Si_2 fuel particles (PS) as a function of the fission density in the particles (FDP). This is a comprehensive plot of all irradiations. The unknown as-fabricated porosity VP has been adjusted for each curve of the OSIRIS experiments to yield an initially smooth relationship. Shown are the data for the OSIRIS homogeneous plate and the OSIRIS mixed plate, all with $3.0gU/cm^3$, as well as the data of the OSIRIS mixed plate and the SILOE results, all with $1.5gU/cm^3$. The straight line represents a fit of all our data with a slope of $6.86\times10^{-21}\%cm3/f$. Also shown are the ANL data of ref. [18, 21] as obtained from a HEU sample with $1.7gU/cm^3$.

[1] Röhrmoser, A., Petry, W., Wieschalla, N. *Transactions of RRFM 2005, Budapest, Hungary*, (2005).

[2] Röhrmoser, A., Petry, W., Boulcourt, P., Chabre, A., Dubois, S., Lemoine, P., Jarousse, C., Falgoux, J., van den Berghe, S., Leenaers, A. *Transactions of RRFM 2008, Hamburg, Germany*, (2008).

[3] Jungwirth, R., Petry, W., Schmid, W., Beck, L., Bergmaier, A. *Transactions of RRFM 2008, Hamburg, Germany*, (2008).

[4] Schmid, W., Jungwirth, R., Petry, W., Böni, P., Beck, L. *Transactions of RRFM 2008, Hamburg, Germany*, (2008).

[5] Jarousse, C., Lemoine, P., Boulcourt, P., Petry, W., Röhrmoser, A. *Transactions of RRFM 2007, Lyon, France*, (2007).

[6] Röhrmoser, A., Petry, W. *Transactions of RRFM 2006, Sofia, Bulgaria*, (2006).

[7] Böning, K., Petry, W. *Journal of Nuclear Materials*. Submitted.

[8] Lemoine, P., Snelgrove, J., Arkhangelsky, N., Alvarez, L. *Transactions of RRFM 2005, Munich, Germany*, (2005).

[9] Lemoine, P., Anselmet, M., Dubois, S. *Transactions of RRFM 2008, Hamburg, Germany*, (2008).

[10] Communication by AREVA-CERCA, .

[11] Walker, D. *Journal of nuclear materials*, 37, (1970), 48 – 58.

[12] Wieschalla, N., Bergmaier, A., Böni, P., Böning, K., Dollinger, G., Grossmann, R., Petry, W., Röhrmoser, A., Schneider, J. *Journal of nuclear materials*, 357, (2006), 191 – 197.

[13] Wieschalla, N. *Out-of-pile examination of the high density U-MoAl dispersion fuel*. Ph.D. thesis, Technische Universität München, Germany (**2006**).

[14] Leenars, A., den Berghe, S. V., Koonen, E., Jarousse, C., Huet, F., Trotabas, M., Boyard, M., Guillot, S., Sannen, L., Verwerft, M. *Journal of nuclear materials*, 335, (2004), 39–47.

[15] Jarousse, C. *Transaction of RRFM 2008, Hamburg, Germany*, (2008).

[16] Clark, C. R. *RETR, Chicago, USA*, (2003).

[17] Wieschalla, N., Böni, P. New manufacturing technique for U-Mo monolithic. Patent reference no. DE 10 2005 055 692 (2005).

[18] Safety evaluation report related to the evaluation of low-enriched Uranium-Silicide dispersion fuel for use in non-power reactors (**July 1988**).

[19] Hofman, G., Snelgrove, J. In Cahn, R., Haasen, P., Kramer, E., editors, *Volume 10 A Nuclear Materials*, chapter Dispersion Fuels (VCH Weinheim, **1994**).

[20] Hofman, G., Copeland, G., Snelgrove, J. *Oak Ridge National Laboratory (ORNL), report ORNL/TM-13061*, (August 1995).

[21] Copeland, G. Private communication (July 2000) as based on the report by J.L. Snelgrove et al.: Evaluation of Existing Technology Base for Candidate Fuels for the HWR-NPR, report ANL/NPR-93/002, February 1993.

2 Diffraction

2.1 SPODI

M. Hoelzel[1], **A. Senyshyn**[1], **H. Boysen**[2], **W. Schmahl**[2], **S. Park**[2], **H. Ehrenberg**[3], **H. Fuess**[1]
[1]Technische Universität Darmstadt, Material- und Geowissenschaften, Darmstadt
[2]Ludwig-Maximilians-Universität, Depart. für Geo- und Umweltwissenschaften, München
[3]Leibniz-Institut für Festkörper- und Werkstoffforschung, Dresden

Instrument development and sample environment

During the year 2007 a new software has been developed to make the data treatment (i.e. the derivation of diffraction patterns from the two dimensional raw data) more user friendly and efficient. In particular, new algorithms have been implemented to overcome asymmetry effects caused by the smearing of Debye-Scherrer cones along the vertical directions at low scattering angles. Thus, high resolution and good profile shapes can be achieved even when the full detector height of 300 mm is used.

New devices of sample environment have been set into operation and successfully applied in user experiments. The ^{3}He insert of the closed-cycle refrigerator has been used for the first time in a user experiment to investigate magnetic scattering at 500 mK. The closed cycle refrigerator was also successfully used in the cryofurnace mode (currently below 450 K) in the framework of user experiments. The high-temperature vacuum furnace was used in powder diffraction experiments at 1775 °C. The mirror furnace (LMU) has been set into operation and applied in a user experiment for high-temperature diffraction experiments in air. After its commissioning, the 7.5 Tesla vertical magnet has been successfully commissioned in frame of a user experiment, where evolution of magnetic structure has been studied as a function of magnetic field (up to 3 Tesla) and temperature.

User service

The Structure Powder Diffractometer SPODI was highly overbooked in the 2007 proposal rounds. Although not much time was used for instrumentation and maintenance in 2007, overload factors higher than 3 (5th proposal round) and even 4 (6th proposal round) have been reached. Besides the regular user service, several days of beamtime have been provided for industrial applications. The diffractometer SPODI has also participated in the practical neutron scattering course organised by Jülich Centre for Neutron Science.

Various investigations in the frame of user service have been published during year 2007. To our knowledge, 11 publications based on the results from structure powder diffractometer SPODI exist in the literature. In the following, two selected examples of scientific highlights from the year 2007, both describing Li diffusion in solids, are illustrated in detail.

Example: S. Park, Li motions in lithosilicates

Li motion in dehydrated microporous RUB-29 ($Cs_{14}Li_{42}Si_{72}O_{172}$)-type lithosilicates as potential Li-cationic conductors has been studied using high-resolution neutron diffraction at SPODI in conjunction with impedance spectroscopy. These materials incorporate lithium not only in spacious channel sites, but also in densely packed Li_2O-layers in the framework (Figure 1), providing new conditions for hosting mobile lithiums. One of the motivations for developing microporous conductors is that "simple" ion-exchange processes can be performed in order to manipulate the structures for fast ionic conduction. Characteristically, a moderate direct current (DC) conductivity value of $2\sim 6\times10^{-5}$ S·cm^{-1} at 873 K in RUB-29 can be enhanced dramatically through Na-exchange processes. Na-exchanged RUB-29 possesses 100-times higher overall conductivity values between 3.2×10^{-3} and 7×10^{-3} S·cm^{-1}, depending on the content of Na. A careful evaluation of impedance spectra combined with Rietveld analysis of neutron powder diffraction data of dehydrated Na-RUB-29 and RUB-29 agree with that the fast relaxation processes can be due to fast dynamic disorder of both Li^+ within Li_2O-layers and Na^+ (or Cs^+ before Na^+-exchanging) within most porous intersections of 10MR-channels [1]. The conductivity values of Na-RUB-29 materials reach in the highest region ever observed in zeolitic cationic conductors. On the other hand, to find optimal structural basis for the Li-ionic conduction which is not affected by water molecules, we have investigated pseudo-microporous Li-bearing silicates, such as the milarite-family. Among them, sugilite and sogdianite contains chains of LiO_4-tetraheda und AO_6-octahedra with A = Fe^{3+} and Zr^{4+}, respectively. Results from Rietveld analysis of diffraction patterns collected at T = 300 - 1273 K can explain the presence of low-frequency relaxations in impedance spectra measured perpendicular to

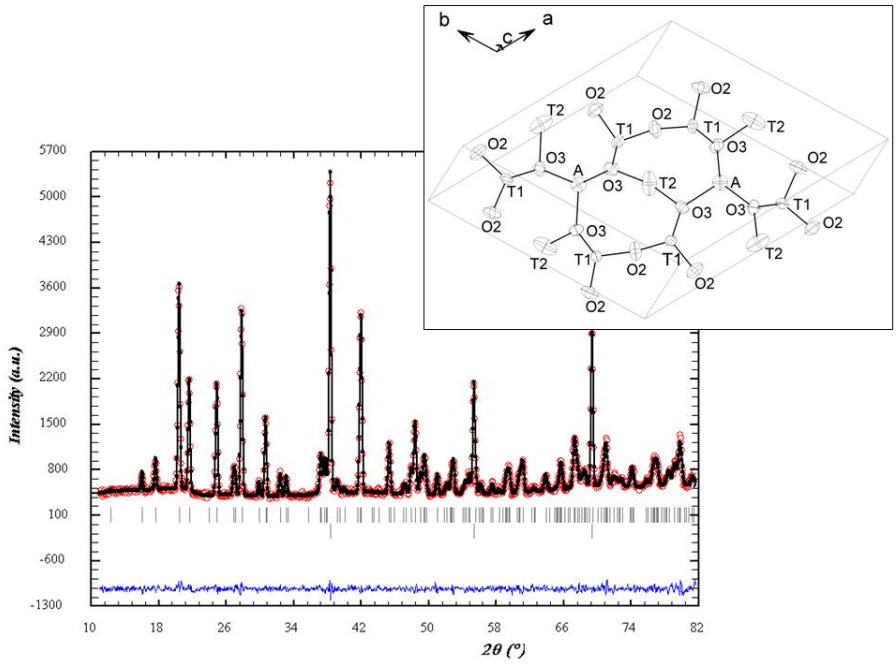

Figure 2.1: Calculated (line) and measured (circles) neutron powder diffraction pattern of sogdianite at 1273 K. The upper and lower tick marks indicate reflections of sogdianite and the Nb-can, respectively. The lower curve shows the difference between the observed and calculated data. The refined structure of sogdianite with anisotropic atomic displacements (ADP) ellipsoids at 1273 K is displayed in inset, emphasizing large ADP at Li sites.

the c-axis of a single crystal of sogdianite as a consequence of the site exchange of Li between tetrahedral and octahedral sites.

Even higher conductivity values of $s = 2.2 \times 10^{-4}$ S·cm^{-1} at 913 K and 1.9×10^{-3} S·cm^{-1} at 1093 K were determined with a plate of massive polycrystalline crystals of sugilite. To explain the structural reasons a set of diffraction patterns at T = 293-923 K was collected in the last period and now Rietveld analysis is in progress. For exploring Li-ionic conductors we have studied with SPODI data on dynamic motions in kunzite (pink spodumen) and a synthetic lithosilicate Li_2SiO_5, as well [2]. Rietveld analysis revealed strong anisotropic atomic displacements at Li sites in both materials. The Li-dynamic motions in both lithium silicates can be mainly responsible for cationic conductivity determined by impedance. Compared to RUB-29, the overall site exchange processes in these materials have to overcome pretty high activation energy barriers of 1∼1.5 eV. The presence of densely packed layers of edge-sharing LiO_4-tetrahedra, which is unique to the topology of RUB-29, may be a better option for providing path ways for fast Li conduction.

Example: H. Ehrenberg, Li ion batteries

Precise structural data have been obtained from a simultaneously Rietveld refinement of high-resolution neutron and X-ray powder diffraction data for the three phases $LiCoPO_4$, Li_zCoPO_4 with a specific intermediate Li content z=0.6(1) and $CoPO_4$, which are obtained by electrochemical Li-extraction from $LiCoPO_4$ [3]. All three phases are isostructural and isosymmetric, which implies first order transitions between these phases. The same collinear antiferromagnetic structures with magnetic moments nearly parallel to the [010] direction are observed for $LiCoPO_4$ and Li_zCoPO_4, but with a significantly higher Néel temperature of 76 K for the latter compound in comparison with 23 K for $LiCoPO_4$.

Olivine-type $CoPO_4$ was prepared from $LiCoPO_4$ by delithiation, and its physical properties were investigated for the first time. An antiferromagnetic arrangement along the [100] direction is observed for $CoPO_4$ with an additional weak ferromagnetic component along the [001] direction (magnetic space group $Pn'm'a$ and T_c=45 K).

The easy axes and the magnetic exchange interactions between Co-ions change dramatically with the $Co^{2+} \leftrightarrow Co^{3+}$ transition. A continuous change of the formal oxidation state of a transition element by electrochemical Li-extraction and a quasi-continuous $in-situ$ observation of the resulting magnetic structure by neutron diffraction appear feasible.

Outlook: developments on instrument and sample environment

In the frame of the "Verbundförderung" of the "Bundesministerium für Bildung und Forschung" upgrades of the Structure Powder Diffractometer SPODI are funded. In January 2008 the installation of a new monochromator focusing unit will be carried out to improve the neutron flux and flexibility of the instrument.

At present various developments on sample environment are under way: automatic sample changer, apparatus for $in-situ$ gas charging of samples (in particular: catalysts and framework materials), improved possibilities for experiments under mechanical stress, a sample stick for the closed-cycle refrigerator to enable experiments under hydrogen atmosphere, devices for $in-situ$ analysis of Li-ion batteries etc.

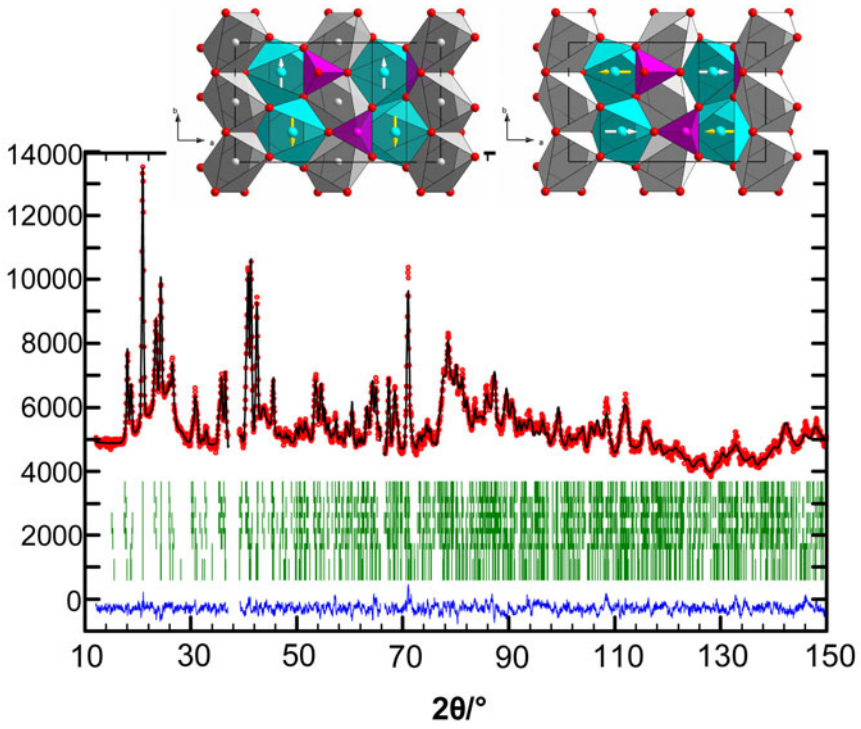

Figure 2.2: Neutron diffraction pattern of "$Li_{0.2}CoPO_4$" at 5 K, measured data as red points, calculated profile in black and the corresponding difference curve in blue at the bottom of each figure. The lines of green marks indicate the calculated positions of allowed reflections. The narrow excluded regions are due to contributions from the cryostat. The line of reflection marks belong from top to bottom to the nuclear contributions from $LiCoPO_4$ and Li_zCoPO_4, the magnetic reflections from $LiCoPO_4$ and Li_zCoPO_4 and the nuclear and magnetic peaks from $CoPO_4$. Magnetic structures of $LiCoPO_4$ and $CoPO_4$ are shown in left and right insets respectively.

[1] Park, S.-H., Senyshyn, A., Paulmann, C. *J. Solid State Chem.*, 180, (2007), 3366–3380.

[2] Park, S.-H. FRM-II experimental report Nr 698.

[3] Ehrenberg, H., Bramnik, N., Senyshyn, A., Fuess, H. In preparation.

2.2 HEiDi – Single crystal diffractometer with hot neutrons

M. Meven[1], **V. Hutanu**[2], **G. Heger**[2]
[1]ZWE FRM II, TU München
[2]Institut für Kristallographie, RWTH Aachen

Introduction

HEiDi is one of the two single crystal diffractometers at the neutron source Heinz Maier-Leibnitz (FRM II). It is placed at beam line SR9B in the experimental hall of the reactor building and uses the hot source (fig. 2.3). The instrument is a collaboration between the RWTH Aachen (Institut für Kristallographie) and the TU München (ZWE FRM II).

HEiDi covers a broad range of scientific cases in the area of structural research on single crystals in the following fields of interest:

- Structure analysis (harmonic and anharmonic MSD (mean square displacements), hydrogen bonds, molecular disorder).
- Investigation of magnetic ordering (magnetic structures, spin density).
- Structural and magnetic phase transitions.

The use of the hot source (graphite cylinder at T(20MW)=2300 K) at beam line SR9 yields a remarkable increase of the neutron flux in the range

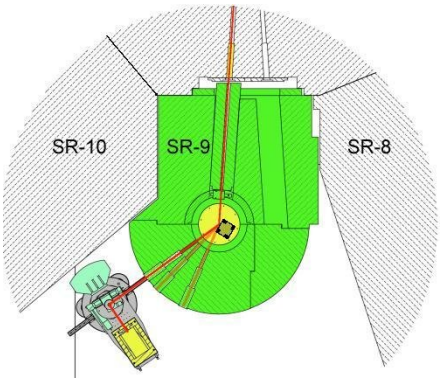

Figure 2.3: Overview of HEiDi

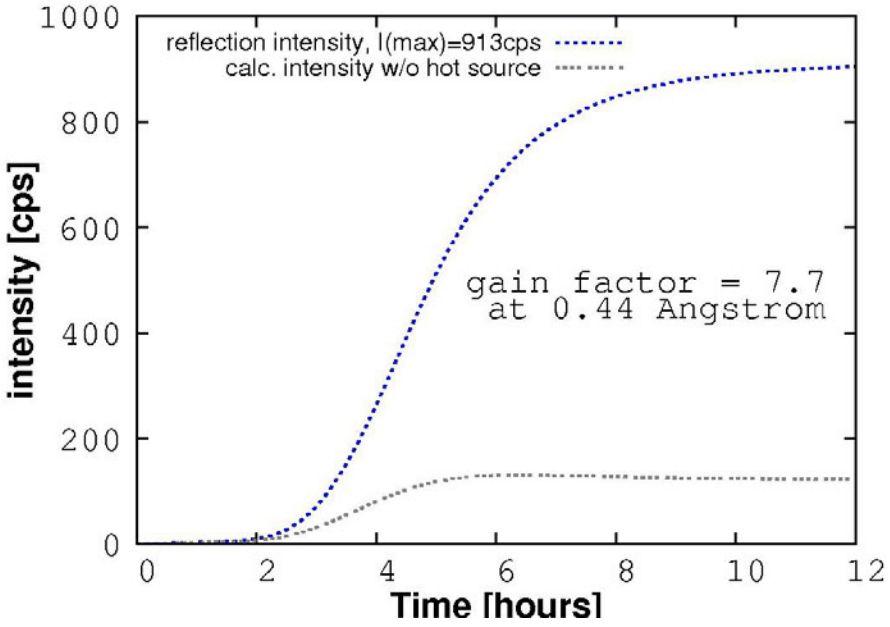

Figure 2.4: Gain factor of hot source at SR9

between 0.6 Å and 0.4 Å with a gain factor about eight (fig. 2.4).

Diffraction experiments that focus on structural and magnetic details profit significantly from the access to a very large reciprocal space ($Q = |\vec{Q}| = \sin\Theta_{max}/\lambda$) with $Q > 1.5$ at 0.55 Å. Other advantages are the

- reduction of extinction effects of large and very perfect single crystals and the
- reduction of absorption effects in compounds with highly absorbing elements like samarium or gadolinium.

To our knowledge there exists only one other neutron single crystal diffractometer worldwide (D9 at ILL) with these unique capabilities. Details of the instrument and its applications were presented in 2007 on the

- annual meeting of the DGK in Bremen [1],
- the 4th European conference on neutron scattering in Lund [2],
- the first user meeting at FRM II and
- Neutron News [3].

Use of sample environment

Low temperature environment

The closed cycle cryostat of HEiDi reaches a minimum temperature of about 2.2 K. This and its reliability make the cryostat very attractive for detailed investigations on magnetism and other structural properties at low temperatures. The movability of the cryostat in the Eulerian cradle was continuously improved in the last year. The tilt range of the χ axis was successfully extended to $\chi_{min} = -38^0$ and $\chi_{max} = +91^0$ while the ϕ range covers a complete sample rotation (fig. 2.5).

Thus in comparison to room temperature experiments the observation of reciprocal space at low temperature is not significantly limited and allows the collection of complete Bragg data sets. More than 65 percent of users beam time were used for experiments with this sample environment.

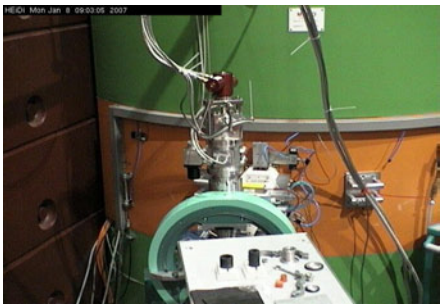

Figure 2.5: Cryostat in cradle with rotating connectors

High temperature environment

The air cooled furnace (fig. 2.6) was used for two high temperature experiments around T =1100 K. At the end of 2007, after two third of the second HT experiment the niobium shielding of the furnace was damaged (probably due to a vacuum leak). In combination with some other repairs and improvements the furnace might be available at the second half of 2008.

Simultaneously, developments for a mirror furnace are in progress. This furnace is designed to have a large beam window for use in the Eulerian cradles of HEiDi and RESI and allows

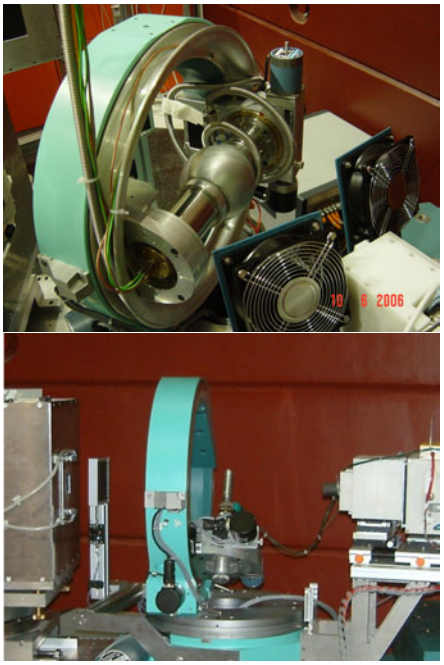

Figure 2.6: Large (top) and small (bottom) furnace in Eulerian cradle

temperatures up to almost 2000 K. Thus, it is very likely that this furnace will replace the air cooled furnace in 2008.

Experiments with slightly increased temperatures up to about 420 K can still be performed with a small furnace developed at the Institut für Kristallographie, RWTH Aachen (fig. 2.6).

In 2007 only about 8 percent of users' beam time were given for HT experiments. The total number of HT proposals and requested beam time for this kind of experiments is significantly higher (about a factor of two). There is no doubt that our efforts to improve the temperature ranges of our single crystal furnaces are mandatory to meet the needs of those of our users who wish to do structural investigations at high temperatures.

Use of beam time

In 2007 both proposal rounds were significantly overbooked concerning user experiments on HEiDi with factors between 2 and 3. Typical scientific cases of the external proposals were

- magnetic superstructures at low temperatures,
- order/disorder phase transitions at low and high temperatures,
- ionic conductors and
- local disorder or vacancies,esp. of H bonds.

Eleven external proposals (of about submitted twenty ones) were accepted and accomplished at HEiDi with altogether 165 days. Thus, more than 71% of the complete beam time of HEiDi could be given to external users in 2007. The average value of 15 days for each proposal seems quite large on the first sight. But on the other hand most of these proposals contained measurements of Bragg data sets at two or more different temperatures and large Q ranges up to $Q = 1.2$.

Additionally, some time was spent to

- check crystal orientations and homogeneities of samples that were used for experiments on other instruments at FRM II, especially the triple axes spectrometers,
- and to perform practical courses for the
  - Advanced practical course for physicist students at the TU München and the
  - JCNS Neutron course of the Forschungszentrum Jülich

and finally for tests of new components of the new single crystal instrument for 3D polarisation analysis at FRM II - Poli-HEiDi (see 2.3).

Two of the most remarkable proposals in 2007 focused on multiferroics, compounds that undergo a variety of magnetic (and sometimes additionally structural) phase transitions.

$GdCuO_3$ (Proposal 684, J. Voigt, A. Möchel) is a compound of the multiferroics family that contains the highly absorbing element Gd. For thermal neutrons the large absorption cross section of Gd of about $\sigma(\lambda = 1.8\text{Å}) = 49700$ barn makes it impossible to get any neutron diffraction data at all. The absorption coefficient about $\mu(\lambda = 1.8\text{Å}) = 873\ \text{Å}^{-1}$ yields a transmission of $T = 10^{-57}$ for a reasonably large sample (cube with 1 to 2 mm length per edge).

Only by using the short wavelengths of HEiDi the absorption coefficient drops down to a reasonable value of $\mu(\lambda = 0.55\ \text{Å}) = 12.7$ barn. The transmission of 16% at this wavelength allowed the collection of two Bragg data sets at room temperature and low temperature with reasonable statistics. A typical Bragg reflection of this experiment is shown in Figure 2.7.

$DyMnO_3$ (Proposal 1449, D. Argyriou, N. Aliouane [4]) is another compound of the multiferroics family. A possible structural phase transition at low temperature should result in slightly different oxygen bond lengths. To clarify the situation relative accuracies better than 10^{-4} for the bond lengths values were requested to make possible structural changes visible. This ambitious goal was achieved by using the short wavelength of HEiDi to measure two Bragg data sets (each one with about 3000 Bragg reflections) up to $Q = 1.2$ above and below the possible phase transition.

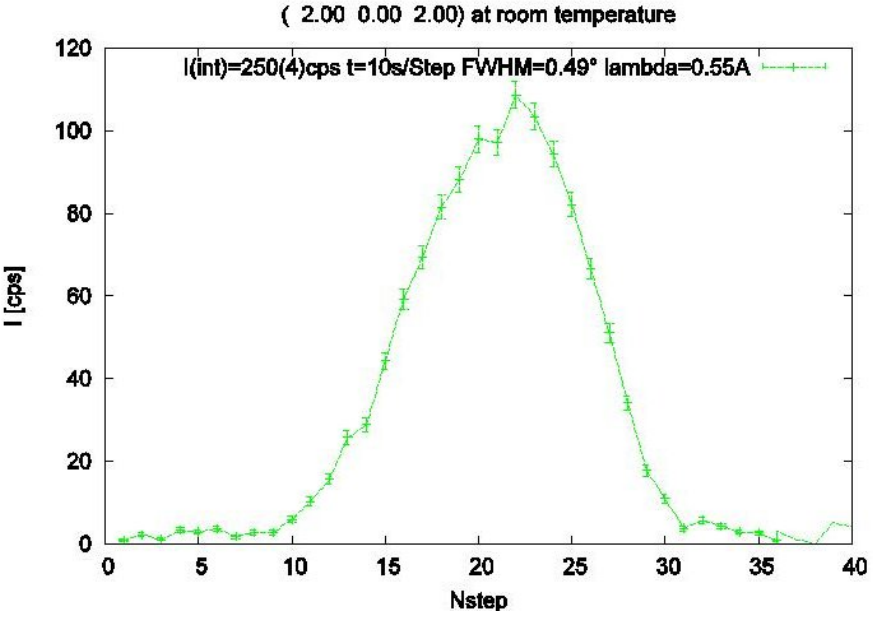

Figure 2.7: Bragg reflection of $GdMnO_3$ measured on HEiDi

Outlook

In 2007 the neutron single crystal diffractometer HEiDi has proven to be an extremely valuable "working horse" for a variety of detailed structural and magnetic investigations.

The low temperature sample environment fulfils the needs of our users and needs only minor improvements. The high temperature sample environment will undergo some substantial improvements in 2008 to allow high temperature experiments significantly above 1000 K, e.g. for investigations on ionic conductors.

Furthermore we wish to establish a collaboration with the Fakultät für Maschinenwesen of the TU München to improve the speed and flexibility of data collection at HEiDi by optimizing the controller design.

[1] Sazonov, A., Meven, M., Heger, G. In *Jahrestagung der Deutschen Gesellschaft für Kristallographie in Bremen*, 5.-9. March, 010–05 (**2007**).

[2] Meven, M. In *ECNS Lund*, 25.-29. June, T038 (**2007**).

[3] M. Meven, G. H., V. Hutanu. *Neutron News*, 18, Issue 2, (2007), 19.

[4] Aliouane, N., Argyriou, D., Strempfer, J., Zegkinoglou, I., Landsgesell, S., v. Zimmermann, M. *Phys. Rev. B*, 73, (2006), 020102.

2.3 Polarisation investigator POLI-HEiDi at SR 9 - the advances of the project

V. Hutanu [1,2], **M. Meven** [2], **G. Heger** [1]
[1] Institut für Kristallographie, RWTH Aachen
[2] ZWE FRM II, TU München

Introduction

Polarised neutron diffraction is one of the most important tools to determine magnetic structures. One-dimensional neutron polarisation analysis is used to determine the directions of magnetic moments. In addition, recently developed spherical neutron polarimetry (SNP) is very useful to investigate complicated magnetic structures in detail [1, 2, 3]. For instance, the non-diagonal terms of polarisation matrices measured in SNP give us important information on chiralities and magnetic domains of magnetic structures.

The new polarised neutron diffractometer POLI-HEiDi – currently under construction on neutron beam 9 (SR 9) – is dedicated to investigate complex magnetic structures by means of SNP. Two zero-field polarimeters, the Cryopad and the MuPAD, are available for this task and could be used with the new instrument. Our project is carried out by the Institut für Kristallographie of RWTH Aachen with financial support of the BMBF. The successful realisation and test of the numerous components of this new polarised instrument in 2005 and 2006 [4, 5] assured further financial support for this project through the BMBF for the next future (2007-2010). A number of important new parts and components for the polarised neutron diffractometer POLI-HEiDi were built and partially tested in 2007. In this report we will present these new components. For 2008 the commissioning of the most important components like the detector-analyser unit Decpol, the zero-field sample environment Cryopad as well as the controlling electronics for the sample table are planned. Also some test experiments with all components assembled in the new instrument will be done.

^{3}He spin filter cells

Based on the successful tests of 130 mm long filter cells for the short wavelength neutrons [4, 5] a number of new filter cells made of quartz glass were produced in collaboration with the HELIOS team. The practising of cell handling and use shows that the most delicate part of the Cs coated filter cells are their refilling valves. On the one hand they should be perfectly tight to high vacuum (up to 10^{-8} mbar, reached in the cell during the preparation procedure). On the other hand they should be tight at high pressure (up to 3 bar working pressure during use). Our experience shows that traditionally used glass vacuum stopcocks sealed with vacuum grease do not always work reliably, especially for multiple refilling at high pressure. Moreover their handling needs special care. Therefore, the search for alternative types of refilling valves and their integration in the cell design was an important issue in our spin filter cell development.

Different types of greasefree valves were tested in the cells Heidi 3 and Heidi 4. Figure 2.8 shows a photograph of the cell Heidi 4.1.

Figure 2.8: Spin filter cell Heidi 4.1 made of quartz glass and Cs coated inside. J. Young type greaseless high vacuum stopcock is used in the edge geometry.

The bodies of the cell have the same dimensions for all Heidi type cells (136 mm outer length, 60 mm diam.). A high vacuum Teflon ring sealed angle stopcock (production J. Young Ltd.) was connected to the cell. The valve was made of borosilicate glass. For this reason, a sealing ring adapter from quartz glass to borosilicate glass was inserted between the cell body and the valve. This greaseless construction successfully withstands high and low pressure tests and now will be the subject to further investigations regarding relaxation characteristics.

Figure 2.9: Main coil of the Decpol during the magnetic field test measurements.

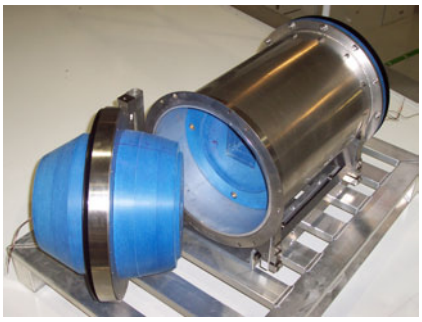

Figure 2.10: Decpol after arriving from workshop. In the open detector door on the left a single tube detector will be housed inside the blue shielding. The construction with the mobile detector allows an easy change of the ^{3}He analyser cells inside the magnetic chamber.

Detector-analyser device Decpol

The idea to combine a single tube neutron detector and a ^{3}He spin filter cell used as polarisation analyser in the same housing was for the first time realised in the Institute Laue-Langevin (ILL) Grenoble [6]. The device was called Decpol. Starting from the original ILL design we realised in 2007 a modified version of Decpol. This new Decpol was optimised to be used together with the Heidi type filter cells. In comparison to the ILL design it is more compact, has a different passive cooling system for the correction coils and uses boron doped PE for the detector screening. The results of the field homogeneity measurements inside the magnetic chamber are in good agreement with previously calculated values. Power supplies suitable for operation with the Decpol were purchased. The optimisation of the coil current ratios as well as the final commissioning of the new Decpol is planned for the first reactor cycle in 2008 (10b). Figure 2.9 shows the main coil of the Decpol during test measurements before the final assembling, situated in the 3D magnetic field mapping device. Figure 2.10 presents the assembled Decpol. The open door shown in this picture offers the possibility for a quick change of the filter cell.

Non-magnetic sample table

After about one year delay in delivery, at the end of 2007, we managed to receive the sample table for our new polarised diffractometer from Fa. Huber Diffraktionstechnik GmbH. Figure 2.11 shows the non-magnetic support unit during the acceptance test at the producer before shipment. The sample table includes a massive basal plate for the stability of the whole instrument. The upper surface of the plate is hardened and serves as a support for the wheels fixed on the bottom part of the detector arm. The basal plate has three pairs of air pads (design and production FRM II) that are adjustable in height. A Huber 440 turn table is used for the movement of the detector arm (2theta circle). A Huber 430 turn table is used for the sample rotation (omega circle). A fixed plate between the two turn tables serves as support for the polarisation analysis devices as well as for other instrumentation, e.g. a magnet. On the top of the omega circle a 2-direction tilting table with a manual flat turn table (partially circle chi, and phi) is mounted. The available tilting angle in the both perpendicular directions is $\pm 5^\circ$.

Polarisation manipulation devices

In cooperation with the ILL in the framework of our project two so called nutators wre realized in 2007 (see figure 2.12). These devices use the precession of the magnetic moment of the neutron in an external magnetic field for adiabatic transition from axial polarisation (along the beam path) to transversal polarisation (in-plane perpendicular to the beam propagation direction). Moreover the mechanical rotation of the nutators around the beam direction axis permits the orientation of the

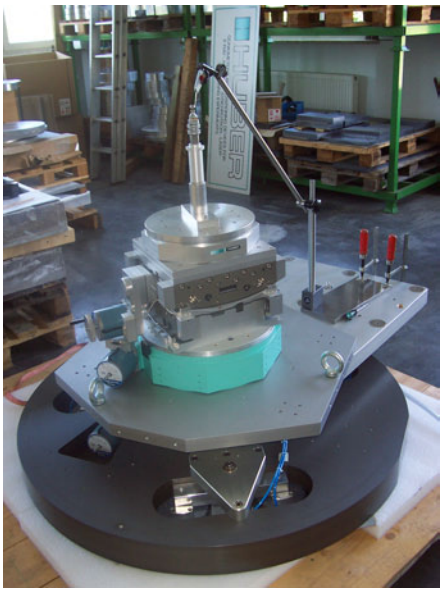

Figure 2.11: Non-magnetic sample table for the new diffractometer POLI-HEiDi during the acceptance tests.

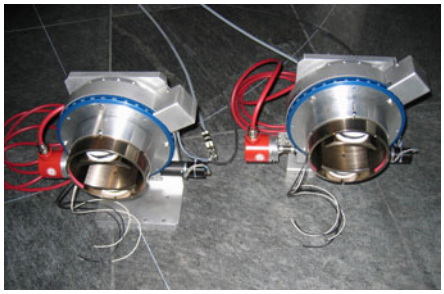

Figure 2.12: Adiabatical spin rotators from the axial to the transversal direction regarding the beam propagation direction (nutators) fixed on their mechanical turn tables.

transversal polarisation vector to any direction between $0°$ and $360°$ in the plane perpendicular to the beam. Therefore, these devices are used for the orientation of the polarisation vector of the incident and the scattered beam in the direction of the required projection of the scattering vector during 3D polarisation analysis experiments. A nutator consists of three magnetic coils fixed in the weak ferromagnetic material body. Two of these coils are connected to polar pieces of special form in order to produce a homogeneous transversal magnetic field in the region of the polarised neutron beam path. The third coil is positioned axially to the beam and assures an adiabatic coupling between the transversal field and the axially polarised neutrons. Bipolar power supplies suitable for the nutator operation were also procured.

Acknowledgements

We are thankful to S. Masalovich and A. Lykhvar from Neutron Optics group of FRM II for the cooperation in the cell preparation. We are also thankful to J. Fink and F. Tralmer from the construction department of FRM II for the work on Decpol and nutators.

This work is supported by the German Federal Ministry for Education and Science (BMBF) through the projects 03HE6AA3 and 03HE7AAC.

[1] Tasset, F., Brown, P., Lelievre-Berna, E., Roberts, T., Pujol, S., Allibon, J., Bourgeat-Lami, E. *Physica B*, 267-268, (1999), 69.

[2] Brown, P., Crangle, J., Neumann, K., Smith, J., Ziebeck, K. *J. Phys: Cond. Matter*, 9, (1997), 4729.

[3] Brown, P., Forsyth, J., Tasset, F. *J. Phys: Cond. Matter*, 10, (1998), 663.

[4] Hutanu, V., Meven, M., Heger, G. Progresses in the development of the polarized neutron diffractometer POLI-HEiDi. Technical report, Annual report 2006 FRM II, TU München (**2007**).

[5] Hutanu, V., Meven, M., Heger, G. *Physica B*, 397, (2007), 135–137.

[6] Lelievre-Berna, E. *Advances in Neutron Scattering Instrumentation, I. Anderson & B. Guerard, Editors, Proceedings of SPIE*, 4785, (2002), 112–125.

2.4 RESI – The single crystal diffractometer

B. Pedersen[1], **G. Seidl**[1], **W. Klein**[1], **W. Scherer**[2], **F. Frey**[3]
[1]ZWE FRM II, TU München
[2]Inst. f. Physik, Universität Augsburg
[3]Sektion Kristallographie, GeoDepartment, LMU München

During 2007 RESI was operating routinely. The use of further sample environment was successfully implemented, including use of the He-3 insert for diffraction experiments down to 500mK.

To improve the performance of the instrument, we are currently designing a focussing secondary neutron guide. This guide will reduce the spot size on the detector for large crystals, thus increasing the (spatial) resolution for these samples.

Sample Environment

During the last year, the sample environment available for RESI has been improved. The closed cycle refrigerator is now equipped with rotating connector for the high pressure lines, which enables full 360° phi-rotation and much freer chi-motion.

The FRM II He-3 insert was successfully used in a number of experiments on magnetic structures, extending the temperature range down to 500 mK. Here the large area detector allows data collection with a single rotation axis. Thanks to the flexible software design, it was even possible to implement a temperature cycling measurement, where each image was measured at 500mK and 3K immediately after each other.

For high temperature experiments, the FRM II mirror furnace has been adopted to the Eulerian craddle. Compared to the standard high temperature furnace, this setup yields much lower background and an improvement in accessible reciprocal space.

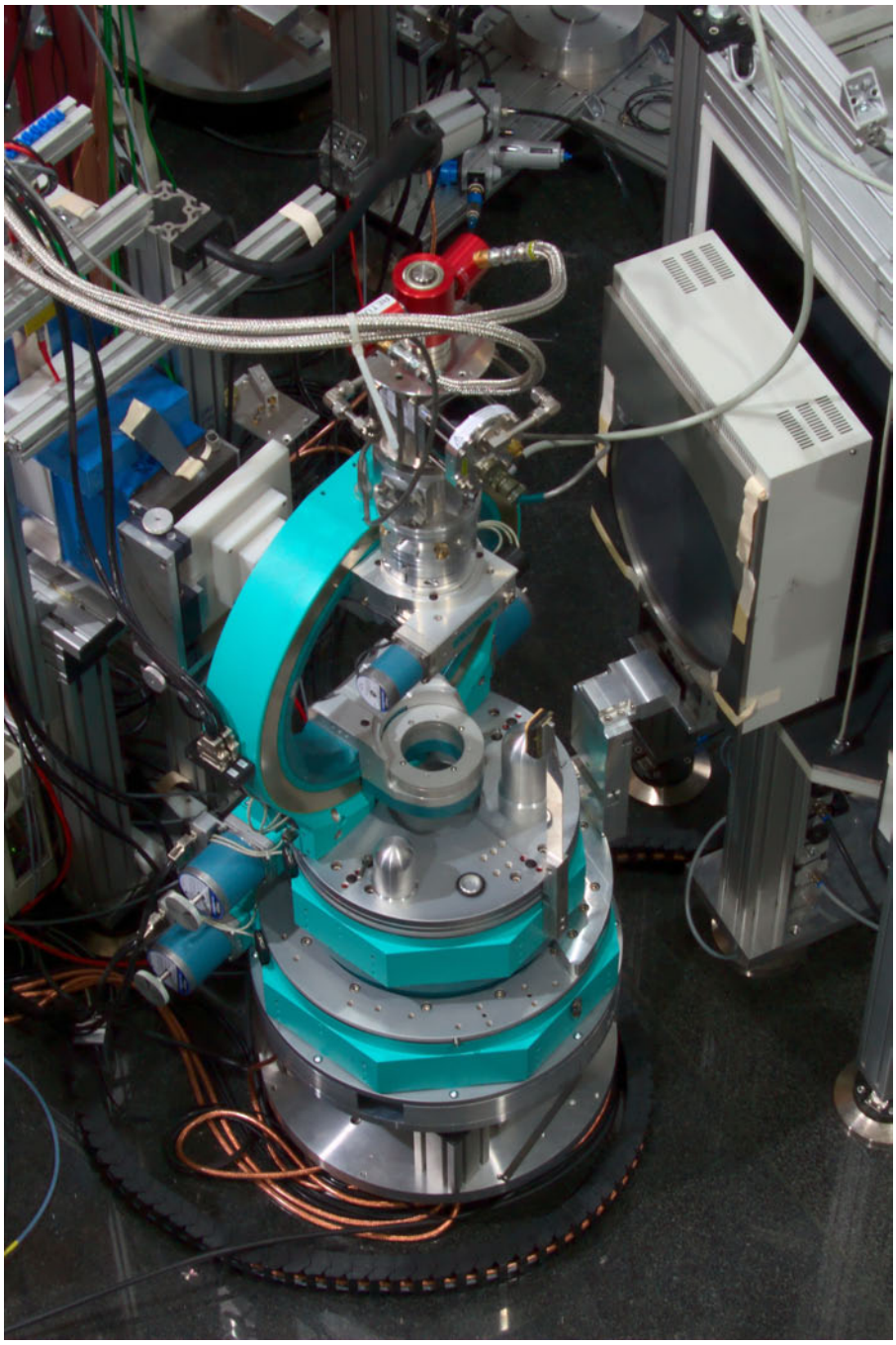

Figure 2.13: RESI in the Eulerian craddle setup, equipped with a closed-cycle refrigerator

2.5 KWS-2 Small-angle neutron diffractometer of JCNS at FRM II

A. Radulescu[1], **H. Frielinghaus**[1], **V. Pipich**[1], **P. Busch**[1], **V. Ossovyi**[1], **T. Kohnke**[1], **A. Ioffe**[1], **D. Schwahn**[2], **M. Heiderich**[2], **U. Bünten**[2], **R. Hanslik**[3], **K. Dahlhoff**[3], **G. Hansen**[3], **G. Kemmerling**[4], **R. Engels**[4], **H. Kleines**[4], **D. Richter**[1,2]

[1]JCNS, Jülich Centre for Neutron Science, outstation at FRM II
[2]IFF-5,Research Centre Jülich
[3]ZAT, Research Centre Jülich
[4]ZEL, Research Centre Jülich

The KWS-2 small-angle neutron diffractometer was moved from the Jülich reactor FRJ-2 to the Munich reactor FRM II in 2006. The instrument is now positioned at the end of the vertically "S-shaped" neutron guide NL3a-o. During the reconstruction phase the instrument was upgraded aiming at its optimization either for high intensity or for high resolution modes. Due to these upgrades, the positioning of the instrument in the FRM II neutron guide hall and the particular beam characteristics, some constituent parts of KWS-2 were subject to major changes.

The first change is concerned with the increase of the beam size from 30x30 mm^2 to 50x50 mm^2. The instrument was equipped with a new system of neutron guides (18 pieces x 1m length, with a m=1.3 NiMo-Ti nonmagnetic coating). New collimation apertures have been installed: 5 variable apertures made of ceramic ^{10}B, which allow either symmetric or slit-like opening with sizes between 1x1 and 50x50 mm^2 (placed at 2, 4, 8, 14 and 20m before the sample position) and 14 fixed ^{10}B coated apertures having a size of 50x50mm^2. The combination of the larger beam size with the old collimation housing required a new design of the working principle and automatic control of the new guide-aperture system: distinct carriers for the neutron guides and apertures allowing them to move independently from each other in or out of the beam have been installed.

Another major change is caused by the high neutron flux delivered by the FRM II reactor: a massive combined lead and boron shielding was installed around the velocity selector and the collimation housing in order to keep the level of γ and neutron background within the limits required by the radioprotection regulations. Optimization, adjustment and test of the new collimation system and shielding was carried out in the first half of 2007. The velocity selector was calibrated using standard samples (opal and silver behenate [1, 2]); the neutron flux at the sample position was measured for different wavelengths and collimation lengths using monitors and was calibrated by gold foils activation measurements (Fig.2.14). For the nominal filling of the FRM II cold source (13 l) KWS-2 has a flux very close (30% lower) to that of the world leading SANS instrument - the D22 at the ILL, Grenoble.

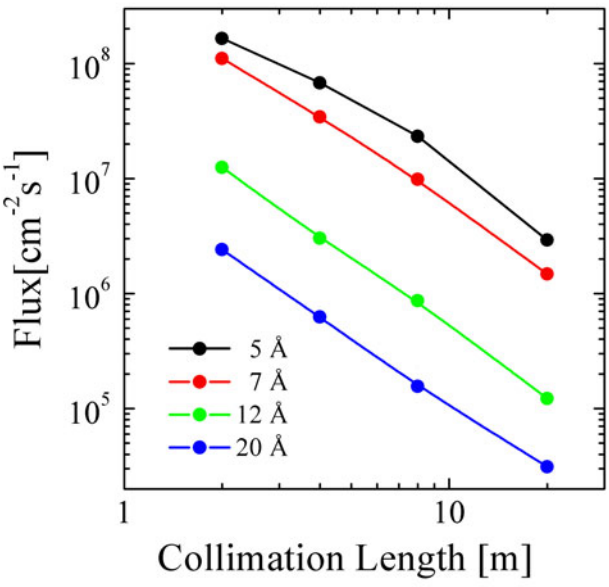

Figure 2.14: The neutron flux at KWS-2 measured at the sample position for the reactor power of 20MW and cold neutron source filling of 10.5 l (with 30x30 mm ^{2} entrance aperture).

Figure 2.15: View of the KWS-2 SANS instrument at FRM II (summer 2007); on the right side the open collimation housing of KWS-1 SANS instrument can be seen.

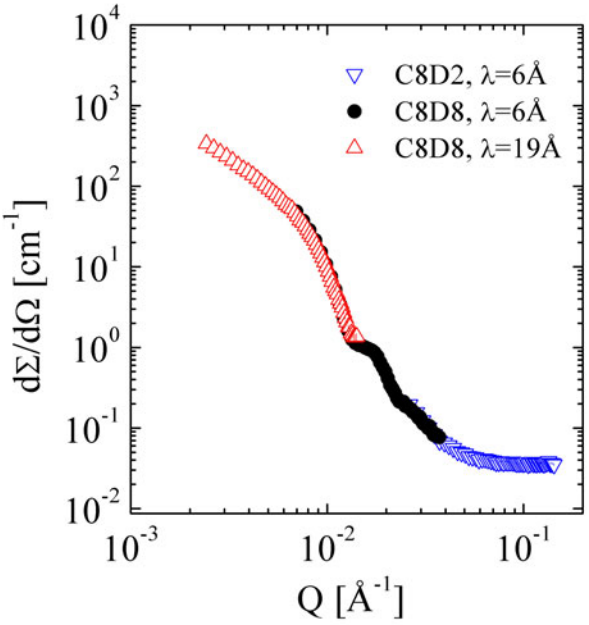

Figure 2.16: The scattering pattern of silica particles in a mixed ethanol/water solvent measured over the nominal Q-range of KWS-2 by using 2 sample-to-detector distances (2m and 8m) and 2 wavelengths, 6 and 19 Å ; the collimation length was in all cases 8m.

Because the presently available space in the FRM II guide hall permits only the installation of a 14 m long detector tube (Fig. 2.15), KWS-2 was set up in a temporary, shorter configuration. The installation of the complete, 20 m long detector housing will be possible only after joining the FRM II guide hall with the FRM-1 ring laboratory in the year 2008.

The shorter version of the detection system (allowing for a maximal sample-to-detector distance of 8m) implied that, in order to cover the nominal Q-range (0.002 - 0.2 $Å^{-1}$), two wavelengths must be used, namely 6Å and 19Å . As an example, the results obtained on the system of silica particles in mixed protonated/deuterated ethanol/water solvent [3] are presented in Fig. 2.16: the experimental data obtained with these two wavelengths were corrected for the scattering from empty cell and detector sensitivity, calibrated in absolute units using a standard sample and radially averaged in order to deliver the scattering cross section of this system.

The KWS-2 instrument became operational in the short version at the beginning of September 2007 when it was opened for internal and external users.

Further upgrading of KWS-2 was continued in the second half of 2007 in parallel with the user program: the optical focusing elements (MgF_2 parabolic lenses, Fig.2.17, left) were implemented within the end segment of the collimation system towards the sample position and a "small" high-resolution detector (spatial resolution of about 1x1 mm^2) was installed in front of the conventional detector (Fig. 2.17), right). The high-resolution detector can be moved to any position covered by the large detector and used in combination with the lenses allowing us to cover the Q-range down to $2x10^{-4}$ÅThe test and optimization of the focusing operational mode and the high-resolution detector are currently in progress.

[1] Graetsch, H., Ibel, K. *Phys.Chem.Minerals*, 24, (1997), 102.

[2] Keiderling, U., Gilles, R., Wiedenmann, A. *J.Appl.Cryst.*, 32, (1999), 456.

[3] Kohlbrecher, J., Buitenhuis, J., Meier, G., Lettinga, M. *J.Chem.Phys*, 125, (2006), 44715.

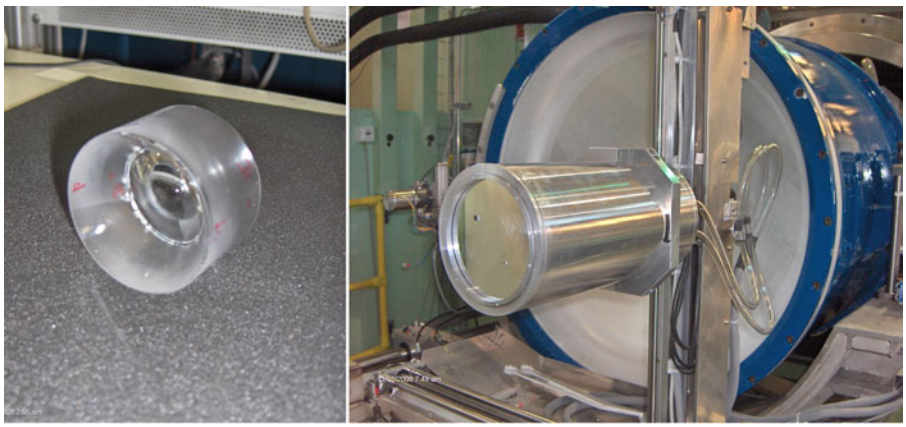

Figure 2.17: The upgrades permitting the high-resolution operation mode of KWS-2: parabolic lenses (left) and high-resolution detector (right).

2.6 STRESS-SPEC Materials science diffractometer

M. Hofmann[1], **U. Garbe**[2], **G.A. Seidl**[1], **J. Rebelo Kornmeier**[3], **J. Repper**[1], **U. Wasmuth**[4], **R.C. Wimpory**[3], **C. Krempaszky**[5], **R. Schneider**[3], **C. Randau**[6], **H.G. Brokmeier**[2,6]
[1]ZWE FRM II, TU München
[2]GKSS, Geesthacht
[3]BENSC, Hahn-Meitner-Institut, Berlin
[4]UTG, TU München
[5]CDL, WKM, TU München
[6]TU Clausthal, Clausthal-Zellerfeld

Introduction

During the last year the materials science diffractometer STRESS-SPEC [1] operated without major difficulties. A total of 23 user experiments have been conducted during this year. They covered a wide area of applications in materials science ranging for instance from kinetic measurements in ausferritic steel (M. Bamberger, Technion, Israel) or residual stresses in integral structures with adhesively bonded crack retarders (D. Liljedhal, Open University, UK) to texture measurements in archeological relevant Mesopotamine seals (D. Visser, Netherlands). For more details the reader is referred to the Experimental Reports section.

The following sections will review recent hardware developments and give a brief overview on current in-house research projects.

New hardware

The following hardware developments are now available for routine use at STRESS-SPEC:

- Top-view camera system for sample alignment
- $1/4$- circle Eulerian cradle for samples up to about 30 kg
- Radial collimator

The new radial collimator acquired from JJ-Xray, Denmark arrived this year and first tests with neutrons were carried out. The measured gauge width of the collimator is $FWHM = 2.05(1)$ mm (see figure 2.18) and its long focusing distance of about 200 mm leaves enough space for sample movement even for larger specimens. The advantages of the radial collimator compared to the conventional slit system are a sharper definition of the gauge volume independent of the distance between sample and collimator and the reduction of peak clipping effects in measurements close to the surface of samples.

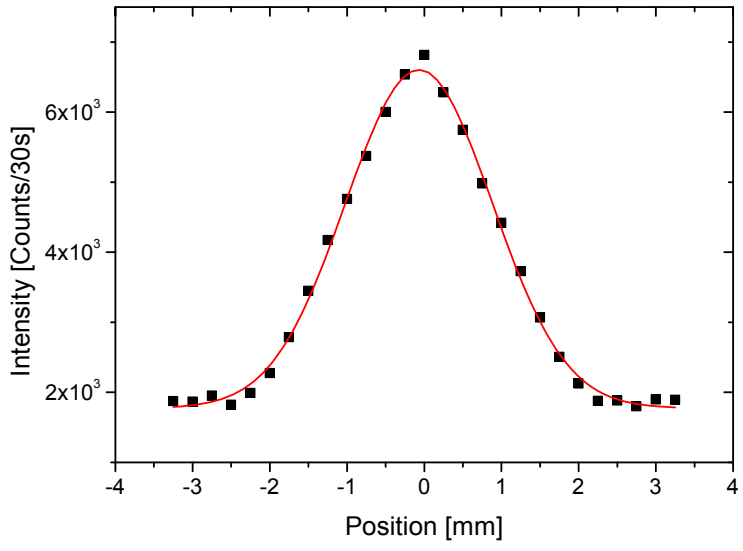

Figure 2.18: Measured intensity on scanning a 1 mm steel pin through the gauge volume as a function of position of the center of the pin.

Science

This section will give some details from two current in-house research projects concerned with "Influence of micro stresses on the residual stress analysis with neutron diffraction" (J. Repper, FRM II, DFG PE-580/7-1) and "Optimisation of Composite Castings by Means of Neutron Measurements" (U. Wasmuth, UTG, DFG-PE 580/2).

Influence of microstructural parameters on macro residual stress analysis

Mechanical and thermal treatments during the manufacturing process inevitably cause the accumulation of residual stresses in parts consisting of materials with complex microstructure (e.g. high performance multiphase Ni- or Ti-alloys). Neutron diffraction is particularly well suited to determine residual stress distributions within the bulk of the component.

The analysis of residual stresses from diffraction data, however, can be strongly influenced by inhomogeneities of microstructural parame-

ters (texture, grain size, distribution of precipitates, phase composition). We were able to show this influence by means of a simple sample geometry (flat disc shaped IN718 specimen, diameter = 100 mm) where process relevant boundary conditions allow us to predict the stress distribution in one principle - here axial - direction [2].

For the determination of the residual stress distribution in the IN718 forged pancake it was not possible to cut a reference sample from the specimen itself as the pancake will be used for further experiments. In this case a reference value was calculated on the basis of mechanical equilibrium assuming the axial stresses to vanish. This assumption is valid in case of thin plate-like components of constant thickness with a thermo-mechanical treatment which is symmetrical to the mid-plane of the disc and homogenous and isotropic with respect to the in-plane coordinates [3]. Mechanical equilibrium then yields that the stress in thickness direction is zero. Taking this into account it could be shown that the calculated reference value varies across the thickness of the pancake [2]. This stems from inhomogeneities in the microstructure caused by the manufacturing process (forging and quenching). The temperature of regions near the surface decreases faster than the interior of the pancake during the quenching. This leads in addition to strain gradients to changes in the chemical composition of the matrix over the thickness of the pancake. Therefore, each measuring point necessitates its own reference value to obtain the true macroscopic stress. Figure 2.19 shows the resulting stress distribution through the thickness of the pancake. The residual stresses derived from the experiment show good quantitative agreement with the predictions of a simple semi-analytical thermo-mechanical model based on the work of Landau et al. [4] elucidating the transient thermal stresses during quenching.

For a detailed understanding of the relations between stresses (macroscopic and microscopic stresses as well) and microstructural parameters further experiments (e.g. tensile tests, relaxation tests) are planned.

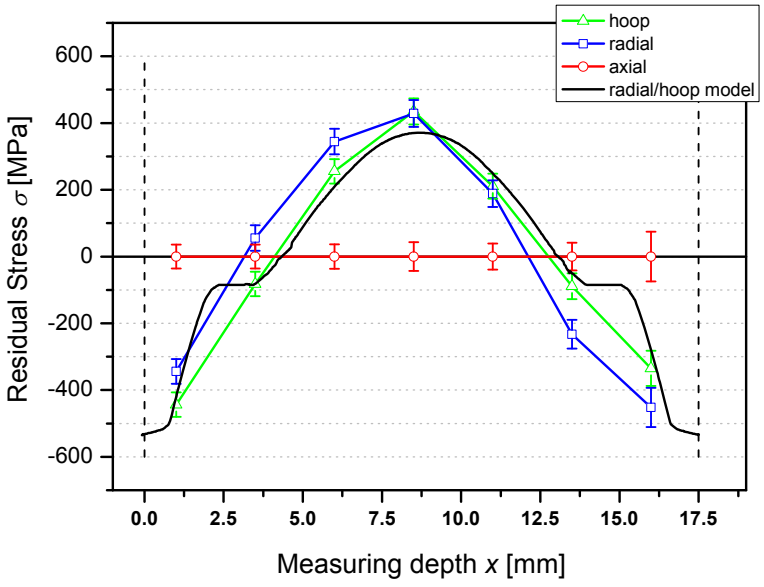

Figure 2.19: Residual stress distribution in the three principal axes hoop, radial and axial plotted against measuring depth x across the thickness of an IN718 disc (dashed lines indicate the position of the surfaces of the disc). The black line shows the stress distribution in the radial and hoop direction predicted by a simple semi-analytical model [2, 3].

Optimisation of composite castings

Composite casting is mainly used to produce composite engine blocks with in-cast liners. Due to different thermal expansion of the casting material and the material of the insert residual stresses occur during solidification. These residual stresses can reduce fatigue strength and lead to distortions of the part. They can be minimised by constructive measures. Casting simulation is a suitable method to predict residual stresses and distortions and thus to optimise design of parts. To improve the accuracy of stress simulations simple composite test castings were designed (see figure 2.20) and characterised by neutron diffraction experiments on STRESS-SPEC [5]. In order to validate the experimentally derived residual stresses the balance of total axial force

(2.1)

$$F_{ax}^{total} = \int_{\phi}\int_{r} \sigma_{ax}(r,\phi)\; r\; \mathrm{d}r\; \mathrm{d}\phi = 0$$

perpendicular to the ring area A was verified at center position z=0 (see Figure 2.20). Because of symmetry the stress function $\sigma_{ax}(r,\phi)$ depends only on the radius r. The steel ring and the aluminium ring forces were calculated individually in accordance to eq. (2.1). Calculated axial forces of 51.9 kN in the aluminium ring and -50.1 kN in the steel ring are adequate results to satisfy stress balance. Axial and hoop stresses obtained by strain gauge methods at surfaces are on the same level as neutron diffraction measurements and verify the neutron data additionally [4].

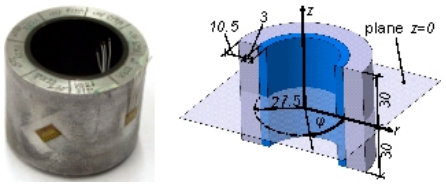

Figure 2.20: Test specimen consisting of a inner steel ring and an outer aluminium casting, (left) photograph with strain gauges for stress measurements, (right) sketch with dimensions and polar coordinate system.

The residual stress simulation was carried out using mechanical parameters of [6, 7]. The start temperature of aluminium and steel was set to solidus temperature (T_S = 479°C). The 0.2% proof stress and tensile strength parameters have been determined experimentally. The simulated stresses proofed to be three times higher compared to the experimental reference as the material model in the mechanical simulation does not include stress relaxation processes during solidification. In general stress relaxation depends strongly on temperature, stress level and time [8]. Especially composite casting processes are influenced by stress relaxation, as stresses are formed even at high temperatures due to different thermal expansion coefficients of materials. In our case stress relaxation was implemented to the mechanical simulation introducing an effective thermal strain term

$$\varepsilon_{th,eff} = \varepsilon_{th} - \varepsilon_{sr} \tag{2.2}$$

with thermal strain ε_{th} and relaxation strain ε_{sr}. The simulation model includes stress relaxation depending on the stress level while neglecting temperature and time dependence. Using Taguchi methods [9] the stress simulations were optimised based on the experimentally derived hoop stresses. Optimised relaxation to thermal strain ratios ranging form 0.357 to 0.367 fit both the level and shape of the stress curves (see figure 2.21). Due to fraction processes during solidification the experimentally determined axial stresses are lower than the simulated stress. Nevertheless the optimised simulation shows sufficient agreement with the neutron diffraction data of the investigated test specimen.

However, the simulation has to be extended by a universal temperature and a time dependent stress relaxation model. As stress relaxation data is difficult to determine experimentally at high temperatures, in-situ strain measurements using neutron diffraction will be carried out during the solidification process of the specimen in the near future. The experimental results could then be used to verify universal relaxation models in casting simulations.

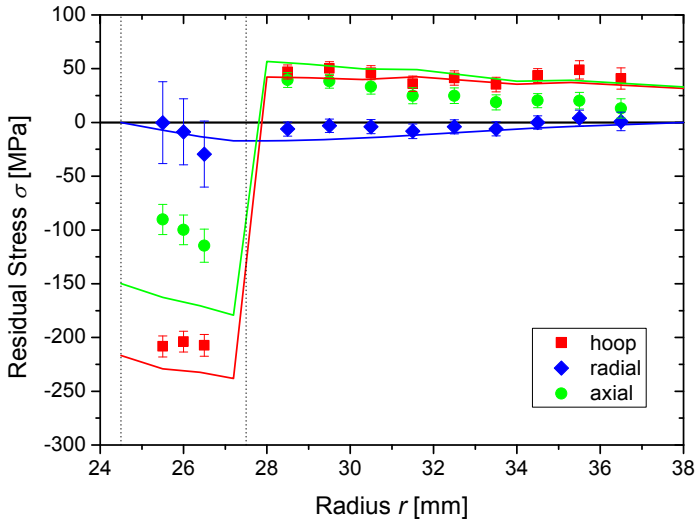

Figure 2.21: Residual stress distribution in the three principal axes hoop, radial and axial plotted against measuring depth x across the radius of the composite casting. The coloured lines are results from the simulation as discussed in text. The vertical dotted lines in the graph adumbrates the position of the steel ring.

[1] Hofmann, M., Kornmeier, J. R., Garbe, U., Wimpory, R., Repper, J., Seidl, G., Brokmeier, H., Schneider, R. *Neutron News*, 18 (4), (2007), 27–30.

[2] Repper, J., Hofmann, M., Krempaszky, C., Petry, W., Werner, E. *Mat. Sci. Forum*, (accepted 2007).

[3] Krempaszky, C., Werner, E., Stockinger, M. *Proceedings of the Sixth International Special Emphasis Symposium on Superalloys 718, 625, 706 and Derivatives*, 527.

[4] Landau, H., Weiner, J., Zwicky, E. *J. Appl. Mech.*, 27, (1960), 297–302.

[5] Wasmuth, U., Meier, L., Hofmann, M., Mühlbauer, M., Stege, V., Hoffmann, H. *Annals of the CIRP*, (submitted 2008).

[6] Hutchings, M. *Taylor & Francis*, (2005).

[7] Bäckerud, L. *Solidification Characteristics of Aluminium Alloys*, Vols. 2-3, (1990), Afs/Skanaluminium.

[8] M.F. Ashby, H. J. *Springer-Verlag*, (1986).

[9] Funkenbusch, P. *Marcel Dekker*, (2005).

2.7 Integration of a new sample goniometer and a further double disc chopper (SC-2) in the ToF-neutron reflectometer REFSANS

R. Kampmann[1], **M. Haese-Seiller**[1], **J.-F. Moulin**[1], **V. Kudryashov**[2], **B. Nickel**[4], **E. Sackmann**[3], **A. Schreyer**[1]
[1]GKSS Forschungszentrum, Geesthacht
[2]Petersburg Nuclear Physics Institute, Russian Federation
[3]Physik-Department E22, TU München
[4]LMU München

New sample goniometer at REFSANS

REFSANS has been designed as a novel ToF neutron reflectometer [1, 2] for comprehensive analyses of surfaces and interfaces. A new sample goniometer could be purchased in 2007 to enable samples inside of large and heavy (up to 200 kg) environments to be analysed at REFSANS. The goniometer comprises x-, y- and z-translation tables, one rotation table and two cradles (Fig. 2.22). The distance from the symmetry centre of the cradles to their upper surface amounts to 300 mm.

Slave-chopper-2

SC-2 was installed in the beam guide chamber of REFSANS in January 2007. The SC-2 discs-5 and -6 have one large window ($W_{5,0}$ and $W_{6,0}$) with an opening of 120° and 5 small windows with openings of only 1° ($W_{5,1}$ … $W_{5,5}$: Fig. 2.23a; disc-5) and 3°, 1°, 2°, 1° and 5° ($W_{6,1}$ … $W_{6,5}$: Fig. 2.23b; disc-6). The angular separation between the closing sides of the small windows of both discs is 10° whereas the gap between the first small and the 120° window amounts to 20°. The linear table is installed in REFSANS vertically and the beam passes SC-2 to the right of the axis if viewed in beam direction. This corresponds to a beam position above the axis in Fig. 2.23a and 2.23b.

SC-2 can be used in different operation modes by adequate setting of the phases of disc-5 and disc-6. For reflectometry and GISANS measurements the phases may be set such that SC-2 opens only one window with an angular width between 0° and 120° in order to define the wavelength range to be used for an experiment. In the calibration mode usually up to 11 small windows with widths between 1° and 5° are adjusted such that only neutrons of various wavelengths λ_i can pass through SC-2. In the inelastic mode only one or a few small windows are opened for inelastic measurements. Furthermore, for reflectivity measurements with a very broad wavelength range SC-2 will not be rotated and the beam penetrates its windows. These different operation modes lead to the unconventional design of discs-5 and -6.

High precision neutron reflectometry at REFSANS

High resolution reflectometry needs precise measurements of both the incidence angle and the wavelength. The incidence angle can accurately be measured at REFSANS by means of the high spatial resolution of the 2D-detector (FWHM ≈ 2 mm in vertical direction [3]) and the long distance of up to ≈ 12 m which can be set between the sample and the detector.

The installation of SC-2 allows of performing accurate λ-calibrations. Those measurements are performed by setting discs-5 and -6 of SC-2 such that only intensity peaks are transmitted. An example of a primary beam and calibration measurement as performed in the frame of measurements for proposal 1542 is shown in Fig. 2.24: The continuous spectrum in Fig. 2.24a represents the primary

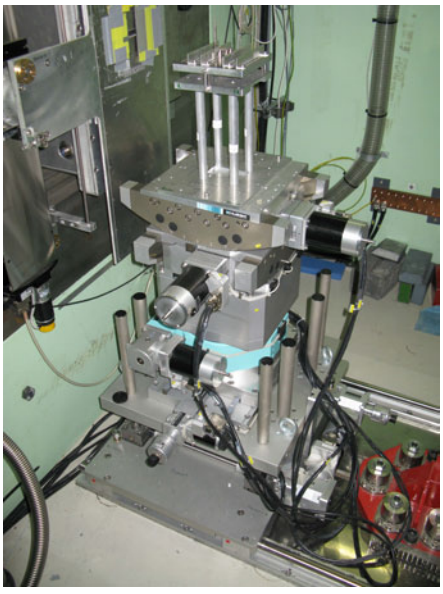

Figure 2.22: Sample goniometer of REFSANS with a sample aligned in the beam.

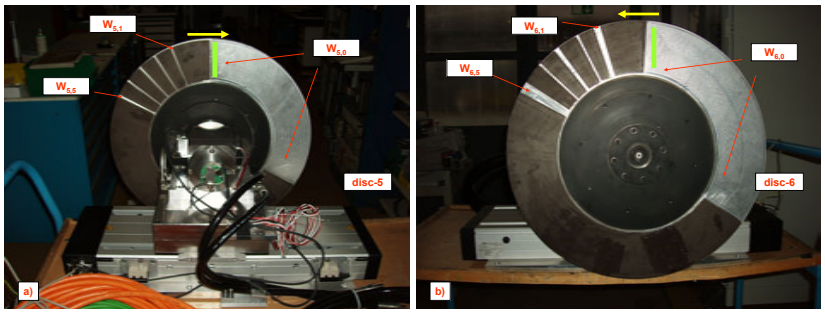

Figure 2.23: Views of SC-2 with rotation drive and linear table in beam direction (Fig. 2.23a) and against it (Fig. 2.23b). The yellow arrows indicate the rotation direction, the green bar indicates the beam area.

beam measurement with non rotating discs-5 and -6 and a sample detector distance of 6697 mm (REFSANS-parameter table=6m). At short flight times ($t < 35$ ms) the spectrum reflects the cold spectrum of neutron guide NG-2b. After ≈ 35 ms the transmission of the chopper decreases more and more and vanishes at ≈ 70 ms. This results from the window setting of the Master-Chopper (MC) and Slave-Chopper-1 (SC-1) for this measurement.

After the primary beam measurement SC-2 was started and the phases of discs-5 and -6 were set such that the small window peaks formed by disc-6 were observed with flight times $t_{6,i} < 30$ ms and those from disc-5 at $t_{5,i} > 40$ ms. A further calibration peak ($t_{5,6} \approx 37$ ms) is formed by the large windows of disc-5 and -6.

Afterwards the calibration peaks were measured at further distances between the sample and the detector corresponding to differences in flight length of ± 5 m (Fig. 2.24b). The time differences of the peak positions are used to determine the velocity and thus the wavelength of the neutrons. It is pointed out that these measurements can be performed in short measuring time, they lead to a very precise lambda-calibration for a set of very different wavelengths.

Such calibration measurements by use of SC-2 significantly improved the reconstruction of reflectivity curves because the flight time at REFSANS depends not only on the wavelength but also on the openings of the windows of the MC and SC-1 (γ_{MC} and γ_{SC-1}) and further on the phase shift between the closing of MC and the opening of SC-1 ($\delta_{MC,SC-1}$). This results from the fact that γ_{MC}, γ_{SC-1} and $\delta_{MC,SC-1}$ define both the position and the starting time of the neutron packages in dependence of the wavelength. After putting SC-2 into operation these parameters are determined from lambda-calibrations by fitting the observed peak arrival times to the chopper settings.

The neutron reflectivity of a film from an implant coating with cell membrane mimics exemplifies the performance of REFSANS for high precision reflectometry (proposal 1542). Firstly, the reflectivity from a metallic Ti-alloy (Ti-6Al-4V; 100nm) sputtered onto a Si wafer was measured at REFSANS. Measurements were performed at different incidence angles as indicated in Fig. 2.25. Afterwards the metallic film was coated with POPE (Palmitoyl-Oleoyl Phosphatidyl-Ethanolamine). Significant changes of the reflectivity curve were observed after ageing of the POPE and adhesion of proteins (fetal bovine serum, containing $3 - 4.5$ g Protein / dl; see Fig. 2.25).

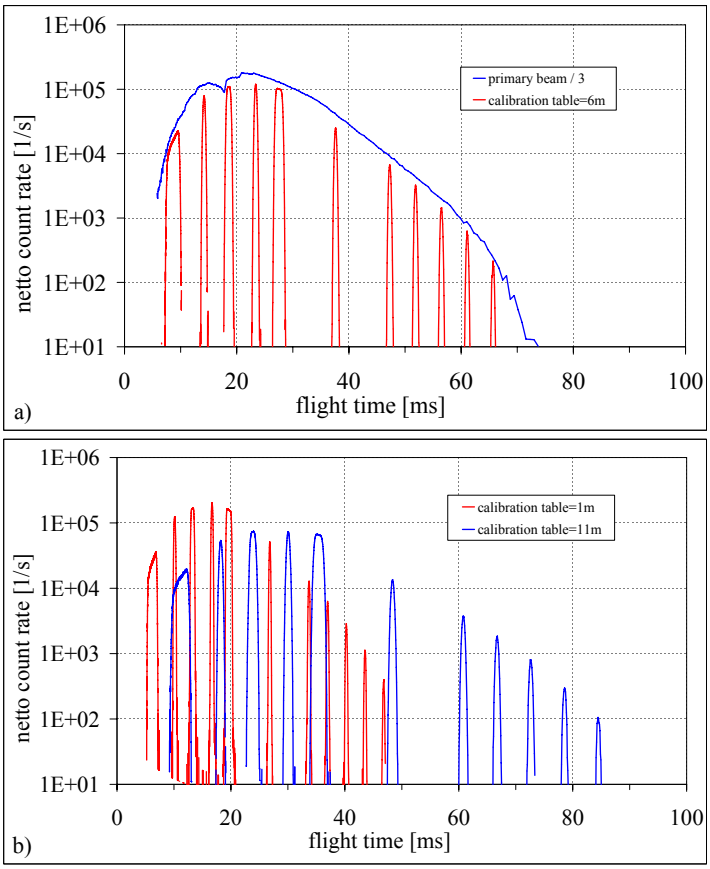

Figure 2.24: Primary beam measurement and λ-calibration at REFSANS. Measurement of the primary beam was performed with non rotating SC-2 at table = 6m corresponding to a sample detector distance of 6697 mm (Fig. 2.24a). The λ-calibration was performed by running SC-2 in calibration mode and setting the detector to table = 1m, 6m and 11m 2.24a and Fig. 2.24b.

Use of REFSANS in 2007

REFSANS could not be used for user proposals to the expected extend. This was due to technical reasons resulting from faulty soft- and hardware systems controlling the neutron optics and the choppers. A strong reduction in staff members from April to November 2007 made running of REFSANS further difficult. Nevertheless, REFSANS has been improved technically and measurements in the frame of exciting internal and external proposals could successively be performed.

Acknowledgements

The great contribution of the technical department of GKSS to constructing and manufacturing of REFSANS components is gratefully acknowledged. The development of REFSANS has been supported by the German Federal Ministry of Education, Research

and Technology (BMBF) under contracts 03-KA5FRM-1 and 03-KAE8X-3.

References

[1] Kampmann, R., Haese-Seiller, M., Marmotti, M., Burmester, J., Deriglazov, V., Syromiatnikov, V., Okorokov, A., Frisius, F., Tristl, M., Sackmann, E. *Applied Physics A*, 74, (2002), 249–251.

[2] Kampmann, R., Haese-Seiller, M., Kudryashov, V., Deriglazov, V., Tristl, M., Daniel, C., Toperverg, B., Schreyer, A., Sackmann, E. *Physica B*, 350, (2004), e763–e766.

[3] Kampmann, R., Marmotti, M., Haese-Seiller, M., Kudryashov, V. *Nuclear Instruments and Methods A*, 529, (2004), 342–347.

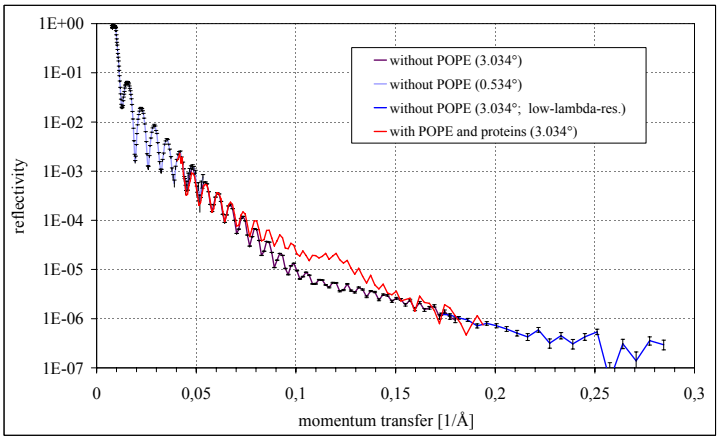

Figure 2.25: Implant coating with cell membrane mimics: Reflectivity curves without POPE phospholipid (see text) and with POPE and proteins are shown (proposal 1542: F. Feyerabend et al.).

2.8 N-REX$^+$ – The neutron / x-ray contrast reflectometer with spin-echo option

A. Rühm[1], **M. Major**[1], **M. Nülle**[1], **J. Franke**[1], **J. Major**[1], **H. Dosch**[1]
[1]Max-Planck-Institut für Metallforschung, Stuttgart

Status

During the year 2007 first user experiments have been conducted at the neutron/X-ray contrast reflectometer with spin-echo option, N-REX$^+$ [1, 2]. Fields covered were soft matter research (interfaces, membranes), magnetism in superconductors, and wear-resistant coatings. We also continued our research on the dewetting of polymer films and further explored the advantages of the novel SERGIS method for this purpose (Spin-Echo Resolved Grazing Incidence Scattering, see [3]). In this context, new triangular spin-echo coils (collaboration with Roger Pynn, Indiana University at Bloomington, USA) have been tested for the first time as an alternative to resonance coils. In addition, further instrument operation modes (PNR, SANS, and GISANS) have been installed and applied for the first time, alongside with conventional neutron

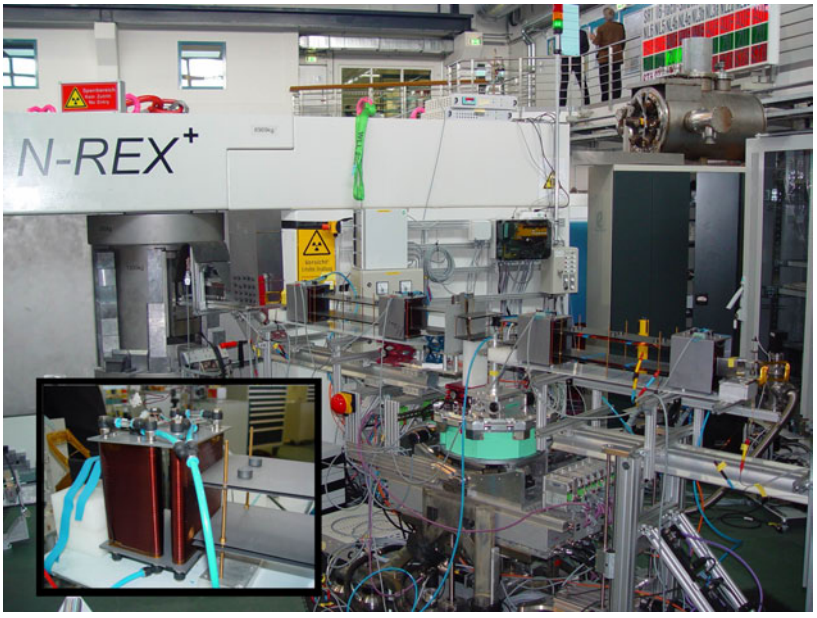

Figure 2.26: N-REX$^+$ in SERGIS mode with triangular spin-echo coils. Inset: Detailed view of a pair of triangular-shaped spin-echo coils. The coils can be water-cooled and air-cooled with additional ventilators (not shown). Currently coil sets with 45°/45° and 30°/60° angles are available.

reflectometry, neutron/X-ray contrast variation, and the SERGIS technique [3], which had already been utilized in the year before. As an example, we describe in the following two sections the results of a SERGIS and a PNR experiment conducted in 2007.

Spin-echo resolved grazing incidence scattering

Fig. 2.26 shows N-REX$^+$ in SERGIS mode with triangular spin-echo coils (one coil pair is shown enlarged in the inset). The two images at the top of Fig. 2.27 show detector images on which the primary beam and the GISANS signal from an optical grating can be discerned (left: experiment with resonance spin-echo coils, right: experiment with triangular spin-echo coils). The corresponding SERGIS data sets as obtained from the GISANS signal are plotted in the graphs below the detector images and compared with each other in the bottom row of Fig. 2.27. Overall the two data sets are well consistent with each other.In the case of resonance spin-echo coils, the achievable spin-echo length is (at the same static current setting) two times larger than in the case of triangular coils with 45°/45° angles. On the other hand, the triangular spin-echo coils provide a better resolution at smaller spin-echo lengths, and as an option, triangular coils with 30°/60° angles are now also available at N-REX$^+$, which can compensate the lost factor of 2.

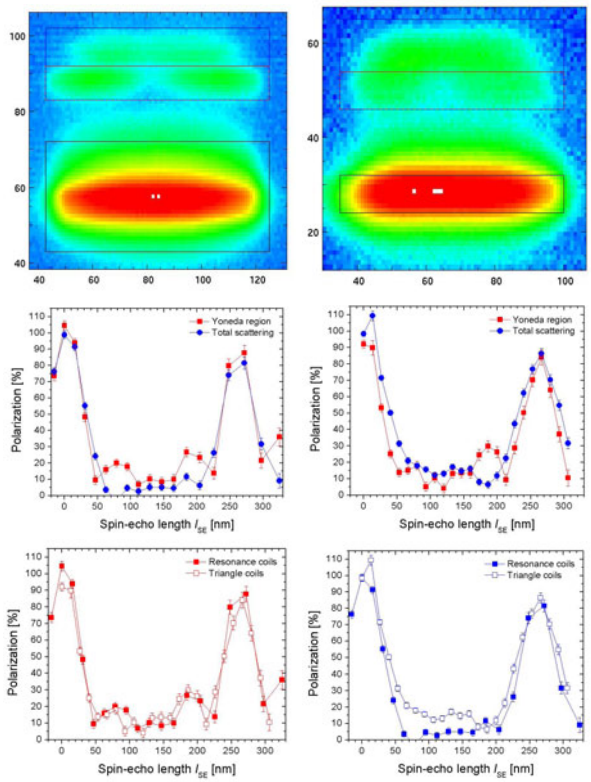

Figure 2.27: Top row: Detector images of the GISANS signal of an optical grating (aluminum 1"×1", 3600 lines/mm), left column: resonance coils, right column: triangle coils. The intense horizontal streak at the bottom is the primary beam, the feature on top is the GISANS signal from the sample. The red and blue regions of interest (ROI) are centered on the Yoneda scattering feature [4, 5] and the total scattering, respectively, where the latter also includes specular contributions. The black ROI centered on the primary beam was used to obtain a reference signal. Middle row: SERGIS data sets obtained from the red and blue ROI as a function of spin-echo length l_{SE}. The total counting time per displayed data point was 24-65 minutes (left column) and 80 minutes (right column), respectively. Bottom row: Comparison of SERGIS data obtained from the Yoneda ROI (red curves) and the total scattering (blue curves) with resonance and triangular spin-echo coils, respectively. In case of the red ROI (Yoneda intensity), which is the more reasonable choice, even details of the scattering length density profile in between two grating lines are reproduced very consistently for the two coil variants.

Polarized neutron reflectometry

The two images in Fig. 2.28 show N-REX$^+$ during a polarized neutron reflectometry (PNR) experiment employing a 7.5 Tesla magnet provided by FRM II (collaboration with Prof. Wolfgang Donner, University of Houston, USA, now Technische Universität Darmstadt). The superconducting NbTi/Nb multilayer sample was cooled to 2.5 K in a cryostat, and the influence of magnetic fields up to 6 Tesla on the magnetic structure of the sample was investigated. For these experiments we used neutrons with a wavelength of 5.5 Å. The initial vertical neutron beam polarisation was preserved at about 80% when passing the magnet, which points to negligible depolarisation in spite of the symmetrical construction of the magnet. Nevertheless the expected small difference between the reflectivity curves of spin-up and spin-down neutrons (shown in Fig. 2.28) could not be verified very clearly, presumably due to problems with the alignment of the sample in the cryostat, which is very critical in this case. It is planned to improve the aligment capabilities inside or outside the cryostat for future experiments. A slight asymmetry between spin-up and spin-down reflectivity was observable, however. The associated maximum in the polarization moves to higher angles (larger momentum transfers) upon increasing the applied magnetic field from 3 T to 5 T (see bottom row of Fig. 2.29). This would hint at a compression of the flux line lattice at larger magnetic field.

Figure 2.28: N-REX$^+$ in polarized neutron reflectometry (PNR) mode. The big 7.5 Tesla magnet and a compatible cryostat were supplied by FRM II.

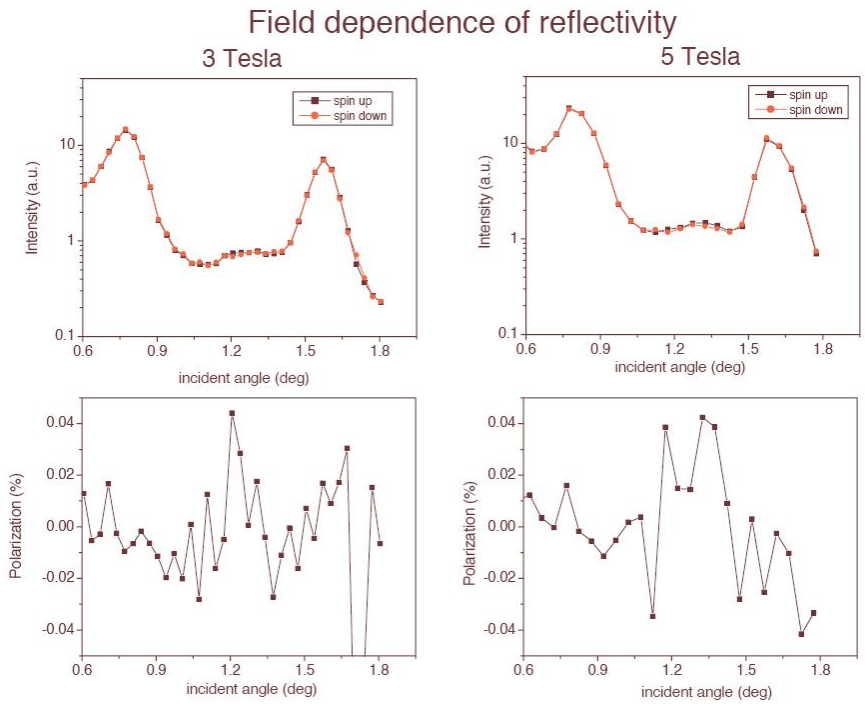

Figure 2.29: Neutron reflectivity curves and corresponding polarization values measured on a superconducting NbTi/Nb multilayer (black: spin-up neutrons, red: spin-down neutrons, the final spin state after reflection was not analyzed). A slight peak-shift was expected between the two curves (see main text). The experimental data on the left and right were measured at a magnetic field of 3 T and 5 T, respectively. The total counting time per displayed data point was 5-25 minutes.

[1] Rühm, A., Wildgruber, U., Franke, J., Major, J., Dosch, H. *In: Neutron Reflectometry, A Probe for Materials Surfaces, Proceedings of a Technical Meeting organized by the International Atomic Energy Agency and held in Vienna, 16-20 August 2004, Vienna, Austria*, 161–175.

[2] Teixeira, S. C. M., Zaccai, G., Ankner, J., Bellissent-Funel, M. C., Bewley, R., Blakeley, M. P., Callow, P., Coates, L., Dahint, R., Dalgliesh, R., Dencher, N. A., Forsyth, V. T., Fragneto, G., Frick, B., Gilles, R., Gutberlet, T., Haertlein, M., Hauß, T., Häußler, W., Heller, W. T., Herwig, K., Holderer, O., Juranyi, F., Kampmann, R., Knott, R., Krueger, S., Langan, P., Lechner, R. E., Lynn, G., Majkrzak, C., May, R. P., Meilleur, F., Mo, Y., Mortensen, K., Myles, D. A. A., Natali, F., Neylon, C., Niimura, N., Ollivier, J., Ostermann, A., Peters, J., Pieper, J., Rühm, A., Schwahn, D., Shibata, K., Soper, A. K., Strässle, T., Suzuki, J., Tanaka, I., Tehei, M., Timmins, P., Torikai, N., Unruh, T., Urban, V., Vavrin, R., Weiss, K. *Chemical Physics*, 345, (2008), 131–151.

[3] Major, J., Dosch, H., Felcher, G. P., Habicht, K., Keller, T., te Velthuis, S. G. E., Vorobiev, A., Wahl, M. *Physica B*, 336, (2003), 8–15.

[4] Yoneda, Y. *Phys. Rev.*, 131, (1963), 2010.

[5] Sinha, S. K., Sirota, E. B., Garoff, S., Stanley, H. B. *Phys. Rev. B*, 38, (1988), 2297.

3 Inelastic scattering

3.1 J-NSE: Performance and first experiments

O. Holderer[1], **M. Monkenbusch**[1], **R. Schätzler**[1], **N. Arend**[1], **G. Borchert**[2], **C. Breunig**[2], **K. Zeitelhack**[2], **W. Westerhausen**[3], **H. Kleines**[4], **M. Wagener**[4], **F. Suxdorf**[4], **M. Drochner**[4]
[1]JCNS, Research Centre Jülich, outstation at FRM II
[2]ZWE FRM II, TU München
[3]ZAT, Research Centre Jülich
[4]ZEL, Research Centre Jülich

Introduction

The neutron spin-echo instrument, J-NSE, has been moved from the FRJ-2 in Jülich to the guide hall of the new FRM II reactor. In order to supply an intense beam of polarized neutrons at the assigned new position of the instrument, a neutron guide system had to be designed and built to transport neutrons from the available partial beam window of the neutron guide NL2 at the wall of the guide hall to the proper spectrometer. Polarization of the short wavelengths is achieved in a bent section with a m=3 FeSi multilayer coating. Due to the total reflection of FeSi, longer wavelengths pass unpolarized and an additional short polarizer at the entrance of the instrument is required. For a neutron wavelength band of 10% FWHM centered at 7Å a flux of $1 \times 10^7/\mathrm{cm}^2\mathrm{s}$ at the sample has been achieved.

The polarizing neutron guide system

Neutron spin echo (NSE) spectroscopy provides the highest resolution (corresponding down to a few nano eV) in inelastic neutron scattering [1, 2], with applications in the study of slow dynamics of soft matter systems as e.g. polymer melts or micro-emulsions, or in paramagnetic scattering (spin glasses). The normalized intermediate scattering function is measured in terms of polarization loss of the scattered neutrons. As input the instrument accepts a polarized beam with a wide velocity distribution and thereby yields the necessary scattering intensity.

The Jülich NSE spectrometer (J-NSE) had been installed in the neutron guide hall of the Jülich research reactor FRJ-2 [3].

With the end-of-operation of the FRJ-2 reactor the instrument (see fig. 3.1) has been technically updated and transferred to the FRM II in Garching supplying a considerably higher neutron flux. The neutrons from the FRM II cold source have to be polarized and transported efficiently to the J-NSE instrument. The dedicated neutron guide system which is described here is designed to serve this purpose.

At the new position at the FRM II, the J-NSE is connected to a dedicated fraction of the neutron guide NL2, i.e. NL2a-o.

Using a mechanical velocity selector included into the guide section it is possible to use wavelengths λ between 4.5 and 19 Å. This gives an enormous increase in the dynamic range of the spin echo spectrometer, since the intermediate scattering function depends on the Fourier

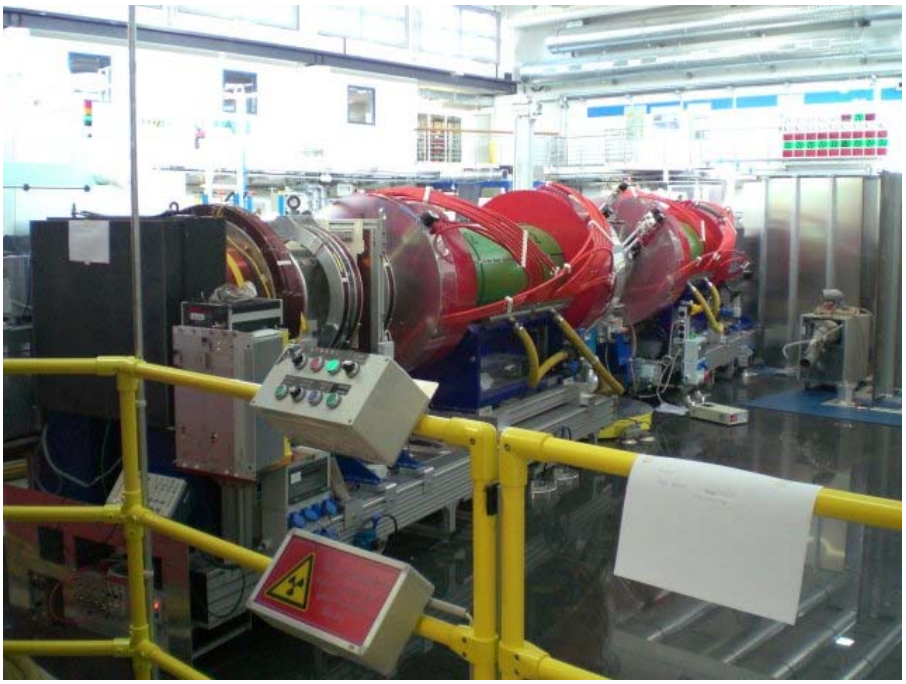

Figure 3.1: View on the J-NSE instrument at the FRMII.

time t with $t \propto \int |B| dl\ \lambda^3$, where the first factor, the field integral $\int |B| dl$ alone allows for a 1:10^3 variation.

The neutron guide NL2a-o separates by a bent part of 8 m length inside the radiation shielding casemate from the neighboring NL2 section that leads to the time-of-flight spectrometer TOF-TOF. The radius of curvature is 160 m which on the one side yields sufficient distance from the TOF-TOF feeding guide at the position of the instrument and on the other hand polarizes the beam in the range from λ=2.5...8 Å by reflection from a m=3 (spin-up) and m=0.65 (spin-down) FeSi multilayer produced by T. Krist, NOB. The m-value denotes the ratio of the total reflection angle compared with that from a plain Ni coating as reference. Due to the high primary flux at the curved section a coating containing cobalt was discarded because the long term buildup of considerable ^{60}Co activation. Because of the unpolarized total reflection of FeSi below m=0.65 the longer wavelengths λ =8...16 Å need an additional short polarizer at the entrance of the actual NSE instrument. After the bent section a mechanical selector (which currently limits the wavelength to $\lambda \geq$4.5Å) is inserted, followed by 10 m of tapered ^{58}Ni covered guide which ends with a cross section of 60×60 mm^2. The NSE-spectrometer uses only a limited divergence of the neutron beam, since the sample position is approximately 3.5 m behind the end of the neutron guide. A supermirror (NiTi) coating instead of ^{58}Ni would mainly increase the flux with high divergence and is therefore not necessary in our case, which also simplifies the shielding of the neutron guide.

The additional long wavelength polarizer consists of a 60 cm long piece of neutron guide with 2 separating walls, the reflecting guide surface and both sides of the walls are covered with an m=3 FeSi multilayer (Swiss Neutronics). For the short wavelength configuration, this polarizer acts as a simple piece of neutron guide. It follows directly the last part of the ^{58}Ni-Guide. For polarizing the long wavelengths, the whole NSE spectrometer needs to be turned by $\Theta = 4^\circ$ and the long wavelength polarizer is moved to an angle of $\Theta/2 = 2^\circ$. This leads to a reflection at the polarizing walls and to a deviation of the beam of 4°.

The initial bent section after the NL2a-o separation is embedded into a vertical guide and magnetization field $>$ 30 mT which is generated by NbFeB magnet columns between soft iron plates on top and below the guide. After the bent section with FeSi multilayer coating the field is reduced to 6mT. On a 1 m section before the selector the vertical field is turned smoothly into the longitudinal direction by a solenoid around the neutron guide. That way the neutron spins and hence the beam polarization follows the field direction adiabatically. The selector is surrounded by a solenoid to preserve the polarization during the neutron passage. The subsequent 10 m of neutron guide are surrounded by a coil with about 2 turns/cm which yields B=2.5 mT at a current of 10A. Finally, the additional polarizer for long wavelengths is surrounded by a solenoid able to sustain 5 mT and to create a (once in a while needed) magnetizing field of 30 mT during a few seconds.

The flux at the end of the neutron guide, i.e. at the entrance of the NSE spectrometer, has been measured by gold-foil activation. The wavelength band is defined by the mechanical velocity selector (10 % FWHM). Short wavelengths are sufficiently polarized, whereas the longer wavelengths need an additional polarizer. Thus beyond 12Å the gold foil activation detects the sum of both spin directions. The flux at the end of the guide ranges from polarized 4.5 $\times 10^7$/cm^{2}s for wavelength shorter than $\lambda = 7$ Å down to 1×10^7/cm^{2}s at λ =16 Å. The wavelengths beyond 9-10Å are insufficiently polarized and need the additional polarizer. On the non-guided path of $\simeq$ 3.5m between neutron guide exit and sample position the larger divergence of the long wavelength neutrons leads to a considerable dilution effect on the flux at the sample position.

A reduction of the flipping ratio with increasing wavelength results from

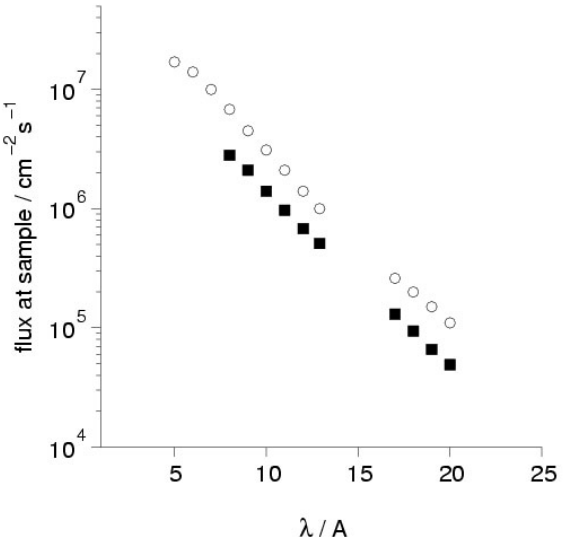

Figure 3.2: Flux at the sample position as function of wavelength setting of the selector. Open symbols correspond to straight configuration of the spectrometer with inactive secondary polarizer, solid symbols show result from the 4^0 setting with active polarizer.

the total reflection of both spin components. The additional polarizer is used at a fixed deviation angle of $4°$. For $\lambda = 8$ Å the flipping ratio is significantly enhanced by the polarizer (from below 7 to above 25), however, the angluar acceptance there is not fully developed to the desired value due to limitation of m. On the other hand at 19Å the total reflection edge (m=0.6) of the polarizer starts to contribute.

The flux at the sample position was measured with a calibrated beam monitor. All correction elements and flippers in the beam path were installed.

Considering the polarization the flux obtained in the straight configuration may be used up to 8 to 9 Å beyond that the 4°configuration with active polarizer needs to be employed.

The wavelength dependence of the flux at the sample position is illustrated in figure 3.2 for the situation without extra polarizer (usable for $\lambda \leq 9$ Å) and with polarizer (usable for $\lambda \geq 8$ Å). A Maxwell spectrum emitted from a small source is expected to deliver a flux $\Phi_0 \lambda^{-5} \exp(-h^2/(2m_n \lambda^2 k_B T))$, since the wavelength band is prepared by a selector with constant relative width, i.e. $\Delta\lambda \propto \lambda$ the λ^{-5} dependence is mitigated to $\Phi \propto \lambda^{-4}$. The flux at the sample for 7 Å matches that of the ILL instrument IN15, however, the decrease at longer wavelength is steeper for the J-NSE. The latter effect has still to be understood.

First experiments

First experiments have been carried out with different setups. The “shorty” option (a spin echo setup with a set of small main precession coils between the main precession coils and the sample position) together with wavelengths of 5 Å allowed for measuring with Fourier times ≥ 4 ps. The standard setup with $\lambda = 8$ Å has been used for comparison with experiments performed at the DIDO reactor in Jülich. First experiments have been performed also at longer wavelengths (12.8 Å) to access Fourier times of ~ 70 ns. For experiments at large field integrals and hence high Fourier times, the resolution of the spectrometer needs to be further improved and development is going on to achieve this with better correction coils in each arm. In Figure 3.3, two spin echo groups recorded at different setups are presented (top) as well as the intermediate scattering function of a polymer solution at q=0.8 1/nm, showing Zimm dynamics.

Conclusion

In summary the flux a the new position of the J-NSE at the FRM II yields 15 times the flux at 8Å that was obtained at the old position in the FRJ-2 guide hall. In addition, the flexibility to choose $4.5 \leq \lambda \leq 19$Å has been gained by the combined effect of the new reactor source and the tailored neutron guide system. First experiments have been performed on the relocated spectrometer. Development is going on for improving the resolution at large field integrals. Further details may be found in ref. [4].

[1] Mezei, F., editor. volume 128 of *Lecture Notes in Physics* (Springer, Berlin, Heidelberg, New York, **1980**).

[2] Mezei, F., Pappas, C., Gutberlet, T., editors. volume 601 of *Lecture Notes in Physics* (Springer, Berlin, Heidelberg, New York, **203**).

[3] Monkenbusch, M., *et al. Nucl. Instr. & Methods In Physics Research A*, 301–323.

[4] Holderer, O., *et al. Nucl. Instr. & Methods In Physics Research A*. In press.

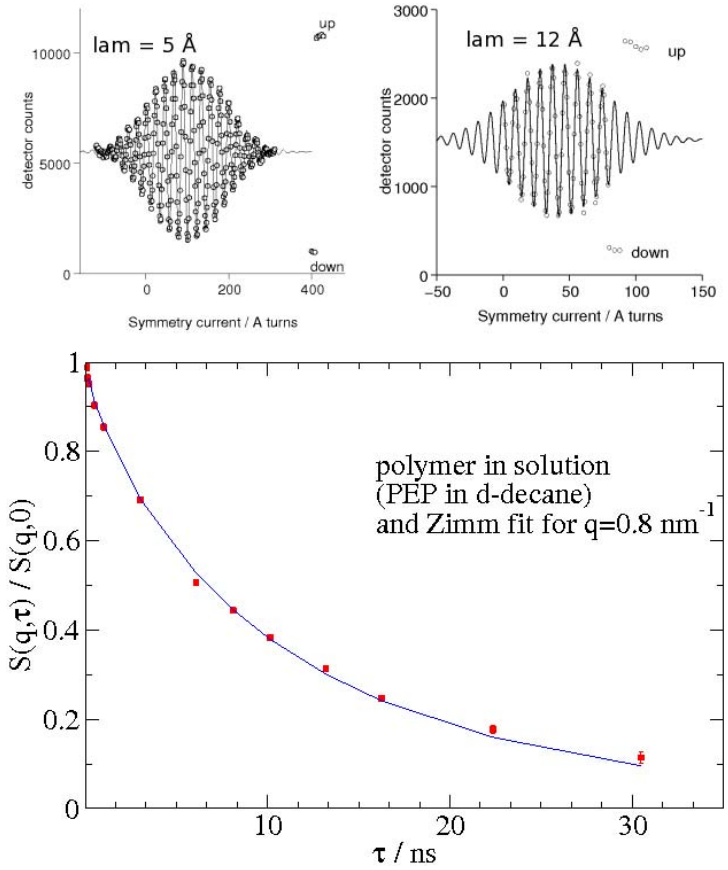

Figure 3.3: Spin echos measured at 5 Å and 12 Å (top) and S(q,τ) from a polymer solution measured at 8 Å.

3.2 MIRA – The beam line for very cold neutrons at the FRM II

R. Georgii[1], **M. Ay**[2], **P. Böni**[3], **R. Gähler**[4], **C. Grünzweig**[2], **Ph. Jüttner**[1], **T. Hils**[3], **A. Mantwill**[1], **S. Mühlbauer**[1], **R. Schwikowski**[1]
[1]ZWE FRM II, TU München
[2]Laboratory for Neutron Scattering ETHZ & PSI,Switzerland
[3]Physics Department E21, TU München
[4]Institut Laue Langevin, Grenoble, France

MIRA is a versatile instrument for very cold neutrons (VCN) using neutrons with a wavelength $\lambda > 8$ Å. The flux at the sample position is $5 \cdot 10^5$ neutrons/(cm^2 s) unpolarised. It is situated at the cold neutron guide NL6b in the neutron guide hall of the FRM II. As the instrument set-up can be changed quickly, MIRA is ideally suited as a testing platform for realizing new instrumental set-ups and ideas. In particular, MIRA is unique in its possibilities of combining different neutron scattering methods as:

- Polarized or non-polarized reflectometry.
- Spherical polarimetry
- Polarized or non-polarized small angle scattering (SANS).
- Classical NRSE (Neutron Resonance Spin Echo) setup as well as using the MIEZE principle.

Figure 3.4: MIRA and the second monochromator shielding

Status

In 2007 year MIRA was again successfully operated for 5 reactor cycles. In total, 16 external and 18 internal proposals, several test and service measurements were performed. Several measurements for diploma theses were finished using mainly data from MIRA. A total of 2 weeks was devoted to the Fortgeschrittenenpraktikum of the Physics Department for 35 students in total.

Currently the upgrade of MIRA to shorter wavelengths is in progress. The goal is to use neutrons with wavelengths between 3 Å and 6 Å from the neutron guide NL 6a (beam area 120 x 60 mm^2) using a PG monochromator. Having neutrons with a wavelength closer to the maximum of the cold flux, having the PG monochromator with a higher reflectivity as the current multilayer monochromator and using also a vertical focusing monochromator, MIRA will then show an significant increase the intensity. This year the new monochromator shielding has already been integrated in the guide NL 6a (see Figure 3.5) and all preparations for installing the new option in January 2008 have been taken.

Multiple small angle neutron scattering (MSANS): A new two-dimensional ultrasmall angle neutron scattering technique

Small angle neutron scattering (SANS) is a powerful technique for studying the structure of materials with lateral correlation lengths in the range of about 0.6 nm up to about 600 nm. This corresponds to a q-range of 1 Å^{-1} to 10^{-3} Å^{-1}. Measuring correlation lengths in the micrometer range being of high interest for the research on biological samples, polymers, colloid systems, cements, micro-porous media leads to unacceptable losses in intensity by a factor 10^4 using the standard SANS technique. With the new MSANS technique we can overcome the intensity problem. The method is based on two 2D-multihole Cd-apertures one placed at the front end of the collimator of a common SANS instrument and the other close to the sample (Fig. 3.6).

By choosing the proper MSANS geometry, individual diffraction patterns are superimposed leading to a large gain in intensity. Using MSANS as an option for SANS beam lines, the q-resolution can be increased to 10^{-5} Å^{-1} without dramatically sacrificing intensity. The first demonstration experiment of the MSANS technique [1] was performed at the diffractometer beam line MIRA, where we already obtained a q-resolution of $3 \cdot 10^{-4}$ Å^{-1}. Fig. 3.7 shows a section of the detector image of a gadolinium (Gd) absorption grating with a period of 2 μm.

Fig. 3.8(a) shows the detector image from a silicon phase grating with a period of 2 μm. The large gain in intensity is clearly visible in Fig. 3.8(c).

Figure 3.5: A close-up of the monochromator shielding

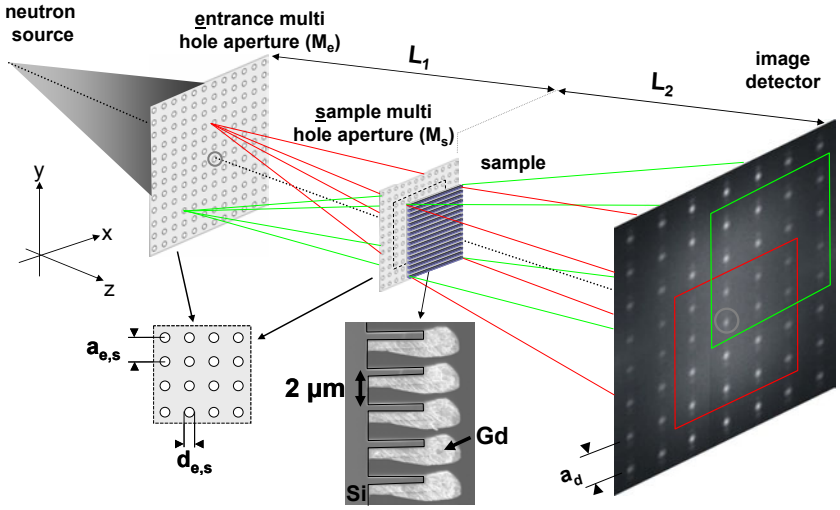

Figure 3.6: Schematic experimental setup of the MSANS option showing the 2D entrance multi hole aperture (M_e) with a lattice constant a_e and hole diameter d_e, and the 2D sample multi hole aperture (M_s) with lattice constant a_s and hole diameter d_s. Using appropriate values a_e= 5 mm, a_s= 2.5 mm and $L_1 = L_2 = 2.6$ m, the individual beams superimpose on the detector on a grid with the lattice constant $a_d = 5$.

Recently, a similar experiment has been performed using D11 at the Institute Laue-Langevin, where a grating with a pitch of 17 μm was resolved using the MSANS technique.

[1] Grünzweig, C., *et al. Appl. Phys. Lett.*, 91, (2007), 203504.

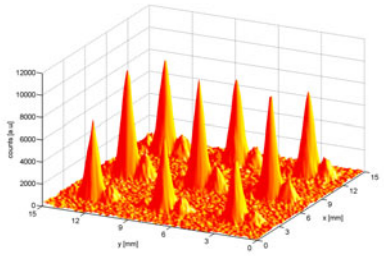

Figure 3.7: Section of an MSANS detector image of a 2 μm period Gd absorption grating.

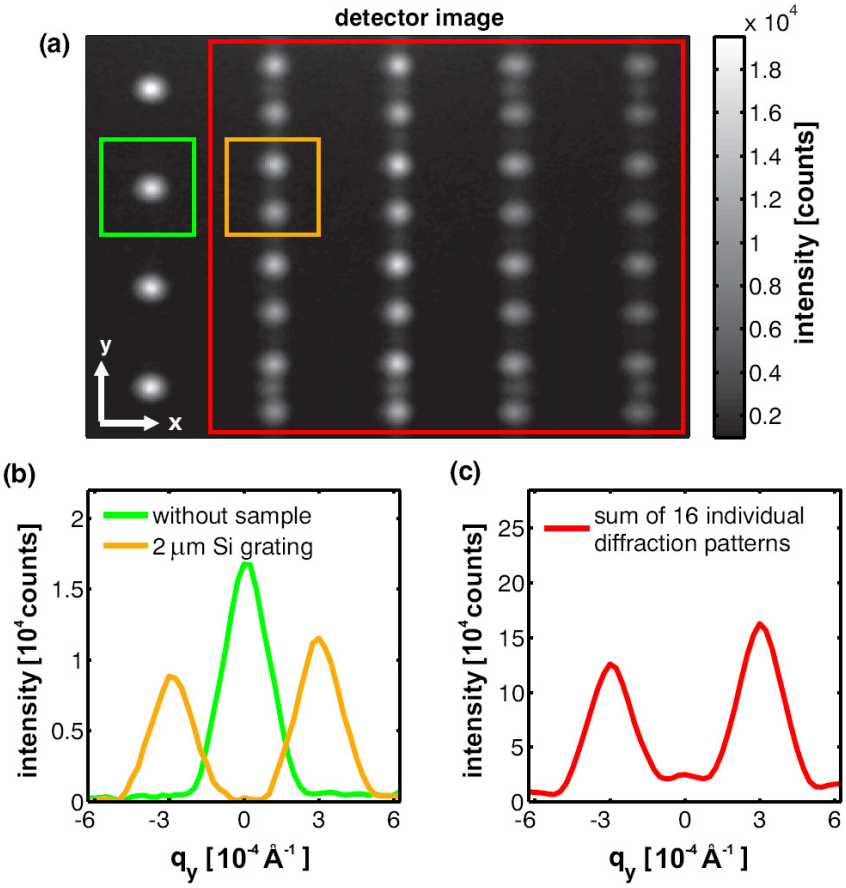

Figure 3.8: MSANS data of Si phase grating with a period of 2 μm. (a) Detector image. (b) Profiles along the y-axis through one hole pattern without sample in the beam (green box in (a)). The orange box in (a) showing the diffraction pattern of a 1D phase grating. (c) Section plot along the y-axis of 16 individual summed up diffraction patterns (red box in (a)).

3.3 PANDA – report from the FRM II cold TAS

P. Link[1], **A. Schneidewind**[2], **D. Etzdorf**[1], **M. Loewenhaupt**[2]
[1]ZWE FRM II, TU München
[2]Institut für Festkörperphysik, Technische Universität Dresden

Introduction

The second year of routine operation on PANDA was governed by major improvements of the instrumental performance as well as the extension of the useable palette of sample environments. Here we report in detail about the final performance of the double focusing PG monochromator evaluated in January 2007 and the tests of the Heusler monochromator and analyzer at the end of the year. Together with the FRM II sample environment group and also external users the variety of sample environments used on PANDA was extended by high pressure cells, a low temperature cryostat, the FRM II high temperature furnace (HTF) and the 7.5 T vertical field magnet. This altogether has been achieved besides a continuous heavy load of external user experiments.

Progress of instrumental performance

Double focusing PG monochromator

In January 2007 the improved focusing drives of the PG monochromator have been commissioned and extensively tested. Allowing for an independent automated adjustment of both, the vertical focus and the horizontal focus drive depending on the monochromator take-off angle, inelastic measurements using the fully focused set-up with the highest available intensity are possible. Fig. 3.9 shows exemplarily constant Q scans of a transverse acoustic phonon of a 0.8 cm^3 Pb single crystal at Q =(2.2,2.2,0) for the different focusing modes of the PG monochromator keeping the analyzer unchanged at $k_f = 2.57$ Å^{-1} with a 6 cm PG filter on k_f. Rather impressive the overall gain in intensity by one order of magnitude while keeping the energy resolution almost unchanged. The inset of the figure reports the wave vector dependence of the gain factor for the three different foci modes with respect to the flat monochromator set-up obtained from scans having a ^{3}He monitor mounted on the sample position with a 1 cm^2 aperture in front of it. While the horizontal focus alone gives a rather constant gain of almost a factor of 2, the vertical focus gain factor varies from 2 to 5 with increasing wave vectors. This variation is due to the increasing active monochromator surface for decreasing scattering angles.

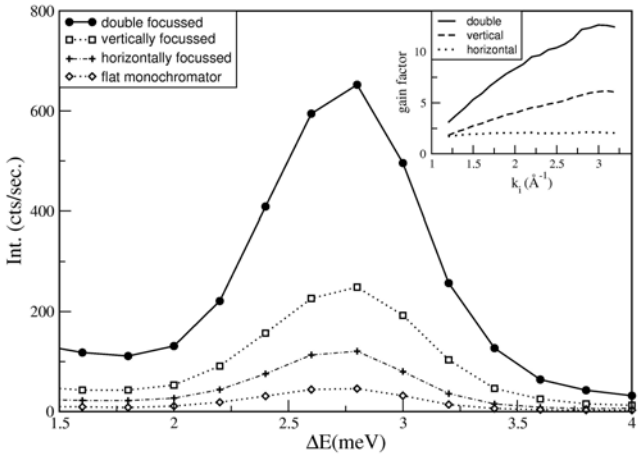

Figure 3.9: Constant–Q scan at Q = (2.2,2.2,0) of a 0.8 cm^3 Pb s.c. for the different foci modes of the PG002 monochromator. The inset shows the wave vector dependance of the gain factor for the three focusing modes.

Polarized neutron set-up with Heusler monochromator and analyzer

In December 2007 we could for the first time introduce both, the Heusler monochromator and analyzer to the PANDA set-up. The monochromator change was done remote controlled (keeping the shielding closed) using the foreseen monochromator changer. Adiabatic spin-flipper's before and after the sample position and guide field elements along the neutron flight path have been mounted. In a first step the currents for the compensation field and for the flip field of the spin-flippers were adjusted to values appropriate for the selected neutron wavelength using the direct beam (no sample). Fig. 3.10 displays a typical scan of the spin-flippers flip-field current, using already the optimal compensation field at a neutron wave vector of 1.64 Å^{-1} and a PG filter in the beam; the line is a fit to a cosine function. In the following we show the results of a number of tests that have been performed. Fig. 3.11 a) shows the non spin-flip (nsf) and spin-flip (sf) intensities of a nuclear Bragg peak of the Pb single crystal. From the picture one may directly

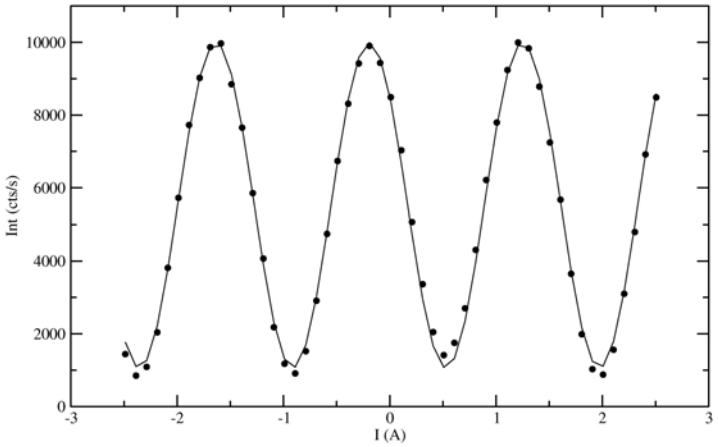

Figure 3.10: Exemplary data of the polarized neutron set-up: Direct beam intensity varying with the spin-flippers flip field current at optimal compensation current.

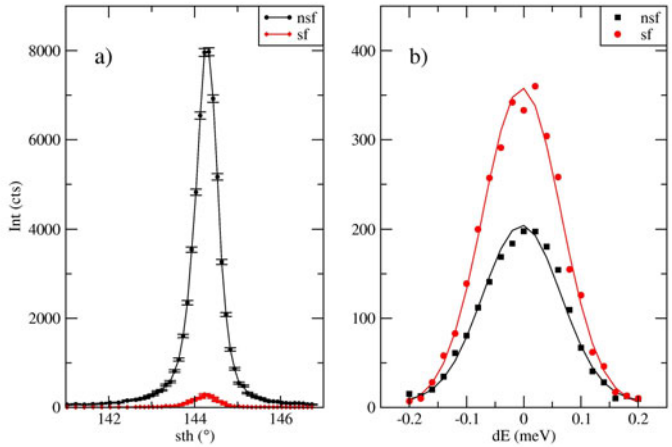

Figure 3.11: Test scans using the PANDA polarized neutron set-up with **P** $\perp$ **Q**: **a)** non spin-flip and spin-flip scattering of the **Q**=(2,0,0) nuclear Bragg peak of Pb **b)** non spin-flip and spin-flip scattering of the Vanadium standard.

read the flipping ratio being in the order of 40, resulting in a beam polarization of about 0.95. The Vanadium sample also (Fig.3.11 b) exhibits the expected 2:1 ratio of the sf versus the nsf intensity arising from nuclear-spin incoherent scattering. In total the commissioning of the Heusler monochromator and analyzer has been a full success enabling us now to perform polarized neutron experiments. The next step will be to introduce Helmholtz coils at the sample space to perform longitudinal polarization analysis or a MuPad / Cryopad set-up for full 3D polarization analysis.

Sample environment

The PANDA instrument faces an important demand of particular sample environments from our users. The overload factor for beam-time using the 14.5 T vertical cryomagnet is continuously 2-3. Besides this low temperatures (T < 1.5 K) make up an important issue for the requested beamtime. Therefore, a Variox cryostat has been purchased by FRM II in 2007 to be used together with the TU Dresden Kelvinox dilution cryostat. After a successful commissioning (see Fig.: 3.12) the Kelvinox has been successfully used for three experiments on PANDA and one experiment on TRISP. The attained base temperature varied between 30 mK and 60 mK for the different runs. In 2007 we also used for the first time the FRM II 7.5 T vertical magnet. Although having a lower maximum field this magnet is an attractive alternative as it allows for larger sample diameters and does not need cryogenic liquids for cooling making the operation on the beam easier. The FRM II standard high temperature furnace (HTF) had been operated during one user experiment completing the usable palette of temperature devices on PANDA. Concerning high pressures there were two experiments where our users brought WcWhan type pressure cells to perform experiments at pressures up to 15 kbar.

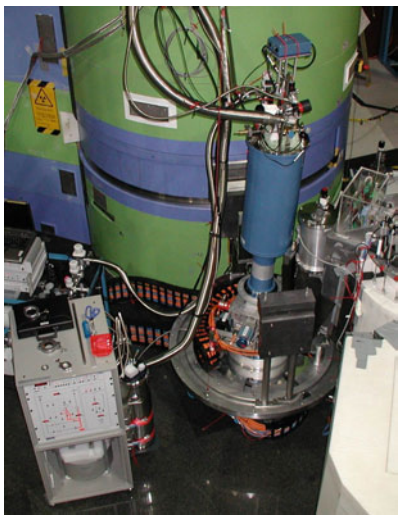

Figure 3.12: The PANDA instrument running with the Variox / Kelvinox cryostat combination.

3.4 First productive experiments on the new backscattering spectrometer SPHERES

J. Wuttke[1], **G. J. Schneider**[1], **L. C. Pardo Soto**[1,2], **M. Prager**[3], **Q. Shi**[4], **A. Budwig**[5], **G. Hansen**[5], **A. Ioffe**[1], **H. Kämmerling**[5], **F.-J. Kayser**[6], **H. Kolb**[7], **A. Nebel**[1], **V. Ossovyi**[1], **H. Schneider**[1], **P. P. Stronciwilk**[1], **D. Richter**[3]
[1]JCNS, outstation at FRM II, Research Centre Jülich
[2]Grup de Caracterització de Materials, Departament de Física i Enginyeria Nuclear, Universitat Politècnica de Catalunya, Barcelona
[3]IFF, Research Centre Jülich
[4]Afdelingen for Materialeforskning, Forskningscenter Risø, Danmarks Tekniske Universitet, Roskilde
[5]ZAT, Research Centre Jülich
[6]ZEL, Research Centre Jülich,
[7]ZWE FRM II, TU München

Status

Commissioning of SPHERES is approaching the final stage. By the end of 2006, we had demonstrated *in principle* that the instrument will produce competitive spectra. By the end of 2007, stability and performance have improved to the point where productive experiments are becoming routine. The signal-to-noise ratio was increased from 165:1 to 330:1. We aspire to obtain the permanent operation permit in the first half of 2008. The instrument is now open for regular user proposals.

Technical upgrades

Initially, test experiments were hampered by instabilities of vital components, namely the neutron velocity selector and the phase-space transform chopper. These problems being understood and solved, all subsystems of SPHERES are now running stable for entire reactor cycles.

A cryostat, lent by FRM II, was adapted to the detector geometry of SPHERES. Accessible temperature ranges are now 4...330 K and 10...550 K, depending on configuration.

Software development continued throughout the year. Computer control has been extended to the Doppler drive. Basic spectrometer operation is now possible through a graphic user interface. Measurements can be scripted. The beam shutter and other safety-critical components are controlled by a SPS.

Neutronic improvements

Extensive tests were performed, aiming at a better understanding of the remaining neutronic noise. We temporarily divided primary and secondary spectrometer by a huge boron rubber barrier, and we moved neutron detectors around to localise leakages. In the event, we improved the shielding around the primary beam path, especially around the monochromator, and around the exit channel of the chopper.

In measurements on a standard scatterer (without sample environment), we achieved a signal-to-noise ratio of 330:1 in the large-angle detectors (Fig. 3.13). At least a third of the remaining noise is caused by fast neutrons that are created in the ^{6}Li absorbers in the chopper. As anticipated in the last report, replacing these absorbers by boron ceramics is a major effort. We are currently installing a purpose-built lifting gear that will give us access to the chopper wheel. As there is no way to balance the activated wheel, it is necessary to build a new one. It is foreseen to transfer the PG crystals from the old to the new wheel in summer 2008. By this measure alone, we will reach a signal-to-noise ratio of 500:1.

Commissioning of the five small-angle detectors just started. After first improvements of the neutronic shielding, we obtained signal-to-noise ra-

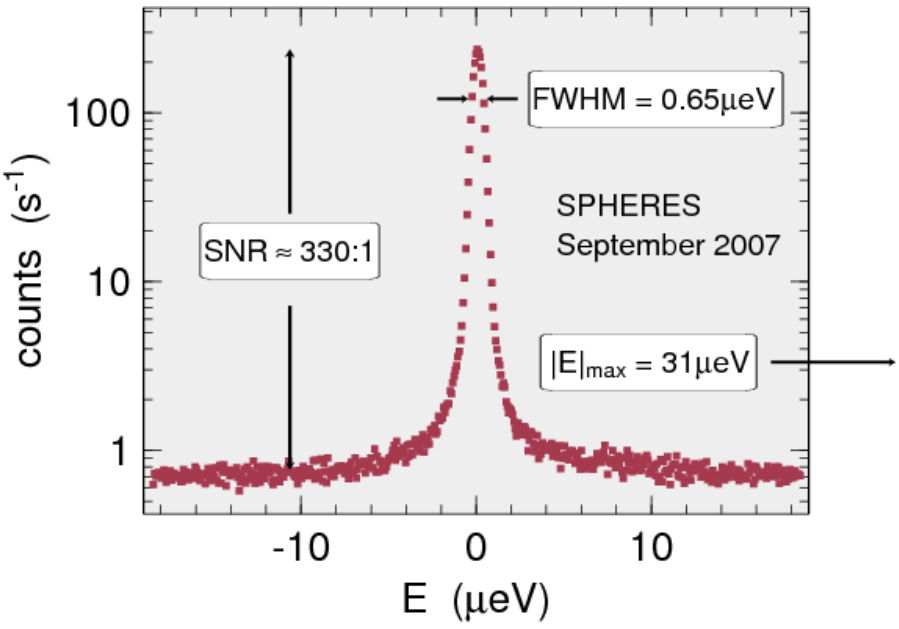

Figure 3.13: Resolution function of the large-angle detectors.

tios between 50:1 and 100:1; the energy resolution (fwhm) lies between a good 0.93 μeV and an unacceptable 2.3 μeV. It might be necessary to rethink the analyser and detector geometry before substantial progress can be made.

Productive experiments

In the last three reactor cycles of 2007, we performed an increasing number of test experiments. These experiments provided us invaluable guidance in preparing for routine operation. At the same time, they produced full-fledged results. First experimental reports from satisfied test users have arrived.

Rotational dynamics and quantum tunneling were studied in several compounds. Measurements on methylxanthines, a biologically important class of molecules, were used to conclude a study that was begun on the old Jülich backscattering spectrometer BSS [1]. In theophylline, a doublet tunneling band is observed at 15.1μeV and 17.5μeV (Fig. 3.14).

This is in agreement with the room temperature crystal structure, implying that no phase transition occurs with cooling. In caffeine, orientational disorder leads to a 2.7μeV broad distribution of tunneling bands around the elastic line.

To characterize the temperature dependence of quasielastic scattering, we went beyond the elastic ("fixed-window") scans customarily measured in neutron backscattering. Given the high flux at SPHERES, it would be a waste of measuring time to restrict temperature scans to the elastic channel. Instead, during temperature ramps we measure a rapid succession of inelastic spectra. After the event, we integrate over appropriate energy windows to obtain elastic and inelastic scattering as function of temperature.

Such inelastic temperature scans are particularly useful in localising dynamic phase transitions. Fig. 3.15 shows a striking example: the rotation of ammonia in $Mg(NH_3)_6Cl_2$ undergoes a transition at 140 K. This transition shows up much more clearly in the inelastic than in the elastic scattering intensity.

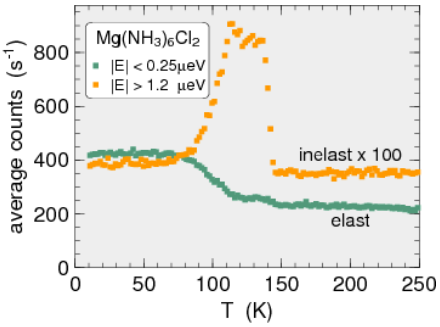

Figure 3.15: Inelastic and elastic scattering from $Mg(NH_3)_6Cl_2$ as function of temperature. Note the phase transition at 140 K which shows up much more clearly in the inelastic than in the elastic signal. From a "friendly-user" experiment of Shi, Jacobsen, Vegge, Lefmann from Risø.

Some Freon compounds form a plastic phase in which the molecules sit in a regular lattice, but rotate more or less freely. This phase has an exceptionally high fragility. Above the glass transition, there is another dynamic phase transition at about 130K. Above this transition, we see a rapid increase of quasielastic broadening, which we attribute to jumps between trans and gauche conformations (Fig. 3.16).

[1] Prager, M., Pawlukojc, A., Wischnewski, A., Wuttke, J. *J. Chem. Phys.*, 127, (2007), 214509.

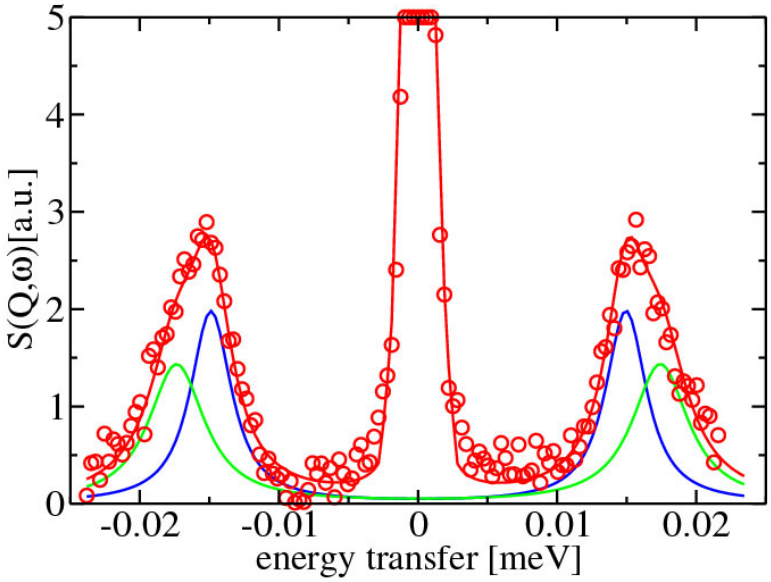

Figure 3.14: Spectrum of anhydrous theophylline at 3K. Based on the crystal structure, the broad tunneling peak could be interpreted as an unresolved doublet of equal intensities [1].

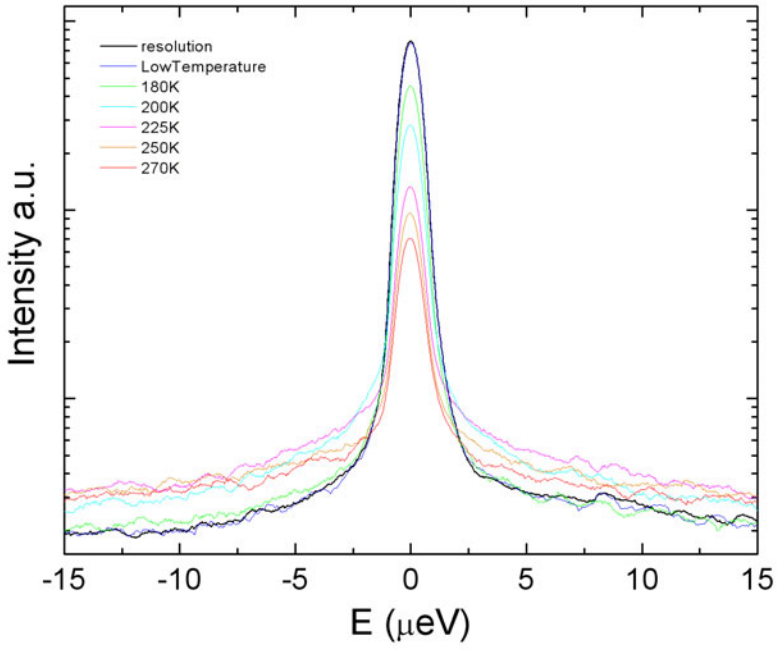

Figure 3.16: In the plastic phase of freon, conformational jumps lead to quasielastic broadening.

3.5 Replacement of the neutron guide and a new polarizer at RESEDA

Wolfgang Häußler[1,2], **Mathias Sandhofer**[1], **Reinhard Schwikowski**[2], **Andreas Mantwill**[1], **Peter Böni**[1]
[1]Physics Department E21, TU München
[2]ZWE FRM II, TU München

One major challenge in 2007 at the Resonance Spin Echo (NRSE) Spectrometer RESEDA has been the replacement of the neutron guide. The old, polarizing neutron guide NL5 had to be removed, due to non-tolerable activation of its magnetic supermirror layers. The new neutron guide NL5 consists of glass furnished with non-magnetic NiTi supermirrors. As a consequence, the neutron beam is not any more polarized, and a supermirror cavity fixed at the very end of the guide is used now as polarizer.

Fig. 3.17 shows an image of this polarizing cavity, being 2 m in length and optimized for neutron wavelengths of 5-8Å. A strong magnetic field produced by permanent magnets and iron plates around the polarizer provides sufficient magnetization of the magnetic supermirror layers. In order to maintain sufficiently strong magnetic field strength along the whole polarizer, several measures were taken. The beam shutter at the end of the neutron guide, having before partly covered the glasswalls of the polarizer, had to be exchanged by a smaller, but nevertheless equally efficient shutter, because more space was needed for the iron plates of the guide field. The number of magnets was increased, in order to reach a field strength of about 400 G.

The instrument was moved on air pads about 80 cm aside the neutron guide, so that the polarization could be measured directly behind the polarizing cavity, before the neutrons traverse the instrument. After some improvements, the biggest ones being a diaphragm, suppressing unpolarised neutrons at larger divergence angles and increased field strength at the end of the polarizer, the polarization reached a mean value over the whole beam cross section of 88 % at neutron wavelength 6 Å.

Fig. 3.18 shows a false color image of the polarization data acquired by means of a polarization measurement setup, consisting of two spin flippers, the ^{3}He cell (kindly provided by the FRM II - He3 group, Dr. Masalovich and O. Lykhvar) used as analyzer and the detectors. For fast

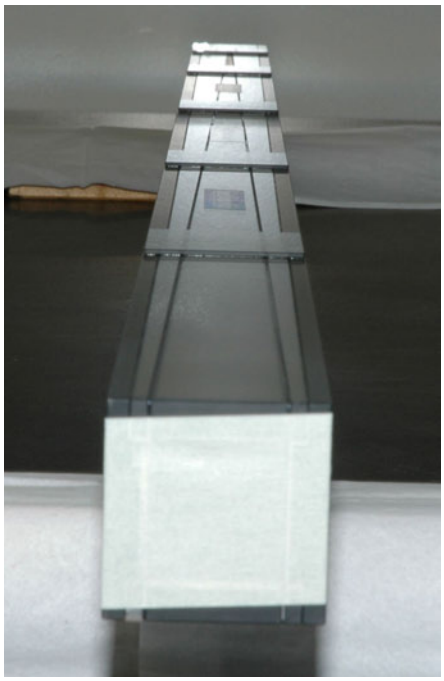

Figure 3.17: The new polarizing cavity (length 2 m), which is now mounted at the end of the neutron guide NL5, in front of RESEDA.

tuning of the spin flippers, we used a standard ^{3}He counter. For the final measurements providing spatial resolved polarization data, we used a CCD camera equipped with a neutron sensitive scintillator. By four measurement steps, this setup allows to determine both the flip efficiency of both flippers and the "true" beam polarization.

In order to detect eventual depolarization effects in the first spectrometer arm of RESEDA, RESEDA has been moved back to the neutron guide, and the polarization measurement setup described above was moved behind the first spectrometer arm.

While moving RESEDA aside and back, it turned out that the air pads worked only partially. The air is pressed through two circular, concentric air gaps for being able to move the instrument easily on an air layer. Imperfect precision of the concentric rings, manufactured out of aluminum, leads to unequally distributed air pressure. The air pads are partially stuck to the floor, when all air pads are simultaneously activated, so that the available air pressure is decreased slightly. In order to avoid similar problems in future, construction of improved air pads has been started in mid 2007. Nevertheless, the instrument was positioned back and aligned according to the neutron beam.

The very first polarization tests show, that the polarization is not equally distributed within the neutron beam behind the first arm of RESEDA. Fig. 3.19 shows a false color image of the polarization distribution. Improving the polarization will be continued during the first cycle in 2008.

Last but not least, big effort in autumn 2007 was put into the placement of the new RESEDA user cabin. Subsequently, after having been put on place, the security installations of the cabin had to be put to place, especially on the top of the cabin, where a big part of the electrics and electronics is placed now. Moving the electronics there has been a major task in late 2007, and will be continued and finished in early 2008.

Then, also the NRSE coils, which have been supplied with motorized goniometers and rotation tables in early 2007, in order to provide fast and efficient positioning of the coils, will be put into operation again. Having finished the polarization measurements, we will start then with spin echo test measurements, employing the NRSE coils together with new NSE coils put into operation also in early 2007, used for measurements at small spin echo times.

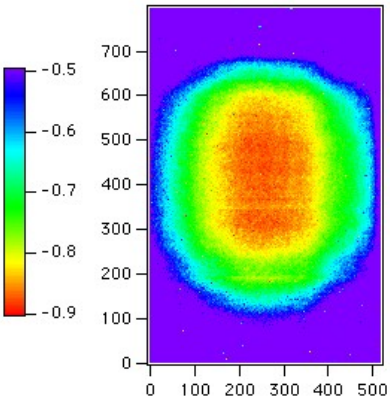

Figure 3.18: False color contour plot of the polarization measured directly behind the new polarizer at the end of NL5. The polarization reaches the maximum value 92 %, the mean value is 88 %.

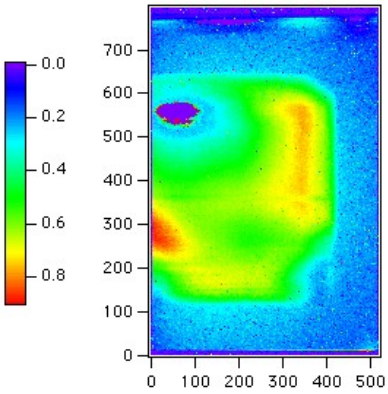

Figure 3.19: False color image of the result of the very first polarization test. The polarization measurement setup was placed behind the first spectrometer arm of RESEDA. The polarization shows some heterogeneity of not yet known origin.

3.6 DNS - An instrument for unraveling complex magnetic correlations via polarization analysis

Y. Su[1,2], **W. Schweika**[2], **R. Mittal**[1,2], **E. Küssel**[2], **F. Gossen**[1,2], **B. Schmitz**[2], **K. Bussmann**[2], **M. Skrobucha**[3], **M. Hölzle**[1,2], **H. Schneider**[1,2], **R. Möller**[4], **M. Wagener**[4], **A. Ioffe**[1,2], **Th. Brückel**[1,2]
[1]Jülich Centre for Neutron Science
[2]IFF, Forschungszentrum Jülich
[3]ZAT, Forschungszentrum Jülich
[4]ZEL, Forschungszentrum Jülich

The construction of the new polarized time-of-flight spectrometer DNS at FRM II has reached the first milestone with the delivery of the first neutrons and intense polarized neutron beams in September of 2007. Shortly after the starting of the instrument commissioning with polarized neutrons in the diffraction mode in the last reactor cycle, DNS has been steadily producing sound experimental results to unravel complex magnetic correlations in a wide range of emergent materials via polarization analysis.

DNS is a new cold neutron multidetector time-of-flight spectrometer with both longitudinal and vector polarization analysis at FRM II. This allows the unambiguous separation of nuclear coherent, spin incoherent and magnetic scattering contributions simultaneously over a large range of scattering **Q**- and E-resolution. DNS is therefore ideal for the vector **Q** and energy transfer E. With its compact size DNS is optimized as a high intensity instrument with medium investigations of magnetic, lattice and polaronic correlations in many frustrated magnets and highly correlated electrons. With its unique combination of single-crystal time-of-flight spectroscopy and polarization analysis, DNS is also complimentary to many modern polarized cold neutron triple-axis spectrometers.

The relocation of major components from FZ Jülich and the construction of the new DNS at FRM II have started in 2006. The first phase of this project is to implement the diffraction mode with polarized neutrons. Soon after the installation of the double-focusing pyrolytic graphite monochromator and secondary spectrometer in the summer (as shown in Fig.3.20), the first neutrons and intense polarized neutron beam were delivered to DNS in September. Newly constructed polarizer and polarization analyzers, both using m = 3 Schärpf bender-type focusing supermirrors, perform extremely well. A polarized neutron flux as high as 5 x 10^6 n/s/cm^2 has been achieved at the neutron wavelength with 4.74 Å. The polarization rate of the incident neutron beams is nearly 96%, as shown in Fig.3.21. The expanded analyser bank over a 2θ range of 120 degrees has largely improved the measurement efficiency. The radiation shielding at both monochromator housing and secondary spectrometer has also been improved. The radiation background at the DNS measurement area has met the strict requirement imposed by the radiation protection regulations. This paves the way for the first commissioning experiments.

In the last reactor cycle of 2007, a number of polarized neutron experiments on both powder and single-crystal samples have been successfully undertaken at DNS. One typical application of polarization analysis on powder samples at DNS is to sep-

Figure 3.20: The new DNS at FRM II

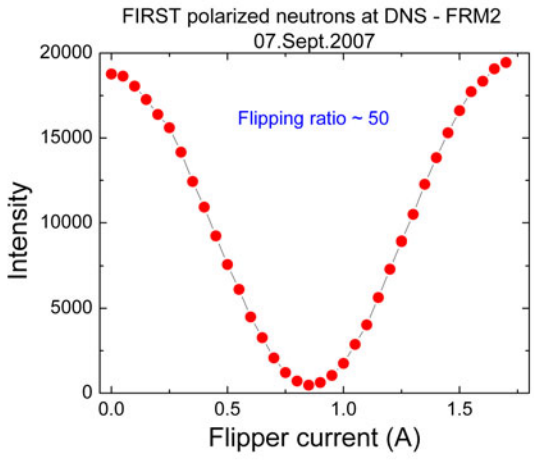

Figure 3.21: First polarized neutrons at the new DNS demonstrating the high flipping ratio of 50 achieved

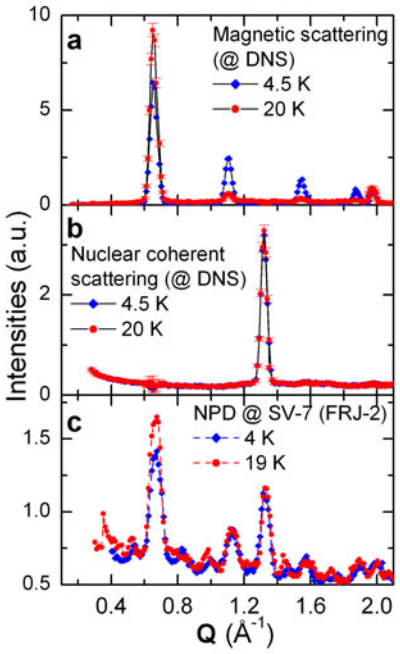

Figure 3.22: Investigations of the magnetic structure of MnNCN via powder neutron diffraction. (a) and (b): pure magnetic and nuclear coherent scattering, respectively determined at DNS with polarization analysis. (c): former data from SV-7 without polarization analysis

arate magnetic scattering from nuclear coherent and spin incoherent scattering on antiferromagnets and paramagnets via XYZ-method. High polarized flux and the improved efficiency on polarization analysis allow us to obtain high quality data on the investigation of the magnetic structure of manganese carbodiimide (MnNCN) powder, as shown in Fig.3.22. In comparison to the old data taken with non-polarized neutron powder diffraction at the dedicated powder diffractomter SV-7 at FRJ-2, the DNS data is much superior. It provides the comprehensive information on magnetic reflections and their temperature dependence.

Another typical application is to map out the reciprocal space together with polarization analysis on single crystal samples. Intensive testing experiments on various Kagome spin systems, pyrochlore spin ice and perovskite CMR manganites have been carried out. The routines for the data treatment have also been implemented. Some types of very peculiar magnetic correlations due to high geometrical frustrations and strong electronic correlations have been revealed from these new experiments with polarization analysis. One such example is the observation of the rod-like paramagnetic diffuse scattering in the so-called cooperative Jahn-Teller distorted regime on highly correlated CMR manganites, as shown in Fig.3.23. This rod-like diffuse feature is a clear indication of the presence of strongly anisotropic magnetic exchange interactions due to orbital ordering.

DNS with intense polarized neutrons in the diffraction mode and subsequent successful applications have proven capabilities of DNS as an unique instrument with polarization analysis. However, the full potential of DNS can only be realized after the completion of the second phase of the DNS project - installations of a massive position sensitive detector bank and high-performance double chopper system. These two new components are expected to be in operation before the end of 2008.

In collaboration with the Institute of Inorganic Chemistry of RWTH Aachen, we would like to thank Manuel Krott and Andreas Houben for permitting us to use the MnMCN data taken both from DNS and SV-7.

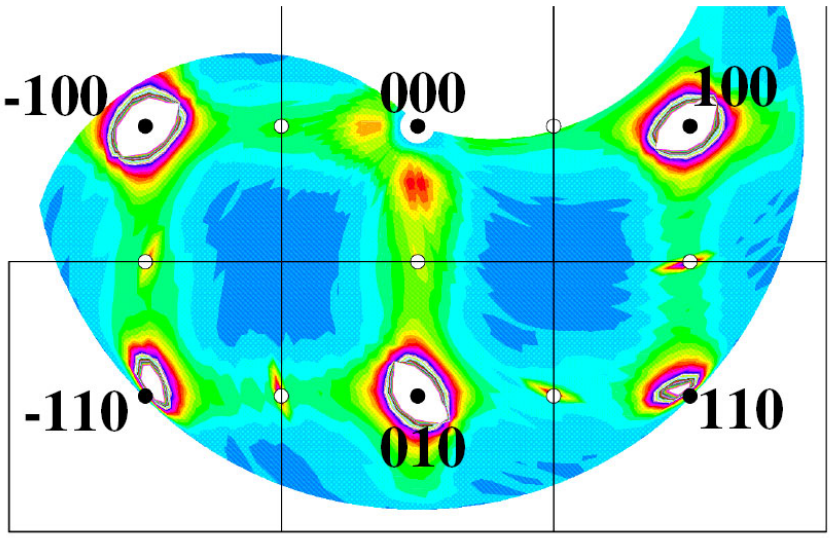

Figure 3.23: Paramagnetic diffuse scattering at 220 K measured on a large single crystal of $La_{0.875}Sr_{0.125}MnO_3$ via polarization analysis

The successful commissioning of

3.7 PUMA – the thermal triple axis spectrometer

K. Hradil[1], **R. A. Mole**[2], **H. Gibhardt**[1], **M. Gründel**[1], **F. Güthoff**[1], **J. Leist**[1], **N. Jünke**[1], **J. Neuhaus**[2], **G. Eckold**[1]
[1]Inst. f. Physikal. Chemie, Universität Göttingen
[2]ZWE FRM II, TU München

Over the last year PUMA in its basic detector version has assigned around 150 days to 10 different external user groups (for the results see experimental reports of FRM II). Beside the external measurements the instrument characterisation was continued and technical advances made with the implementation of some new devices. The stroboscopic measuring technique to investigate the real time behaviour of excitations in dependence of external fields (temperature, electrical fields) is now available also for the user community. Additionally, first successful test measurements were performed using a focussing guide in front of the sample.

Stroboscopic measuring technique - real time investigations of excitations

Inelastic neutron scattering technique provides information about the microscopic dynamics of solids. Investigations on a real time scale within external fields (temperature, pressure, magnetic/electrical fields) yields the microscopic information of relaxation processes (phase transitions, domain order/disorder processes, decomposition processes). The time scales of these types of processes are normally much smaller than the time needed to perform an inelastic measuring scan (measuring times are typically in the range of seconds or minutes per point), even on high flux instruments. Such long measuring times mean conventionally inelastic neutron scattering is not suitable for real-time experiments. A method to combine real time resolution together with inelastic neutron scattering using a stroboscopic measuring technique was developed by our group for the triple-axis spectrometer UNIDAS in Jülich in the early 1990's [1]. Fig. 3.24 shows a schematic time diagram of the stroboscopic technique. By cycling the sample in an external field, the scattered intensity is not only detected as a function of momentum and energy transfer but also sorted within time channels. Measuring for several cycles provides the necessary counting statistics for analysing the individual time channels. Therefore, the repeatability of the processes is a necessary condition for the application of the technique. The basics of the measurement protocol are as follows: the instrument is periodically checked to see if the positioning step has finished. A trigger signal then controls both the start of the counter card and the sample environment. This trigger can be given from an external source or produced from an internal clock of the card. The time resolved counter board in use was developed by the FRM II detector group. The data accumulation takes place in eight 1-dimensional arrays with 8192 channels. For internal triggering the time base can be defined in such a way that the time channels are defined from microseconds up to serveral seconds. In case of external triggering the time channel is defined by a wave function generator.

This technique was recently implemented within the spectrometer electronics of PUMA and provides the possibility to analyse excitations

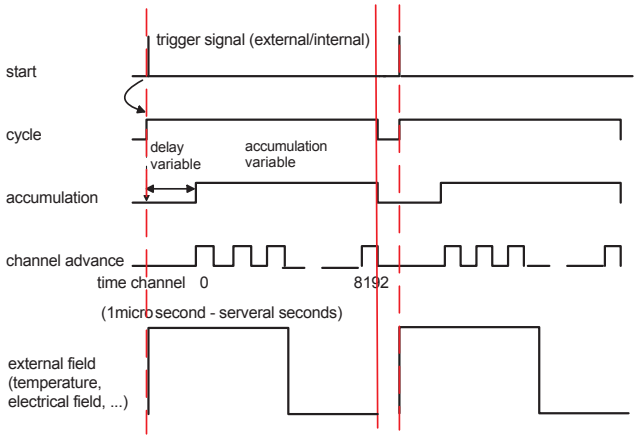

Figure 3.24: schematic time diagram of the stroboscopic technique

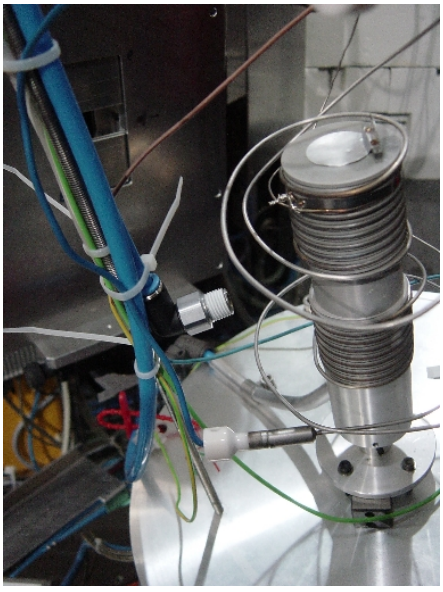

Figure 3.25: Furnace for fast temperature changes (5K/s) for the time-resolved measurements. The crystal is heated by a heating wire which is mounted around an aluminum cyclinder placed around the sample. The fast cooling is supported by air presse flow on the aluminum cyclinder controlled by the heat power supply.

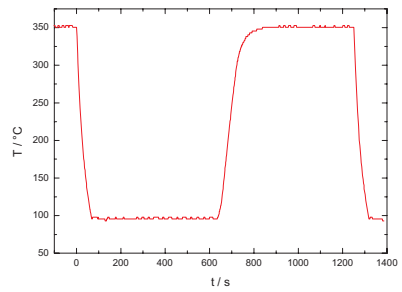

Figure 3.26: Time dependent characteristics of the temperature jumps (370/670K) investigating demixing processes within the system NaBr/AgBr

within relaxation processes on a timescale down to microseconds. The technique described above is strongly dependent on the ability to control the external field on the sample in a very precise way as well as assuring the reproducibility. In Fig. 3.25 a furnace is shown to cycle the temperature between 300 and 670K. The cooling rate is about 10K/s using air pressure cooling. The requirement concerning the control of the temperature for a sucessful time-resolved measurement is shown in Fig. 3.26 where the temperature is logged for this experiment. Using this equipment we performed a time-resolved measurement of a demixing process within the system $Ag_{0.22}Na_{0.78}Br$ following an transvers acoustic phonon in the temerature range of 370K/670K. In Fig 3.27 a TA phonon for the fully mixed phase at 670 K and the time evolution within 2 hours is represented. Already shortly after decreasing temperature (145 s) a clear splitting into two peaks can be observed synonymous with a demixing in a AgBr and NaBr phase.

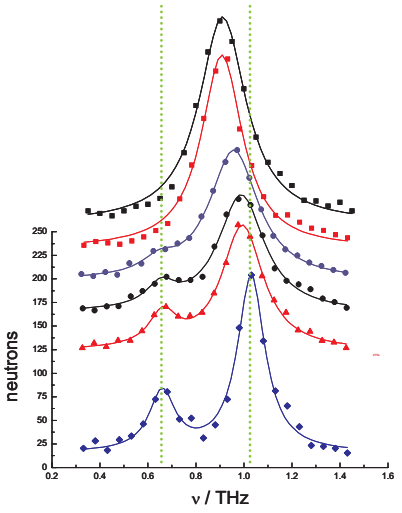

Figure 3.27: Time evolution of the q = [0.4 0 0] phonon within the $Ag_{0.22}Na_{0.78}Br$ system for a temperature change from 670K to 370K

Inelastic measurements on small crystals - focussing guide test

The weak interaction of neutrons with condensed matter typically restricts the investigations to large samples with dimensions of the order of cubic centimeters. There are many areas of scientific interest, where it would be advantageous to use TAS techniques, however, this is often prohibited because of the difficulty of growing large, high quality single crystals. Topics of interest range from typical TAS applications such as superconducting materials with various doping levels, but also extend to examples such as biomolecules and molecular materials, where TAS methods are very infrequently used due to the problems with crystal growth. Furthermore, certain sample environment such as pressure cells also restricts the size of the sample allowed. To overcome this problem with sample size on TAS instruments we have been investigating the use of supermirror focusing guides [2], to generate a very small but intense beam spot at the sample position of the thermal three axis instrument PUMA.

The guide used has a length of 500 mm and has been described previously [3]. The guide was installed on PUMA between the monochromator and the sample (fig. 3.28). In the first instance we used a neutron CCD camera to both correctly align the guide and to analyze the shape and intensity of the beam at the sample position. These measurements, along with Monte-Carlo simulations of the profile are shown in Fig. 3.29. Both, measurement and simulations show that the beam has a FWHM of approximately 2 mm in the horizontal direction and 8 mm in the vertical direction. Such a profile is ideal for studying samples with mm dimensions, unlike the conventional PUMA profile where the primary beam has dimensions of roughly 25 mm in the horizontal direction and 28 mm in the vertical direction and any adjustment for sample size is done by adjustable, neutron absorbing slits. The CCD camera images also revealed that using the guide results in a very low background.

We performed sucessful test ex-

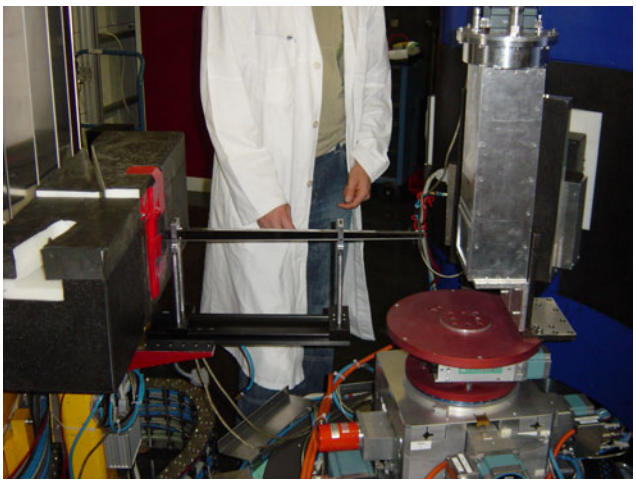

Figure 3.28: Photograph of the elliptical guide on the primary beam path of PUMA

periments on quartz samples with the guide and in the conventional focussed monochromator setting of PUMA. In both cases the PG(002) monochromator and analyser was used. Due to the guide entrance dimensions and the horizontally flat monochromator only neutrons coming from one of the 117 monochromator crystals are guided to the sample position for the guide configuration. A direct comparison between the conventional PUMA configuration and the guide (Fig. 3.30) shows that we can measure a sample with a volume that is 250 times smaller than the original crystal, with a low background and improved energy resolution. Further tests, experiments and simulations are ongoing so that these guides can be used routinely on PUMA in the future. Ultimatively guides designed and optimised for PUMA will be manufactured and offered to users as a possible setup.

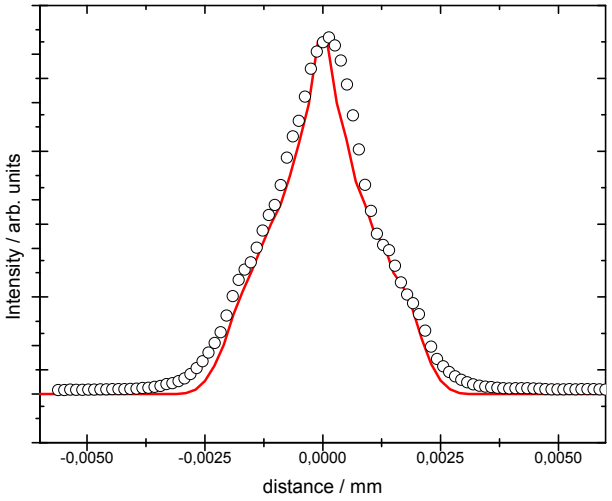

Figure 3.29: Horizontal beam profile measured with a delCAM neutron CCD camera. Red: Simulation of the horizontal beam profile.

Conclusion

In conclusion both new techniques introduced to the instrument will allow new and exciting experiments to be performed. The stroboscopic technique together with challenging sample environment allows the exploration of real time relaxation processes (phase transitions, domain order/disorder processes, decomposition processes). Using elliptic guides will open triple axis spectrometers for tiny crystals or sample environments with limited accepting volumns, while still having excellent energy resolution.

[1] Eckold, G. *Nucl. Instr. and Methods*, A289, (1990), 221–230.

[2] Schanzer, C., Böni, P., Filges, U. *Nucl. Inst. and Meth. A*, 529, (2006), 63–68.

[3] Mühlbauer, S., Stadlbauer, M., Böni, P., Schanzer, C., Stahn, J., Filges, U. *Physica B*, 385-386, (2006), 1247–1249.

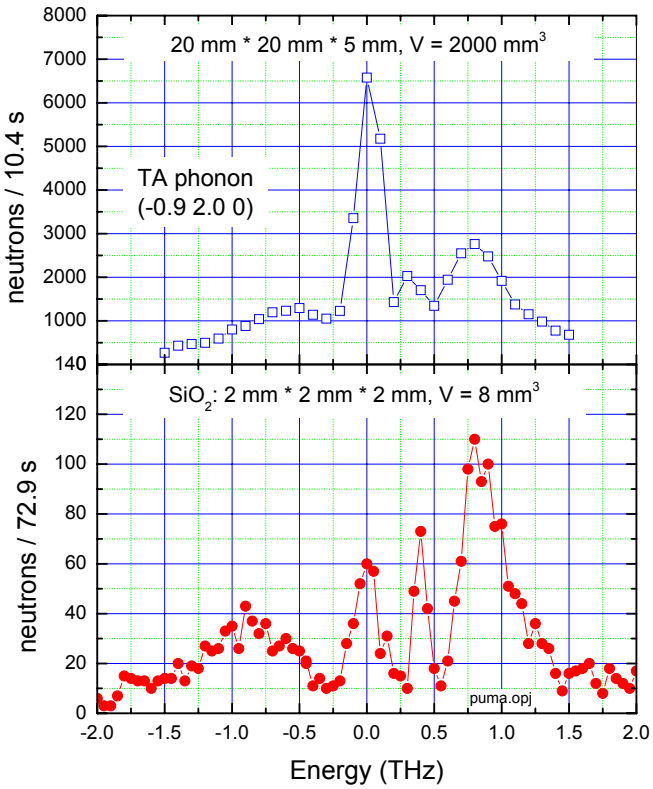

Figure 3.30: Top: Normal PUMA configuration, bottom: Same measurement using the focusing guide with a sample that is 250 times smaller.

3.8 Quasielastic and inelastic neutron scattering experiments at the time-of-flight spectrometer TOFTOF

C. Smuda[1], **S. Busch**[1], **G. Gemmecker**[2], **T. Unruh**[1]
[1]ZWE FRM II, TU München
[2]Bayerisches NMR-Zentrum, Chemie Department, TU München

Introduction

During 2007 the multi–chopper time–of–flight spectrometer TOFTOF [1] was in full user operation. Therefore, only minor optimizations of the instrument were carried out. The most important improvement is the installation of an automatic gas handling system for the sample chamber, which allows to flush the whole chamber with argon gas. By this way the air scattering inside the chamber could be reduced leading to a further reduction of the already extreme low background of the spectrometer. This low background can exemplarily be observed in the high resolution measurement recently recorded at TOFTOF with an incident neutronwavelength of 14 Å (cf. Fig. 3.31). The presented raw data have not been corrected for background. In this measurement it could also be demonstrated that even with a resolution of 4 μeV a signal to noise ratio better than 10^4 could be achieved in the vicinity of the elastic line.

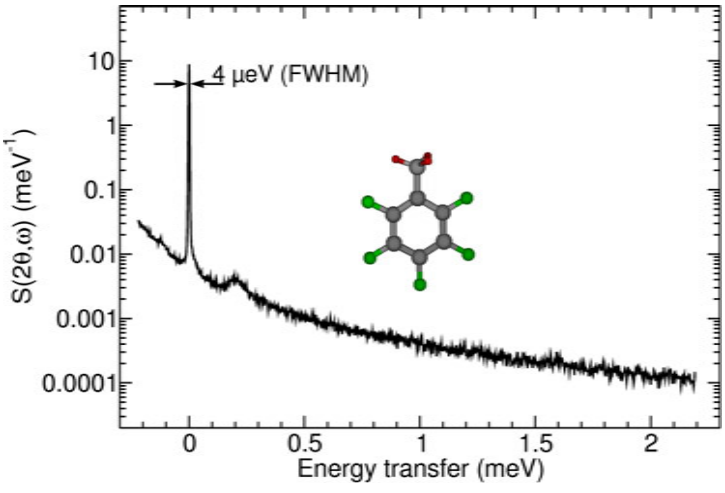

Figure 3.31: Methyl tunneling in pentafluorotoluene (graphic formula displayed in the inset) at 5 K measured with a resolution of 4 μeV obtained with neutrons of wavelength $\lambda = 14$ Å, chopper frequency of 16.000 rpm and frame overlap reduction ratio 8 (recording time: 14 h).

In the following sections of this report some exemplary results of the inhouse research at TOFTOF in 2007 are briefly summarized.

Rotational dynamics of methyl groups in pentafluorotoluene and pentafluoroanisole

Almost half of the hydrogen atoms in the oligoisoprene derivative coenzyme Q_{10} are bound to methyl groups. For a detailed evaluation of QENS spectra obtained from TOFTOF measurements of liquid Q_{10}, it is essential to know the scattering contribution of these methyl group hydrogen atoms to the quasielastic intensity [2]. Up to now the rotation of methyl groups in liquids of organic molecules is scarcely investigated. Therefore it is of special and general interest to characterize methyl group rotation in the solid as well as in the liquid state. The aim of the investigations is to find a preferably universally applicable model for the description of the QENS of methyl groups in liquids of small organic molecules.

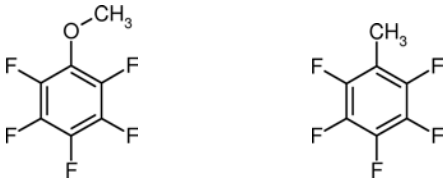

Figure 3.32: Structural formulae of pentafluoroanisole (left) and pentafluorotoluene (right).

Pentafluoroanisole and pentafluorotoluene were investigated as model compounds (cf. Fig. 3.32) in the liquid and solid state.

QENS spectra of solid pentafluoroanisole could satisfactorily be modelled by a scattering function $S(Q,\omega)$ which comprises only one Lorentzian function, whereas the dynamics of methyl groups in solid pentafluorotoluene could only be described by a combination of two Lorentzian functions indicating two different types of methyl groups. The obtained linewidths for the compounds in the solid state are displayed in Fig. 3.33 [3].

As the methyl group dynamics is a thermally activated process, it shows an Arrhenius behaviour in the solid state for both compounds, whereas in the liquid state it was found that the frequency of the methyl group rotation is independent of temperature. The used model for data analysis includes not only the methyl group rotation but also long-range diffusion and isotropic rotational diffusion of the molecule

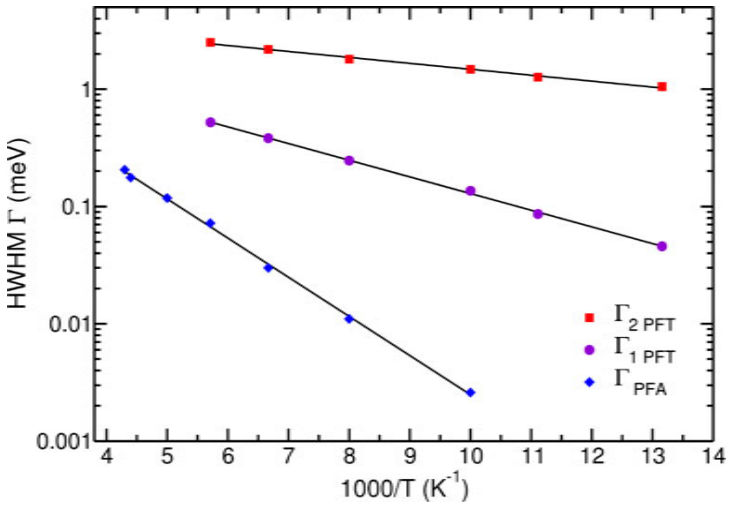

Figure 3.33: Arrhenius plot of half widths at half maximum (HWHM) Γ obtained from best fits for the two non-equivalent methyl group in polycrystalline pentafluorotoluene (PFT) and pentafluoroanisole (PFA), respectively. The solid lines represent bests fits to the Arrhenius equation yielding activation energies of 6.4 kJ/mol for PFA and 2.74 kJ/mol and 0.96 kJ/mol for the two different types of methyl groups in the lattice of PFT, respectively.

$$S(Q,\omega) = S_{\text{Methyl}}(Q,\omega) \otimes S_{\text{Trans}}(Q,\omega) \otimes S_{\text{IRD}}(Q,\omega)$$

and describes the experimental data perfectly. Evaluation of the QENS spectra without consideration of the methyl group rotation results in worse fits. The long-range diffusion of the molecules in the liquid phase could for all investigated temperatures clearly be separated from the internal motions. Diffusion constants extracted from the model are comparable to PFG-NMR diffusion coefficients. The temperature dependence of the obtained Q independent rotational diffusion constants can be described by the Arrhenius equation. The Q independent HWHM for the methyl group rotation was determined to be about 1 meV for pentafluorotoluene as well as pentafluoroanisole.

Self-diffusion measurements of medium-chain molecules

It could be demonstrated in [4] that QENS is best suited for investigations on molecular self-diffusion inside nanosized droplets dispersed in another liquid. However, by measurements of the self-diffusion coefficients of the oligoisoprene derivative coenzyme Q_{10} in nanosized droplets and in the bulk, respectively, at the time-of-flight spectrometer TOFTOF discrepancies to the PFG-NMR diffusion constants of more than one order of magnitude have been found [2]. In order to study this effect more systematically QENS measurements on a series of different medium-chain *n*-alkanes was performed with the aim to understand the influence of the chain length of the molecules to their diffusivities.

For data evaluation, different models for the dynamic structure factor $S(Q,\omega)$ were used to extract diffusion constants: (i) sum of two Lorentzian functions, (ii) convolution of long-range diffusion and isotropic rotational motion, and (iii) convolution of long-range diffusion and diffusion inside a sphere. The experimental data could be described by each of the three models and it turned out that the determined diffusion constants are independent of the applied model. The derived diffusion constants were compared with values obtained by PFG-NMR [5].

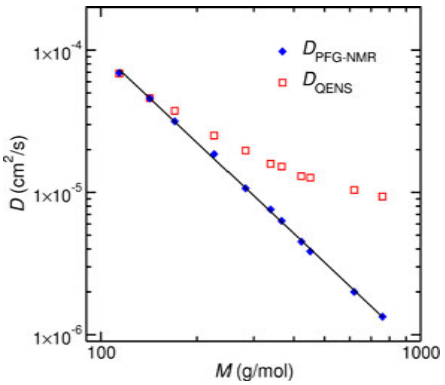

Figure 3.34: Diffusion constants of *n*-alkanes determined by QENS at 110°C as a function of the molecular weight in comparison with PFG-NMR values [5].

One main result is that with increasing chain length the ratio of the QENS diffusion coefficient to the PFG-NMR diffusion coefficient increases [6]. The increase of this ratio can easily be recognized when plotting an isotherm of the diffusion constants of different *n*-alkanes on a double logarithmic scale as it is demonstrated in Fig. 3.34 for 110°C.

The discrepancies of the diffusion constants determined by the two different methods might be due to (i) a change of the diffusion mechanism on a nm length scale for molecules of medium-chain length or to (ii) contributions of internal motions.

Further efforts with respect to data evaluation have to be made in order to find the true reason for the observed discrepancies of the QENS and NMR results. Some more experimental information will be obtained by neutron spin-echo measurements, which are in progress to determine the Q dependence of the diffusion constants at low Q-values. In addition the study is intended to be extended on other medium-chain molecules like oligomers of polyoxyethylene, fatty acids, alky alcohols or silicon oils.

Dynamics of phospholipids in stabilizing monolayers

Many modern drugs are not water-soluble. To facilitate their intravenous applicability, a drug carrier has to

be employed. Dispersions of lipid nanoparticles stabilized by dimyristoylphosphatidylcholine (DMPC) are promising candidates. It has been shown that not only the drug release rate but also the storage stability of these systems highly depends on the properties of the stabilizer [7, 8, 9]. These properties were investigated i. a. by SAXS [10], revealing that the structure of the monolayer is clearly distinct from what one would expect from the well-known structure of bilayers: It is thinner and the peaks in the electron density profile are less pronounced.

A series of experiments aiming to determine the dynamic characteristics of DMPC-monolayers is planned at TOFTOF. A major goal is to link the molecular dynamics with the beforementioned properties like storage stability. First experiments were done comparing the picosecond-dynamics in a dispersion of vesicles, serving as model for phospholipid bilayers, which had a diameter of ≈ 40 nm (PCS z-average) with the one of a stabilizing phospholipid monolayer in an emulsion of deuterated hexadecane in D_2O (diameter ≈ 57 nm). The main difficulty in these measurements is the low content of phospholipid, being only 1.3 weight % of the sample in the beam.

The part of the sample spectra due to scattering from D_2O and possibly hexadecane molecules has to be subtracted. Then the quasielastic broadening caused by the dynamics of DMPC becomes visible which is depicted in figure 3.35 along with the instrumental resolution, determined by the measurement of a vanadium standard. The broadening caused by the dynamics of DMPC in a monolayer is clearly larger, indicating faster dynamics.

To determine the type of dynamics, the spectra were fitted with a simple model consisting of a sum of two Lorentzians, which can roughly be assigned to diffusion of the DMPC molecules (narrow component) and internal motions of the DMPC (broad component). As both, water and hexadecane, are faster than the phospholipids, their dynamics does not influence the line width of the narrow component even if the subtraction was non-ideal but would only be visible in the broad component. The width of the narrow component shows a linearish dependence of Q^2 (confer to figure 3.35) which is a sign for non-local diffusive motions. The diffusion coefficient of DMPC is proportional to the slope and therefore in a monolayer about two times the one in a bilayer.

The looser molecular arrangement of the phospholipid molecules in the monolayer [10] can intuitively be correlated with the increase of diffusional dynamics. This will be investigated more thoroughly. Currently, we try to find a more elaborated method to subtract the contributions of D_2O and hexadecane to the spectra so that the broad component can be evaluated more reliably. Furthermore, experiments investigating the influence of stabilizing co-emulgators on the phospholipid dynamics are planned.

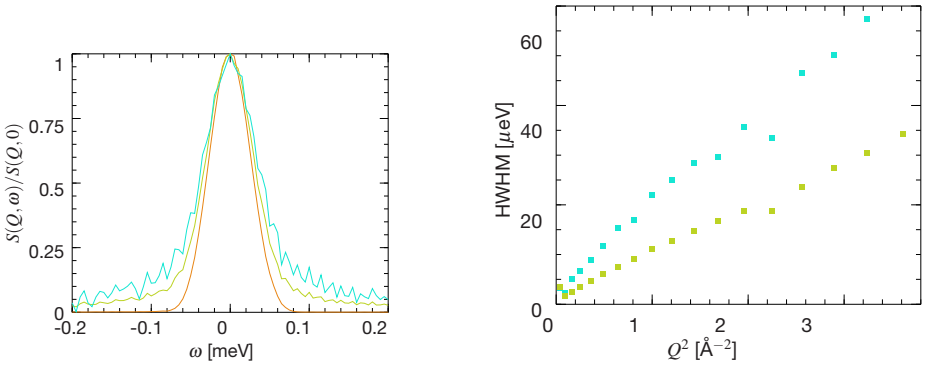

Figure 3.35: Left: Spectra of vanadium (innermost), vesicles, and emulsion (outermost) after background subtraction as described in the text plotted versus energy transfer at a momentum transfer of 1 Å^{-1}. It is visible that the quasielastic broadening of the central line is larger in the case of the emulsion (phospholipid monolayer). Right: The linewidth of the narrow component of a two-Lorentzian fit plotted versus the squared momentum transfer Q^2. The one steming from the monolayer is about double the one of the bilayer.

The TOFTOF team

The TOFTOF team (cf. Fig. 3.36) is looking forward to seeing you performing your forthcoming experiment at FRM II.

[1] Unruh, T., Neuhaus, J., Petry, W. *Nucl. Instr. Methods A*, 580, (2007), 1414–1422.

[2] Smuda, C., Gemmecker, G., Bunjes, H., Unruh, T. *FRM II Annual Report*, 84–86.

[3] Smuda, C., Gemmecker, G., Unruh, T. *J. Phys. Chem.*, (submitted).

[4] Unruh, T., Smuda, C., Gemmecker, G., Bunjes, H. *MRS QENS 2006 Conf. Proc.*, 137–145.

[5] von Meerwall, E., Beckman, S., Jang, J., Mattice, W. L. *J. Chem. Phys.*, 108, (1998), 4299.

[6] Smuda, C., Gemmecker, G., Unruh, T. *Langmuir*, (in prep.).

[7] Westesen, K., Siekmann, B. *Int. J. Pharm.*, 151, (1997), 35.

[8] Bunjes, H., Koch, M. H. J., Westesen, K. *J. Pharm. Sci.*, 92, (2003), 1509.

[9] Bunjes, H., Steiniger, F., Richter, W. *Langmuir*, 23, (2007), 4005.

[10] Unruh, T. *J. Appl. Cryst.*, 40, (2007), 1008.

Figure 3.36: The TOFTOF team in front of the flight chamber of the spectrometer (from left to right): Christoph Smuda, Tobias Unruh, Sebastian Busch, Winfried Petry, Jandal Ringe, Reinhold Funer, Jürgen Neuhaus and Raffael Jahrstorfer.

4 Nuclear physics and applied science

4.1 Irradiation facilities

X. Li[1], **H. Gerstenberg**[1], **J. Favoli**[1], **V. Loder**[1], **J. Molch**[1], **A. Richter**[1], **H. Schulz**[1]
[1]ZWE FRM II, TU München

General

The irradiation service of the FRM II continued its routine operation successfully during the five reactor operation cycles in 2007. Altogether more than 500 irradiations were carried out for different research projects and commercial purposes on our facilities. The 1000th irradiation since the starting up of FRM II was achieved in November 2007. Table 4.1 shows the irradiation batches on each system. Our service could extend in many countries in 3 continents. A big jump in this year was the installation of the final automatic silicon doping system which went into a routine production phase after the successful commissioning controlled by TÜV at the beginning of this year. The silicon doping became the main part of the irradiation service and amounted almost to the half of total number of irradiations in 2007. Four tons silicon ingots with broad range of target resistivities from 1050 Ω*cm* till 22 Ω*cm* were irradiated. Beside this big commercial service, irradiation of samples for nuclear medicine and geological dating was arranged at the second place with about 100 batches. In 2007 We began some works of neutron activation analysis for scientific research, application in industry and education aim. Some important and interesting projects supported by our irradiation systems are described in the following text.

Production of isotopes for the nuclear medicine

An interesting project for the nuclear pharmacy is the optimization of an effective production of the radioactive isotope ^{177}Lu, which may help create the first successful radiopharmaceutical for solid tumors. ^{177}Lu emits a low beta energy, which reduces radiation side effects and produces a tissue-penetration range appropriate for smaller tumors. As a bonus, ^{177}Lu emits gamma radiation, which allows physicians to also use it for both imaging and therapeutic purposes. In order to prepare the ^{177}Lu, two production ways are tested in the institute for radiochemistry of the TU München. One is direct neutron activation of enriched ^{176}Lu. The results of a series of test irradiation in the last years showed that the production throughput of this way is high but the co-produced long-lived isotope ^{177m}Lu ($T_{1/2}$=161*d*) causes a big disadvantage. The other indirect way is the production of ^{177}Lu via the nuclear reaction $^{176}Yb(n,\gamma)^{176}Yb(\beta^-)\rightarrow^{177}Lu$. No ^{177m}Lu is produced in the decay chain [1]. After a long time irradiation of a sample of ^{176}Yb with 9 days on the capsule irradiation system (KBA) in October 2007 and a successful separation of Yb/Lu, a first effective labeling of ^{177}Lu on some bio molecules was obtained. This new and more effective way to prepare ^{177}Lu will be optimized and test irradiations are going on.

The goal of the project BetaMo supported by the Bavarian science foundation is the development of radioactive implants for a possible application in the medicine, above all for the wound healing process after inflammations and operative procedures. Suitable radioactive radiation can have positive influence on the healing process. Samples made of PEEK foil or copper-wire containing phosphorus were irradiated with different irradiation durations on our capsule irradiation system to produce the pure beta-ray source ^{32}P for the physics department of the LMU and cooperating clinics. The calculation of the actual radiation dose of the implants in the hospital was based on the information of the neutron flux determined by measuring the activity of a co-irradiated Au-wire in each irradiation in order to guarantee an uncertainty limit of 5% on the sample activity calculation as required. The neutron flux determination was performed at the FRM II after the irradiation of the samples.

After a first successful irradiation of tungsten in the high flux irradiation position in the control rod of the FRM II during the 8^{th} reactor cycle in 2006, two following samples enriched to 99.9% in ^{186}W were irradiated during an entire reactor cycle in 2007 for the production of ^{188}Re via a double neutron capture reaction with thermal neutrons: $^{186}W(n,\gamma) \rightarrow^{187} W(n,\gamma) \rightarrow^{188} W(\beta^-)(T_{1/2} = 69\text{d}) \rightarrow {}^{188}Re(T_{1/2} = 17\text{h})$. The samples were loaded before the reactor was started and unloaded after the reactor was shut down, i.e. after completion of 52-

Table 4.1: Irradiation batches at the FRM II in 2007

position	PRA	KBA	SDA	SDA1	RS	total
irradiation No.	122	42	225	113	2	504

days. ^{188}Re emits beta particles (E_{max} = 2.12 *MeV*) having an ideal range for intravascular brachytherapy and certain cancer brachytherapies. It can be usually extracted for medical applications by a so-called $^{188}W/^{188}Re$ generator.

Irradiations for the fission track dating

About 100 apatite samples from different geological institutes were irradiated in our irradiation channels in 2007 for the fission track dating of geological substances. This method is a radiometric dating technique based on analysis of the damage trails, or tracks, left by fission fragments in certain uranium bearing minerals and glasses. The number of tracks correlates directly with the age of the sample and the uranium content. To determine the uranium content the sample is annealed by heating and exposed to a barrage of thermal neutrons [2]. Due to the high uranium content in the geological samples, the samples are usually irradiated in the position SDA-1 with a relatively low neutron fluence between 1×10^{15} and 1×10^{16} (cm^{-2}), which was achieved within few minutes. In several cases standard neutron flux monitors (Au/Co) were irradiated simultaneously with the samples and analyzed separately, in order to obtain the information about the local neutron fluxes within the sample sets, which typically consist of more than 10 single disc-shaped samples.

Measurements of γ-dosage in spent fuel units

In order to use the very strong gamma radiation in the spent fuel elements as a supplementary irradiation source at FRM II, two measurements with 45 min and 2 h irradiation time respectively were performed to study the dose rate in the central position of a spent fuel element. Figure 4.1 shows the measurement device in a spent fuel unit. Special dosimeters made of small pieces of radiation-sensitive material which change color when irradiated were used. By measuring the amount of color-change by means of a spectrophotometer, the total dosage can be calculated. Because almost no neutrons exist in spent fuel, what is a big advantage in comparison to our other irradiation positions with high neutron dose term, the gamma radiation dose could be here determined clearly without any interference. The radiation-induced darkening of our samples was measured at the Jülich research center. Some results are shown in Table 4.2.

Neutron activation analysis (NAA) at FRM II

As well known, the neutron activation analysis (NAA) is a very precise analysis method for determination of trace elements. Very low concentration down to ppb- and ppt-level can be measured under favorable conditions. Samples for scientific research projects, industrial applications and purposes of education were analyzed via NAA directly at FRM II in 2007. To mention but a few, trace ele-

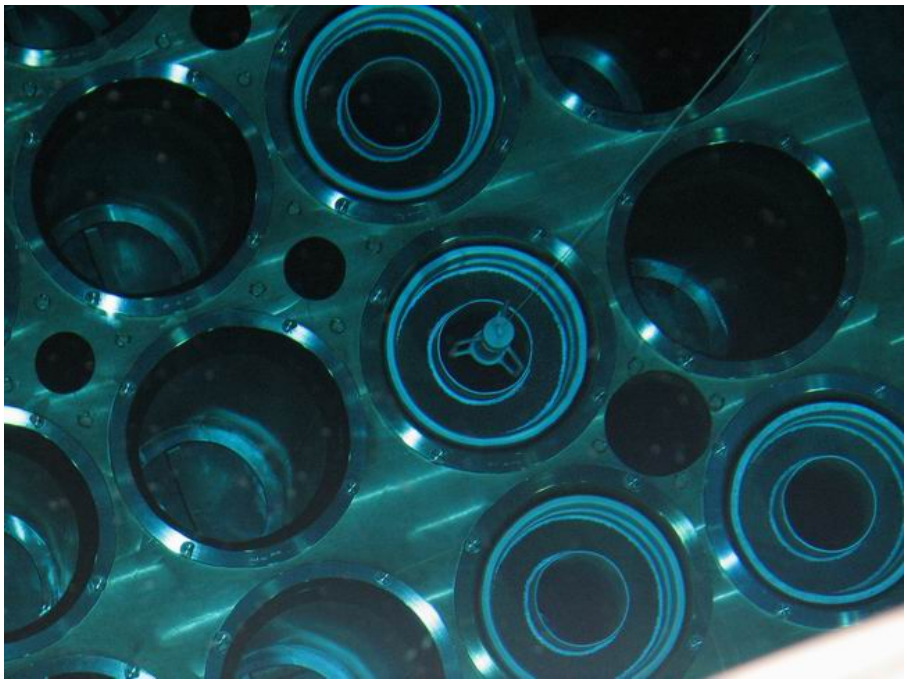

Figure 4.1: dose measurement in a spent fuel unit.

Table 4.2: radiation dose in spent fuels at FRM II

dosimeter	source	cooling time (d)	radiation time (min)	dose rate (kGy/h)
HL 255 321	FRM II - 012	212	45	16.2
HL 255 323	FRM II - 012	214	120	16.1
HL 255 325	FRM II - 012	214	120	14.9

ments in samples of silicon nano pellets with diameter of 10 nm from the Walter-Schottky-Institute, in pure silicon wafers from Infineon AG and in different color pigments were analyzed. Impurity could be determined down to the ppb-level in the very pure semiconductor materials. Different concentrations of silicon in the nano particles depending on the production procedure were determined also by using NAA.

The analysis of the color materials can help the art historians getting information about the background of the paintings and a possible relationship between the colors. Up to 20 elements could be determined in the samples by using k_0 multi-element analysis method after one single irradiation. Another interesting work was an analysis work of 2 meteorites from a museum in Nördlingen within the framework of a laboratory training course. High concentration of metal elements, above all of elements in the iron-platinum-group was determined in both samples. The remarkably high concentration of iridium of almost 1 ppm indicates the extraterrestrial background of our samples.

Iridium is notable for its significance in the determination of the probable cause of the extinction, by a meteorite strike, of the dinosaurs. Figure 4.2 shows analysis result of a meteorite.

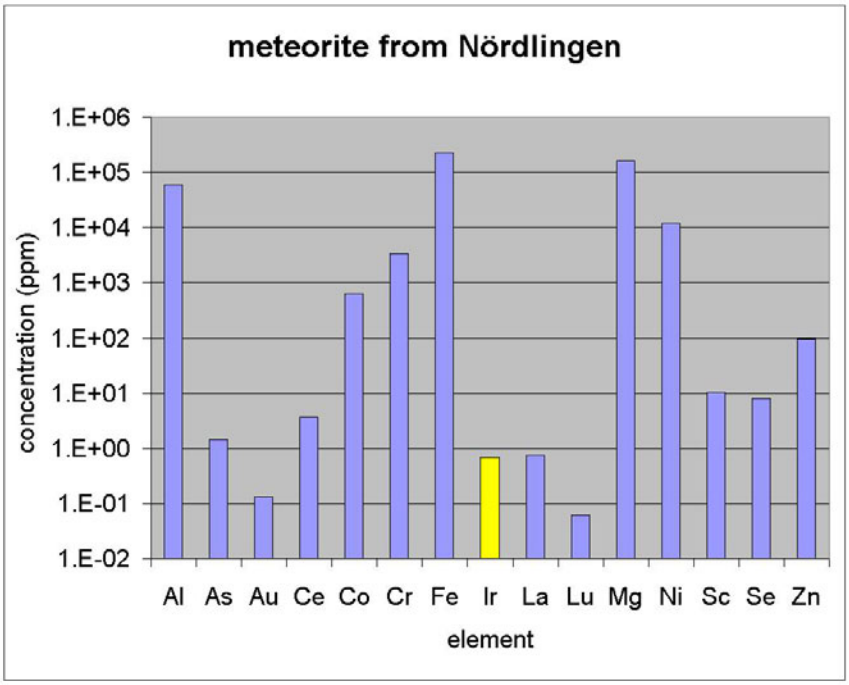

Figure 4.2: trace elements determined in a meteorite. Ir concentration is about 100 times higher than in the earth's crust.

Silicon doping facility (SDA)

The silicon doping for commercial purposes had already begun by using a prototype facility (SDA-opt) at the end of 2005. In 2006 almost 3 tons silicon ingots were irradiated. In January 2007 the final silicon doping facility offering a semi automatic operation was completely installed at FRM II. After a successful commissioning program containing about 30 tests, the doping system was verified by TÜV and the regulatory authority. In March the silicon doping service succeeded in being ISO9001:2000 certified by TÜV Süd Management Service GmbH. It went into a routine production phase in the following 3 reactor cycles. About 4 tons silicon ingots were doped during this time. The demand increases drastically.We entered into a business relationship with 5 companies from Europe and Asia.

Already on the prototype facility, a special nickel absorber was mounted on the outside of the irradiation container and tested in order to reduce the axial inhomogeneity of the neutron flux density at the irradiation position to a value below 5% as required by most industrial clients. Based on the earlier flux measurements, the special absorber shape was constructed and optimized by means of Monte Carlo calculations. The distribution of local neutron flux in the new system was monitored by measuring the activity of gold standards located in different positions within the ingot with a total length of 500 mm. The result of the measurement is shown in Figure 4.3. New calibration factors for the calculation of doping time were optimized again under the new conditions. Based on our neutron flux measurements and some feedbacks about the doping quality from our clients, we are sure, that the new nickel absorber layer in our doping system was correctly constructed and coated on the liner pipe.

The doping results show that the compliance with the target resistivity and the axial resistivity variation is less than $4 \sim 5\%$. The radial variation is below $3 \sim 4\%$ and seems to be completely hidden in measurement noise. With the new calibration factors, which connect the irradiation dose and the target resistivity, the conditions of the doping specifications for target resistivities from 22 Ωcm up to even 1050 Ωcm can be fulfilled very well. Worthy of mention is the doping of ingots with high target resistivities, because the doping time is short, usually between 20 and 30 minutes. The influence of time uncertainty during drive-in and drive-out is here significantly higher than in the case of lower target resistivities. On the other hand, the radiation damage caused by the fast neutron-induced reactions has more influence in the ingots with higher target resistivities than with lower. Due to the very pure thermal flux in our position, this effect is minimized effectively. The doping

results show that the lifetime of free electrons in the doped ingots is high, around 400-700 *msec*, what means low content of irradiation defects.

Most of the ingots have diameters of 4, 5 and 6 inches. 3 batches of 8 inches ingots were irradiated in 2007. The effect of self shielding in radial direction was analyzed and is shown in Figure 4.4. Generally the starting material was *n*-type Si exhibiting a resistivity of several thousand Ωcm but also some *p*-type prior-doped ingots were doped at FRM II. We are confident to increase our throughput in two shifts operation considerably in 2008.

[1] Dvorakova, Z. *Production and chemical processing of 177Lu for nuclear medicine at the Munich research reactor FRM-II*. Ph.D. thesis, TU München (**2007**).

[2] Glasmacher, U., Wagner, G., Puchkov, V. *Techonophysics*, 354, (2002), 25–48.

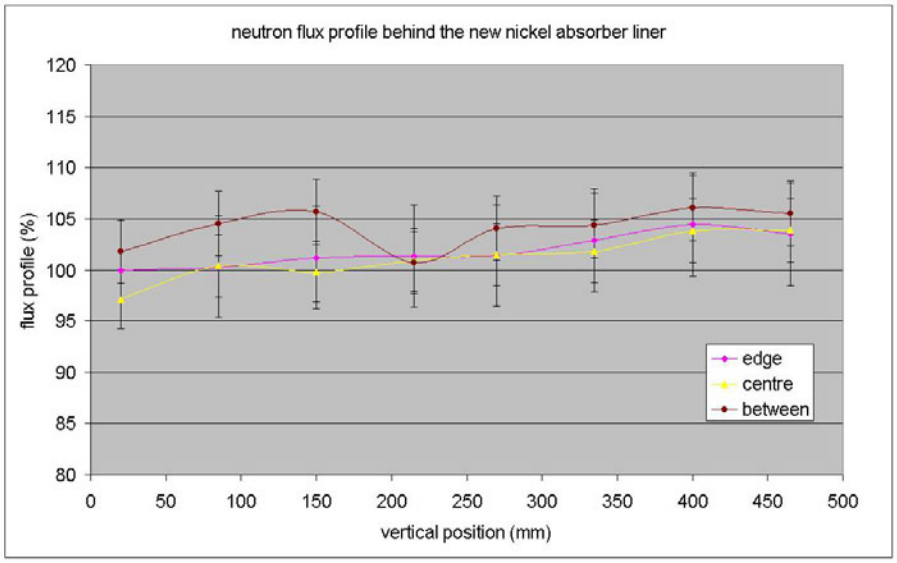

Figure 4.3: neutron flux profile in a 6 inches ingot behind the new nickel absorber liner.

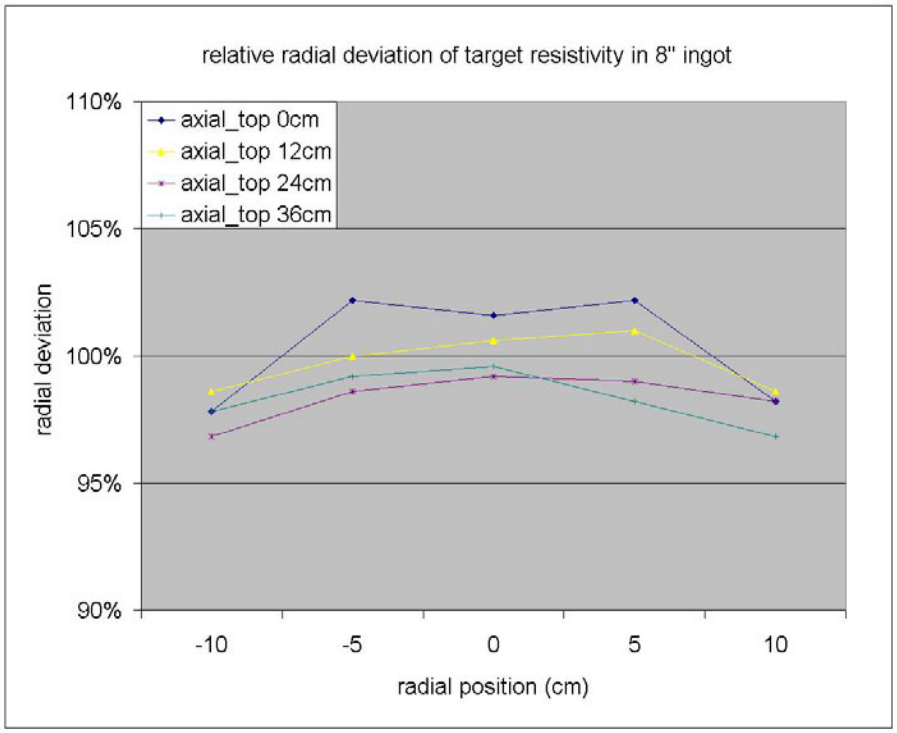

Figure 4.4: relative radial resistivity deviation within an 8 inches ingot.

4.2 Particle physics at the cold neutron beam facility MEPHISTO

J. Klenke[1], **H. Abele**[2], **S. Mironov**[3], **H.-F. Wirth**[2], **O. Zimmer**[3,2]
[1]ZWE FRM II, TU München
[2]Physik-Department E18, TU München
[3]Institute Laue-Langevin, Grenoble

Motivation

Particle physics with neutrons is in some respect a description of low energy physics experimentation. Experiments with neutrons fit in a greater field of precision measurements comprising cold or ultracold neutrons, cold or ultracold ions or atoms, protons, electrons, and their antiparticles. These experiments have obtained an extreme level of sensitivity and precision. Although it is difficult to determine an exact range, basic questions - relating the standard model of particle physics to cosmology and other areas of physics and astronomy - come into reach for low energy experimentation, where tiny signs from corresponding effects are detectable, but remain so far and in the future mostly unaccessible for high-energy accelerator experiments. Therefore, due to their extreme precision, low-energy experiments can be sensitive to processes occuring at much higher energies than accessed with today's accelerators. The experiments provide the zero-energy values of the standard model, improve its internal consistency and define the point of departure for new physics.

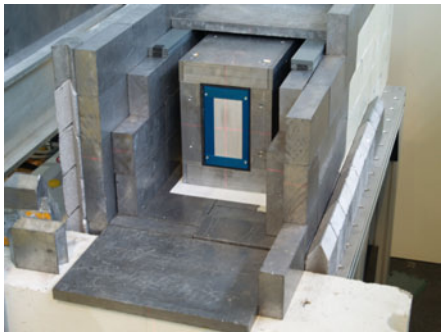

Figure 4.5: The polariser (blue) during the build up of the lead shielding

Status

The work at the beamline MEPHISTO in the year 2007 was splitted in two main parts. The first part was concentrating on Helimephisto, a new source of ultracold neutrons extracted from the cold MEPHISTO beam, the second part was the improvement of the beam line by testing a new removable polariser and the refurbishment of parts of the neutron guide system.

Helimephisto

During the first half year of 2007 the experiments with the setup Helimephisto proceeded before it was moved to the ILL. Helimephisto is the prototype of a superthermal source for ultracold neutrons (UCN). Incoming cold neutrons were downscattered in superfluid ^{4}He (below 1.3 K) to UCN energies (below 170 neV). Last tests with a new coating in the liquid ^{4}He chamber were done to improve the ultracold neutron density. The experiment showed for the first time that it is possible to extract UCN with a high efficiency from a ^{4}He converter. The experiment itself is reported in detail in the Ref. [1]. The main idea for the experiment is to use a phonon excitation in liquid ^{4}He to slow down neutrons with a wavelength around 9 Å. Therefore the experiment needed an accurate knowledge of the neutron spectra, especially at λ=9 Å. Former measurements were already done [2] at the neutron guide NL1, but only at the position of the NRex$^+$ monochromator, which is situated 5.7 m away from the sample volume facing upwards to the cold source. For the measurements the same time-of-flight (TOF) spectrometer was used as in [2]. The spectrometer need a complete radiation shielding which had to be build up, because former

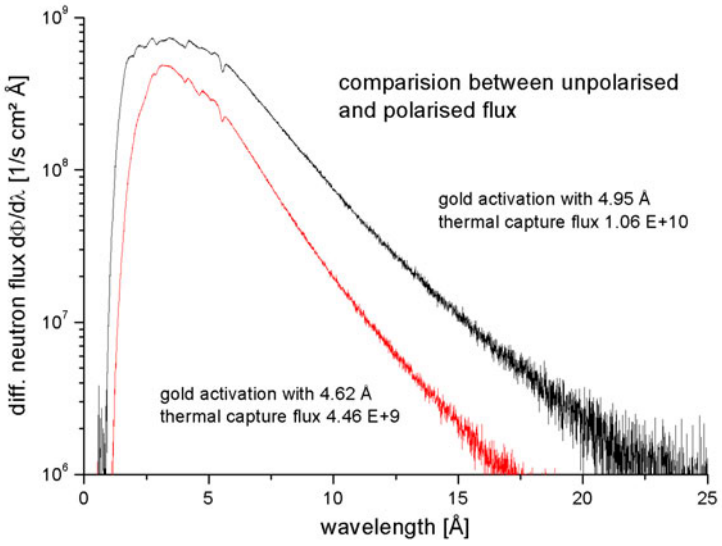

Figure 4.6: Comparison between the transmissive spectra of the polarised and unpolarised beam

measurements took advantage of the NRex$^+$ monochromator housing. It was measured the integral flux (via gold-foil activation) and the shape of the spectrum (via the TOF spectrometer). These informations allow a more precise analysis of the data from Helimephisto.

In a first step the beam was characterised as before for the Helimephisto experiment but without the long collimation tubes after the neutron guide. Goldfoil activation and shape of the spectrum were taken at this position direct behind the neutron guide. After that the polariser was inserted and the transmission spectrum of the polariser was measured. The two spectra were shown in Fig. 4.6. The new polariser will be part of the experimental equipment offered by FRM II for all users.

During the end the of the year the first 2 m of neutron guide between the gap for the NRex$^+$ monochromator and the experiment shutter of MEPHISTO were exchanged.

The authors kindly appreciate the effort of the students M.Aßmann and M.Helmecke working on the experiments at MEPHISTO.

[1] Zimmer, O., *et al. Phys.Rev.Lett.*, 99, (2007), 104801.

[2] K.Zeitelhack, *et al. Nuclear Instruments and Methods in Physics Research A*, 560, (2006), 444–453.

4.3 PGAA – Prompt gamma activation analysis

P. Kudejova[1,2], **G. Meierhofer**[3], **L. Canella**[2], **K. Zeitelhack**[4], **R. Schulze**[1], **J. Jolie**[1], **A. Türler**[2]
[1]Inst. für Kernphysik, Universität zu Köln
[2]Inst. für Radiochemie, TU München
[3]Physikalisches Inst., Universität Tübingen
[4]ZWE FRM II, TU München

General

In April 2007, first cold neutrons flew through the neutron guide NL4b dedicated to Prompt Gamma-Ray Activation Analysis (PGAA) instrument. The rest of the year 2007 was used to test and characterize the instrument and to work on the proper shielding. We measured the intensity and neutron spectrum of the cold neutron flux at the first exit window of the guide. Further on, we used a tomography camera and made radiographs of the beam at different positions from the exit window of the neutron guide. Finally, we have measured first samples and analysed the PGAA spectra.

Introduction

Prompt Gamma-Ray Activation Analysis is a nuclear analytical technique using the (n,γ) reaction to determine the elemental (or chemical) composition of various samples. PGAA determines the major, minor and trace elements in the entire volume of the sample non-destructively, therefore it is a preferred method for small archaeological objects as well as for other valuable samples.

In general, PGAA is an effective technique for the quantitative determination of H, B, Na, Cl, K, Sc, Ti, V, Cr, Mn, Fe, Co, Ni, Cu, As, Se, Br, Sr, Mo, Ag, Cd, In, Xe, Cs, Hf, Ta, Re, Os, Pt, Au, Hg, Nd, Sm, Eu, Gd, Dy, Er and U. The limits of detection for these elements is in range between 1 ng/g for Gd and 100 μg/g for Ti. PGAA can also detect practically all the other elements, but with limits of detection already of the order of hundreds of μg/g up to units of percent (e.g. for C, N, O, F, Sn, Pb and Bi).

Experimental

The PGAA instrument is shown in Figure 4.7. The prompt γ-rays are detected by a Compton-suppressed spectrometer, which consists of a central HPGe detector inserted into a BGO scintillator annulus and operating in anti-coincidence mode with it. In Figure 4.7, there are two positions for the detectors available and will serve for different applications: standard PGAA, position sensitive PGAA - called PGA-Imaging (PGAI) and for a Pair Spectrometer, which measures only prompt γ-rays of higher energies (above 2 MeV).

In November 2007, we tested the PGAA acquisition system on medical

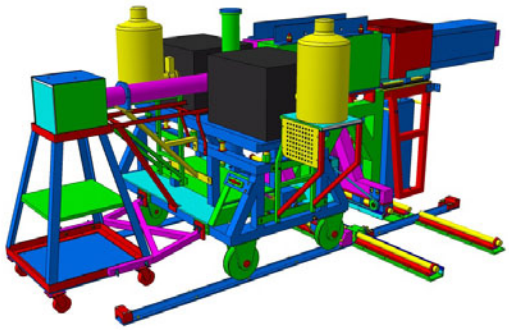

Figure 4.7: The flexible PGAA set-up with two detector positions: one is dedicated for standard PGAA measurements (left), another is exchangeable between pair spectrometer and PGAI detector (right).

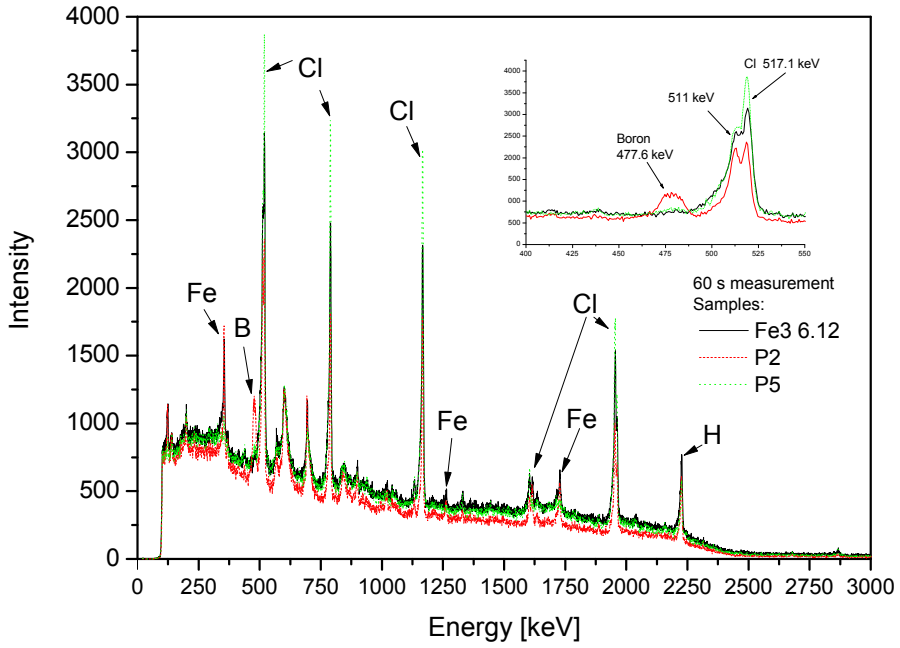

Figure 4.8: First PGAA spectra were taken on medical samples with simple chemical composition - mostly H, Cl and Fe are presented, in one of them Boron (P2-sample) occurs as well.

samples with relatively simple composition. The task was to determine, if there is boron inside or not. Preliminary results show boron in some samples, one example is presented in Figure 4.8.

Nevertheless, we will yield reliable quantitative results not sooner than thorough measurements and analysis are performed. This task is already planned for the first half of the year 2008.

Neutron flux at NL4b

The NL4b neutron guide is about 51 m long, with a curvature of 390 m. Because of the strong curvature of the guide the neutron flux is not homogeneous - the intensity at the left part (following the n-flux) is higher than the right part of the guide. To homogenize the neutron beam and to yield more intensity, the last 6.9 m were designed to be straight and elliptically tapered. To have more flexibility for the PGAA measurements, the elliptical guide was divided into two parts, first of them 5.8 m long.

Intensity

In April 2007, the neutron flux at the exit window of the 5800 mm long elliptical guide was measured. Using a set of 6 round pieces of gold foils (11 mm in diameter), we covered an area of 25 mm$\times$51 mm. Using the mean neutron wavelength of about 6.7 Å(1.83 meV), we measured an average neutron intensity of 6.0×10^9 n/cm^{2}s. This neutron flux intensity corresponds to about 2.2×10^{10} n/cm^{2}s of thermal equivalent neutron flux.

Due to the elliptical shape, the focus of the beam is not at the exit of the guide but about 30-35 cm from the first exit window (5.8 m of the elliptical guide). According to the simulations - while taken into consideration the real flux measurements - the neutron flux intensity of the focused beam at the distance of 35 cm should be about 7.3×10^9 n/cm^{2}s with useful dimensions of 14 mm$\times$38 mm. With an additional 1.1 m of the focusing elliptical "nose", the intensity in the focal point about 9 cm far from its exit window should reach even 2.0×10^{10} n/cm^{2}s with useful area of about 4 mm$\times$11 mm.

Mean wavelength

To measure the mean neutron wavelength at NL4b, we have used a compact Time-Of-Flight spectrometer constructed specially at FRM II for these purposes [1]. Its external diameters are about 1000 mm$\times$600 mm with the aim to fit to most of the beam guides. We have scanned the neutron flux in horizontal direction about 30 cm far from the exit window between -2° and + 2° with a step of 0.5° to determine not only the neutron mean wavelength, but also the divergence curve. The acquired data are only partially analysed and the mean wavelength has a preliminary value of about 6.7 Å, corresponding to an average neutron energy of 1.8 meV. More details to these measurements can be found in the diploma thesis of G. Meierhofer [2].

2D images

Due to the high intensity of the neutron flux, the 2D profiles of the

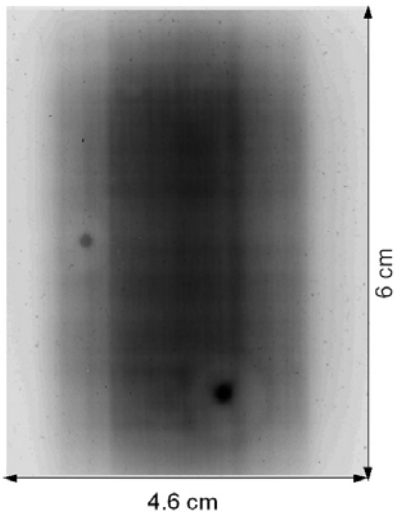

Figure 4.9: 2D-image of the neutron beam obtained by the DEL CCD Camera at 35 cm distance from the first exit window (after 5.8 m of the elliptical guide).

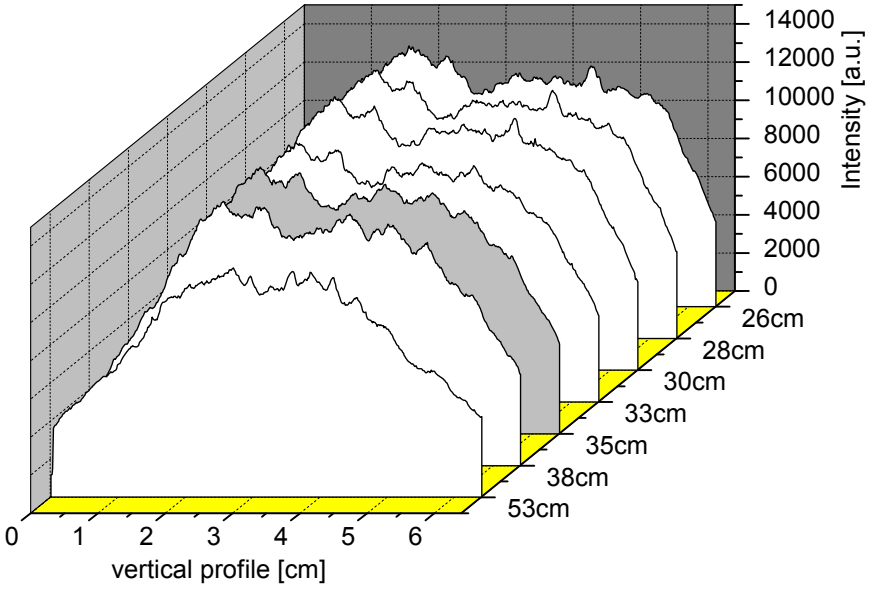

Figure 4.10: Vertical profiles of the 2D images at different distances from the neutron guide exit window. For the distance at 35 cm given by Figure 4.9, the profile is grayed.

n-beam could be measured only with a flux reduced to about 6% of the full neutron intensity. The average intensity measured at the exit of the guide was 3.6×10^8 n/cm^{2}s.

One example of the 2D images measured at the distance of 35 cm from the neutron guide exit window is presented in Figure 4.9. The dark spot in the bottom right corner of the 2D image is an optical effect in the lens system of the DEL camera developed at FRM II. The shutter time of the camera was set to 2-3 s because the intensity of the beam was on the camera's upper limit. The vertical profiles of the neutron beam at different distances from the exit window are presented in Figure 4.10 and described in the reference [3]. For the PGAA measurements, we will select a homogeneous part of the n-beam intensity with an appropriate aperture.

Outlook

The very next task is to follow up the commissioning of the PGAA instrument and to come to routine operation. We will start to measure samples of scientifc interest in the next reactor cycle. We will characterize the neutron flux at the second exit window, using the extendable elliptically focusing guide of 1.1 m length. The HPGe detectors need a proper efficiency calibration before we can start accurate sample analysis. Further it is necessary to decrease the beam background to achieve the expected limits of detection by the measurements.

[1] Zeitelhack, K., Schanzer, C., Kastenmüller, A., Röhrmoser, A., Daniel, C., Franke, J., Gutsmiedl, E., Kudryashov, V., Maier, D., Päthe, D., Petry, W., Schöffel, T., Schreckenbach, K., Urban, A., Wildgruber, U. *NIM A*, 560, (2006), 444–453.

[2] Meierhofer, G. Diploma thesis. Graz University of Technology, Austria (**2007**).

[3] Kudejova, P., Meierhofer, G., Zeitelhack, K., Jolie, J., Schulze, R., Türler, A., Materna, T. *JRNC*. In press.

4.4 Fission neutron source - MEDAPP

F. M. Wagner[1], **A. Kastenmüller**[1], **H. Breitkreutz**[1], **B. Loeper-Kabasakal**[1], **J. Kummermehr**[2]
[1]ZWE FRM II, TU München
[2]Strahlenbiologisches Institut der Universität München

The irradiation facility

Fig. 4.11 shows a plan view of the beam SR10. It is supplied by unmoderated fission neutrons which are generated in a pair of uranium converter plates near to the entrance of the beam. The spectrum was adapted to the medical requirements by beam filters consisting of lead and borated epoxy resin [1].

Determination of neutron fluence data

The total flux was measured by help of a method which was originally developed for the spectrum-independent determination of the source strength of neutron emitters. The source would be placed in the centre of a water bath which contains thermal neutron absorbers, e.g., gold. If the bath is so big that the neutrons are fully thermalized, the total activation of the probes is a measure for the total fluence. At the SR10 instead of the radioactive source, a beam channel from the surface to the centre of the bath was inserted into the phantom the influence of which had to be corrected with respect to the efflux. Fig.4.12 shows the 200-l-water phantom furnished with gold probes in one quadrant around the beam axis (it is the phantom used for the standard dosimetry, too). The total neutron flux of the beam was determined to be $3.2 \cdot 10^8$ $s^{-1}cm^{-2}$; this value is in line with other experimental assessments. The neutron energy spectrum was determined by resonance and threshold foil activation [2]. The effective cross sections were adjusted by help of MCNP simulations of the spectrum.

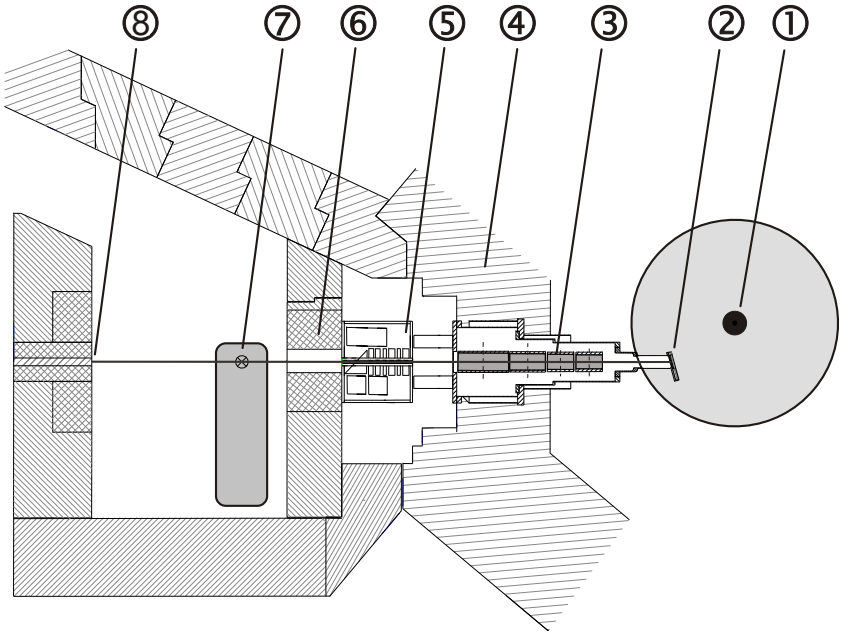

Figure 4.11: Horizontal section of the irradiation facility: 1 Compact reactor core in the centre of the D_2O moderator tank (diameter 2.5 m); **2** thermal-to-fast neutron converter plates; **3** beam tube with four revolving shutter drums; **4** cavern containing the shutter motors, filters, light projection, and beam monitor chambers; **5** multi leaf collimator (MLC); **6** patient couch; **7** beam dump.

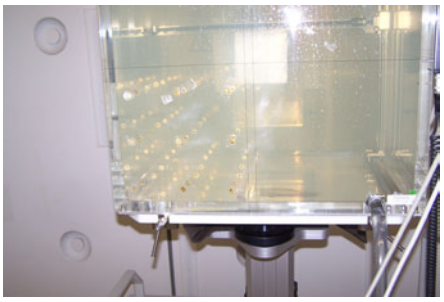

Figure 4.12: Phantom with gold probes[2].

The result is the expected fission spectrum with an addition of epithermal neutrons, see Fig. 4.13. A transmission calculation applied to the spectrum at the entrance of the beam tube confirms the MCNP simulations and shows that neutrons once scattered do not any more contribute to the flux at the irradiation site. The weak thermal peak is mainly the result of scattering in the collimator; therefore the transmission calculation of the filtered source spectrum does not show thermal neutrons.

The experimental determinations of the fluence and doses showed that the simulations using MCNP 4C2 overestimated the total fluence by a factor of 1.3. The most probable reason is that this version does not take into account any delayed effects by activation or fission products like Xe-135 with $2.65 \cdot 10^6$ barn thermal capture cross section. The form of the calculated spectrum, however, is not biased. For the same reason, the contribution of all activation products is not calculated so that the total gamma dose rate is underestimated. This was shown by measurement of the gamma dose during the first seconds rate after fast shut down of the reactor. The new version MCNPX 2.6 Beta does take into account all these delayed effects, but is still to be tested.

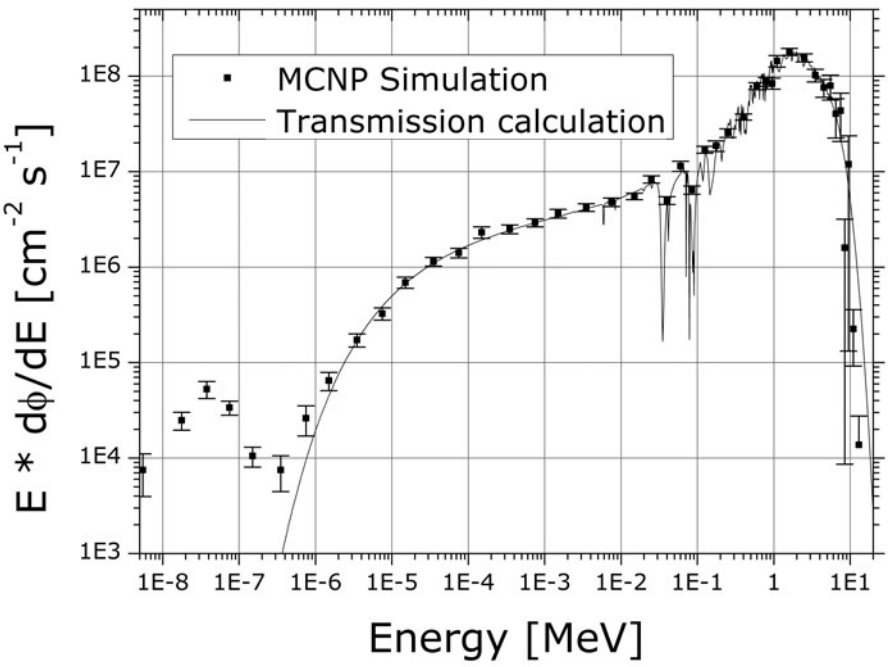

Figure 4.13: Neutron spectrum free in air. Dots: MCNP simulation, full line: Transmission calculation

Patient therapy

The permission of the patient therapy was issued in February 2007 by Bayerisches Landesamt für Umwelt. On the basis of a three dimensional dosimetry of the water phantom for all relevant collimations (S. Kampfer, Klinikum r. d. Isar), the first medical irradiation was performed on June 11, 2007. The patients were treated with single doses of 1.5 to 2 Gy, by 3 to 4 (1-6) fractions, 1 to 4 fields per patient. In total, 80 fields have been irradiated. 12 patients were treated within a combined photon/neutron therapy, 4 patients got neutrons only (pre-irradiation was more than 3 months before).

With curative intention, the treatment was carried out on 6 patients. They had no further tumor lesions. Their diagnoses were: 3 adenoid cystic carcinoma (ACC) of salivary glands, 1 lymph node and 1 skin metastasis of squamous cell carcinoma (SCC) and 1 skin metastasis of malignant melanoma. One patient had bone metastases of breast cancer, while the neutron therapy of the chest wall was indicated in locally curative intention. For all these patients it is to early to give a statement about efficacy. The acute side effects were within the expected range.

The other 9 patients got neutron therapy for palliation: 3 extended skin metastases of breast cancer, 2 locally advanced recurrences of ACC, 2 extended cervical lymph node metastases of SCC, 1 multiple skin metastases of malignant melanoma, and 1 locally advanced angiosarcoma of the chest wall. The palliative effectiveness became apparent in visible regression of tumor lesions (e.g. malignant melanoma), in more mobility of the jaw joint for better eating and speaking (ACC) or in less bleeding and secretion of ulcerous tumor lesions (SCC).

Preclinical screening of the biological effectiveness of the therapeutic beam

In order to render a sound radiobiological basis to the clinical application of fission neutron radiation, a pilot study into the Relative Biological Effectiveness, RBE, was performed [3]. As a simplified in vitro tumor model epithelial megacolonies generated from human squamous cell carcinoma line UTSCC5 (a) were employed. The hallmark of this system is that the cells are in close intercellular contact before, during and after the irradiation. Furthermore, the treatment effects can be quantified by in situ endpoints such as clonal expansion of surviving cells, colony regrowth delay, and permanent colony control (cure). The dose dependence of permanent control to single dose irradiation was performed in a polyethylene phantom at the depths of 0, 3, and 6 cm, and compared to a reference beam of 300 kV X-rays is shown in Fig. 4.14. The typical sigmoid dose-cure curves have been analyzed according to the generally accepted linear-quadratic model of cell survival S:

$$-\ln(S) = \alpha D + \beta D^2$$

with D = energy dose. RBE values can be read off directly as dose ratios at the mean tumor cure probability (TCP) of 0.5; values estimated by statistical analysis are listed in Table 4.3.

The RBE varies mainly with the ratio of photon to neutron dose which depends on the depth in the phantom; these results should also be descriptive of the situation in patients. By assuming a common coefficient β of the quadratic dose term, the dependence of RBE was also calculated as a function of dose (Fig. 6). Extrapolation to an infinitesimally small dose renders the maximum RBE, equivalent to the ratio of the linear dose coefficients for fission radiation and X-rays, α_f/α_x.

As can be expected from the physical properties and the complexity of fission radiation, the RBE undergoes substantial variation with depth in tissue and dose employed. The rather big RBE at clinical doses per fraction (1 to 2 Gy) was also confirmed by multifractionated single cell survival experiments (colony formation assay).

Compared with other neutron sources used for patient treatment, the fission neutron beam at FRM II is highly efficient. The pronounced

decrease of the RBE with depth as a consequence of the drop of the neutron-to-gamma ratio has to be taken into account in treatment planning. In suitable situations it may even be advantageous in sparing healthy tissue underlying superficial tumours, e.g. the irradiation of breast wall metastases of mammary cancer.

The investigations have been performed in partial fulfilment of a master thesis by V. Magaddino (University of Naples, Italy). This project was conducted within the course "European Master of Science in Radiation Biology" under the auspices of the University College London (Prof. K.-R. Trott), and in co-operation with the Radiobiological Institute of the University of Munich, LMU (Dr. J. Kummermehr).

[1] Kampfer, S., Wagner, F., Löper-Kabasakal, B., Kneschaurek, P. *Strahlenther. Onkol.*, 183 (Sondernr. 1), (2007), 72.

[2] Breitkreutz, H. *Spektrale Charakterisierung des Spaltneutronenstrahls der Neutronentherapieanlage MEDAPP am FRM II*. Master's thesis, Fakultät für Physik E13 (**2007**).

[3] Magaddino, V., Wagner, F., Kummermehr, J. *Experimentelle Strahlentherapie und Klinische Strahlenbiologie*, 16, (2007), 129–131.

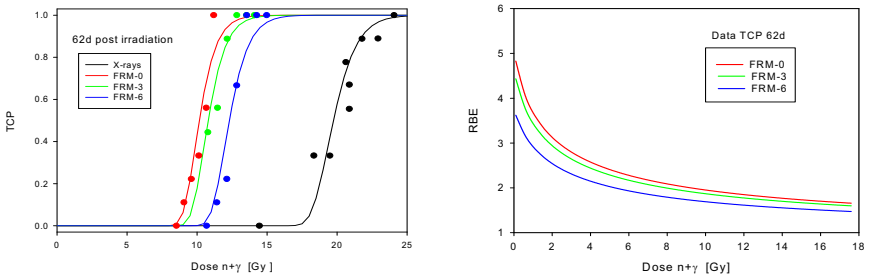

Figure 4.14: (left) Mean tumour cure probability(TCP) vs. dose at depths 0 cm (red), 3 cm (green), and 6 cm (blue) in a PE phantom; black: TCP of 300 kV X-rays. (right) Relative biological effectiveness vs. single dose at depths 0, 3, and 6 cm (denoted by FRM0, FRM3, and FRM6, respectively.)

Table 4.3: Summary of RBE, α, and RBE_{max} derived from the data in Figures 1 and 2.

	FRM-0	FRM-3	FRM-6	300 kV X-rays
RBE (TCP=0.5)	1.95 ± 0.044	1.82 ± 0.048	1.61 ± 0.036	-
α [Gy^{-1}]	0.84 ± 0.11	0.76 ± 0.09	0.62 ± 0.08	0.17
RBE_{max}	5.10	4.62	3.76	-

4.5 The positron beam facility NEPOMUC and instrumentation for positron physics

Christoph Hugenschmidt[1,2], **Benjamin Löwe**[2], **Jakob Mayer**[2], **Philip Pikart**[2], **Christian Piochacz**[1], **Reinhard Repper**[1], **Martin Stadlbauer**[1], **Klaus Schreckenbach**[2], **Werner Egger**[3], **Gottfried Kögel**[3], **Peter Sperr**[3], **Günther Dollinger**[3]

[1]ZWE FRM-II, Technische Universität München

[2]Physik Department E21, Technische Universität München

[3]LRT2, Universität der Bundeswehr München, Neubiberg

The low-energy positron beam of high intensity at NEPOMUC

In 2007 various experiments were performed at the high intensity positron beam facility at NEPOMUC –NEutron induced POsitron source MUniCh– which delivers up to $5 \cdot 10^8$ moderated positrons per second at a kinetic energy of 1 keV. A new positron remoderation unit, which is operated with a W(100) single crystal in back reflection geometry, has been implemented in order to improve the beam brilliance. At present, the primary beam energy is 1 keV, and the beam energy of the remoderated beam is set to 20 eV. A longitudinal magnetic guide field of 5-7 mT is applied for positron beam guidance, and the beam diameter amounts typically to 2.5-4 mm. A

survey of recent positron beam experiments can be found in [1].

Experiments at NEPOMUC

The present status of NEPOMUC and the spectrometers connected to the positron beam facility are shown Fig. 4.15.

The set-up of the coincident Doppler-broadening spectrometer (CDBS) was improved which now allows coincident measurements within shorter data acquisition times (<6 h per spectrum), and the background due to small-angle Compton scattering of annihiliation quanta in the sample was reduced to a minimum. This spectrometer is routinely operated up to a beam energy of 30 keV with a beam diameter focused to about 1 mm onto the sample in order to allow spatially resolved defect studies. In addition, a cryostat allows temperature dependent measurements down to 76 K. Various experiments have been performed in order to investigate crystal defects and the chemical surrounding at open-volume defects: e.g.: ion-irradiated metals and Mg-based alloys [2], defects in Al-based alloys after mechanical load, metallic layered systems.

At the positron annihilation induced Auger-electron spectrometer (PAES) for surface studies we succeeded to record PAE-spectra within only 1 h acquisition time, which is about two orders of magnitude lower than in lab-beam based experiments. The Auger-yield and the surface selectivity of PAES at Cu-covered surfaces of single crystalline silicon were determined and compared with conventional EAES [3]. At the end of 2007 a new electron energy analyzer with higher efficiency was installed which is currently set into operation.

The pulsed low-energy positron system (PLEPS), which was previously running with a ^{22}Na-based beam at the UniBW, was transferred to the FRM II. First positron lifetime measurements have been performed with positron energies between 0.5 and 20 keV. The results of this unique spectrometer are promising for lifetime experiments with mono-energetic positrons: An acquisition time of only 3 min lead to $2.5 \cdot 10^6$ counts in the lifetime spectrum, the overall timing resolution is 240 ps, and the peak-to-background ratio is better than $3 \cdot 10^4$ [4].

Two additional experimental setups were installed at the multipurpose beam port: The apparatus for the production of the negatively charged positronium (Ps^-) (developed at the Max-Planck-Institute for nuclear physics [5].) allowed to measure the Ps^--decay rate with superior signal-to-noise ratio. These experiments will be continued in 2008 with reduced systematic errors and high statistics.

Another apparatus was connected to the beam line for the investigation of positron moderation in a gas-filled drift chamber. Inelastic positron-nitrogen scattering, positron cooling efficiency, energy and intensity loss mechanisms were quantified in order to estimate the moderation efficiency of this device [6].

[1] Hugenschmidt, C., *et al. Appl. Surf. Sci,*, (in press, avialable online).

[2] Stadlbauer, M., Hugenschmidt, C., Schreckenbach, K., Böni, P. *Physical Review B (Condensed Matter and Materials Physics)*, 76(17), (2007), 174104.

[3] Hugenschmidt, C., Mayer, J., Schreckenbach, K. *Surf. Sci.*, 601, (2007), 2459–2466.

[4] P.Sperr, Egger, W., Kögel, G., Dollinger, G., Repper, R., Hugenschmidt, C. *Appl. Surf. Sci.*, (in press, available online).

[5] Fleischer, F., Degreif, K., Gwinner, G., Lestinsky, M., Liechtenstein, V., Plenge, F., Schwalm, D. *Phys. Rev. Lett.*, 96, (2006), 063401.

[6] Löwe, B., *et al. Appl. Surf. Sci.*, (in press, available online).

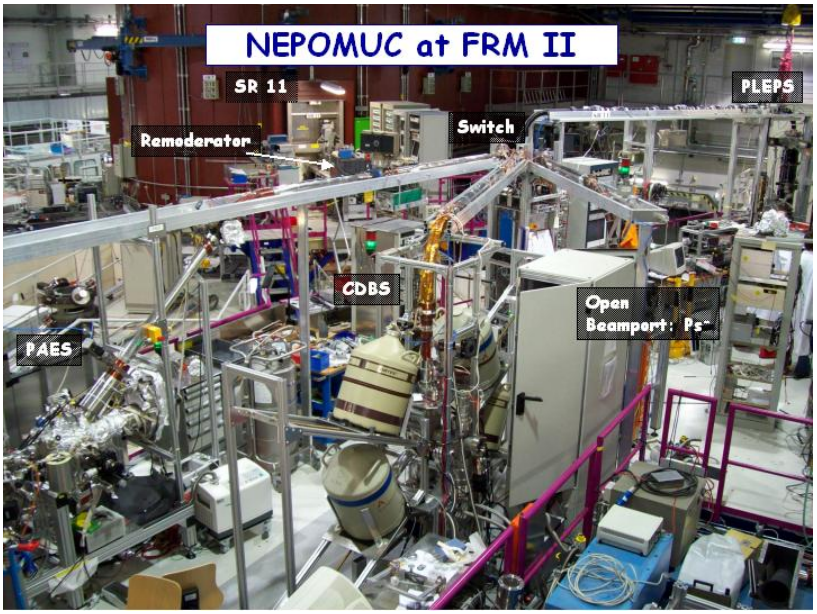

Figure 4.15: The positron spectrometers at the positron beam facility NEPOMUC at FRM II: CDB spectrometer (TUM), PAES-facility (TUM), apparatus for Ps^--production (MPI nuclear physics, Heidelberg), and the pulsed-beam facility PLEPS (UniBW München).

Part II

Scientific highlights

5 Soft matter

5.1 Separation of coherent and spin-incoherent neutron scattering from protein samples by polarization analysis

A.M. Gaspar[1,2], **W. Doster**[2], **M.-S. Appavou**[2], **S. Busch**[2], **M. Diehl**[2], **W. Häussler**[1,3], **R. Georgii**[1,3], **S. Masalovich**[1]
[1]ZWE FRM II, TU München
[2]Physik-Department E13, TU München
[3]Physik-Department E21, TU München

We explored the possibility to perform polarization analysis to experimentally separate coherent and spin-incoherent nuclear scattering processes, from a representative set of samples of interest for protein studies. Such a method [1, 2] had so far limited application in the study of amorphous materials [3, 4, 5], despite of the relevance of the information that it provides. For instance, it allows for the experimental determination of the coherent structure factor $S_{coh}(Q)$ of materials containing a significant amount of hydrogen atoms, such as proteins, uncontaminated by the enormous incoherent background. Knowledge of the relative importance of the coherent and incoherent terms at different Q values is also a pre-requisite for the interpretation of dynamical neutron scattering experiments, performed at instruments in which the total dynamic structure factor is measured, as is generally the case of neutron time-of-flight and backscattering instruments.

The experiments performed rely on the principle that using a polarized incident neutron beam and counting separately neutrons scattered with and without spin-flip, a separation of the coherent from spin-incoherent nuclear scattering processes can be achieved. This is because only $1/3$ of the spin-incoherent scattering events from a sample with random nuclear polarization are without spin flip (the other $2/3$ being with spin flip), while all the coherent nuclear scattering events correspond to scattering without spin flip [6].

Hence from $I_{NSF} = I_{coh} + 1/3\ I_{inc}$, $I_{SF} = 2/3\ I_{inc}$ one directly obtains $I_{coh} = I_{NSF} - 1/2\ I_{SF}$, $I_{inc} = 3/2\ I_{SF}$. It should be noted however that in practice, the scattered intensities need to be corrected for a total finite flipping ratio, accumulating the effect of the imperfections in the spin analysis and manipulation components of the instrument (see e.g. [2]). Figure 5.1 illustrates how this separation was successfully achieved at the MIRA instrument at the FRM II, over the small-angle scattering region of a concentrated hemoglobin solution.

A more complete set of static scattering measurements was obtained on different samples of myoglobin (in dry powder, hydrated powder, and in deuterated solutions of different

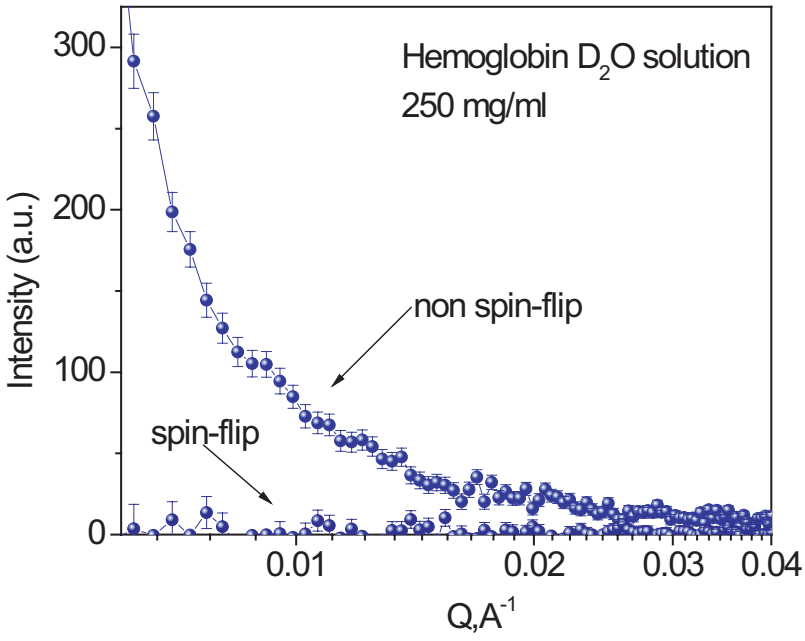

Figure 5.1: Small-angle scattering intensities of neutrons scattered with and without spin flip from a concentrated solution of hemoglobin in D_2O. Results obtained at the MIRA instrument at the FRM II.

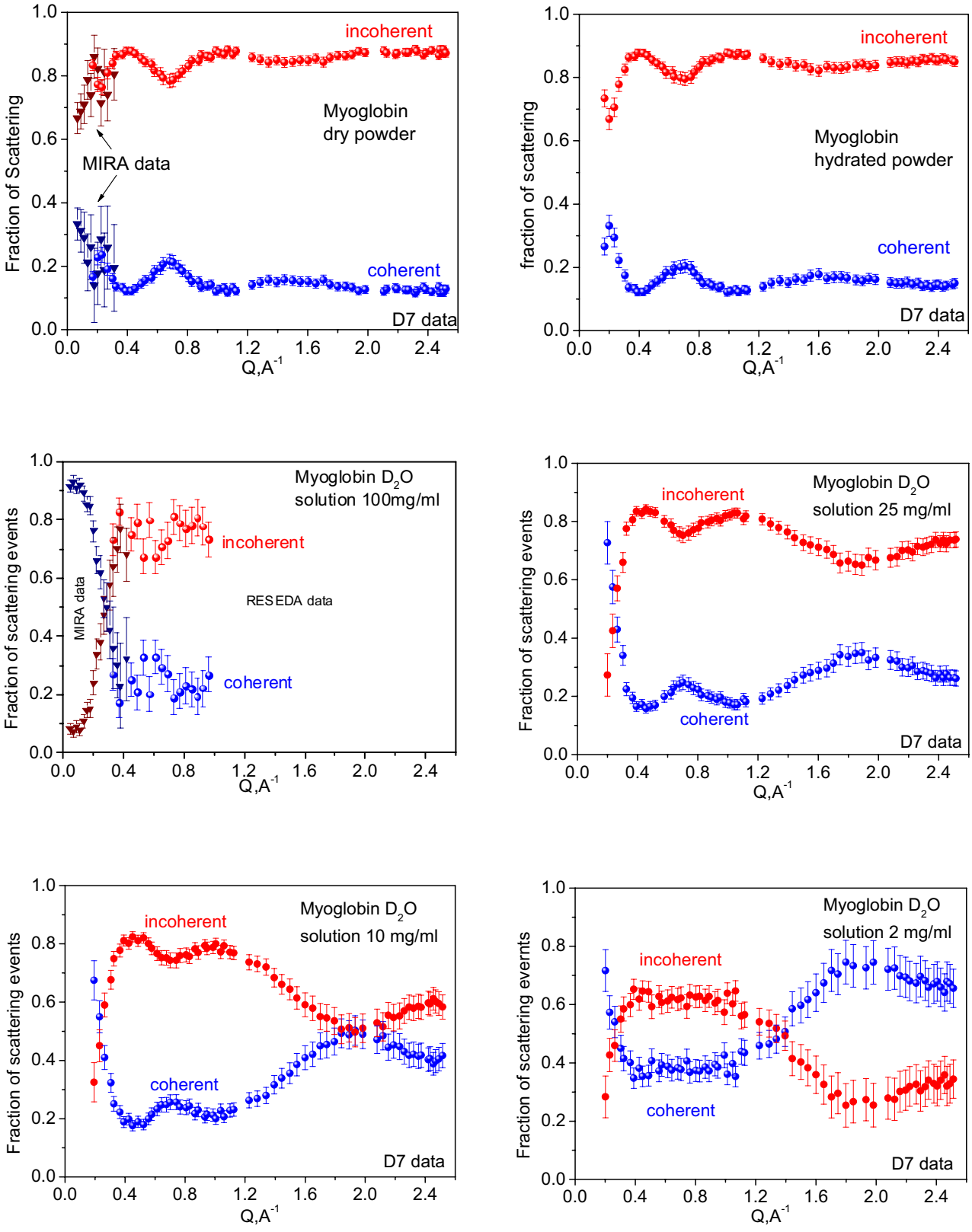

Figure 5.2: Fractions of the total scattering corresponding to coherent and to spin-incoherent events, obtained for the different myoglobin samples investigated. Analyzer rocking scan of the primary beam.

concentrations), combining data from the MIRA and RESEDA instruments at the FRM II with data from the D7 instrument at the ILL, thereby covering a wide Q range, from the small ($0.005 < Q < 0.05$ Å^{-1}) to the wide angle region (up to ~ 2.5 Å^{-1}). Results allowed obtaining quantitative information on the fractions of coherent and spin-incoherent scattering, which is displayed in figure 5.2 for the different myoglobin samples. From this figure it is possible to conclude that for the powder samples, for Q values above 0.3 Å^{-1}, the static incoherent term represents more than 80% of the signal and that, for $Q > 0.9$ Å^{-1}, the coherent and incoherent terms converge to the coherent and incoherent fractions of the total cross section. This is not the case for the protein solutions. Only at high protein concentrations (say >100 mg/ml), and especially if the analysis can be restricted to $0.4 < Q < 1.2$ Å^{-1}, we may also assume a dominating incoherent contribution of approximately 80% of the total scattering.

Otherwise, as in the case of the more diluted solutions, the coherent and incoherent scattering contributions appear similarly important, even with interchangeable predominance.

These results are particularly relevant to the interpretation of time-of-flight or backscattering results obtained on protein solutions, or on any other liquid or soft matter system, for which the structure factor changes significantly over the Q region generally investigated. Since the dynamical correlations at the origin of the coherent and incoherent parts of the spectra are not the same [7, 8], interpretation of the spectra requires appropriate consideration of these two terms and of their relative importance.

A.M. Gaspar acknowledges the Portuguese Science and Technology Foundation (FCT) for support in the form of a post-doc grant SFRH / BDP / 17571 / 2004

[1] Moon, R. M., Riste, T., Koehler, W. C. *Phys. Rev.*, 181, (1969), 920.

[2] Schaerpf, O. *Physica B*, 182, (1982), 376–388.

[3] Dore, J. C., Clarke, J. H., Wenzel, J. T. *Nucl. Instr. & Meth.*, 138, (1976), 317–319.

[4] Gabrys, B. J. *Physica B*, 267-268, (1999), 122–130.

[5] Gabrys, B. J., Zajac, W., Schaerpf, O. *Physica B*, 301, (2001), 69–77.

[6] Hicks, T. J. *Adv. Phys.*, 45, (1996), 243–248.

[7] Skoeld, K. *Phys. Rev. Lett.*, 19, (1967), 1023–1025.

[8] Bee, M. *Quasielastic Neutron Scattering* (Adam Hilger, **1988**).

5.2 Time-of-flight grazing incidence small angle neutron scattering

P. Müller-Buschbaum[1], **J.-F. Moulin**[2], **V. Kudryashov**[2], **M. Haese-Seiller**[2], **R. Kampmann**[2]
[1]ZWE FRM II, TU München
[2]GKSS Forschungszentrum, Geesthacht

Polymers with controlled nanoscale morphologies continue to be of considerable interest for a wide range of applications in electronics, optoelectronics, photonics, sensors, and drug delivery. In particular, nanostructured polymer films allow for new properties, which are mainly based on surface effects and a size reduction down to a regime in which a characteristic length scale of a physical phenomenon becomes comparable with the typical length scale of the nanostructure. In many applications polymers are favoured because many of them are transparent, compliant, and biocompatible and/or biodegradable. Moreover, polymer devices are inexpensive and disposable, which is highly desirable for cost-effective applications.

In addition to a real space image of surface structures, a meaningful statistical analysis is advantageously performed with scattering techniques. Synchrotron radiation based grazing incidence small angle X-ray scattering (GISAXS) turned out to be a powerful advanced scattering technique to probe nanostructured polymer films. Similar to AFM a large interval of length scales between molecular and mesoscopic ones is detectable with this surface sensitive scattering method. While with AFM only surface topographies are accessible, with GISAXS in addition the buried structure is probed. Due to the larger area probed by GISAXS, this technique provides data having a much higher statistical quality than AFM. However, contrast between different components building-up nanostructures might be small and consequently, the possibility of tuning contrasts, which is possible by (partial) deuteration in case of neutron scattering, can be extremely advantageous. Thus neutron surface scattering as analytical technique is a very successful technique. Using neutrons instead of x-rays in combination with the grazing incidence small angle scattering geometry results in grazing incidence small angle neutron scattering (GISANS). As compared to GISAXS measurements based on synchrotron radiation, experiments using neutrons are still very rare. So far all GISANS experiments were performed with a monochromatic neutron beam. These single wavelength experiments are typically very time consuming in case several different incident angles are probed. Within this article we report on a new approach, combining GISANS with the time-of flight mode (TOF). TOF mode allows for a specular and off-specular scattering experiment, in which neutrons with a broad range of wavelengths are used simultaneously and recorded as

a function of their respective times of flight. Such white beam experiments are impossible with x-ray beams due to the immediate radiation damage to the sensitive (bio-) polymer structure. Due to the different interaction, neutron scattering experiments overcome all problems related to radiation damage and are thus a unique probe to detect radiation sensitive surface structures. So far TOF-mode based surface sensitive neutron scattering experiments were restricted to neutron reflectivity and standard off-specular scattering.

To demonstrate the possibilities of the new analytical technique TOF-GISANS we focus on a simple polymer nanostructure. The model system consists of an arrangement of small droplets, called nano-dots, containing a deuterated homopolymer whichi prepared on top of a solid support [1]. Historically, a comparable polymer nano-dot sample was used as model system for the first GISANS experiments as well [2]. Thus the nanostructure is accessible with AFM and single wavelength GISANS measurements exist, which allows for a detailed evaluation of a TOF-GISANS experiment.

The presented experiments were carried out at the REFSANS beamline at the neutron research source Heinz Maier-Leibnitz (FRM II). The total intensity, integrated over all TOF channels, and hence over all wavelengths is strongly dominated by the channels with highest intensity. However, the wavelength integration is equivalent to a strong smearing, because at individual wavelengths the detector pixels cover different $q_y q_z$-areas.

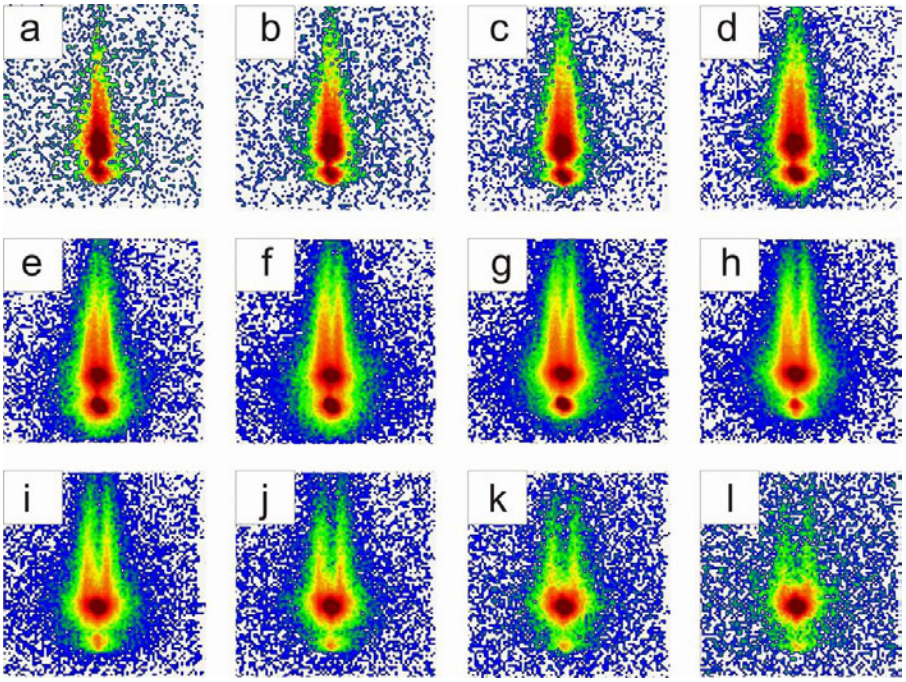

Figure 5.3: Selection of twelve 2d intensities measured simultaneously in the TOF-GISANS experiment. The corresponding mean wavelengths are a) 0.50, b) 0.55, c) 0.61, d) 0.68, e) 0.75, f) 0.82, g) 0.91, h) 1.00, i) 1.11, j) 1.22, k) 1.35 and l) 1.48 nm. The intensity is shown on a logarithmic scale represented by colours following the EOS2 palette (white= low and black= high intensity). Taken from [3].

Thus for a quantitative analysis only the 2d intensities related to individual TOF channels are suited. In figure 5.3 the 2d intensity distributions at 12 TOF channels is shown for a fixed number of effective pixels. Due to the different wavelengths each 2d intensity in figure 5.3 corresponds to a different (q_y, q_z)-range. Thus each 2d image in figure 5.3 is equivalent to the GISANS signal obtainable in a standard GISANS set-up [4] for the wavelength of the TOF channel.

Figure 5.3 shows the anisotropy of all observed scattering patterns. Different main features are already determined right from the two-dimensional images: The intense specular reflected peak, the Yoneda peak (which position depends on the related wavelength) and the splitting of the diffuse scattering into two strong Bragg-rods. The Yoneda peak is located at the position of the critical angle α_c. [3]

[1] Müller-Buschbaum, P., *et al. J. Phys. Condens. Matter*, 17, (2005), S363.

[2] Müller-Buschbaum, P., *et al. Phys Chem Chem Phys*, 1, (1999), 3857.

[3] Müller-Buschbaum, P., *et al.* Submitted.

[4] Müller-Buschbaum, P., *et al. Physica B*, 283, (2000), 53.

6 Condensed matter

6.1 Field and temperature dependence of the magnetization in ferromagnetic EuO thin films

S. Mühlbauer[1], **P. Böni**[2], **R. Georgii**[1], **A. Schmehl**[3], **D.G. Schlom**[3], **J. Mannhart**[4]
[1]ZWE FRM II, TU München
[2]Physics Department E21, TU München
[3]Department of Materials Science and Engineering, Pennsylvania State University, Pennsylvania, USA
[4]Experimentalphysik VI, Institut für Physik, Universität Augsburg

Introduction

The ferromagnetic semiconductor EuO is the only known binary oxide that can be grown in a thermodynamically stable form in contact with silicon. The conductivity can be matched to the conductivity of silicon by introducing oxygen vacancies, which is a key necessity for coherent spin injection in spintronic devices. Therefore, heterostructures composed of Si and EuO may be used as model systems for studying applications of devices in the field of spintronics, where besides the charge, the spin degree of freedom is also used to control the flow of conduction electrons. Recently, it became possible to grow epitaxial films of EuO_{1-x} on Si with spin polarization above 90 percent. The direct integration of EuO with Si will allow the fabrication of model systems for studying devices in the field of spintronics.[1]

While the magnetization of EuO grown on $YAlO_3$ has been measured by means of a superconducting quantum interference device (SQUID) yielding a saturation moment $\mu_{sat} = 6.7\mu_B$ per Eu atom and a coercive field $H_c = 60$ Oe at 5 K , the magnetic moment of EuO_{1-x} grown on Si has not yet been determined. The reason being that the large and rather elusive samples are supposed to be used for additional bulk measurements and should therefore not be reduced in size for measuring the magnetization with a SQUID. Moreover, bulk measurements would not provide information on the re-orientation process of the domains, a property that is of importance for device applications.

In order to non-destructively determine the magnetic properties of thin films of EuO on Si, we have measured the critical angle of reflection by using polarized neutrons. The results confirm that the magnetic moment in the films is consistent with the bulk value. In addition, we show that the change of magnetization is not caused by repopulation of domains but by domain rotation.

Experimental details

The EuO_{1-x} films were deposited by reactive molecular beam epitaxy on thermally cleaned (001) Si and (110) $YAlO_3$ and have been protected in situ against degradation when exposed to air by a 130 Å thick capping layer of Si or other materials. X-ray diffraction scans showed that the structural properties were of exceptionally high quality, comparable to single-crystalline EuO.

The reflectivity measurements were performed on the beam line for very

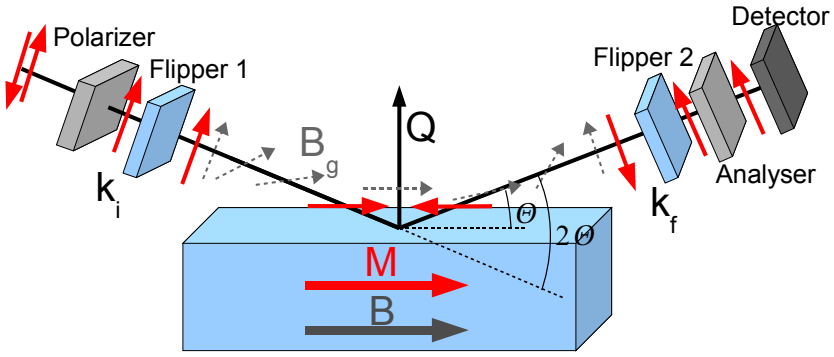

Figure 6.1: Schematics of the polarized neutron reflectometer MIRA. The incoming neutrons $\mathbf{k}_i$ are elastically reflected by the sample. **Q** designates the momentum transfer. The polarization of the neutron beam is selected by means of spin flippers before and after the sample. The polarization of the neutrons follows adiabatically the direction of the guide field $\mathbf{B_g}$. This setup allows the measurement of the four cross-sections I_{++}, I_{--}, I_{-+} and I_{+-}

cold neutrons MIRA. The sample was mounted inside a closed cycle cryostat on a flat aluminium holder. A magnetic field was applied parallel to the incident neutron beam with wavelength $\lambda = 9.7 \pm 0.05$ Å and parallel to the sample surface, as sketched in figure 6.1. As the magnetic field is also guiding the neutron polarization, $\mathbf{P}$ is therefore parallel or antiparallel to the sample and perpendicular to **Q**.

The amplitude of the magnetic moments can be determined by two means: i) either by conducting measurements up to reasonably large q and fitting the data with a bilayer model that includes the EuO and the capping layer or by ii) determining the angle of total reflection. Due to the low intensity of the beam line MIRA we have chosen method ii) that is also used for the characterization of supermirrors. The reflection profiles I_{++}, I_{+-}, I_{-+}, I_{--} were measured by performing $\Theta - 2\Theta$ scans with fixed initial wavevector $\mathbf{k}_i$ for temperatures 6 K $\leq T \leq$ 71 K in magnetic fields B=0 Oe, 125 Oe and 250 Oe.

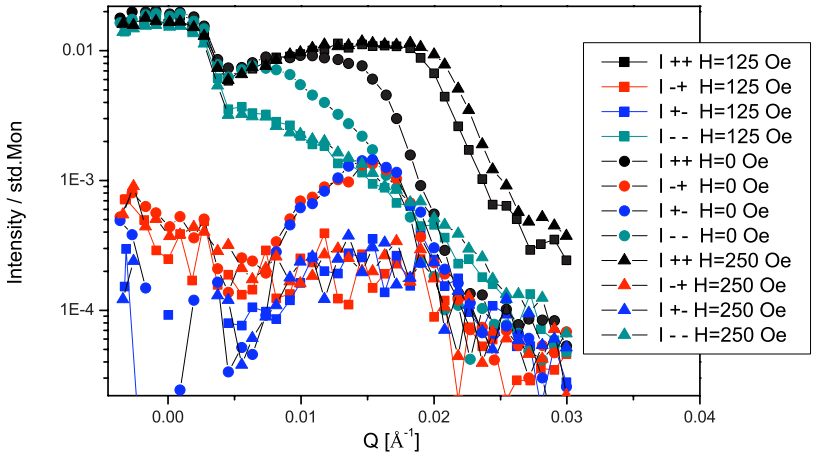

Figure 6.2: Reflectivity profile of EuO on Si (001), T=6 K, B= 0 Oe, 125 Oe and 250 Oe, full polarization analysis. The crosstalk between the individual channels due to finite beam polarization and flipper efficiencies has been corrected. The pronounced peak on the left hand side identifies the un-scattered direct beam, the dip between the plateau of total reflection and direct beam is due to foot-print effects on the small sample. The critical angle of total reflection was determined at 50 percent reflectivity normalized on the total reflection plateau. Both spin-flip cross-sections I_{+-} and I_{-+} vanish for B=125 Oe and B=250 Oe while the data for B=0 Oe shows spin flip scattering.

Results and discussion

The obtained results can be summarized as follows: Figure 6.2 shows a typical reflectivity profile of the EuO sample recorded at 6 K and fields B=0 Oe, B=125 Oe and B=250 Oe. The direct beam is visible around 0°. Due to footprint effects, the plateau of total reflection for I_{++} is reached at roughly 0.011 Å^{-1}, while I_{--} shows no total reflection. Due to the limited length of the sample, the total reflection plateau does not reach the full direct beam intensity. The critical angle of total reflection was determined at 50 percent reflectivity, normalized to the plateau of total reflection. The data has been corrected for a finite beam polarization of 92%.

The observed lack of spin-flip intensity for B=125 Oe and B= 50 Oe shows, that the magnetization of the EuO is strictly parallel to the applied magnetic field, whereas the data recorded at B=0 Oe clearly exhibits spin-flip scattering. This demonstrates, that the change of magnetization is caused by domain rotation and not repopulation, ruling out $B \parallel M$.

In figure 6.3, the temperature and field dependence of the critical angle of total reflection for I_{++} and I_{--} is shown. The merging of the critical angles for T = T_c = 69 K, where the ferromagnetism of the sample vanishes, is obvious. $M(T)$ qualitatively exhibits the expected decrease with increasing temperature. A slight shift of the ferromagnetic to paramagnetic transition to higher temperatures for increasing magnetic field is visible, due to the field induced smearing of the ferromagnetic phase transition. The observed increasing magnetization with increasing field of the EuO layer is due to domain reorientation in direction of the external applied magnetic field.

Two independent features of the measured reflectivity data can be used to verify the obtained values for Θ_c:

The direct beam direction, defining $\Theta_c = 0$ has been used for performing an absolute calibration of Θ_c. This yields a value $b_{mag}(Eu^{2+})$ = 1.78±0.19 · 10^{-12} cm for T=6.5 K and B=250 Oe, which is within 6.5 percent of the literature value ($b_{lit}(Eu^{2+})$ = 1.904 · 10^{-12} cm).

To crosscheck these results, the obtained data has also been normalized to the angle of total reflection of the nuclear contribution of $b_{nuc}(Eu^{2+})$ and $b_{nuc}(O)$, obtained above T_c, where no magnetic contribution is present, giving identical results for $b_{mag}(Eu^{2+})$. With $b_{mag} = (\frac{\gamma r_0}{2}) g f(\mathbf{Q}) \mathbf{S}$ and $(\frac{\gamma r_0}{2}) = 0.2695 \cdot 10^{-12}\, cm$ a magnetic moment $\mu_{sat} = 6.6 \pm 0.7\ \mu_B$ is obtained per Eu atom, which is consistent with results from bulk single crystals.

Conclusion

By measuring the critical angle of total reflection with polarized neutron reflectometry, we demonstrated that the saturation moment of EuO grown epitaxially on Si (001) matches the

moment of EuO grown on $YAlO_3$ as measured using a SQUID, without the need of cutting the samples into small pieces. The observed magnetic moment of the EuO_{1-x} layers agrees very well with values from bulk single crystals, proving the extraordinary high quality of the samples, whereas earlier measurements on EuO layers showed a reduced magnetic moment. The samples clearly show a well defined ferromagnetic transition at T_c= 69 K. Thus, EuO_{1-x}, matched to the conductivity of silicon and grown epitaxially on silicon may be broadly used for spintronic devices within the well established Si-based technology.

Furthermore, the ability of polarized neutron reflectometry being sensitive to the orientation of the magnetic moment in the sample proves, that domain reorientation and not repopulation is responsible for the process of magnetization.

[1] Schmehl, A., *et al. Nature Materials*, 6, (2007), 882 – 887.

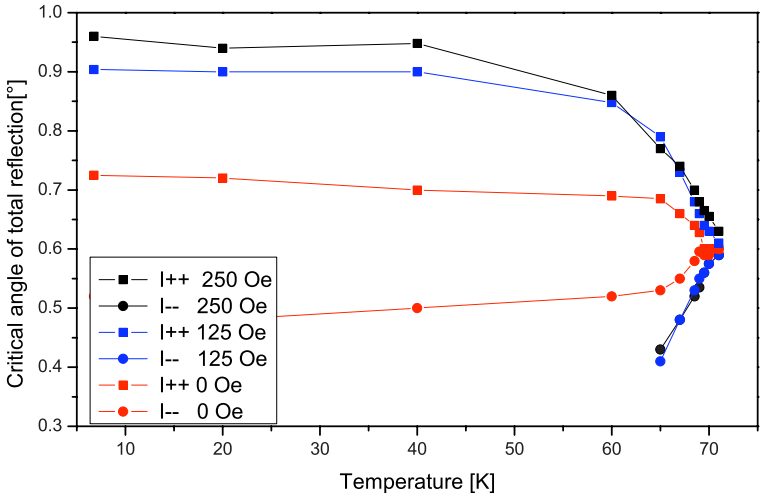

Figure 6.3: Temperature dependence of the critical angle of total reflection of EuO on Si (001) for different temperatures from 6 K $\leq$T$\leq$ 71 K and different applied magnetic fields B=0, 125 and 250 Oe; For T=T_c, the magnetic contribution vanishes. The clear field dependence indicates domain repopulation for increasing external fields in direction of the applied external field.

6.2 Examination of rat lungs by neutron computed micro tomography

B. Schillinger[1,2], **Andrew Comerford**[3], **Elbio Calzada**[1,2], **Josef Guttmann**[4], **Robert Metzke**[3], **Martin Mühlbauer**[1,2], **Hanna Runck**[4], **Matthias Schneider**[4], **Michael Schulz**[1,2], **Claudius Stahl**[4], **Lena Wiechert**[3], **Wolfgang Wall**[3]
[1]ZWE FRM II, TU München
[2]Physics Department E21, TU München
[3]Chair for Computational Mechanics,TU München
[4]Department of Anesthesiology and Critical Care Medicine, University of Freiburg

Abstract

By means of a thinned scintillation screen and a high resolution optical system an effective resolution in the order of 30-40 μm is achieved at the ANTARES facility for neutron imaging. This setup was used to gather structural information of freshly extracted rat lungs. The aim of the measurement is the development of a numerical lung model for improvement of artificial respiration in human medicine in hospitals.

Introduction

Patients who need artificial respiration in hospital over several days often suffer lung damages because the respiration pressure cannot be set with sufficient precision due to insufficient knowledge about the exact composition of the lung. The chair for computational mechanics of TU München aims to develop a numerical model of a lung in order to simulate pressure and air flow in the branching of the air vessels. As it turned out, the structure of the lung is known in principle, but not in detail, and very little is known about the actual branching and diameters of the pulmonary air passages. As the volume of the lung consists mostly of air, with very thin air and blood vessels, normal X-ray examinations deliver insufficient contrast of the tissue to image the structure of the lung. Neutron imaging delivers a high contrast of the hydrogen content in the tissue and was successfully employed to deliver 3D images of the lung structure.

Experimental setup

Since neutron imaging employs a parallel beam, there is no inherent magnification of the sample, and the im-

age resolution is limited to the actual detector resolution. ANTARES used a thinned scintillation screen (50μmthickness) and a ZEISS planar high resolution lens on a 2048 x 2048 pixel cooled CCD camera. With an effective pixel size of 20μm, the achieved resolution (due to blurring of the scintillation screen) was estimated in the order of 30-40μm. Live laboratory rats were delivered to the engineering faculty, were anaesthetised and killed. The lungs were extracted and sewn with their main air pipe onto on a plastic tube, then put inside an aluminium tube that both simulated the confinement of the rib cage and also fixated the lung against movement during the measurement. The lung was then inflated with 20-30 mbar air pressure and mounted on a rotation table in front of the detector.

Measurement

At this high resolution, the incident neutron flux per pixel is very low. One projection required between 13 and 80 seconds exposure time, totalling in 2.5 to 9 hours for 400 projections for the computed tomography. Additional experiments were conducted with a Gadolinium containing contrast agent that was directly injected into the main airway. Due to the capillary forces, this contrast agent penetrated into the finest air vessels.

Fig. 6.4 shows one projection of a lung confined in the Aluminium tube, fig. 6.5 shows a lung with added Gadolinium contrast agent. Fig. 6.6 shows a lung that was taken out of the Aluminium container and had consecutively inflated to double its original volume. Fig. 6.7 shows a three-dimensional reconstruction of a lung with the threshold set so high as to see only larger air vessels. Fig. 6.8 shows another lung with a lower threshold level, showing many fine vessels as well as apparently a major blood vessel that branches towards different sections of the lung.

Fig. 6.9 shows a lung filled with Gadolinium contrast agent that had dissipated into the finest branches. Since the liquid had followed gravity during injection, the upper parts of the lung were not filled.

Conclusion

For the first time, neutron computed tomography has been used for the determination of the structure of lung tissue. The results will be employed in the development of a numerical model of a lung in order to improve clinical treatment of human patients. Further examinations are under way.

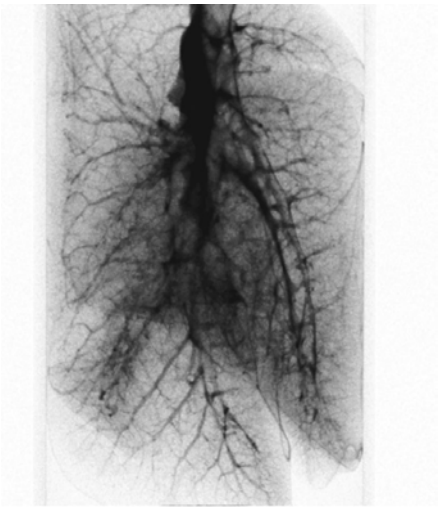

Figure 6.4: One projection of a lung confined in the Aluminium tube.

Figure 6.5: A lung with added Gadolinium contrast agent

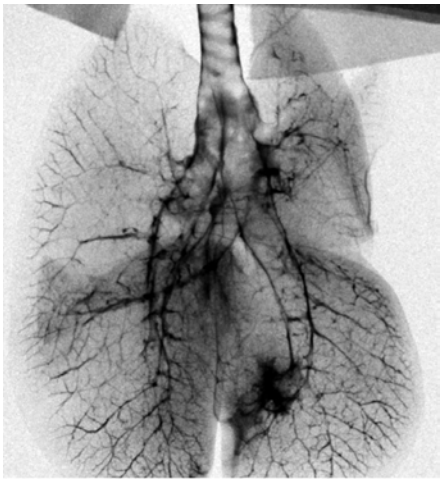

Figure 6.6: A lung that was taken out of the Aluminium container and had consecutively inflated to double its original volume.

Figure 6.7: A three-dimensional reconstruction of a lung with the threshold set so high as to see only larger air vessels.

Figure 6.8: Another lung with a lower threshold level, showing many fine vessels as well as apparently a major blood vessel that branches towards different sections of the lung.

Figure 6.9: A lung filled with Gadolinium contrast agent that had dissipated into the finest branches. Since the liquid had followed gravity during injection, the upper parts of the lung were not filled.

6.3 Thermal expansion under extreme conditions at TRISP

Christian Pfleiderer[1], **Peter Böni**[1], **Thomas Keller**[2,3], **Ulrich K. Rössler**[4], **Achim Rosch**[5]
[1]Physik-Department E21, TU München
[2]Max-Planck-Institut für Festkörperforschung, Stuttgart
[3]ZWE FRM II, TU München
[4]IFW Dresden
[5]Universität Köln

The resolution of conventional neutron and x-ray diffractometers is limited by the beam divergence and monochromaticity. The Larmor-diffraction technique (LD) at TRISP surpasses the resolution of conventional diffractometers by 1-2 orders of magnitude and reaches in the present configuration $\Delta d/d \simeq 10^{-6}$. This makes possible the reexamination of a large number of prominent scientific questions in physics, chemistry, geoscience and engineering through high-precision measurements of lattice parameters under extreme conditions like ultra-low or very high temperatures, high hydrostatic or uniaxial pressures and high electric fields.

Here we report on a study of the thermal expansion of the cubic metal MnSi under pressures up to 21kbar and temperatures down to 0.5K [1] at TRISP. MnSi attracted great interest because it is probably the best candidate for a non-Fermi liquid (NFL) metallic state in a pure three-dimensional metal that is not sensitive to a fine tuning of the underlying interactions [2, 3]. This possibility is inferred from an abrupt transition of the temperature dependence of the resistivity from a well understood T^2 Fermi liquid behavior to a $T^{3/2}$ non-Fermi liquid behavior above $p_c = 14.6$kbar. The NFL resistivity is remarkably insensitive to pressure up to at least 50kbar ($\sim 3p_c$) [4, 5].

The question whether the NFL resistivity in MnSi is driven by a QCP or is the characteristic of a novel metallic phase is settled by the thermal expansion data shown in Fig. 6.10 and 6.11(b). (QCPs are defined as zero-temperature second-order phase transitions that are tuned by non-thermal control parameters such as hydrostatic pressure or magnetic field). For the zero temperature limit the variation of the lattice spacing a_2 shows expansion for $p < p^*$, while it shows contraction above p_c (see phase diagram in Fig. 6.11(a)).

However, the change of sign is already present for $T > T_C$ when T_C is suppressed below $\sim 15K$. Further, for pressures above p_c the temperature dependence of a_2 remains essentially unchanged without any signature of T_0. This both rules out quantum criticality for $T_c \to 0$ at p_c and a QCP for $T_C \to 0$.

Our results concerning the nature of the phase diagram of MnSi show that the transition at p_c is first order, and the onset of partial order at T_0 (and thus p_0) seen in neutron scattering is clearly not related to a thermodynamic phase transition. This establishes that the observed NFL behavior is not connected to a QCP. Instead, it is the characteristic of an extended genuine NFL state. More generally, this finding suggests that novel forms of order may be expected elsewhere than at quantum phase transitions.

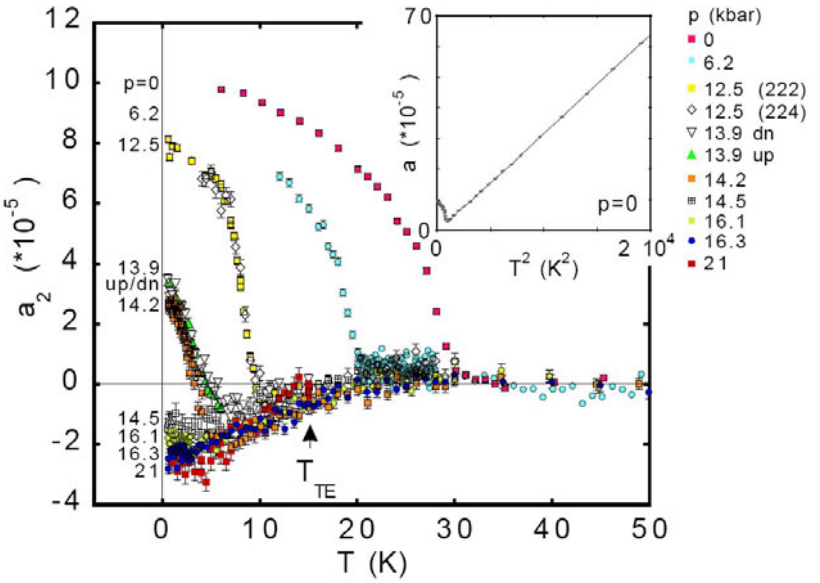

Figure 6.10: Temperature dependence of magnetic and electronic contributions a_2 of the lattice constant of MnSi at various pressures as obtained by Larmor diffraction at TRISP. The relative resolution obtained in this experiment is in the order of 1.6×10^{-6}. The inset displays the lattice constant a at ambient pressure.

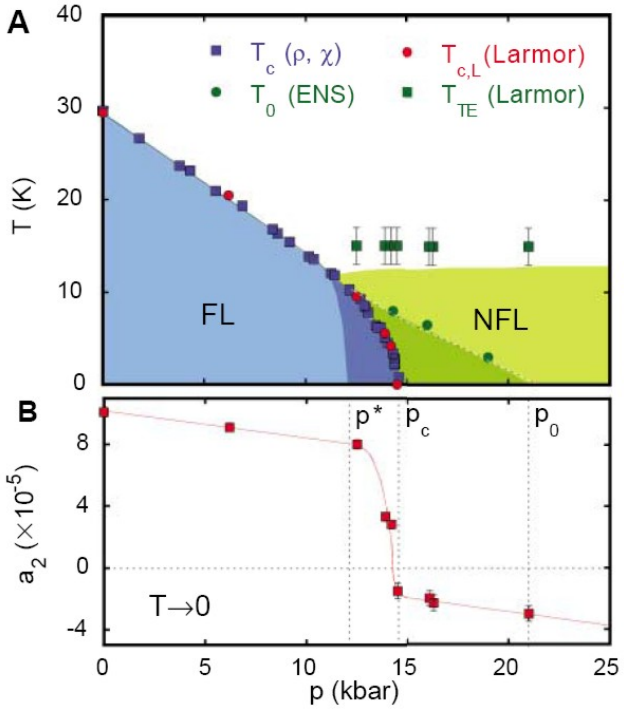

Figure 6.11: (**A**) Phase diagram of MnSi as a function of pressure. Data for T_C are based on the resistivity ρ and the ac susceptibility χ reported in [6]. T_0 is based on elastic neutron scattering [7]. The blue shading indicates the regime of Fermi liquid behaviour, where dark blue shading shows the regime of phase segregation seen in μ-SR [8]. The green shading represents the regime of NFL resistivity, where dark green shading indicates the regime of partial order. The transition temperature $T_{C,L}$ observed in the lattice constant by Larmor diffraction is in excellent agreement with previous work. The crossover temperature T_{TE} represents the appearance of lattice contraction in a_2 as measured by Larmor diffraction. (**B**) Extrapolated zero-temperature variation of a_2. The spontaneous magnetostriction varies very weakly under pressure up to $p^* \sim 12.5$kbar before dropping distinctly and changing sign. It also varies very weakly above p_c.

[1] Pfleiderer, C., Böni, P., Keller, T., ler, U. R., Rosch, A. *Science*, 326, (2007), 1871.

[2] Pfleiderer, C., Julian, S., Lonzarich, G. *Nature*, 414, (2001), 427.

[3] Pfleiderer, C. *Physica B*, 328, (2003), 100.

[4] Doiron-Leyraud, N., *et al. Nature*, 425, (2003), 595.

[5] Pedrazzini, P., *et al. Physica B*, 378-380, (2006), 165.

[6] Pfleiderer, C., *et al. Phys. Rev. B*, 55, (1997), 8330.

[7] Pfleiderer, C., *et al. Nature*, 427, (2004), 227.

[8] Uemura, Y. J., *et al. Nat. Phys.*, 3, (2007), 29.

6.4 Investigation of embedded submono-layers in Al using positron annihilation

Christoph Hugenschmidt[2,1], **Philip Pikart**[1,2], **Martin Stadlbauer**[1,2], **Klaus Schreckenbach**[1,2]
[1]Physics Department E21, Technical University Munich, 85747 Garching, Germany
[2]ZWE FRM-II, Technical University Munich, 85747 Garching, Germany

In the presented work we demonstrate that metal layers in the submonolayer range embedded in a matrix are revealed with unprecedented sensitivity by coincident Doppler-broadening spectroscopy (CDBS) of the positron annihilation using a mono-energetic positron beam. Besides the application of a non-destructive technique, one aim has been to reveal the elemental signature of Sn of various thickness in the CDB-spectra in order to investigate the positron trapping properties of the embedded Sn layer.

A set of four layered samples was prepared in an UHV-chamber: Pure Al was evaporated onto water-cooled glass substrates ($\geq 99.99\%$, thickness of $5.5 \pm 0.3\,\mu$m). Afterwards, the Sn layer ($\geq 99.999\%$) of various thickness d_{Sn} ($d_{Sn} = 0.10 \pm 0.03$ nm, 1.60 ± 0.1 nm, 25 ± 1 nm, and 200 ± 8 nm) was evaporated on top of the Al, which was finally by 200 ± 8 nm Al. Annealed Al and annealed Sn serve as reference materials. We performed calculations of the Makhovian implantation profile (before diffusion) of the layered samples in order to maximize the overlap of the positron distribution with the Sn layer by variation of the kinetic energy of the positrons. As a result of these calculations the kinetic energy was set to 6 keV for the three samples with a Sn-thickness of 0.10 nm, 1.6 nm, and 25 nm, respectively, and to 15 keV for the others.

The measurements were carried out with the CDB-spectrometer [1] located at the high intensity positron source NEPOMUC – NEutron induced POsitron source MUniCh [2]. The raw data of the CDB-spectra are normalized to the same integrated intensity of the 511 keV photo-peak (figure 6.12). Note the low background leading to a peak-to-background ratio of better than 10^5. For a more detailed view, all spectra have been divided by the spectrum obtained for pure annealed Al in order to reveal the element specific contribution of Sn (figure 6.13). The solid lines represent least-square fits of a linear combination of the photon intensities recorded for pure Sn and pure Al with only one free fit parameter, which corresponds to the amount of positrons annihilating in the Sn layer.

The higher photon intensity for larger electron momenta with increasing amounts of Sn is attributed to the higher binding energy of the annihilating core electrons in Sn. Even at an amount of 0.1 nm Sn below the 200 nm Al coating, the photon intensity increases significantly for $10 \cdot 10^{-3} m_0 c < p_L < 25 \cdot 10^{-3} m_0 c$. The strongly disproportional increase of the positron annihilation rate with core electrons from Sn is interpreted as follows: After implantation, thermalized positrons diffuse to the Al/Sn-interface, where they are efficiently trapped in open-volume defects and hence could annihilate with localized core electrons of Sn atoms. The number of those defects are expected to be particularly large due to the lattice mismatch at the Al/Sn-interface. On the other hand, the smaller core annihilation probability for positrons trapped in open volume defects would lead to a lower photon intensity in the high electron momentum range than annihilation in the unperturbed Sn lattice. It is hence unlikely that defect trapping is solely responsible for the large enhancement of the Sn signature. The main reason for the observed high annihilation rate in the Sn layer can be understood in terms of the element specific positron affinity: Due to the much stronger positron affinity of Sn compared to that for Al, the Sn layer can be regarded as a well with a potential depth of ~ 3.2 eV. Therefore, positrons thermalized inside the Sn layer are repelled at the Sn/Al interface during their diffusion, and a certain amount of those thermalized in Al diffuse to the Sn layer where they are efficiently trapped inside the Sn layer or Sn clusters.

With this experiment we demonstrated that CDBS with mono-energetic positrons is clearly a very powerful technique for the investigation of thin layered structures that are hidden below coatings of hundreds of atomic layers. We envisage to investigate layers of various elements embedded in a matrix by CDBS as a function of positron implantation energy not only to reveal the elemental information of the embedded layer but also to determine its depth below the coating.

[1] Stadlbauer, M., Hugenschmidt, C., Straßer, B., Schreckenbach, K. *Appl. Surf. Sci.*, 252, (2006), 3269–3273.

[2] Hugenschmidt, C., Schreckenbach, K., Stadlbauer, M., Straßer, B. *Nucl. Instr. Meth. A*, 554, (2005), 384–391.

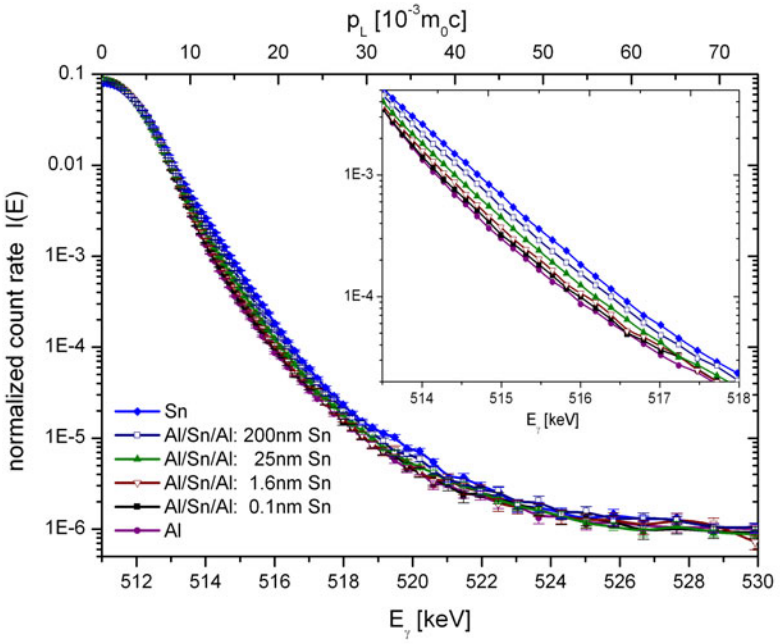

Figure 6.12: CDBS of the 511 keV annihilation line for pure Al, Sn, and the Al/Sn/Al layered samples.(normalized to same intensity).

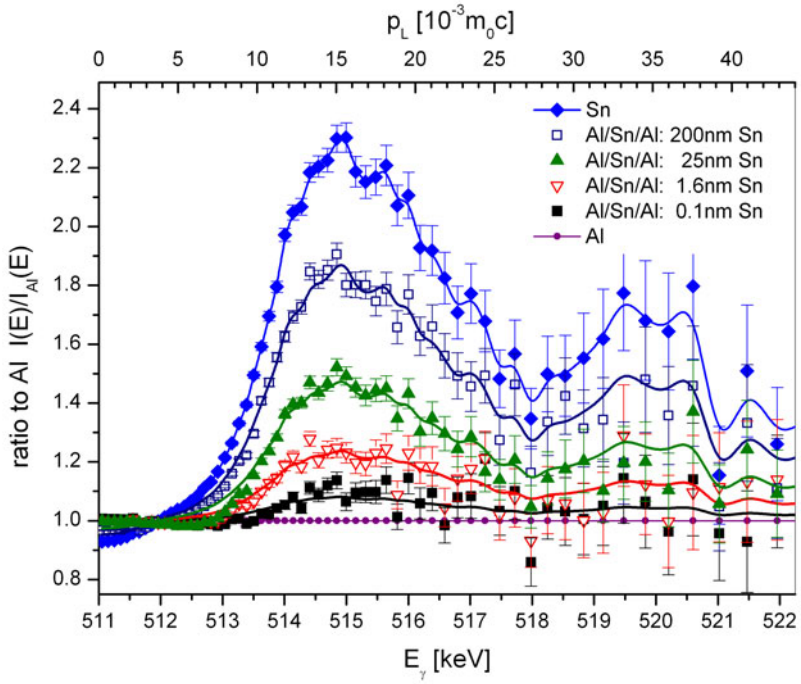

Figure 6.13: Ratio curves of the photon intensities: All spectra (see fig. 6.12) are divided by the Al reference spectrum. The uppermost curve shows the elemental signature of Sn. (Details see text.)

Part III

Facts and figures

7 Facts

7.1 User office and public relations

J. Neuhaus [1], **U. Kurz** [1], **B. Tonin** [1]
[1] ZWE FRM II, TU München

On May 9th 2007 the hand-over of keys of the new east building was celebrated. About 150 visitors joined the party welcomed by officials from TUM and the Forschungszentrum Jülich GmbH - of which the Jülich Centre for Neutron Science occupies this building as lodger of the second floor - to former colleagues and friends from neighboring and foreign institutes. A night with movies in the huge and at that time still empty east hall completed the event.

In autumn 2007 the Campus of Garching celebrated its 50th anniversary. Everything started with the first neutrons at the Forschungsreaktor München (FRM), the so-called "Atomic Egg" on October 31st 1957. Preparing the birthday activities started already in 2006. In a close collaboration between the Technische Universität München, the Max-Planck-Institute for Plasma Physics, the European Southern Observatory (ESO) and the city of Garching several activities were organized.

Figure 7.1: Prof. Dr. Dr.h.c. mult. Wolfgang A. Herrmann received the keys of the new east building from Mr. Heinrich Mayer, responsible building director of BaTUM.

The "Festveranstaltung" with presentations from science and politics took place on September 26th in the lecture hall of the Faculty for Engineering in Garching. On this occasion the resigning prime minister Dr. Edmund Stoiber pointed out the key role of the FRM and FRM II for the Garching Campus. The national press and Bavarian television responded well to the long list of prominent speakers including the noble prize winner Prof. Dr. Theodor W. Hänsch and the president of the TUM, Prof. Dr. Dr. h.c.mult. Wolfgang A. Herrmann.

This event was followed by the "Long Night of Science" on October 13th. Until midnight all institutions in Garching opened their doors and attracted several thousands of visitors. A panel discussion in the lecture hall of the Faculty for Engineering on "Von Garching nach Europa – Forschung im globalisierten Wettbewerb" opened the evening events. FRM II offered visitor tours through the reactor building as well as overview talks in the Physics Department accompanied by presentations of the radiation protection service and movies presenting the research opportunities at FRM II. The offer to visit FRM II was in great demand as usual and quickly fully booked. Altogether 455 visitors toured the FRM II. The guided tour included the view into the reactor hall and the presentation of the instruments in the experimental and neutron guide hall.

Figure 7.2: Prime minister Dr. Edmund Stoiber and president of the TUM, Prof. Dr. Dr. h.c.mult. Wolfgang A. Herrmann.

Figure 7.3: The Möbius strip symbolizing the interaction of the numerous research institutes at the campus and between the campus and the city of Garching.

Figure 7.4: The winner of the contest, Franziska Ipfelkofer, together with Raimund Fries, deputy director of Donau-Gymnasium, Kelheim and Dr. Jürgen Neuhaus, FRM II.

The “Long Night of Science” attracted especially younger people to visit the scientific institutes. In the very beginning of the “Long Night” even very young visitors were welcomed. In particular, children of staff members gained insight in the work of their parents. Tobias Unruh, known for his expertise to explain difficult scientific subjects to young pupils, delivered fascinating insights into daily scientific work.

On the occasion of the celebration of the 50th anniversary of the Garching Campus a new logo was created “Forschen in Garching”. The depicted Möbius strip symbolizes the interdisciplinary research on a campus of many different facilities.

In addition to the program of the individual institutes a competition for high school students was organized: “Das Unsichtbare sichtbar machen (Making the invisible visible)”. The idea behind this contest was to bring together science and art classes from schools and to create art objects which illustrate length and time scales ranging from sub-atomic particles up to the universe. The winner was Franziska Ipfelkofer from the Donau-Gymnasium, Kehlheim.

Last but not least, at the anniversary day on October 31st the FRM II and the Faculty of Physics organized a colloquium, entitled “50 years of research with neutrons in Garching – and its future”. There the newly appointed prime minister Dr. Günther Beckstein renewed the engagement of the Free State of Bavaria for the Campus Garching in general and in particular for the Forschungsneutronenquelle Heinz Maier-Leibnitz.

A very special event took place on September 27th in the neutron guide hall of FRM II. The well known Munich writer Asta Scheib read from her autobiographical novel “Sei froh, dass du lebst”. This reading was part of a series of performances entitled “Garching liest”. Each event happened at another special location. Certainly the most unusual of all of them was the gallery of the neutron guide hall, where about 40 listeners found place. In addition to the literary pleasure the music of the “Garchinger Pfeiffer” guarantied for enjoyment. The participants were impressed not only by the interesting presentation, but as well by the unique ambience. The local organization was due to Christoph Morkel.

FRM II also participated at the Garchinger Herbsttage from September 15th to 16th. Biannually the City of Garching together with local companies organizes a trade show in the town center. Two years ago the FRM II displayed the research doing at our institute for the first time. This year a common booth was organized together with the Max-Planck-Institute for Plasma Physics. The public has been informed about research projects of the two institutes for two days.

Figure 7.5: The Bavarian prime minister Dr. Günther Beckstein during his speech on October 31st.

Figure 7.6: Poster advertising the reading of Ms. Asta Scheib at FRM II.

Each autumn the University of Applied Sciences Munich organizes a job fair, especially for engineering students. In order to attract young engineers for scientific instrumentation, Toni Kastenmüller and Jürgen Neuhaus presented the employment possibilities at the FRM II. Among many traineeships, several open positions for engineers in the area of civil engineering, physics engineering, mechanical engineering and electro engineering were highlighted. As the job fair mainly addresses students, a number of internships could be accomplished at the FRM II.

By opening its doors to general visitors FRM II helps to explain to a greater public the safety and usefulness of nuclear technology. In 2007 we welcomed a total of 2612 non scientific visitors, 526 of them were students and 522 were pupils from high schools. They were guided through the reactor building, could take a look over the reactor hall from the visitors window at the sixth floor and passed the experimental hall as well as the gallery of the neutron guide hall. Concerning our scientific program two calls for proposals were launched in 2007, as usual in January and July. 509 experiments could be performed within 2007 using the 234 days of reactor operation. About 800 scientists visited the FRM II for neutron and positron experiments. About 60% of the beam time, distributed by the proposal procedure, were occupied by scientists from Germany, 32% came from European countries and 8% from overseas. The distribution of the beam time was reviewed by an international referee committee. In addition, the newly created Jülich Centre for Neutron Science outstation at FRM II of the Forschungszentrum Jülich GmbH had two proposal rounds in 2007. 85 experiments were realized at their instruments at FRM II.

Last but not least, in 2007 the first user meeting of the FRM II took place on 30th October. About 95 participants followed the talks in the lecture hall of the Physics Department of LMU at Campus Garching. The presentations covered the wide range of scientific topics investigated at FRM II. A Bavarian buffet supported the long-lasting and interesting discussions on the scientific results obtained. All instruments were presented during the poster session which provided a detailed insight into the experimental possibilities of the FRM II. Simultaneously, the first PLEPS workshop was hold. The 40 participants joined the poster session in the evening hours making the event a marvellous success.

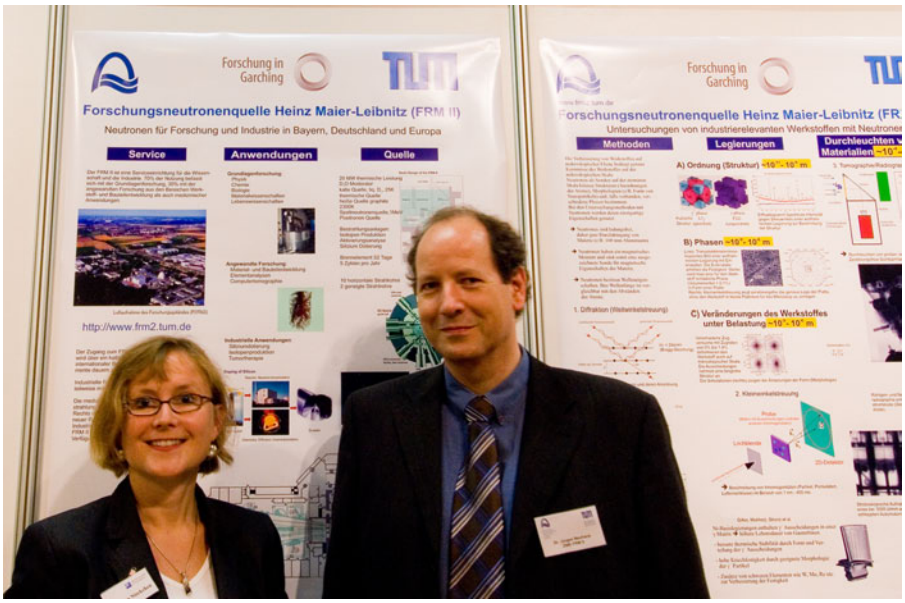

Figure 7.7: Dr. Petra Nieckchen, Max-Planck-Institute for Plasma Physics, and Dr. Jürgen Neuhaus, FRM II at their booth at Gewerbeschau Garching

7.2 "Fortgeschrittenenpraktikum" Neutron scattering at the FRM II

R. Georgii[1], **M. Hofmann**[1], **M. Meven**[1], **R. Mole**[1], **K. Schrechenbach**[2], **T. Unruh**[1]
[1]ZWE FRM II, TU München
[2]Physik Department E21, TU München

In the winter term 2006/07 the neutron scattering practical training of students was started at the FRM II. Students in the 5th and 6th semester from the physics department of the TU were participating in it as part of their "Fortgeschrittenenpraktikum".

On five instruments, HEIDI, MIRA, PUMA, Stress-Spec and TofToF, a total of 35 students were participating in 2007. After a half a day of introduction in the technology of the FRM II and the theory of neutron scattering, each student was participating in two different experiments. The experiments were adopted from standard measurements typical for each of the instruments and lasted a day each including night measurements. During the experiments the students had the possibility of a guided tour through the reactor. The results of the experiments were then documented in a short report by the students. Finally a short colloquium based on this report had to be passed by the students.

The response of the students, which we tested with a short questionnaire, was very enthusiastic. The main highlight for them was the possibility to work on "real" user experiments in normal operation contrary to lab experiments.

7.3 11th JCNS Laboratory course on neutron scattering

Th. Brückel[1], **G. Heger**[2], **R. Zorn**[3]
[1]Institute for scattering methods, Research Centre Jülich
[2]Institute of Crystallography, RWTH Aachen
[3]Institute for neutron scattering , Research Centre Jülich

September 3 - 14 the 11th JCNS Laboratory course on neutron scattering was held by the Jülich Centre for Neutron Science. For the first time in the history of the labcourse the lecture part and the experimental part were held at different locations. The lectures took place at Forschungszentrum Jülich as in the past years and the experiments were carried out at the reactor FRM. The labcourse is open for students of Physics, Chemistry, and other natural sciences from all around the world. It is part of the curricula of the Universities of Aachen and Münster. The course was supported by the Integrated Infrastructure Initiative for Neutron Scattering and Muon Spectroscopy (NMI3) and SoftComp, the European Network of Excellence for Soft Matter Composites. The neutron scattering course consists of one week of lectures and one week of hands-on training on the instruments. The lectures encompass an introduction to neutron sources, into scattering theory and instrumentation. Furthermore, selected topics of condensed matter research are presented. The second week of the labcourse consisted of hands-on experiments at dedicated instruments at FRM II. Students performed on experiments at the backscattering instrument SPHERES, the neutron reflectometer TREFF, the Jülich neutron spin-echo spectrometer J-NSE, small and ultra-small angle scattering at KWS-2 and KWS-3, single crystal and powder diffraction at HEIDI and SPODI, polarisation analysis at DNS and triple-axis spectroscopy at PUMA. 47 students participated in the labcourse. The students came from 13 countries in total of which 10 belong to the EU. The participation of female students was 43The students experienced real life scientific work and atmosphere at the Forschungszentrum Jülich as well as at the FRM II neutron facility. The response was overwhelmingly positive. The splitting of the locations was surprisingly not seen as a burden although it implied a daylong bus trip from Jülich to Munich. Rather the students appreciated the possibility to get to know two major research centres in Germany.

7.4 Workshop – Neutrons for applied research in the field of material development and material technology

R. Gilles [1]
[1] ZWE FRM II, TU München

On the invitation of the chair “Metallurgy of iron and steel” RWTH Aachen (Prof. Senk) a meeting was held in Aachen on 19.10.2007. The workshop was organized under the auspices of the Werkstoff-FORUM of RWTH Aachen.

After the introduction of Prof. Heger (RWTH Aachen), the general aspects of instrumentation using neutrons for applied science were demonstrated by Prof. Petry (TU München). The other talks were focused on special instruments at FRM II or JCNS which are useful for material development and material technology.

Burkhard Schillinger’s presentation gave an overview about the variety of objects which could be x-rayed non-destructively with neutrons (motors, alloys, cochlea, lungs of a rat, pieces of wood etc.).

Michael Hofmann reported on strain measurements (for example crank, railroad tracks etc.) using the diffraction method to determine stress and texture.

Hans Boysen focused his talk on the different possibilities of sample environment (high temperature, low temperature, tensile test machine) available at the structure powder diffractometer SPODI.

Figure 7.8: Speakers of the workshop (from left to right): Burkhard Schillinger, Michael Hofmann, Ralph Gilles, Prof. Winfried Petry, Andrea Brings (manager of Werkstoff-Forum RWTH Aachen), Hans Boysen and Prof. Gernot Heger.

Ralph Gilles introduced the small-angle scattering method to characterize on the nanometer scale for example precipitates of superalloys in situ at high temperatures. Prof. Brückel gave an overview on the method of neutron reflectometry on thin films, especially about their electric and magnetic properties.

At the end of the workshop Prof. Petry, Prof. Heger and Prof. Brückel informed the audience how to apply and to prepare for beam time at the FRM II. After excited discussions with many people from the audience in the poster session the speakers met before leaving Aachen for a short farewell photo.

7.5 Biannual workshop at Burg Rothenfels

R. Georgii [1]
[1] ZWE FRM II, TU München

From Monday, 23.07 until Thursday, 26.07.07 the 3rd workshop on neutron scattering of the FRM II took place at Burg Rothenfels (see figure 7.9). 60 participants from E21 and E13 (Physics department, TU München), from the LMU, JCNS, GKSS and the FRM II spent four days of intense discussion in the pleasant surrounding of Mainfranken (see figure 7.10). The program was very diverse and intense (see table 7.1) and included an evening talk by Stefan Paul, E18, TU München about "Ultra Cold Neutrons". Half a day was devoted to a short hiking tour in the beautiful landscape around Burg Rothenfels.

Figure 7.9: Burg Rothenfels

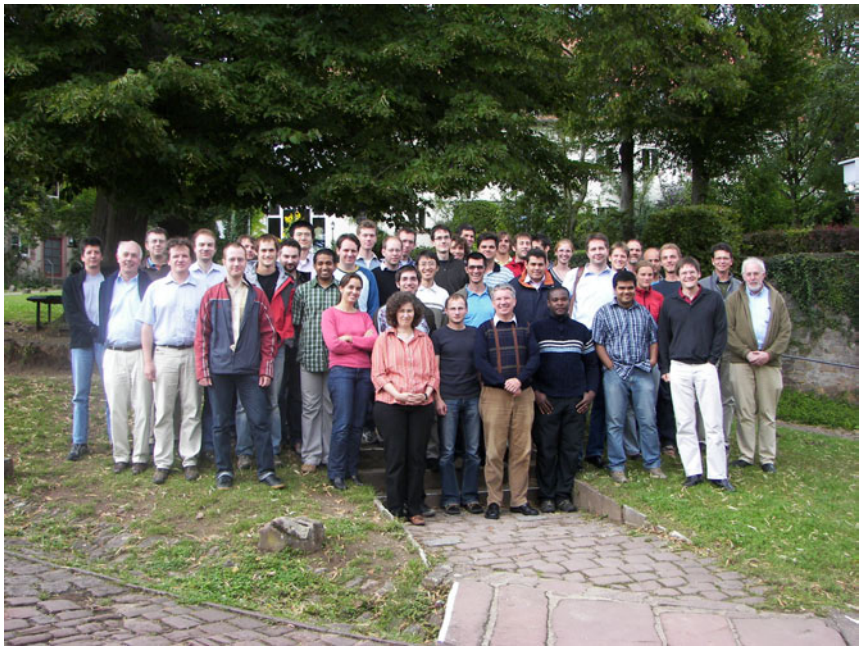

Figure 7.10: The participants of the workshop

Table 7.1: Summary of all talks

Abul Kashem M.	Magnetic nanoparticles in supported polymer structure
Appavou M-S.	Influence of pressure on the dynamics of Human hemoglobin
Breitkreuz, H.	Spektrale Charaktersierung des Spaltneutronenstrahls
Darko C.	Thin films from crystalline diblock copolymers
Doster W.	Protein Diffusion in Biological Cells
Frielinghaus, H.	Tailormade Microemulsions with Polymer Additives
Gaspar A.	Using polarized neutrons for the study of the dynamical structure of proteins
Hugenschmidt, C.	Positron annihilation spectroscopy
Ivanova R.	Multicompartment polymeric hydrogels studied using SANS
Kaune G.	GISAXS Investigation of Organic-Anorganic Nanostructures for Photovoltaics
Keller, T.	Introduction to Lamor diffraction
Klein, W.	Mo_2B_5 vs. Mo_2B_4 - Strukturlösung mit allen Mitteln
Kudejova, P.	PGAA and PGAI for the ANCIENT CHARM project and other applications
Kulkarni,A.	Smart hydrogels from amphiphilic triblock copolymers
Lorenz, K.	First measurements with the new multi filter at ANTARES
Löwe, B.	Beam brightness enhancement with a gas-moderator
Mayer, J.	Positron annihilation induced Auger-electron spectroscopy
Mehaddene, T.	Dynamics of magnetic shape memory alloys investigated by inelastic neutron scattering
Metwalli Ali E.	Water-vapor swelling response of thin casein films
Moulin J.-F.	In situ characterisation of a fluidic cell
Müller-Buschbaum P.	TOF-GISANS at REFSANS
Nickel, B.	Reflectivity experiments on membranes and membrane associated protein layers
Nülle, M.	Investigation of the dewetting of thin diblock copolymer films
Ostermann, A.	Dynamical properties of the hydration shell of proteins
Papadakis C.	The inner structure of thin block copolymer films
Perlich J.	Investigation of the solvent content in spin-coated thin polymer films
Pikart, Ph.	Coincident Doppler-broadening sepctroscopy on Al-Sn-layers
Pipich, V.	The diblock copolymer as an external field in A/B/A-B polymer mixtures
Radulescu, A.	Wide-Q SANS investigation of crystalline and semi-crystalline polymers in soloutions
Repper, J.	Residual stress analysis on IN718 samples
Ruderer M.	Characterisation of semi-conducting polymer blend thin films for photovoltaic applications
Sazonov, A.	Crystallographic and magnetic study of synthetic cobalt-olivine
Schirmacher W.	Theory of scattering from vibrational excitations of disordered solids
Schreckenbach, K.	Production and lifetime determination of the negatively charged Positronium ion
Smuda, Ch.	QENS und PFG-NMR-Untersuchungen zur Diffusion in Schmelzen mittelkettiger Moleküle
Stüber S.	Em levitation for time-of-flight spectroscopy - studying the dynamics of metallic melts
Visser,D.	Ancients objects investigated with neutron beams
Wang W.	Swelling of Diblock and Triblock Copolymer Thin Hydrogel Films
Wudke, J.	Erste Messungen und neue Perspektiven am Höchstfluss-Rückstreuspektrometer SPHERES
Yang F.	Hydrous silicates: structure and dynamics
Zhenyu D.	Time-resolved GISAXS on thin diblock copolymer films

7.6 PLEPS workshop and 2nd user-meeting at NEPOMUC

C. Hugenschmidt[1], **M. Hofmann**[1]
[1]ZWE FRM II, TU München
[2]Physik Department E21, TU München

In the winter term 2006/07 the neutron scattering practical training of students was started at the FRM II. Students in the 5th and 6th semester from the physics department of the TU were participating in it as part of their "Fortgeschrittenenpraktikum".

This second user meeting at NEPOMUC/FRM II has been dedicated to the pulsed low-energy positron system (PLEPS) which was transferred from the University of the Bundeswehr Munich (UniBwM) to the FRM II. The one-day workshop at October 30th, 2007 at the Technische Universität München (TUM) was organized by our positron group at E21 and FRM II together with the research group of Prof. G. Dollinger at the institute for applied physics and measurement technology of the UniBwM.

The aim of the meeting was to advertise the feasibility of positron lifetime measurements for defect spectroscopy with variable depth using the PLEPS at the high intensity positron beam NEPOMUC. A total of 32 colleagues from all over Europe (France, Belgium, Finland, Hungary,...) attended the workshop. After welcome talks of Prof. W. Petry and Prof. G. Dollinger the positron beam facility (C. Hugenschmidt) and the PLEPS-apparatus (P. Sperr, W. Egger) were presented. The following sessions consisted of 18 short oral contributions concerning proposals for positron lifetime experiments. The attendees presented a large variety of experiments on defects in metals, irradiated samples, free volume of polymers and membranes. In addition we offered an extended guided tour of FRM II with special emphasis on the PLEPS apparatus and the other positron spectrometers located at NEPOMUC. In the evening the workshop was closed at the poster session, where all experiments of the FRM II were presented, and we had a Bavarian "Brotzeit" together with the colleagues of the FRM II user meeting.

We gratefully acknowledge financial support through NMI3 of the European Community, by the Technische Universität München and the team of FRM II.

8 People

8.1 Committees

Strategierat FRM II

Chairman

Prof. Dr. Gernot Heger
Institut für Kristallographie
RWTH Aachen

Members

MRin Dr. Ulrike Kirste
Bayerisches Staatsministerium für Wissenschaft, Forschung und Kunst

Dr. Rainer Koepke
Bundesministerium für Bildung und Forschung

Prof. Dr. Georg Büldt
Institut für Biologische Informationsverarbeitung
Forschungszentrum Jülich

Prof. Dr. Dosch
Max-Planck-Institut für Metallforschung
Stuttgart

Prof. Dr. Dieter Richter
Institut für Festkörperphysik
Forschungszentrum Jülich

Prof. Dr. Dirk Schwalm
Max-Planck-Institut für Kernphysik
Heidelberg

Prof. Dr. Helmut Schwarz
Institute of Chemistry
Technische Universität Berlin

Prof. Dr. Dr. Michael Wannenmacher
Radiologische Klinik und Poliklinik
Abteilung Strahlentherapie
Universität Heidelberg

Prof. Dr. Ewald Werner
Lehrstuhl für Werkstoffkunde und -mechanik
Technische Universität München

Prof. Dr.-Ing. Heinz Voggenreiter
Director of the Institute of Structure and Design
German Aerospace Center (DLR) Köln

Prof. Dr. Markus Braden
Physikalisches Institut
Universität zu Köln

Honorary Members

MDgt i.R. Jürgen Großkreutz

Prof. Dr. Tasso Springer

Guests

Prof. Dr. Dr. h.c. mult. Wolfgang A. Herrmann
Präsident
Technische Universität München

Dr.-Ing. Rainer Kuch
Beauftragter der Hochschulleitung
Technische Universität München

Dr. Michael Klimke
Referent der Hochschulleitung
Technische Universität München

Prof. Dr. Winfried Petry
ZWE FRM II
Technische Universität München

Dr. Ingo Neuhaus
ZWE FRM II
Technische Universität München

Dr. Klaus Seebach
ZWE FRM II
Technische Universität München

Secretary

Dr. Jürgen Neuhaus
ZWE FRM II

Instrumentation advisory board (Subcommittee of the Strategierat)

Chairman

Prof. Dr. Markus Braden
Physikalisches Institut
Universität zu Köln

Members

Prof. Dr. Dirk Dubbers
Physikalisches Institut
Universität Heidelberg

Prof. Dr. Michael Gradzielski
Institut für Chemie
Technische Universität Berlin

Prof. Dr. Rainer Hock
Lehrstuhl für Kristallographie und Strukturphysik
Universität Erlangen

Prof. Dr. Werner Kuhs
GZG Abteilung Kristallographie
Universität Göttingen

Prof. Dr. Stephan Paul
Physik Department E18
Technische Universität München

Prof. Dr. Wolfgang Scherer
Lehrstuhl für Chemische Physik
Universität Augsburg

Prof. Dr. Wolfgang Schmahl
Dept. für Geo- und Umweltwissenschaften
Ludwig-Maximilians-Universität München
Deputy of the Chairman

Dr. habil. Dieter Schwahn
Institut für Festkörperforschung
Forschungszentrum Jülich

Prof. Dr. Andreas Türler
Institut für Radiochemie
Technische Universität München

Prof. Dr. Albrecht Wiedenmann
Abteilung SF3
Hahn-Meitner-Institut Berlin

Dr. habil. Regine Willumeit
GKSS Forschungszentrum Geesthacht

Guests

Dr. Michael Klimke
Referent der Hochschulleitung
Technische Universität München

Dr. Klaus Feldmann
BEO-PFR
Forschungszentrum Jülich

MRin Dr. Ulrike Kirste
Bayerisches Staatsministerium für Wissenschaft,
Forschung und Kunst

Prof. Dr. Gernot Heger
Institut für Kristallographie
RWTH Aachen

Dr. Jürgen Neuhaus
ZWE FRM II
Technische Universität München

Prof. Dr. Winfried Petry
ZWE FRM II
Technische Universität München

Dr. Klaus Seebach
ZWE FRM II
Technische Universität München

Dr. Ingo Neuhaus
ZWE FRM II
Technische Universität München

Secretary

Dr. Peter Link
ZWE FRM II

Committee for industrial and medical use (Subcommittee of the Strategierat)

Chairman
Prof. Dr.-Ing. Heinz Voggenreiter
German Aerospace Center (DLR) Köln

Members

Automobile industry
Dr.-Ing. Rainer Simon
BMW AG München

Dr.-Ing. Maik Broda
Ford Forschungszentrum Aachen

Aerospace industry
Dr.-Ing. Rainer Rauh
Airbus Deutschland Bremen

Chemistry and environment
Dr. Jens Rieger
BASF AG Ludwigshafen

Secretary
Dr. Ralph Gilles
ZWE FRM II

Scientific committee - Evaluation of beamtime proposals (Subcommittee of the Strategierat)

Chairman
Prof. Dr. Wolfgang Scherer
Lehrstuhl für Chemische Physik
Universität Augsburg

Members

Prof. Dr. John Banhart
Abteilung Werkstoffe (SF3)
Hahn-Meitner-Institut Berlin

Dr. Philippe Bourges
Laboratoire Léon Brillouin
CEA Saclay

Prof. Dr. Markus Braden
Physikalisches Institut
Universität zu Köln

Prof. Dr. Heinz-Günther Brokmeier
Institut für Werkstoffforschung
GKSS - Forschungszentrum Geesthacht

Prof. Dr. Thomas Brückel
Institut für Festkörperforschung
FZ-Jülich

Dr. Olwyn Byron
Infection and Immunity
University of Glasgow

PD Dr. Mechthild Enderle
Institut Laue Langevin
Grenoble

Dr. Hermann Heumann
Max-Planck-Institut für Biochemie
Martinsried bei München

Prof. Dr. Jan Jolie
Institute of Nuclear Physics
Universität zu Köln

Prof. Dr. Bernhard Keimer
Max-Planck-Institut für Festkörperforschung
Stuttgart

Prof. Dr. Andreas Magerl
LS für Kristallographie und Strukturphysik
Universität Erlangen

Prof. Dr. Karl Maier
Helmholtz-Institut für Strahlen- und Kernphysik
Universität Bonn

Dr. Joël Mesot
ETH Zürich und
Paul-Scherrer-Institut Villigen, Schweiz

Prof. Reinhard Dr. Krause-Rehberg
Department of Physics
Universität Halle

Dr. Stéphane Longeville
Laboratoire Léon Brillouin
Laboratoire de la Diffusion Neutronique
CEA Saclay

Prof. Dr. Andreas Meyer
Institut für Materialphysik im Weltraum
Deutsches Zentrum für Luft- und Raumfahrt (DLR)
Köln

Dr. Michael Monkenbusch
Institut für Festkörperforschung
Forschungszentrum Jülich

Prof. Dr. Werner Paulus
Structures et Propriétés de la Matière
Université de Rennes 1

Prof. Dr.-Ing. Anke Pyzalla
Max-Planck-Institut für Eisenforschung
Düsseldorf

Prof. Dr. Joachim Rädler
Fakultät für Physik
Ludwig-Maximilians-Universität München

Prof. Dr. Günther Roth
Institut für Kristallographie
RWTH Aachen

Prof. Dr. Michael Ruck
Institut für Anorganische Chemie
Technische Universität Dresden

Prof. Dr. Wolfgang Schmahl
Dep. für Geo- und Umweltwissenschaften
Ludwig-Maximilians-Universität München

Prof. Dr. Bernd Stühn
Institut für Festkörperphysik
Technische Universität Darmstadt

Prof. Dr. Monika Willert-Porada
Lehrstuhl für Werkstoffverarbeitung
Universität Bayreuth

Scientific secretaries

Dr. Jürgen Neuhaus
ZWE FRM II

Dr. Christoph Hugenschmidt
ZWE FRM II

Dr. Peter Link
ZWE FRM II

Dr. Martin Meven
ZWE FRM II

Dr. Tobias Unruh
ZWE FRM II

TUM Advisory board

Chairman

Prof. Dr. Ewald Werner
Lehrstuhl für Werkstoffkunde und -mechanik
Technische Universität München

Members

Prof. Dr. Peter Böni
Physik Department E21
Technische Universität München

Prof. Dr. Andreas Türler
Institut für Radiochemie
Technische Universität München

Prof. Dr. Markus Schwaiger
represented by Prof. Dr. Senekowitsch-Schmidtke
Nuklearmedizinische Klinik und Poliklinik
Klinikum Rechts der Isar
Technische Universität München

Prof. Dr. Bernhard Wolf
Heinz Nixdorf-Lehrstuhl für medizinische Elektronik
Technische Universität München

Prof. Dr. Arne Skerra
Lehrstuhl für Biologische Chemie
Technische Universität München

Guests

Dr. Michael Klimke
Referent der Hochschulleitung
Technische Universität München

Dr. Klaus Seebach
ZWE FRM II
Technische Universität München

Prof. Dr. Winfried Petry
ZWE FRM II
Technische Universität München

Dr. Ingo Neuhaus
ZWE FRM II
Technische Universität München

Scientific steering committee

Chairman

Prof. Dr. Winfried Petry
ZWE FRM II
Technische Universität München

Members

Dr. Hans Boysen
Sektion Kristallographie
Ludwig-Maximilians-Universität München

Prof. Dr. Bernhard Keimer
Max-Planck-Institut für Festkörperforschung Stuttgart

Prof. Dr. Dieter Richter
Jülich Centre for Neutron Science
Forschungszentrum Jülich

8.2 Staff

Board of directors of ZWE FRM II

Scientific director
Prof. Dr. W. Petry

Technical director
Dr. Ingo Neuhaus

Administrative director
Dr. K. Seebach

Experiments

Head
Prof. Dr. W. Petry

Secretaries
W. Wittowetz
E. Jörg-Müller

Coordination
Dr. J. Neuhaus
H. Türck

Instruments
Prof. Dr. H. Abele (E18)
P. Aynajian (MPI-Stuttgart)
Prof. Dr. P. Böni (E21)
J. Brunner
K. Buchner (MPI-Stuttgart)
Dr. T. Bücherl
S. Busch
H. Breitkreutz
Dr. H.-G. Brokmeier (GKSS)
E. Calzada
L. Canella (Universität zu Köln)
D. Etzdorf
J. Franke (MPI-Stuttgart)
Dr. U. Garbe (GKSS)
Dr. A.-M. Gaspar (Visiting scientist)
Dr. R. Georgii
Dr. R. Gilles
R. Hähnel
Dr. M. Haese-Seiller (GKSS)
Dr. W. Häußler
Dr. M. Hofmann
Dr. M. Hölzel (TU Darmstadt)
W. Hornauer
Dr. K. Hradil (Univ. Göttingen)
Dr. C. Hugenschmidt
Dr. V. Hutanu (RWTH Aachen)
N. Jünke
S. Kampfer
R. Kampmann (GKSS)
Dr. T. Keller (MPI-Stuttgart)
Dr. W. Klein
Dr. J. Klenke
P. Kudejova (Universität zu Köln)
Dr. V. Kudryaschov (GKSS)
Dr. P. Link
Dr. B. Loeper-Kabasakal
K. Lorenz
A. Mantwill (E21)
J. Major (MPI-Stuttgart)
Dr. M. Major (MPI-Stuttgart)
F. Maye (MPI-Stuttgart)
T. Mehaddene
Dr. M. Meven
Dr. R. Mole
Dr. P. Moulin (GKSS)
S. Mühlbauer
Dr. A. Ostermann
Dr. B. Pedersen
Ph. Pikart
C. Piochacz
Dr. J. Rebelo-Kornmeier (HMI Berlin)
J. Repper
R. Repper
J. Ringe
Dr. A. Rühm (MPI Stuttgart)
Ch. Sauer
A. Sazonov
Dr. B. Schillinger
Dr. A. Schneidewind (TU Dresden)
Prof. Dr. K. Schreckenbach (E21)
M. Schulz
R. Schwikowski
Dr. A. Senyshyn (TU Darmstadt)
G. Seidl
C. Smuda
M. Stadlbauer
Dr. R. Stöpler (E18)
B. Straßer
Dr. T. Unruh
F. M. Wagner
Dr. R. Wimpory (HMI Berlin)
Dr. H.-F. Wirth
Prof. Dr. O. Zimmer (E18)

Instruments - JCNS
Prof. Dr. Dieter Richter (Director JCNS)
Prof. Dr. Thomas Brückel (Director JCNS)
Dr. A. Ioffe (Head of outstation at FRM II)

Secretary
S. Mintmans

N. Arend
Dr. P. Busch
A. Erven
Dr. H. Frielinghaus
F. Gossen
Dr. Th. Gutberlet
Dr. O. Holderer
M. Hölzle
E. Kentzinger
Th. Kohnke
Dr. Mattauch
Dr. R. Mittal
A. Nebel
Dr. M. Prager
Dr. V. Pipich
Dr. A. Radelescu
H. Schneider
P. Stronciwilk
Dr. Y. Su
Dr. J. Wuttke

Detectors and electronics
Dr. K. Zeitelhack
I. Defendi
Chr. Hesse
M. Panradl
Th. Schöffel

Sample environment
Dr. J. Peters
P. Biber
H. Kolb
A. Pscheidt
A. Schmidt
J. Wenzlaff

Neutron optics
Prof. Dr. G. Borchert
C. Breunig
H. Hofmann
R. Iannucci
E. Kahle
O. Lykhvar
Dr. S. Masalovich
A. Ofner
R. Valicu

IT services
J. Krüger
H. Wenninger
J. Ertl
S. Galinski
F. Hänsel
J.-P. Innocente
N. Ivanova
R. Müller
A. Preller
J. Pulz
C. Rajczak
S. Roth
A. Schwertner
A. Steinberger
M. Stowasser
B. Wildmoser
A. Wimmer

Construction
K. Lichtenstein

Administration

Head
Dr. K. Seebach

Secretary
C. Zeller

Members
R. Obermeier
B. Bendak
B. Gallenberger
I. Heinath
K. Lüttig

Public relations
Dr. Ulrich Marsch(ZV TUM)
A. Schaumlöffel(ZV TUM)

Visitors service
U. Kurz
Dr. B. Tonin-Schebesta

Reactor operation

Head
Dr. Ingo Neuhaus

Secretaries
M. Neuberger
S. Rubsch

Management
Dr. H. Gerstenberg
(Irradiation and fuel cycles)
Dr. J. Meier
(Reactor operation)
R. Schätzlein
(Electric and control technology)
Dr. A. Kastenmüller
(Reactor enhancement)

Shift members
F. Gründer
A. Bancsov
A. Benke
M. Danner
Chr. Feil
M. Flieher
H. Groß
L. Herdam
F. Hofstetter
K. Höglauer
T. Kalk
G. Kaltenegger
U. Kappenberg
F. Kewitz
M. G. Krümpelmann
J. Kund
A. Lochinger
G. Mauermann
A. Meilinger
M. Moser
L. Rottenkolber
G. Schlittenbauer

Technical services
K. Pfaff
R. Binsch
A. Cziasto
H. Gampfer
W. Glashauser
G. Guld
S. Manz
B. Heck
G. Wagner
A. Weber
M. Wöhner
C. Ziller
J. Zöybek

Sources
C. Müller
D. Päthe
A. Wirtz

Electric and control technology
R. Schätzlein
G. Aigner
W. Buchner
R. Krammer
K.-H. Mayr
Ü. Sarikaya
H. Schwaighofer
J. Wildgruber

Job safety
H. Bamberger

Irradiation
Dr. H. Gerstenberg
J.-M. Favoli
W. Fries
Dr. X. Li
M. Oberndorfer
W. Lange
V. Loder
J. Molch
A. Richter
H. Schulz
F.-M. Wagner
N. Wiegner

Reactor enhancement
W. Bünten
F. Henkel
R. Lorenz
B. Pollom
M. Schmitt
V. Zill

Technical design
F.-L. Tralmer
J. Fink
H. Fußstetter
J. Jüttner
S. Küçük
K. Lichtenstein

Workshops
C. Herzog
U. Stiegel
A. Begic
M. Fuß
A. Huber
A. Scharl
R. Schlecht

Radiation protection
Dr. H. Zeising
Dr. B. Wierczinski
S. Dambeck
W. Dollrieß
H. Hottmann
D. Lewin
B. Neugebauer
D. Schrulle
H.-J. Werth
S. Wolff
D. Bahmet
W. Kluge
A. Schindler
D. Strobl

Chemical laboratory
C. Auer
R. Bertsch
P. Müller
S. Uhlmann

Technical safety service
J. Wetzl
R. Maier
J. Aigner
K. Otto
N. Hodzic
J. Schreiner

Reactor physics

Dr. A. Röhrmoser
C. Bogenberger
R.M. Hengstler
R. Jungwirth
W. Schmid

Security department

L. Stienen
J. Stephani

8.3 Partner institutions

GKSS Research Centre GmbH
Max-Planck-Straße 1
21502 Geesthacht
Germany
http://www.gkss.de/index_e.html

Hahn-Meitner-Institute GmbH (HMI)
Glienickerstraße 100
14109 Berlin
Germany
http://www.hmi.de/index_en.html

Jülich Centre for Neutron Science JCNS
Research Centre Jülich GmbH
52425 Jülich, Germany
Outstation at FRM II: 85747 Garching
http://www.jcns.info

Ludwig-Maximilians-Universität München
Sektion Kristallographie (Prof. Schmahl)
and Sektion Physik (Prof. Rädler)
Geschwister-Scholl-Platz 1
80539 Munich
Germany
http://www.uni-muenchen.de

Max-Planck-Institut für Festkörperphysik
Heisenbergstraße 1
70569 Stuttgart
Germany
www.fkf.mpg.de/main.html

Max-Planck-Institut für Metallforschung
Heisenbergstraße 3
70569 Stuttgart
Germany
http://www.mf.mpg.de/de/index.html

RWTH Aachen
Institute of Crystallography
Jägerstraße 17 - 19
52056 Aachen
Germany
http://www.xtal.rwth-aachen.de/index_e.html

Technische Universität Darmstadt
Material- und Geowissenschaften
Petersenstraße 23
64287 Darmstadt
Germany
http://www.tu-darmstadt.de/fb/matgeo/

Technische Universität Dresden
Institut für Festkörperphysik
01062 Dresden
Germany
http://www.physik.tu-dresden.de/ifp/ifp.php

Universität Augsburg
Institut für Physik
Lehrstuhl für Chemische Physik und Materialwissenschaften
86135 Augsburg
Germany
http://physik.uni-augsburg.de/exp3/home.html

Universität der Bundeswehr München
Institut Angewandte Physik und Messtechnik
Werner-Heisenberg-Weg 39
85579 Neubiberg
Germany
http://www.unibw.de/lrt2/

Universität Göttingen
Institut für Physikalische Chemie
Tammannstraße 6
37077 Göttingen
Germany
http://www.uni-pc.gwdg.de/eckold/home.html

Universität zu Köln
Institut für Kernphysik
Zülpicherstraße 77
50937 Köln
Germany
http://www.ipk.uni-koeln.de/

9 Figures

9.1 FRM II in the Press

Lange Nacht der Wissenschaften

Tausende neugierig auf die Welt der Technik

23 Einrichtungen am Forschungscampus Garching stellen neueste Forschungsergebnisse vor

[Süddt. Zeitung, 2007-10-15]

Besucherandrang wie noch nie

[Münchner Merkur, 2007-10-15]

Aus dem Garchinger Ei wird ein bedeutendes Forschungsgelände

Erste atomare Kettenreaktion vor 50 Jahren

Universität präsentiert umfangreiches Festprogramm zum Jubiläum / Reaktorgegner kündigen Protestaktionen an

[Süddt. Zeitung, 2007-10-01]

Year of construction: 1957 –
a tractor by Escher Wyss AG on the parking site of the FRM II. Unlike the „Atom-Ei" it is still running...

Forschungszentrum Garching feiert 50-jähriges Bestehen

Mit einem Festakt ist am Mittwochabend das 50-jährige Bestehen des Forschungszentrums Garching gefeiert worden.

[http://www.heise.de/newsticker/meldung/96611]

Ost-Gebäude eingeweiht
Jülich Centre of Neutron Science am FRM II

http://www.stadtspiegel-online.de/archiv/2007/06/0706_Ost_Gebaeude.htm

„Irgendwer drückt immer an den Knöpfen rum"

[Süddt. Zeitung, 2007-10-01]

Blick in laufende Motoren
Die neuen Augen der Welt

Im Forschungsreaktor der Technischen Universität München werfen Forscher einen Blick in das Innere eines Ottomotors – bei laufendem Betrieb.

[http://www.3sat.de/hitec/magazin/104271/index.html]

9.2 Publications

[1] Appavou M.-S., Busch S., Doster W., Unruh T. *The Effect of Packing in Internal Molecular Motions of Hydrated Myoglobin*. *MRS Bulletin - Proceedings of the 8th International Conference on Quasi-Elastic Neutron Scattering (QENS2006) held June 14 -17, 2006, Bloomington, Indiana, USA*, **–**, (2007), 83 – 88.

[2] Aynajian P., Keller T., Boeri L., Shapiro S., Habicht K., Keimer B. *Energy Gaps and Kohn Anomalies in Elemental Superconductors*. *Science*, **319**, (2008), 1509 – 1512.

[3] Babcock E., Petoukhov A., Andersen K., Chastagnier J., Jullien D., Lelièvre-Berna E., Georgii R., Masalovich S., Boag S., Frost C., Parnell S. *AFP flipper devices: Polarized 3He spin flipper and shorter wavelength neutron flipper; Proceedings of PCMI 2006, Berlin, Germany*. *Physica B*, EU-publication, **397**, (2007), 172 – 175.

[4] Balsanova L., Mikhailova D., Senyshyn A., Trots D., Ehrenberg H. *Structure and properties of* $\alpha - AgFe_2(MoO_4)_3$. *Sol. State Sciences*, submitted.

[5] Bouwman W., Plomp J., de Haan V., Kraan W., van Well A., Habicht K., Keller T., Rekveldt M. *Real-space scattering methods*. *Nuclear Instruments and Methods A*, **586**, (2008), 9–14.

[6] Boysen H., Lerch M., Stys A., Senyshyn A., Hoelzel M. *Oxygen mobility in the ionic conductor mayenite* $(Ca_{12}Al_{14}O_{33}$*: a high temperature neutron diffraction study*. *Acta Cryst. B.*, **63**, (2007), 675 – 683.

[7] Breitkreutz H., Wagner F., Petry W. *Spektrale Charakterisierung des Spaltneutronenstrahls der Neutronentherapieanlage MEDAPP am FRM II*. *Conference Proceedings of the Three-Country-Convention of the German, Austrian and Swiss Societies of Medial Physics, Bern, Switzerland, 2007*, **–**, (2007), 2.

[8] Brunner T., Hugenschmidt C. *Spectrometer for the investigation of temperature dependant Ps formation and material dependent moderation efficiency*. *Physica status solidi C*, **4**, (2007), 3989–3992.

[9] Bunjes H., Unruh T. *Characterization of Lipid Nanoparticles by Differential Scanning Calorimetry, X- Ray and Neutron Scattering*. *Advanced Drug Delivery Reviews*, **59**, (2007), 379 – 402.

[10] Busch S., Doster W., Longeville S., Sakai V., Unruh T. *Microscopic Protein Diffusion at High Concentration*. *MRS Bulletin - Proceedings of the 8th International Conference on Quasi-Elastic Neutron Scattering (QENS2006) held June 14 -17, 2006, Bloomington, Indiana, USA*, **–**, (2007), 107 – 114.

[11] Böni P. *New concepts for neutron instrumentation*. *Nuclear Instruments and Methods A*, **586**, (2008), 1–8.

[12] Böning K., Petry W. *Test Irradiations of Full Sized* $U_3Si_2 - Al$ *Fuel Plates up to Very High Fission Densities*. *Journal of Nuclear Science*, submitted.

[13] Dittrich W., Zeising H. *Radio Protection Design of the FRM II*. *Transactions of the RRFM - IGORR 2007, Lyon, France, March 5 - 11, 2007*, **–**, (2007), 299–303.

[14] Dubbers D., Abele H., Baeßler S., Märkisch B., Schumann M., Soldner T., Zimmer O. *A clean, bright, and versatile source of neutron decay products*. *Nuclear Instruments and Methods in Physics Research*. `http://arxiv.org/abs/0709.4440`.

[15] Eichhöfer A., Wood P., Viswanath R., Mole R. *Synthesis, Structure and Magnetic Behaviour of Manganese(II) Selenolate Complexes* $^1_\infty[Mn(SePh)_2], [Mn(SePh)2(bipy)_2] and [Mn(SePh)_2(phen)_2](bipy = bipyridyl, phen = phenanthroline)$. *Eur. J. Inorg. Chem.*, **2007, 30**, (2007), 4794–4799.

[16] Eichhöfer A., Wood P., Viswanath R. N., Mole R. A. *Synthesis, structure and physical properties of the manganese(II) selenide/selenolate cluster complexes [Mn32Se14(SePh)36(PnPr3)4] and [Na(benzene-15-crown-5)(C4H8O)2]2[Mn8Se(SePh)16]*. *Chemical Communications*, accepted.

[17] Eichhöfer A., Wood P. T., Viswanath R., Mole R. A. *Synthesis, structure and physical properties of the manganese (II) selenide/selenolate cluster complexes* $[Mn_{32}Se_{14}(SePh)_{36}(PnPr_3)_4]$ *and* $[Na(benzene-15-crown-5)(C_4H_8O)_2]_2[Mn_8Se(SePh)_{16}]$. *Chemical Communications*, **–**, (2008), 1596 – 1598.

[18] Fleischer F., Gwinner G., Hugenschmidt C., Schreckenbach K., Thirolf P., Wolf A., Schwalm D. *The negative ion of positronium: measurement of the decay rate and prospects for further experiments*. *Canadian Journal of Physics*, submitted.

[19] Frotscher M., Klein W., Bauer J., C.-M. F., Halet J.-F., Senyshyn A., Baehtz C., Alberta B. *M2B5 or M2B4? A Reinvestigation of the Mo/B and W/B System*. *Z. Anorg. Allg. Chem.*, **633**, (2007), 2626 – 2630.

[20] Gaspar A. *Methods for analytically estimating the resolution and intensity of neutron time-of-flight spectrometers. The case of the TOFTOF spectrometer. Electronic publication at www.arxiv.org*. `http://arxiv.org/abs/0710.5319`.

[21] Gaspar A., Appavou M.-S., Busch S., Unruh T., Doster W. *Dynamics of well-folded and natively disordered proteins in solution: a time of flight neutron scattering study*. *Eur. Biophys. J.*, published online. `http://dx.doi.org/10.1007/s00249-008-0266-3`.

[22] Georgii R., Arend N., Böni P., Lamago D., Mühlbauer S., Pfleiderer C. *MIRA: Very Cold Neutrons for New Methods*. *Neutron News*, **18, 2**, (2007), 25 – 28.

[23] Georgii R., Böni P., Janoschek M., Schanzer C., Valloppilly S. *MIRA - A flexible instrument for VCN*. *Physica B*, **397**, (2007), 150–152.

[24] Gilles R., Ostermann A., Petry W. *Monte Carlo simulations of the new Small-Angle Neutron Scattering instrument SANS-1 at the Heinz Maier-Leibnitz Forschungsneutronenquelle*. *J. Appl. Cryst.*, **40**, (2007), s428 – s432.

[25] Grünzweig C., Hils R., Mühlbauer S., Ay M., Lorenz K., Georgii R., Gähler R., Böni P. *Multiple Small Angle Neutron Scattering (MSANS): A new Two-dimensional Ultra Small Angle Neutron Scattering Technique*. *Appl. Phys. Lett.*, **91**, (2007), 203504–1–3.

[26] Hoelzel M., Senyshyn A., Gilles R., Boysen H., Fuess H. *The Structure Powder Diffractometer*. *Neutron News*, **18:4**, (2007), 23 – 26.

[27] Hofmann A., Rebelo-Kornmeier J., Garbe U., Wimpory R., Repper J., Seidl G., Brokmeier H., Schneider R. *Stress Spec: Advanced Materials Science at the FRM II*. *Neutron News*, **18:4**, (2007), 27 – 30.

[28] Hugenschmidt C. *NEPOMUC: The New Positron Beam Facility at the FRM II*. *Neutron News*, **18, 2**, (2007), 29 – 31.

[29] Hugenschmidt C., Brunner T., Legl S., Mayer J., Piochacz C., Stadlbauer M., Schreckenbach K. *Positron experiments at the new positron beam facility NEPOMUC at FRM II*. *Physica status solidi C*, **4**, (2007), 3947 – 3952.

[30] Hugenschmidt C., Dollinger G., Egger W., Kögel G., Löwe B., Mayer J., Pikart C., P. Piochacz, Repper R., Schreckenbach K., Sperr P., Stadlbauer M. *Surface and Bulk Investigations at the High Intensity Positron Beam Facility NEPOMUC*. *Applied Surface Science*, in press.

[31] Hugenschmidt C., Mayer J., Schreckenbach K. *Surface investigation of Si (100), Cu, Cu on Si (100), and Au on Cu with positron annihilation induced Auger-electron spectroscopy*. *Surface Science*, **601**, (2007), 2459–2466.

[32] Hugenschmidt C., Mayer J., Stadlbauer M. *Investigation of the near surface region of chemically treated and Al-coated PMMA by Doppler-broadening spectroscopy*. *Radiat. Phys. Chem.*, **76**, (2007), 217–219.

[33] Hugenschmidt C., Pikart P., Stadlbauer M., Schreckenbach K. *High elemental selectivity to Sn submonolayers embedded in Al using positron annihilation spectroscopy*. *Phys. Rev. B*, in press, 4.

[34] Hugenschmidt C., T. B., Mayer J., Piochacz C., Schreckenbach K., Stadbauer M. *Determination of Positron Beam Parameters by Various Diagnostic Techniques*. *Applied Surface Science*, in press.

[35] Hutanu A., Masalovich S., Meven M., Lykvar O., Borchert G., Heger G. *Polarized 3HeSpin Filters for Hot Neutrons at the FRM II*. *Neutron News*, **18:4**, (2007), 14 – 16.

[36] Hutanu V., Meven M., Heger G. *Construction of the New Polarised Hot Neutrons Single Crystal Diffractometer POLI-HEiDi at FRM-II (Proceedings of PNCMI 2006, Berlin, Germany)*. *Physica B*, **397, 1-2**, (2007), 135–137.

[37] Hutanu V., Rupp A., Klenke J., Heil W., Schmiedeskamp J. *Magnetization of 3He spin filter cells*. *Journal of Physics D: Applied Physics*, **40**, (2007), 4405–4412.

[38] Hutanu V., Rupp A., Sander-Thömmes T. *SQUID measurements of remanent magnetisation in refillable 3He spin-filtre celles (SFC)*. *Physica B*, **397**, (2007), 185–187.

[39] Häußler W., Gohla-Neudecker B., Schwikowski R., Streibl D., Böni P. *RESEDA - the new Resonance Spin Echo Spectrometer using cold neutrons at the FRM II*. *Physica B*, **397**, (2007), 112 – 114.

[40] Häußler W., Schwikowski R., Streibl D., Böni P. *The Resonance Spin Echo Spectrometer RESEDA at the FRM II*. *Neutron News*, **18:4**, (2007), 17 – 19.

[41] Häußler W., Streibl D., P. B. *RESEDA: Double and Multi Detector Arms for Neutron Resonance Spin Echo Spectrometers*. *Measurement Science and Technology - Proceedings ECNS 2007*, submitted.

[42] Ioffe A. *A new neutron spin-echo technique with time gradient magnetic fields*. *Nuclear Instruments and Methods A*, **586**, (2008), 31–35.

[43] Ioffe A., Bodnarchuk V., Bussmann K., Müller R., Georgii R. *A new neutron spin-echo spectrometer with time-gradient magnetic fields: First experimental test*. *Nuclear Instruments and Methods in Physics Research A*, **586**, (2008), 36–40.

[44] Ioffe A., Bodnarchuk V., Bussmann K., Mueller R. *Larmor labeling by time-gradient magnetic fields*. *Physica B Condensed Matter*, **397, 108-111**, (2007), 54–55.

[45] Janoschek M., Klimko S., Gähler R., Roessli B., Böni P. *Spherical neutron polarimetry wiht MuPAD*. *Physica B*, **397**, (2007), 125 – 130.

[46] Jarousse C., Lemoine P., Boulcourt P., Röhrmoser A., Petry W. *Monolithic UMO Full Size Prototype Plates for IRIS V Irradiation*. *Proceedings of IGORR - RRFM 2007, March 11 - 15, 2007, Lyon, France*, submitted.

[47] Jungwirth R., Petry W., Schmid W., Beck L., Bergmaier A. *Progress in Heavy-Ion Bombardement of U-Mo/Al Dispersion Fuel*. *Transactions of the RRFM 2008, Hamburg, Germany, March 2008*, **–**, (2008), 5.

[48] Jungwirth R., Wieschalla N., Schmid W., Röhrmoser A., Petry W., Pfleiderer C. *Thermal Conductivity of Heavy-Ion-Bombarded U-Mo/AL Dispersion Fuel*. *Proceedings on the 11th International Topical Meeting in Research Fuel Management (RRFM) 2007, Lyon*, **–**, (2007), 7.

[49] Kampfer S., Wagner F., Loeper B., Kneschaurek P. *MEDAPP: Die neue Neutronentherapieanlage am FRM II in Garching*. *Strahlentherapie, Onkologie*, **Sondernummer 1**, (2007), 72.

[50] Kashem M. A., Perlich J., Schulz L., Roth S., Petry W., Müller-Buschbaum P. *Maghemite nanoparticles on supported diblock polymer nanostructures*. *Macromolecules*, **40**, (2007), 5075–5083.

[51] Keller T., Aynajian P., Bayrakci S., Bucher K., Habicht K., Klann H., Ohl M., Keimer B. *The Triple Axis-Spin-Echo Spectrometer TRISP at the FRM II*. *Neutron News*, **18, 2**, (2007), 16 –18.

[52] Kudejova P., Cizek J., Schulze R., Jolie J., Schillinger B., Lorenz K., Mühlbauer M., Masschaele B., Dierick M., Vlassenbroeck J. *A marker-free 3D image registration for the ANCIENT CHARM project. Case study with neutron and X-ray tomography datasets*. *Notiziario, Neutroni e Luce di Sincrotrone*, **12/2**, (2007), 6 – 13.

[53] Köper I., Comet S., Petry W., Bellissent-Funel M.-C. *Dynamics of C-Phycocynanin in various deuterated Threhalose/Water Environments by Quasielastic and Elastic Neutron Scattering*. *European Biophysical Journal*, published online, 10.

[54] Legl S., Hugenschmidt C. *A Novel Time-of-flight Spectrometer for PAES*. *Physica status solidi C*, **4**, (2007), 3981 – 3984.

[55] Lerch M., Boysen H., Rödel T., Kaiser-Bischoff I., Hoelzel M., Senyshyn A. *High temperature neutron powder diffraction study of scandia/nitrogen co-doped zirconia*. *Z. Kristallogr.*, **222**, (2007), 335 – 340.

[56] Magaddino V., Wagner F. M., Kummermehr J. *Preclinical screening of the biological effectiveness of a therapeutic neutron beam at the FRM-II*. *Proceedings of the 16h symposium "Experimentelle Strahlentherapie und Klinische Strahlenbiologie", Dresden, March 01-03, 2007 (ISSN 1432-864X)*, **–**, (2007), 129 – 131.

[57] Martinez Meta N., Schweda E., Boysen H., Haug A., T. C., Hoelzel M. $Zr_{50}Sc_{12}O_{43}N_{50}$ *and* $Zr_3Sc_4O_{43}N_8$ *- Synthesis, Neutron Powder Diffraction and Raman Spectroscopy*. *Z. Anorg. Allg. Chem.*, **633**, (2007), 790 – 794.

[58] Masalovich S. *Method to measure neutron beam polarization with 2 x 1 Neutron Spin Filter*. *Nuclear Instruments and Methods in Physics Research A*, **581**, (2007), 791–798.

[59] Mayer J., Hugenschmidt C., Schreckenbach K. *Study of the surface contamination of copper with the improved Positron annihilation induced auger electron spectrometer at NEPOMUC*. *Applied Surface Science*, in press.

[60] Mayer J., Hugenschmidt C., Schreckenbach K. *Positron annihilation induced Auger electron spectroscopy of Cu and Si*. *Physica status solidi C*, **4**, (2007), 3928–3931.

[61] Meven M., Hutanu V., Heger G. *HEiDi: Single Crystal Diffractometer at the Hot Source of the FRM II*. *Neutron News*, **18, 2**, (2007), 19 – 21.

[62] Meyer A., Stüber S., Holland-Moritz D., Heinen O., Unruh T. *Determination of self-diffusion coefficients by quasielastic neutron scattering measurements on levitated Ni droplets*. *Phys. Rev. B.*, **77**, (2008), 092201–1–4.

[63] Mukherji D., Del Genovese D., Strunz P., Gilles R., Wiedenmann A., Rösler J. *Microstructural characterisation of a Ni-Fe-based superalloy by in-situ SANS measurements*. *J. Phys. Condens. Matter*, **20**, (2008), 104220–104228.

[64] Mühlbauer S., Böni P., Georgii R., Schmehl A., Schlohm D., Mannhart J. *Field and temperature dependence of the magnetisation in the ferromagnetic EuO thin films*. *J. Phys. Condens. Matter*, **20**, (2008), 4 pp.

[65] Mühlbauer S., Niklowitz P., Stadlbauer M., Georgii R., Link P., Stahn J., Böni P. *Elliptic neutron guides - focusing on tiny samples; Proceedings "European Workshop on Neutron Optics", March 5 -7, 2007, Paul-Scherer-Institute, Villingen, Switzerland. Nuclear Instruments and Methods in Physics Research A*, **586**, (2008), 77 – 80.

[66] Müller-Buschbaum P., Ittner T., Mauerer E., Körstgens V., Petry W. *Pressure-Sensitive Adhesive Blend Films for Low-Tack Applications*. *Macromol. Mater. Eng.*, **292**, (2007), 825–834.

[67] Neuhaus J., Petry W. *Forschungsneutronenquelle Heinz Maier-Leibnitz (FRM II)*. *Neutron News*, **18, 2**, (2007), 13 – 15.

[68] Park S., Senyshyn A., Paulmann C. *Increase of ionic conductivity in the microporous lithosilicate RUB-29 by Na-ion exchange processes*. *Journal of Solid State Chemistry*, **180, 12**, (2007), 3366 – 3380.

[69] Park S.-H., Hoelzel M., Boysen H., Schmidbauer E. *Lithium conductivity in a Li-bearing ring-silicate mineral, sogdianite*. *J.Sol. State Chem.*, **180**, (2007), 1306 – 1317.

[70] Pedersen B., Frey F., Scherer W. *The Single Crystal Diffractometer RESI*. *Neutron News*, **18:4**, (2007), 20 – 22.

[71] Peters L., Knorr K., Evan J. S., Senyshyn A., Rahmoun N.-S., Depmeier W. *Proton positions in and thermal behaviour of the phase* $CaO*3AL_2O_3*3H_2O$ *and its thermal decomposition to* $<|(OCa_4)_2|[Al_{12}O_{24}]-SOD$*, determined by neutron/X-ray powder diffraction and IR spectroscopic investigations*. *Z. Kristallogr.*, **222**, (2007), 365–375.

[72] Petry W., Neuhaus J. *Neutronen nach Maß*. *Physik-Journal*, **6/7**, (2007), 31–37.

[73] Pfleiderer C., Böni P., Keller U., T. Rößler, Rosch A. *Non-Fermi liquid metal without quantum criticality*. *Science*, **316**, (2007), 1871 – 1874.

[74] Piochacz C., Egger W., Hugenschmidt C., Kögel G., Schreckenbach K., Sperr P., Dollinger G. *Implementation of the Munich scanning positron microscope at the positron soucre NEPOMUC*. *Physica status solidi C*, **4**, (2007), 4028–4031.

[75] Prager M., Desmedt A., Unruh J., T. und Allgaier. *Dynamics and adsorption sites for guest molecules in methyl chloride hydrate*. *J. Phys. Condens. Matter*, **20**, (2008), 125219 – 6 pp.

[76] Prager M., Grimm H., Natkaniec I., Nowak D., Unruh T. *The dimensionality of ammonium reorientation in* $(NH_4)_2S_2O_8$*: the view from neutron spectroscopy*. *J. Phys. Condens. Matter*, **20**, (2008), 125218+11.

[77] Prager M., Pawlukojc A., Wischnewski A., Wuttke J. *Inelastic neutron scattering study of methyl group rotation in some methylxanthines. J. Chem. Phys.*, **127**, (2007), 214509.

[78] Ranjan R., Senyshyn A., Frey F., Boysen H. *Crystal structure of $Na_{1/2}Ln_{1/2}TiO_3\,(Ln:La,Eu,Tb)$*. *J. Sol. State Chem.*, **180 (3)**, (2007), 995–1001.

[79] Ranjan R., Senyshyn A., Vashook V., Niewa R., Boysen H., Frey F. *Structural stability of conducting oxide $CaRuO_3$ at high temperatures*. *Appl. Phys. Lett.*, **80**, (2007), 251913.

[80] Rebelo Kornmeier J., Hofmann M., Schmidt S. *Non-destructive testing of satellite nozzles made of carbon fibre ceramic matrix composite, C/SiC*. *Materials Characterization*, **58**, (2007), 922 – 927.

[81] Repper J., Hofmann M., Krempaszky C., Petry W., Werner E. *Influence of microstructural parameters in macroscopic residual stress analysis of complex materials by neutron diffraction*. *Proceedings of Meca-SENS, Vienna, 24 - 26 September 2007*, **–**, (2007), 6.

[82] Röhrmoser A., Petry W., Boulcourt P., Chabre A., Dubois S., Lemoine P., Jarousse C., Falgoux J. *Status of UMo full size plates irradiation program IRIS-TUM*. *Proceedings of the RRFM - IGORR 2007, March 11 - 15, 2007, Lyon*, **–**, (2007), 8.

[83] Röhrmoser A., Petry W., Boulcourt P., Chabre A., Dubois S., Lemoine P., Jarousse C., Falgoux J., van den Berghe S., Leenaers A. *UMo full plate size irradiation experiment IRIS - TUM - a progress report*. *Transactions of the RRFM 2008, Hamburg, Germany, March 2008*, **–**, (2008), 11.

[84] Schmehl A., Vaithyanathan V., Herrnberger A., Thiel S., Richter C., Liberati M., Heeg T., Röckerath M., Fitting Kourkoutis L., Mühlbauer S., Böni P., Müller D. A., Barash Y., Schubert J., Idzerda Y., Mannhart D. G., Jochen und Schlom. *Epitaxial integration of the highly spin-polarized ferromagnetic semiconductor EuO with silicon and GaN*. *Nature Materials*, **6**, (2007), 882 – 887.

[85] Schmid W., Jungwirth R., Petry W., Böni P., Beck L. *Manufacturing of Thick Monolithic Layers by DC-Magnetron Sputtering*. *Transactions of the RRFM 2008, Hamburg, Germany, March 2008*, **–**, (2008), 4.

[86] Schneidewind A., Link P., Etzdorf D., Stockert O., Loewenhaupt M. *PANDA: The Cold Three-Axis Spectrometer at FRM II*. *Neutron News*, **18:4**, (2007), 9–13.

[87] Senff D., Link P., Aliouane N., Argyriou D., Braden M. *Magnetic memory effect and Field dependence of magnetic excitations iin multiferroic $TbMnO_3$: a neutron scattering study*. *PR B: Rapid Communications*, accepted.

[88] Senff D., Link P., Hradil K., Hiess A., Regnault L., Sidis Y., Aliouan N., Argyriou D., Braden M. *Magnetic Excitations in Multiferroic $TbMnO_3$: Evidence for a Hybridized Soft Mode*. *Phys. Rev. Lett.*, **98**, (2007), 137206–1–4.

[89] Smirnov G., van Bürck U., Arthur J., Brown G. S., Chumakov A., Baron A., Petry W., Ruby S. *Currents and fields reveal the propagation of nuclear polaritons through a resonant target*. *Phys. Rev. A*, **76**, (2007), 043811.

[90] Smuda C., Busch S., Gemmecker G., Unruh T. *Self-diffusion in molecular liquids: medium-chain $n-$alkanes and coenzyme Q_{10} studied by Quens*. *J. Chem. Phys.*, submitted.

[91] Smuda C., Gemmecker G., Unruh T. *Quasi-elastic an inelastic neutron scattering study of methyl group rotation in solid and liquid pentafluoroanisole and pentafluorotoluene*. *J. Chem. Phys.*, in print.

[92] Stadlbauer M., Hugenschmidt C., Schreckenbach K. *New design of CDB-spectrometer at NEPOMUC for T-dependent defect spectroscopy in Mg*. *Applied Surface Science*, in press.

[93] Stadlbauer M., Hugenschmidt C., Schreckenbach K. *Characterization of the chemical vicinity of open volume defects in magnesium and AZ 31 with coincident Doppler broadening spectroscopy*. *Physica status solidi C*, **4**, (2007), 3489–3492.

[94] Stadlbauer M., Hugenschmidt C., Schreckenbach K., Böni B. *Investigation of the chemical vicinity of crystal defects in ion-irradiated Mg and a Mg-Al-Zn alloy with coincident Doppler broadening spectroscopy*. *Phys. Rev. B*, **76**, (2007), 174104.

[95] Stampanoni M., Groso A., Borchert G., Abela R. *Bragg Magnifier: High Efficiency, High Resolution X-Ray Detector*. *Proc. Syn. Rad. Instr.; Ninth International Conference*, **CP 879**, (2007), 1168 – 1171.

[96] Steffens P., Sidis Y., Link P., Schmalzl K., Nakatsuji S., Maeono Y., Braden M. *Field-induced paramagnons at the metamagnetic transitions in* $Ca_{1.8}Sr_{0.2}RuO_4$. *Phys. Rev. Lett.*, **99**, (2007), 217402–1–4.

[97] Stockert O., Arndt J., Schneidewind A., Schneider H., Jeevan H., Geibel C., Steglich F., Loewenhaupt M. *Magnetism and superconductivity in the heavy-fermion compound CeCu2Si2 studied by neutron scattering*. *Physica B Condensed Matter*, **403, 5-9**, (2008), 973–976.

[98] Strunz P., Mukherji D., Pigozzi G., Gilles R., Geue T., Pranzas K. *Characterization of core-shell nanoparticles by Small Angle Neutron Scattering*. *Appl. Phys. A*, **88**, (2007), 277.

[99] Strunz P., Mukherji D., Rösler J., Gilles R., Näth O., Haug J., Wiedenmann A. *In-situ SANS investigation of solution treatment of single crystal Ni-base superalloys containing rhenium*. *tbc*, submitted.

[100] Teixeira S., Ankner J., Bellissent-Funel M., Bewley R., Blakeley M., Coates L., Dahint R., Dalgliesh R., Dencher N., Dhont J., Fischer P., Forsyth V., Fragneto G., Frick B., Geue T., Gilles R., Gutberlet T., Haertlein M., Hauß T., Häußler W., Heller W., Herwig K., Holderer O., Juranyi F., Kampmann R., Knott R., Kohlbrecher J., Kreuger S., Langan P., Lechner R., Lynn G., Majkrzak C., May R., Meilleur F., Mo Y., Mortensen K., Myles D., Natali F., Neylon C., Niimura N., Ollivier J., Ostermann A., Peters J., Pieper J., Rühm A., Schwahn D., Shibata K., Soper A., Straessle T., Suzuki U.-I., Tanakai I., Tehei M., Timmins P., Torikai N., Unruh T., Urban V., Varvrin R., Weiss K., Zaccai G. *New Sources and Instrumentation for Neutrons Biology*. *Chemical Physics*, **345**, (2008), 133–151.

[101] Trots D., Senshyn A., Mikhailova D., Knapp M., Hoelzel M., Fuess H., Hofmann M. *High-temperature thermal expansion and structural behaviour of stromeyerite, AgCuS*. *J. Phys. Condens. Matter*, **19**, (2007), 136204.

[102] Unruh T. *Interpretation of small-angle X-rax scattering patterns of crystalline triglyceride nanoparticles in dispersion*. *J. Appl. Cryst.*, **40**, (2007), 1008 – 1018.

[103] Unruh T., Meyer A., Neuhaus J., Petry W. *The Time-of-flight Spectrometer TOFTOF*. *Neutron News*, **18, 2**, (2007), 22 – 24.

[104] Unruh T., Neuhaus J., Petry W. *The high-resolution time-of-flight spectrometer TOFTOF*. *Nuclear Instruments and Methods in Physics Research A*, **580**, (2007), 1414–1422 & erratum 585 (2008) 201.

[105] Unruh T., Smuda C., Gemmecker G., Bunjes H. *Molecular Dynamics in Pharmaceutical Drug Delivery Systems - The Potential of QENS and First Experimental Results. MRS Bulletin - Proceedings of the 8th International Conference on Quasi-Elastic Neutron Scattering (QENS2006) held June 14 -17, 2006, Bloomington, Indiana, USA*, **–**, (2007), 137 – 145.

[106] Wagner F., Bücherl T., Kampfer S., Kastenmüller A., Waschkowski W. *Thermal Neutron Converter for Irradiations with Fission Neutrons*. *Nuclear Physics and Atomic Energy*, **3 (31)**, (2007), 30–36.

[107] Wagner F., Kneschaurek P., Kastenmüller A., Loeper-Kabasakal B., Kampfer S., Breitkreutz H., Waschkowski W., Molls M., Petry W. *The Munich Fission Neutron Therapy Facility MEDAPP at FRM II*. *Strahlentherapie und Onkologie (Urban & Vogel)*, submitted.

[108] Wasmuth U., Meier L., Hofmann M., Mühlbauer M., Stege V., Hoffmann H. *Optimisation of Composite Castings by Means of Neutron-Measurements*. *Annals of CIRP*, **57/1**, (2008), 4 pp.

[109] Wimpory R., Mikula P., Saroun J., Poeste T., Li J., Hofmann M., Schneider R. *Effiency Boost of the Materials Science Diffractometer E3 at BENSC: One Order of Magnitude Due to a Horizontally and Vertically Focusing Monochromator*. *Neutron News*, **19 /1**, (2008), 16 – 19.

[110] Zimmer O., Baumann K., Fertl M., Franke B., Mironov S., Plonka C., Rich D., Schmidt-Wellenburg P., Wirth H.-F., van der Brandt B. *Superfluid-Helium Converter for Accumulations and Extraction of Ultracold Neutrons*. *Phys. Rev. Lett.*, **99**, (2007), 104801–1–4.

Imprint

Publisher:
Technische Universität München
Forschungs-Neutronenquelle Heinz Maier-Leibnitz (FRM II)
Lichtenbergstr. 1
85747 Garching
Germany
Phone: +49 89-289-14966
Fax: +49 89-289-14995
Internet: http://www.frm2.tum.de
email: mailto://userinfo@frm2.tum.de

Editors:
J. Neuhaus
B. Pedersen
E. Jörg-Müller, TUM

Photographic credits:
All images: TUM, except otherwise noted

Design:
B. Pedersen, TUM
J. Neuhaus, TUM
E. Jörg-Müller, TUM

Typesetting(LaTeX 2_ε):
B. Pedersen, TUM
E. Jörg-Müller, TUM